Università di Trento

Dipartimento di Fisica

~ · ~

Academic Year 2025–2026

Dihedral non-Abelian Lattice Gauge Theories: Physics and Quantum Simulation

PhD Candidate

Edoardo Ballini

Supervisor
Prof. Philipp Hauke

Co-supervisor
Dr. Matteo M. Wauters

Acknowledgments

I watched The Office during the pandemic. I don't really remember when, in that vague, chaotic, and at the same time flat period that lasted for 2 years, short and long at the same time. But, at the end of the show, a sentence said by Andy fixed in my mind: "I wish there was a way to know you're in the good old days, before you've actually left them".

In that not easy period, I used to remember with nostalgia the years of the Bachelor's degree in Siena. I have spent three years studying and doing little else, in that lonely building, in the countryside, yet in the city center of Siena at the same time, between goats, peacocks, squirrels, wild rabbits, and wood pigeons. I remember that, in the months before graduating, I was melancholy. The idea of detaching from that (very small) community was pretty sad.

Years later, that sentence by Andy hit me. I realized that I was so lucky to know that *I was* in the good old days, and I felt grateful for that. I am still grateful to the companions of those years, and I am deeply happy whenever I meet them: Stefano, Barto, Maggio, Giggi, Teo, Singoletto, Pietro, Giada, Denise, Cristina, Anna, Bianca, Rosa, Bucalo, Riccardo, Antonio, Saverio, Passa. I limit the list to those whom I meet with a sort of periodicity, but many others are in my happy memories.

Andy's sentence gave me new will to wait for the end of the pandemic and to look for a new situation where I could feel as I did during my bachelor's years. While writing the Master's thesis, during the first months of the War in Ukraine, I had a call with Stefano about the PhD, what to expect, and how to decide whether to do it. He told me that there are three important things, and that it is very difficult to have all of them at the same time: working with people you work well with, on something you like, in a place you like. Of course, they matter for everyone, but if you have to decide to take a (usually) underpaid PhD away from friends and those you love, with no idea of what it will happen after that, they matter a little more.

In the middle of a May night, 4 years ago, completely unsure whether I would apply for at least one PhD position or not, I searched "quantum computation lattice gauge theories" on the internet. I found a presentation given by a professor about his work and I thought it was interesting. This is how I heard about Philipp for the first time.

The goal of this long preamble is to give a little context of how the last three

and a half years were for me: one of those rare moments in life when it seems that all the pieces of the puzzle fell into place. I had the privilege to work with people I have worked well with, on something I have liked, in a place I really love. I worked in a relaxed environment with little pressure, an immeasurable luck. A huge thanks, hence, goes to Philipp for his capabilities of managing such a big group, for his kindness, and for being humble despite his position. One of the first times we talked about physics, he asked me to explain something to him. A second huge thanks goes to Matteo, who followed me for the last two and a half years, teaching me a lot. One of my purposes for the future is to work with the same motivation and methods as the two of them.

I also have to thank all the members of the group that I have met during this year. The international environment really enriched me, thanks to Sebastian, Gopal, Veronica, Julius, David, Alex, Chiara, Andrea, Soumik, Sudipto, Ricardo, Kevin, Philipp U., and the Ganeshes. A special thanks goes to Alberto, with whom I shared the main part of this journey—and the office!—from day 1. Thanks to this community, I learned a lot, much more than what I would have been able to do alone, and I enjoyed a crazy amount of funny lunches. Thanks to Sara, who made our lives much easier. I enjoyed these years also thanks to the other colleagues, especially Tomasz—Hauke group member honoris causa, the only Polish (and person) able to make me enjoy coffee, Andrea, Ludovica, Matteo, Stefano, Margherita, Gianmarco, and many others, whom I apologize to if I do not enumerate them all. Among the members of the stimulating BEC centre, whose I enjoyed the atmosphere and the social events, I want to thank Alberto Biella, with whom we worked, and Iacopo for the funny conversations we had. I hope to share, one day, one Nando's Cecina with him. Yes, an entire one.

Thanks to all of them, waking up to go to work was a pleasing activity. Thanks also to Giuseppe, Pavel, Michele Burrello, and Pietro Silvi, who taught me a lot.

Another aspect of the lovely community I have found in Trento is represented by the *calcetto* group. Special thanks go to Luca, Irene, Benjamin, Comi, Matt, Tommaso, Yohannes, Alessandro, Danial, Giulio, Andrea, Ulysse, Paolo and many others for the countless matches in the last years, organized under the wise supervision of Gianmarco and Tomasz.

Now my thanks leave the Physics Department, but my focus remains on the city of Trento to thank my dear friend and flatmate, Menzo. It is extremely rare to have a friend who wants to move with you to another city, and maintaining a household balance for all this time is anything but obvious. However, Menzo has been my anchor to a life outside of the Department. Thanks to him, I rarely thought about work once at home. We spent several nights playing video games, we shared hundreds and hundreds of dinners, and we went to the supermarket together almost every week. He encouraged me to do more sport, and thanks to him, I started running on the roads at first, and then on the mountains. He accompanied me on several vie ferrate, and we did many hikes together. I spent a lot of time outdoors in nature, and I saw a bunch of mountains that I would never have seen if I had

moved to Trento alone. If I enjoyed my free time so much, if I did not feel alone at home, and, in the end, if I almost did not suffer the stress of doing a PhD, it was largely thanks to him.

In the last four years, our flat has become a perfect basis to host friends with a certain periodicity, especially Giovanni and Alessia. I have to thank Giovanni for the continuous discussions on the future, for his points of view and opinions, which are always precious and welcome. Another special thanks goes to my *old* friend Carlo. *Old* means long-term, but also refers to his age. It is not so common to have a friendship with a 87 years old guy. He taught me that working is easier if you really enjoy what you do, that dedication and willingness to learn from others pay off in the future, that we can do an insane amount of things in a lifespan, and that every obstacle in life, no matter how great, can be best tackled in small steps. During the years, he gave me such great responsibilities that I will hardly ever face more difficult ones in life, and thanks to his generosity and idealism, he made me meet Menzo, Giovanni, Lorenzo, and Luca.

I thank my tuscanian friends, whom I was unable to meet as they deserve during these years. In alphabetical order, thanks to Alessia for being my longest-term friend, Aurelia for surprising me every time, Cecca e Martina for the laughter and generosity, Eli and Simo for their altruism, Jack and Amalia for the sofa in Bologna where they hosted me multiple times, Lulli for her epicity, Panti and Claudia for their hospitality, and Tommi for the organization of games that I, unfortunately, rarely participate to. Meeting you always makes me happy.

Zooming closer and closer, I want to thank my parents for all they did. Counting on a safe base, always willing to help for every possible reason, is not granted. Having always had support for any choice, not even.

Then, I want to thank Donatella and Carlos for their kindness.

In the end, I have to thank Giulia. Over all these years, from Siena to Trento, passing through Pisa, you have helped me in the hardest moments and you always encouraged me, even when I didn't know what to do. You have been not only a stable constant of the last decade, but the reason why I try to plan my future to the best of my abilities. You definitely made me a better person and motivated me on several aspects of my life. The prospect of sharing our future is always at the heart of my choices.

I have finally finished.

Thank you, everyone, for these *good old days*.

When I was a child, maybe 8 years old, I received an Encyclopaedia for kids as a Christmas present. The first volume, if my memory is correct, was about Space and the Universe. I remember the printed images of Astronauts, of the Solar System, and of science-fiction cities built on platforms in outer space. That was, as far as I remember, my first encounter with something comparable to Physics. In almost all my memories, when I was exposed, as a child, to Science or scientific knowledge outside of school, it was because of my grandfather Carlo. Whether it was a TV program by Piero Angela watched in the living room or in the bedroom, whether it was some (unsolicited) explanations of how an internal combustion engine works, whether it was researching in his Encyclopaedia a new species of bird that started to migrate outside our home, or a DVD with the future engineering challenges given as a gift and watched together, he sat beside me. In all these cases but the engines, he never tried to teach me anything. It was, instead, a way to discover something together. He was not a scientist or had a degree, even if he had a good education compared to the average of his time. He was just curious, I guess, of how the world works, and he felt pleasure in learning new things, understanding something new, or seeing what the technology could do, one day in the future. These are the motivations that pushed me to study Physics, and I have never had the maturity to thank him. This paragraph tries to repay this debt.

Abstract

Lattice gauge theories provide a first-principles, non-perturbative formulation of the fundamental interactions of the Standard Model, and their Hamiltonian reformulation on a quantum simulator offers a promising route to regimes—real-time dynamics, finite baryon density—that lie beyond the reach of Euclidean Monte Carlo methods. With the ultimate goal of overcoming these shortcomings, over the last decade, quantum simulations of Abelian lattice gauge theories have expanded from the first proofs of principle to the experimental study of confinement and string breaking by pair production. One of the next frontiers lies in the simulation of non-Abelian theories, which are significantly more demanding both in local Hilbert space dimension and in symmetry-protection requirements, and ultimately essential for addressing open problems in high-energy physics. In this thesis, we investigate dihedral non-Abelian lattice gauge theories D_N—whose small order and finite local dimension make D_3 and D_4 natural targets for near-term quantum platforms—as a minimal yet physically rich arena for the study of non-Abelian gauge dynamics. After introducing dihedral groups and the associated lattice gauge theories, we propose a gauge-fixed ladder model that reduces the effective dimensionality while preserving the essential physics. We use it to show that the D_3 theory on a ladder displays a smooth crossover—rather than a sharp phase transition—between electric- and magnetic-dominated regimes, with the nonstabilizerness peaking in the crossover region. Furthermore, we introduce a formulation of the model compatible with the analysis of the Eigenstate Thermalization Hypothesis. We then study string breaking in pure-gauge D_N ladders in the presence of static charges through tensor-network DMRG simulations in the rishon formalism. We show that for odd N static charges are screened by gluelumps—charge-glueball bound states enabled by the trivial centre of the group—while for even N a fundamental flux string persists. Turning to the quantum-simulation side, we introduce a dynamical post-selection (DPS) protocol in which the local gauge charges are tested by mid-circuit measurements on auxiliary registers, and we show that gauge protection emerges through a sharp quantum Zeno transition in the spectrum of an associated Liouvillian. We verify the generality of this picture on $\mathbb{Z}_2$, $\mathbb{Z}_3$, and truncated $U(1)$ gauge groups, identifying an optimal window of measurement frequencies that survives also in the presence of noisy measurements. Finally, we benchmark DPS against an alternative post-processed symmetry verification scheme on a two-plaquette D_3 model designed

for state-of-the-art qudit hardware. We find that both protocols significantly improve the reconstructed dynamics, with DPS tracking the exact evolution over longer times. Taken together, the results of this thesis position dihedral gauge theories as a concrete stepping stone from Abelian proofs of principle toward genuinely non-Abelian quantum simulation on near-term devices.

Sommario

Le teorie di gauge su reticolo (lattice gauge theories) forniscono una formulazione non perturbativa e da principi primi delle interazioni fondamentali del modello Standard, e la loro riformulazione Hamiltoniana su un simulatore quantistico offre una promettente prospettiva verso regimi—come la dinamica in tempo reale o con densità barionica finita—che sono fuori dalla portata dei metodi Monte Carlo Euclidei. Con l'obbiettivo ultimo di superare questi limiti, durante l'ultimo decennio, le simulazioni quantistiche di teorie di gauge Abeliane su reticolo sono passate dalle prime dimostrazioni di principio a studi sperimentali sul confinamento e sulla rottura di stringhe di campo elettrico dovuta a produzione di coppie. La simulazione di teorie non Abeliane, essenziali per affrontare un giorno i problemi aperti in fisica delle alte energie, può essere identificata come una delle prossime frontiere del campo, richiedendo spazi di Hilbert locali più grandi e una protezione delle simmetrie più complicata. In questa tesi, approfondiamo le teorie di gauge non Abeliane su reticolo con il gruppo di gauge diedrale D_N—la limitata cardinalità e la dimensione locale finita rendono D_3 e D_4 degli obbiettivi naturali per piattaforme quantistiche a breve termine—come un candidato minimale ma fisicamente ricco per lo studio delle dinamiche di gauge non-Abeliane. Dopo aver introdotto i gruppi diedrali e le teorie di gauge su reticolo associate, proponiamo un modello su una geometria simile a una scala a pioli (ladder) in cui fissiamo alcuni campi di gauge, in modo da ridurre la dimensione effettiva del modello, preservandone al contempo la fisica essenziale. Usiamo questo modello per mostrare che una teoria D_3 su una ladder mostra un passaggio graduale—piuttosto che una transizione di fase netta—tra regimi dominati dal termine elettrico o magnetico, con la nonstabilizerness che raggiunge valori massimi nella regione intermedia. Inoltre, introduciamo una formulazione del modello compatibile con l'analisi dell'ipotesi di termalizzazione degli autostati. Procediamo con lo studio della rottura di stringa in teorie D_N di pura gauge in presenza di cariche statiche attraverso simulazioni su tensor network, con l'algoritmo DMRG, su una ladder, nel formalismo rishonico. Mostriamo che per N dispari le cariche statiche sono schermate dalle "gluelumps"—stati legati della carica e di una glueball che sono permessi dal fatto che il gruppo ha un centro banale—mentre per N pari una stringa di flusso nella rappresentazione fondamentale persiste. Passando alla parte di quantum simulation, introduciamo un protocollo di selezione dinamica a posteriori (DPS), in cui le cariche di gauge locali sono testate per mezzo di misure

effettuate durante la misurazione del circuito su registri ausiliari, e mostriamo che la protezione della gauge emerge attraverso una transizione Zeno netta nello spettro del Liouvilliano associato. Verifichiamo la generalità di questo quadro sui gruppi di gauge $\mathbb{Z}_2$, $\mathbb{Z}_3$, e $U(1)$ troncato, evidenziando una finestra ottimale nella frequenza delle misure che sopravvive anche in presenza di misurazioni rumorose. Infine, testiamo il metodo DPS, comparandolo con uno schema alternativo per verificare le simmetrie a posteriori, su un modello con D_3 di due plaquette, progettato per un hardware attuale basato sui qudit. Mostriamo che entrambi i protocolli migliorano significativamente la dinamica ricostruita, con il DPS che segue l'evoluzione esatta per tempi più lunghi. Nel complesso, i risultati di questa tesi posizionano le teorie di gauge diedrali come un concreto passo avanti dalle dimostrazioni di principio su teorie Abeliane verso simulazioni quantistiche autenticamente non-Abeliane su piattaforme quantistiche a breve termine.

Contents

Introduction

Gauge theories are one of the cornerstones of modern physics. They are not only the backbone of the Standard Model in particle physics, but also emerge naturally in condensed matter physics and play a role in topological quantum computing [1–3]. The defining characteristic of a gauge theory is an extensive set of local symmetries under which the theory is invariant [1]. These symmetries are parametrized by a group—the "gauge group"—whose algebraic properties are deeply connected to the physical content of the theory. The Abelian group $U(1)$ is the gauge group of quantum electrodynamics. Its associated local constraint is the Gauss law of classical electromagnetism, $\nabla \cdot \mathbf{E} = \rho/\varepsilon$: the local divergence of the electric field equals the local charge density. The electroweak interaction is described by the gauge group $SU(2)_L \times U(1)_Y$, where the $SU(2)_L$ factor governs the weak isospin sector, responsible for nuclear decays such as beta decay. Finally, the non-Abelian group $SU(3)$ is the gauge group of quantum chromodynamics (QCD), the fundamental theory of the strong nuclear interaction, which confines quarks and gluons into hadrons.

The formulation of continuous gauge theories on a spatial discrete lattice was proposed by Wilson as a gauge-invariant, non-perturbative regularization of QCD, providing a well-defined framework for studying the strong-coupling regime that is inaccessible to perturbation theory [2, 4–6]. In particular, the Monte Carlo formulation of lattice QCD has enabled several landmark results, including the computation of the hadron mass spectrum, and the study of the QCD phase transition and the properties of the quark-gluon plasma [7–9]. These successes, however, are confined to regimes accessible by Monte Carlo methods. The latter are hindered by the sign problem at finite fermion densities [10] or non-trivial topological angles [11], and are inherently restricted to Euclidean time evolution, because in real time the path-integral measure acquires oscillating phases e^{iS}—where S is the action—that cannot be interpreted as probabilities and hence cannot be sampled stochastically.

In Feynman's spirit of using quantum mechanics to simulate quantum physics [12], quantum simulation represents a promising tool for lattice gauge theories. Mapping a lattice gauge theory onto a quantum simulator would circumvent the sign problem and open access to real-time dynamics [13, 14], with the ultimate goal of exploring the full phase diagram of QCD [15, 16].

In the last decades, quantum simulation has been developed under two main paradigms: analog and digital quantum simulation [17–20]. On one hand, analog

quantum simulators realize the target quantum system by engineering a controllable quantum platform whose continuous time evolution faithfully mimics that of the target theory. On the other hand, in digital quantum simulation, a universal set of logical quantum gates [21] allows for the mapping of a target Hamiltonian onto a quantum computer. A central feature of the digital paradigm is the need to discretize time evolution, typically achieved via the Trotter–Suzuki decomposition [22, 23].

Quantum simulation can be obtained on several platforms based on different technologies, such as superconducting qubits [24, 25], trapped ions [26–29], ultracold atoms [30–33], photonic platforms [34, 35], or quantum dots [36, 37]. However, the boundary between the analog and digital paradigms is not always sharp: several platforms can be operated in both regimes, and hybrid analog-digital protocols—where a continuously evolving analog background is periodically interspersed with discrete digital gates—have been explored as a practical intermediate strategy [38–40]. Quantum hardware has shown important progress in recent years [41, 42], such as the first demonstrations of quantum computational advantages in random circuit sampling computational problems and Gaussian Boson sampling problems, on superconducting quantum devices and photonic systems [43–50].

With the perspective of simulating lattice gauge theories on quantum hardware [14, 15, 51–57], many proposals for various gauge groups have been made on diverse platforms, like superconducting qubits [58], trapped ions [59–63], ultracold atoms [13, 64–73], or cavity quantum electrodynamic setups [74]. Hardware improvements and deeper theoretical understanding enabled experimental quantum simulations to reach important milestones in addressing lattice gauge theories, on superconducting qubits [75–82], trapped ions [83–86], and ultracold atoms [87–93].

In both analog and digital quantum simulations, since the gauge groups of the Standard Model are continuous Lie groups, the infinite-dimensional Hilbert space describing the gauge fields must be discretized. Several strategies have been proposed: truncation in the representation space [63, 94–97], quantum link models [98–101], reformulations of the theories in new bases [62, 102–106], and the use of discrete subgroups of a continuous group to approximate the parent Lie theory [73, 107–113]. A central and persistent obstacle is the scaling from Abelian to non-Abelian gauge theories. Experimental results for Abelian groups are at present mostly limited to systems whose gauge fields have local dimension $d = 2$, which can be efficiently encoded on qubits. Non-Abelian groups, however, require working with larger local Hilbert spaces even in their most minimal formulations. To appreciate this, consider $SU(2)$: the smallest non-trivial representation-space truncation gives a local dimension $d = 5$ for the gauge fields, while its smallest non-Abelian discrete subgroup, the quaternion group $\mathcal{Q}_8$, has $|\mathcal{Q}_8| = 8$ group elements. Furthermore, the smallest non-Abelian group, D_3, already has six elements.

In all cases, simulating non-Abelian lattice gauge theories requires encoding gauge fields on a quantum register of at least three qubits, which increases even for local operations the number of entangling gates—one of the principal bottlenecks of current quantum hardware in the Noisy Intermediate-Scale Quantum (NISQ)

era [114]. The large local dimension of gauge fields in lattice gauge theories therefore represents a natural application for quantum hardware based on qudits, i.e., quantum systems with $d > 2$ levels [115, 116]. Qudit-based computation has been developed on several platforms: trapped ions [116–118], transmons [119–126], Rydberg arrays [127], photonic circuits [128], ultra-cold atomic mixture [129], and superconducting radio-frequency (SRF) cavities [130, 131].
Formulations of lattice gauge theories on qudits have been recently explored, with several proposals [63, 73, 110, 132–135]. Seminal experimental results demonstrate the advantages of this approach in a trapped ion platform, simulating one plaquette in truncated quantum electrodynamics [136].

In the NISQ era, quantum hardware is subject to errors that compromise the reliability of its outputs [137]. In the context of lattice gauge theories, errors can drive the quantum state outside of the physical gauge-invariant sector, effectively breaking the local symmetry that defines the theory. This problem can be addressed through quantum error correction [138–142] or error mitigation [143]. On the quantum error correction side, important progress has been made toward fault-tolerant quantum computing: several platforms have surpassed the "break-even point", where the logical error rate falls below the physical one, and have demonstrated error-corrected logical qubits with extended coherence times, marking a significant step toward scalable fault-tolerant devices [144–148]. However, these advances are still remarkable proof-of-concept demonstrations, and, in the current generation of hardware, error mitigation remains an essential tool for near-term quantum computation.

In this context, identifying and studying non-Abelian gauge theories that are tractable in near-term quantum hardware represents an important and timely research direction. Discrete non-Abelian dihedral groups D_N—the symmetry groups of regular polygons—are valid candidates. Their relative algebraic simplicity and the finite dimension make them an ideal setup for proof-of-concept experiments with non-Abelian gauge theories. Further, D_3 is the smallest non-Abelian group, while D_4, having 8 elements, can be efficiently encoded in 3 qubits. As the minimal testing ground for non-Abelian quantum computation, they appear at the basis of several proposals [72, 134, 149, 150], and have been tested in quantum annealing [151]. Furthermore, they can play a role in topological quantum computation [152–155], thus connecting to communities beyond high-energy physics, from condensed matter to quantum information.

Yet, the rich physics of these theories is still vastly underexplored, and this thesis aims to contribute to filling this gap. Investigating the physics of DN theories, identifying benchmarks that are challenging yet within the reach of near-term devices, and testing symmetry-protection methods in the presence of noise can lay the groundwork for meaningful proof-of-concept experimental results that would constitute a novel fundamental ingredient for quantum simulation of lattice gauge theories.

A natural question in this context is whether quantum simulation of lattice gauge theories can realistically achieve a quantum advantage over classical methods—i.e.,

address computationally relevant problems that are genuinely intractable classically. The answer is not yet settled, since quantum simulation and classical simulation methods are strongly stimulating each other. In particular, tensor-network (TN) methods—most notably matrix product states (MPS) and projected entangled pair states (PEPS), employed via algorithms such as DMRG and iTEBD—have proven extremely powerful for one-dimensional and quasi-one-dimensional gauge theories, providing benchmarks against which quantum hardware can be validated [15, 156, 157]. At the same time, the entanglement structure probed by TN simulations helps identify the regimes where classical methods become insufficient and where a genuine quantum computational advantage may emerge. The interplay between TN methods and quantum simulation is thus one of the most productive axes of current research in the field.

This thesis is structured as follows. In chapter 1, we provide theoretical background on lattice gauge theories and their formulation for digital quantum simulation, before introducing the dihedral groups and their implementation for digital quantum simulation. We then introduce qudit hardware and discuss how to implement lattice gauge theories on it.

The rest of the thesis is divided into two parts. In the first part, we discuss the physics that can be studied on dihedral lattice gauge theories. In chapter 2, we analyze the structure of gauge-invariant sectors for dihedral lattice gauge theories, comparing them with those of an Abelian theory. We introduce the ladder geometry and derive an effective Hamiltonian after gauge-fixing. We investigate the physics of the effective model, including the crossover between the weak- and strong-coupling regimes, the measurement of quantum resources, and the analysis of the integrability of the model. In chapter 3, we study a ladder system with a D_N gauge group in the presence of static charges connected by a flux string. We relate the string-breaking of this configuration, mediated by the formation of gluelumps, to the presence of a non-trivial center of the gauge group. We compare D_3 and D_4 numerically, showing that string breaking occurs for D_3, which has a trivial center, but not for D_4, which has a non-trivial center.

In the second part, we discuss error mitigation methods to verify local gauge symmetries in the NISQ era. In chapter 4, we introduce an error mitigation scheme based on the measurement of gauge charges on auxiliary registers. We test it on a one-dimensional model with $\mathbb{Z}_2$ as the gauge group, for which we model a quantum simulation in the presence of gauge-breaking errors. We show a Zeno phase transition as a function of the frequency with which the local gauge charges are measured, and characterize the error mitigation scheme for other Abelian groups and in the presence of noisy measurements. In chapter 5, we study symmetry verification methods for a D_3 gauge theory. In particular, we compare error mitigation based on the measurement of local gauge charges with an effective projection onto the physical subspace based on the measurement of an extensive set of observables. Finally, we summarize the conclusions in chapter 6, discussing the possible outlooks of what we studied in this thesis.

This thesis is largely based on the following papers:

- Quantum Resources in Non-Abelian Lattice Gauge Theories: Nonstabilizerness, Multipartite Entanglement, and Fermionic Non-Gaussianity, Gopal Chandra Santra, Julius Mildenberger, **Edoardo Ballini**, Alberto Bottarelli, Matteo M. Wauters, Philipp Hauke.
  arXiv:2510.07385 [quant-ph] (*under review*) [158]. Chapter 2

  In this paper, we compute different quantities to characterize quantum resources in non-Abelian lattice gauge theories on a ladder. I contributed by writing the code for the Hamiltonian formulation of the D_3 gauge-fixed model and the $\mathbb{Z}_N$ clock model, as a function of the coupling, the electric energies, and the system size. Furthermore, I derived the gauge-fixed Hamiltonian for the D_3 theory. On the same system, I studied the crossover between the electric and the magnetic phase by computing the energy gap, investigating the role of global gauge transformations to correctly track it.

- When the center matters: color screening and gluelumps in dihedral lattice gauge theories, Pavel P. Popov*, **Edoardo Ballini***, Alberto Bottarelli, Michele Burrello, Pietro Silvi, Matteo M. Wauters, Philipp Hauke.
  arXiv:2512.00152 [hep-lat] (*under review*) [159].
  Chapter 3

  In this paper, we study dihedral lattice gauge theories on a ladder in the presence of static charges, which cause a string-flux in the strong coupling regime. We show that for D_3 string-breaking may occur without matter production, due to the presence of a trivial center. As main contributions, I formulated the rishon formalism for D_3 and D_4 theories on a ladder, I identified the gauge-invariant states on the dressed sites basis, and I wrote the selection rules. On the dressed sites basis, I formulated the transformation operators, I wrote the electric Hamiltonian of the theory, and worked on the magnetic term.

  *Equal contribution

- Symmetry-protection Zeno phase transition in monitored lattice gauge theories, Matteo M. Wauters, **Edoardo Ballini**, Alberto Biella, and Philipp Hauke.
  Phys. Rev. B, 111, 094315 (2025) [160].
  Chapter 4

  Here, we studied a Zeno-phase transition triggered by the measurement rate of local gauge charges on Abelian lattice gauge theories, such as $\mathbb{Z}_2$, $\mathbb{Z}_3$, and truncated $U(1)$ gauge symmetries. I collaborated with Matteo Wauters and Alberto Biella to develop the framework for the dynamical post-selection error mitigation scheme we explored. I performed some of the numerical simulations.

- Symmetry verification for noisy quantum simulations of non-Abelian lattice gauge theories, **Edoardo Ballini**, Julius Mildenberger, Matteo M. Wauters,

and Philipp Hauke.
Quantum, 9, 1802 (2025) [161].
Chapter 5

In this work, we compared two different symmetry verification techniques to mitigate errors in quantum simulations of non-Abelian lattice gauge theories, where the standard post-selection fails. I studied how to apply a quantum circuit to a specific case and how to implement it on qudit hardware. I performed numerical simulations of a noisy time evolution for a non-Abelian lattice gauge theory, modelling a noise model and two different error mitigation techniques: dynamical post-selection and post-processed symmetry verification. For the former, I studied the frequency of the mid-circuit measurements to achieve a reliable error-mitigated time evolution, and how to implement them with circuits on qudit hardware. I compared the two schemes, highlighting the advantages and disadvantages of their implementation on real hardware.

Under preparation

- Eigenstate Thermalization Hypothesis in discrete non-Abelian lattice gauge theories, Marco Vaia, **Edoardo Ballini**, Alberto Bottarelli, Matteo M. Wauters, Philipp Hauke.
  Chapter 2

  In this project, we use a gauge-fixed model on a ladder to test the Eigenstate Thermalization Hypothesis in discrete pure-gauge non-Abelian lattice gauge theories, implementing D_3 as the gauge group. I contributed by identifying the gauge-invariant sectors in D_N lattice gauge theories and by identifying the global symmetries of the theory, like the vertical spatial inversion that is taken into account to find a proper set of quantum numbers.

Others (not included in this thesis)

- Quantum computation of thermal averages for a non-Abelian D_4 lattice gauge theory via quantum Metropolis sampling, **Edoardo Ballini**, Giuseppe Clemente, Massimo D'Elia, Lorenzo Maio, Kevin Zambello.
  Phys. Rev. D 109, 034510 (2024) [162].

- First order phase transition in a dihedral lattice gauge theory, Alberto Bottarelli, **Edoardo Ballini**, Matteo M. Wauters, Philipp Hauke.
  Under preparation

- Non-Hermitian Hamiltonian engineering, Paolo Boschetto, Matteo M. Wauters, **Edoardo Ballini**, Alberto Biella, Philipp Hauke.
  Under preparation

Chapter 1

Theoretical Background

This chapter summarizes the background of the Hamiltonian formulation and quantum simulation in lattice gauge theories (LGTs). After that, we introduce the dihedral groups D_N, and we show how to implement operators necessary for the quantum simulation of dihedral LGTs. Finally, we introduce the framework of digital quantum simulation of LGTs on qudit hardware.

1.1 Lattice Gauge Theories

The main ingredient for a quantum simulation of lattice gauge theories is their Hamiltonian formulation [5]. Gauge theories are many-body systems characterized by local symmetries that strongly constrain their dynamics. The symmetries, i.e., the gauge transformations, are described by the "gauge group" $\mathcal{G}$ of the theory. In the Standard Model, $U(1)$, $SU(2)$, and $SU(3)$ are the gauge groups of quantum electrodynamics, the weak interaction, and the strong interactions, respectively. We speak of "Abelian theories" when the gauge group is Abelian and of "non-Abelian theories" when the gauge group is not.

Spatial degrees of freedom of gauge theories are discretized on a lattice, which has two fundamental components: sites and links. The sites, denoted by $x \in \mathbb{Z}^d$, are populated by matter fields. The gauge fields mediating the interaction between particles live on the links between matter sites, labelled as (x, k) with $k \in \{1, \dots, d\}$, where k denotes the spatial direction along which the link points, associated with the positively oriented unit vectors $\{\hat{k}_{k=1}^{d}\}$.

In this thesis, we will consider a square lattice. The local symmetries are discretized in the lattice by operating on a site n and on the connected links according to their directionality [149]:

$$\Theta_{h,n} = \prod_{o} \theta_{h,o}^{L} \prod_{i} \theta_{h,i}^{R} \theta_{h,n}^{Q} \ , \tag{1.1}$$

where i and o label the *incoming* and *outgoing* links connected to the site n, $\theta_{h,n}^{Q}$

describes how the matter field transforms, and $\theta_h^{L(R)}$ is the left(right) multiplication operator by the group element h, such that

$$\begin{aligned} \theta_h^L |k\rangle &= |hk\rangle \ , \\ \theta_h^R |k\rangle &= |kh^{-1}\rangle \ . \end{aligned} \tag{1.2}$$

In Abelian theories, one does not need both operators, as one of them is sufficient to describe the theory. In non-Abelian theories, however, one must take both operators into account. Physical observables are invariant under local gauge transformations,

$$\Theta_{h,n} \hat{O} \Theta_{h,n}^\dagger = \hat{O} \ , \tag{1.3}$$

that also holds for the Hamiltonian operator H, which, hence, commutes with all the local symmetries

$$[H, \Theta_{h,n}] = 0 \quad \forall \ n \in \mathbb{Z}^d, \ h \in \mathcal{G} \ . \tag{1.4}$$

Eq. (1.4) implies that for every local symmetry a conserved quantity exists, the "gauge charge" $\alpha_{h,n}$, which is nothing but an eigenvalue of $\Theta_{h,n}$. Since $\theta^{L(R)}$ are unitary operators, $\alpha_{h,n}$ is a root of the unity. The set $\{\alpha_{h,n}\}$ defines the "gauge sector", i.e., the Hilbert subspace that is not connected to other sectors by gauge-invariant operations. Gauge-invariant states are those that belong to a gauge sector, such that

$$\Theta_{h,n} |\psi\rangle = \alpha_{h,n} |\psi\rangle \quad \forall \ n \in \mathbb{Z}^d, \ h \in \mathcal{G} \ . \tag{1.5}$$

The physical neutral sector corresponds to $\alpha_{h,n} = 1 \ \forall n, h$, which corresponds to the Gauss law constraint. For example, in electromagnetism, it corresponds to $\nabla \cdot \mathbf{E} = \rho/\varepsilon_0$.

In Lie theories described by continuous groups, as in the Standard Model, the operators in Eq. (1.1) are given by the generators of the group's algebra – left generators $\{L_a\}$, right generators $\{R_a\}$, and local charge generators $\{Q_{a,n}\}$ and group parameters

$$\begin{aligned} \theta_h^L &= e^{i\phi_a(h) L_a} \ , \\ \theta_h^R &= e^{i\phi_a(h) R_a} \ , \\ \theta_{h,n}^Q &= e^{i\phi_a(h) Q_{a,n}} \ . \end{aligned} \tag{1.6}$$

The sum of generators generates the local gauge transformations [163]

$$G_a = \sum_i L_{a,i} - \sum_o R_{a,o} - Q_{a,n} \ . \tag{1.7}$$

For the results we expose in this thesis, it is worth introducing a discrete non-Abelian group with elements $h \in \mathcal{G}$ and order $|\mathcal{G}| \in \mathbb{N}$. We denote a unitary matrix

representation of the group elements as $D^j_{mn}(h)$, where j labels the irreducible representations and m, n are the row and column indices of the matrix. A representation ρ of a group $\mathcal{G}$ on a vector space V is a homomorphism from the group $\mathcal{G}$ to the general linear group on V, $\mathrm{GL}(V)$. Hence,

$$\rho : \mathcal{G} \mapsto \mathrm{GL}(V) \ . \tag{1.8}$$

For finite groups, one has $|\mathcal{G}| = \sum_j \dim(j)^2$, where $\dim(j)$ is the dimension of the jth irreducible representation [164]. The representation basis $|jmn\rangle$ may be connected to the group element basis $|g\rangle$ following the great orthogonality theorem as

$$\langle g|jmn\rangle = \sqrt{\frac{\dim(j)}{|\mathcal{G}|}} D^j_{mn}(g) \ , \tag{1.9}$$

which describes the generalized Fourier transform of the group. The group Fourier transform is one of the elementary unitary operations needed to implement digital quantum simulations of a lattice gauge theory with discrete groups [149, 150], as it is the change of basis from the group element (magnetic) basis to the irrep (electric) basis. To give an example from an Abelian setting, the group Fourier transform for a $\mathbb{Z}_2$ gauge symmetry is the Hadamard gate on the qubit Hilbert space. In general, the commonly known *Quantum Fourier Transform* algorithm is the Fourier transform for the group $\mathbb{Z}_{2^n}$. In Eq. (1.2), we described the action of $\theta^{L(R)}$ operators in the group element basis, but they can be expressed in the irrep basis using Eq. (1.9) as the change of basis.

Finally, the parallel transporter U^j_ℓ is an operator that acts on the link degree of freedom. It associates the states $|g\rangle$ with the $j-$th representation of the corresponding group element $U^j_{mn}|g\rangle = D^j_{mn}(g)|g\rangle$. They transform with the group multiplication operators as

$$\begin{aligned} \theta^L_g U^j_{mn} \theta^{L\dagger}_g &= D^j_{mk}(g^{-1}) U^j_{kn} \ , \\ \theta^R_g U^j_{mn} \theta^{R\dagger}_g &= U^j_{mk} D^j_{kn}(g) \ . \end{aligned} \tag{1.10}$$

Equation (1.10) can be verified by combining Eq. (1.2) with the representation of U^j_{mn} in the computational basis $\{|g\rangle\}$. The parallel transporter U can be expressed in discrete groups as

$$U^j_{mn} = \sum_g D^j_{mn}(g) |g\rangle \langle g| \ , \tag{1.11}$$

and in continuous groups as

$$U^j_{mn} = \int dg D^j_{mn}(g) |g\rangle \langle g| \ , \tag{1.12}$$

where the integration is over the group's Haar measure for compact Lie groups.

Finally, matter can be introduced. In this thesis, we always work with fermionic matter coupled with gauge fields. We introduce the spinors $\psi_a^{\dagger j}$, where a may identify spin, flavour, or color, and j labels the irreducible representation of the group the spinor belongs to. Local unitary transformations for the matter, then, read as [149]

$$\begin{aligned} \theta^{Q,j}_{h,n}\psi^{\dagger,j}_a(n)\theta^{Q\dagger,j}_{h,n} &= \psi^{\dagger j}_b(n)D^j_{ba}(h) \ , \\ \theta^{Q,j}_{h,n}\psi^{j}_a(n)\theta^{Q\dagger,j}_{h,n} &= D^j_{ab}(h^{-1})\psi^{j}_b(n) \ . \end{aligned} \tag{1.13}$$

The choice of j is usually fixed to the fundamental representation, hence we will omit it in the following.

These are the ingredients needed to describe the Kogut–Susskind Hamiltonian in $d+1$ dimensions, which consists of four terms: the electric term, the magnetic term, the mass term, and the hopping term. The first two, the electric and the magnetic terms, depend on the gauge field, forming the so-called "pure gauge" Hamiltonian. The other two, the mass and the hopping term, describe the mass density energy and how the particles can spatially move in the lattice.

The electric term is diagonal in the irrep basis, that is also known as the "electric basis", and is expressed as a direct sum over all the links,

$$H_E = \frac{c\hbar}{a} g^2 \sum_{\ell \in \text{links}} \sum_{j;m,n} \alpha_j \left|j, mn\right\rangle_\ell \left\langle j, mn\right| \ , \tag{1.14}$$

where g is the coupling of the theory, a is the spatial lattice spacing, and α_j is the electric energy associated with the representation j. For $SU(2)$ theories, it holds that $\alpha_j = j(j+1)$, while for discrete groups there is not a unique way to define α_j. In the group element basis, the projector over the irrep j, $P^j = \sum_{mn} |j, mn\rangle\langle j, mn|$, is written as

$$P^j = \sum_h \frac{\dim(j)}{|\mathcal{G}|} \chi^j(h)\theta^L_h \ , \tag{1.15}$$

where the sum is over the group elements h, $\chi^j(h)$ is the character, i.e., the trace, of the group element h in the representation j. Without loss of generality, we used θ^L when writing the projectors P^j, but one could equally well choose θ^R.

The magnetic term is diagonal in the group element basis, and consists of the sum over the plaquette terms

$$H_B = -\frac{c\hbar}{ag^2} \sum_p \Re\left[\mathrm{Tr}\left(U_{p_1}U_{p_2}U^\dagger_{p_3}U^\dagger_{p_4}\right)\right] \ . \tag{1.16}$$

In the following, we work with natural units $c = \hbar = 1$ so that the inverse of the lattice spacing a sets the energy scale. In general, we also fix $a = 1$. The sum runs over all plaquettes in the lattice and $p_1, \ldots, p_4$ are the four links of a plaquette taken in anticlockwise order and starting from the lower edge, see Fig. 1.1. The directionality of the lattice links determines whether we have to take the operator

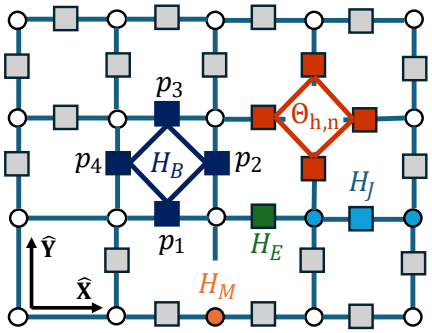

Figure 1.1: Square lattice with gauge degrees of freedom on the links and matter fields on the sites. Highlighted are a four-body term entering the magnetic Hamiltonian H_B, a single-body term of the electric Hamiltonian H_E, a three-body term of the hopping Hamiltonian H_J, a single-body term of the mass Hamiltonian H_M, and a local gauge transformation $\Theta_{h,n}$. The arrows in the bottom-left corner indicate the directionality of the lattice.

$U^j_{p_\alpha}$ or its Hermitian conjugate. We set the $+\hat{x}$ and $+\hat{y}$ directions to be positive, consistently with Eq. (1.16).

The mass term of the matter is written as

$$H_M = M \sum_n (-1)^n \psi^\dagger_a(n)\psi_a(n) \ , \tag{1.17}$$

where the sum of the particle density is over all the sites of the lattice, the sum over different species of fermions a is implied, and $(-1)^n$ means that fermionic matter is represented by staggered fermions, such that the "empty state", i.e., the state without particles, is described by an absence of fermionic particles on the matter sites (with n even) and by the presence of two fermions in the anti-matter sites (with n odd). Staggered fermions are one of the most common choices to avoid the fermion doubling problem, which occurs in the continuum limit [165–168].

Finally, the hopping term describes how particles move in the space by coupling matter and gauge fields

$$H_J = J \sum_{n,k\in\{1,\dots,d\}} \psi^\dagger_a(n) U_{ab}(x,k) \psi_b(n+\hat{k}) + \text{H.c.} \ , \tag{1.18}$$

where J is the hopping parameter. The interaction between matter and gauge fields ensures the gauge invariance of the hopping, i.e., if a fermion moves in the space, the gauge field changes accordingly to preserve the gauge charges.

1.2 Quantum Simulation of Lattice Gauge Theories

1.2.1 Motivations for Hamiltonian quantum simulation

In the last decades, LGTs have been formulated in the Lagrangian framework in order to numerically study them by Monte Carlo algorithms [165, 169–171]. Lattice quantum chromodynamics (Lattice QCD) represents the most important success of this framework, allowing the computation of the hadron mass spectrum, and the study of the QCD phase transition and the properties of the quark-gluon plasma [7–9]. However, some important shortcomings strongly reduced the applicability of Lattice QCD. In the exploration of the phase diagram, the "infamous" sign problem [172, 173] prevents studying systems in the presence of high fermion density or of the topological theta angle, being the statistical weights not positive-defined. It is possible to fix this issue by taking the absolute value of the statistical weights, but the price to pay is to incur an **NP** numerical problem, which is thought to be **NP-hard** [10]. Furthermore, a Wick rotation is needed in the Lagrangian formulation, i.e., a rotation from the real to the Euclidean time by $t \to -i\tau$, where τ is the Euclidean time. This rotation prevents performing the Real-time evolution.

All these limitations can be resolved by the Hamiltonian formulation of LGTs [5], at the price of an exponential Hilbert space scaling with the system size, which prevents the Hamiltonian formulation from being useful on classical computers. Quantum simulation can help address this issue, making the exponential scaling of the Hilbert space dimension a linear requirement in the quantum resources [12]. The goals of quantum simulation of LGTs are manifold [15, 57, 163, 174]. In the short term, even modest-sized quantum simulators can provide access to real-time dynamics—such as thermalization, string-breaking, and particle production—that are intrinsically inaccessible to Euclidean Monte Carlo approaches. In the medium term, the exploration of the QCD phase diagram at finite baryon density, currently blocked by the sign problem, represents one of the primary targets. In the long term, the ultimate goal is a full-scale, first-principles quantum simulation of non-Abelian gauge theories such as QCD, enabling the study of non-perturbative phenomena—including confinement, hadron structure, and the properties of dense nuclear matter—from first principles.

A complementary classical approach to lattice gauge theories is provided by tensor network methods [175–178]. Their applicability is subject to two distinct limitations of different origin: on one hand, one-dimensional architectures such as matrix product states are structurally restricted to one spatial dimension, a constraint that tree tensor networks [157] or two-dimensional generalizations such as PEPS attempt to overcome [179, 180]; on the other hand, and more fundamentally, the computational cost of tensor network contractions grows exponentially with entanglement, making highly entangled states—even in one dimension—out of reach regardless of the network geometry. Despite these challenges, tensor network methods in lattice gauge theories constitute a prolific research field [14, 157, 181, 182], with new approaches continually expanding the scope of tractable problems [94, 95,

97, 183–192].

Both approaches have already delivered preliminary explorations of equilibrium features [193, 194] and dynamics [195, 196] in one-dimensional $SU(3)$-symmetric LGTs, although the large number of degrees of freedom involved still poses formidable challenges. In this thesis, numerical results in Chapter 3 are obtained using the Density Matrix Renormalization Group (DMRG) [197] to compute the ground state. In Chapters 4 and 5, instead, we focus on digital quantum simulation of real-time dynamics, which requires a discretization of the time evolution via the Trotter–Suzuki decomposition [22, 23].

1.2.2 Trotterized time evolution

Since one of the main advantages of quantum simulation of LGTs is the possibility to implement the real-time evolution, in the following, we recall how to encode the first-order Trotterized time evolution on quantum computers, such that

$$e^{-iHt} = (e^{-iH\Delta t})^{n_t} \simeq \left(e^{-iH_E\Delta t}e^{-iH_B\Delta t}e^{-iH_M\Delta t}e^{-iH_J\Delta t}\right)^{n_t} \ , \tag{1.19}$$

where $n_t = t/\Delta t$ is the number of Trotter steps. Thus, a single Trotter step can be implemented by sequentially applying unitary operators $\mathcal{U}$ that evolve the state according to each term of the Hamiltonian. The Trotterized time evolution is an approximation, since different Hamiltonian terms don't commute in general. Hence, we are introducing a Trotter error, which is known to have a threshold behaviour depending on the Trotter step Δt [198]: below a certain Trotter step size, the Trotter errors are controllable; above the threshold value, the system enters a quantum chaotic regime.

From Ref. [150], to perform a single Trotter step $e^{-iH\Delta t} \simeq \mathcal{U}^E\mathcal{U}^B\mathcal{U}^M\mathcal{U}^J$, it is convenient to introduce a set of *primitive* gates: high-level constructs that implement the time evolution corresponding to the electric, magnetic, mass, and hopping terms. Choosing the group element basis for the gauge degrees of freedom, one can implement the electric Hamiltonian H_E by rotating into the electric basis, i.e., by applying to every link degree of freedom the Quantum Fourier Transform (QFT) gate $\mathfrak{U}_{\mathrm{QFT}}$. In the electric basis, the action of H_E is diagonal, as well as its contribution to the time evolution, which can be implemented by a phase gate whose entries are

$$\langle j, mn|\, \mathfrak{U}_{\mathrm{ph}}(\alpha_j g^2\Delta t)\, |j, mn\rangle = \langle j, mn| \left(\mathrm{e}^{-i\alpha_j g^2\Delta t}\right) |j, mn\rangle \ , \tag{1.20}$$

where α_j is the electric energy associated with the representation j. So, the evolution of the electric Hamiltonian H_E reads

$$\mathrm{e}^{-iH_E\Delta t} = \bigotimes_{\ell} \mathfrak{U}_{\mathrm{QFT},\ell}\mathfrak{U}_{\mathrm{ph},\ell}(\alpha_j g^2\Delta t)\mathfrak{U}^{-1}_{\mathrm{QFT},\ell} \ . \tag{1.21}$$

The unitary operator generated by the four-body interaction described by the magnetic term H_B in Eq. (1.16) is more complicated to implement. A possible

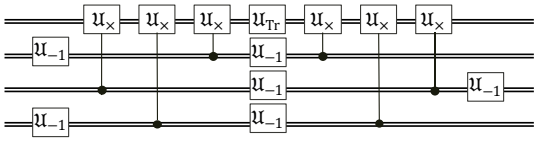

Figure 1.2: Circuit decomposition implementing the time evolution generated by a plaquette term in H_B. It has to be applied to every plaquette of the lattice. Each double line represents the quantum register of a group element subspace. The plaquette product is computed on the above register, then the trace gate is performed, and the product is undone. This architecture is taken from Ref. [150].

circuit decomposition [150], depicted in Fig. 1.2, is a generalization of a standard four-body Pauli-Z interaction for qubits: three *control-multiplication* gates acting on the fourth, onto which subsequently a *trace* gate is applied. Finally, the state of the four registers is restored by applying the inverse of the multiplication gates. The procedure also requires the application of the *inversion* gate, which maps an element of the group g into its inverse $\mathfrak{U}_{-1}|h\rangle = |h^{-1}\rangle$. The trace gate is diagonal in the group-element basis and implements the parametric operation

$$\langle h'|\,\mathfrak{U}_{\mathrm{Tr}}(\frac{1}{g^2}\Delta t)\,|h\rangle = \mathrm{e}^{i\frac{1}{g^2}\Delta t \mathrm{Tr} D^j(g)}\delta_{h'h}\ . \tag{1.22}$$

The control-multiplication gate is defined as

$$\mathfrak{U}_X(|g\rangle\otimes|h\rangle) = \sum_{k\in\mathcal{G}}(|k\rangle\langle k|\otimes\Theta_k^L)(|g\rangle\otimes|h\rangle) = |g\rangle\otimes|gh\rangle\ , \tag{1.23}$$

where the first register $|g\rangle$ is the control and the second is the target.

We now show the implementation of the mass and the hopping terms, where fermionic matter fields enter the game. The elementary Trotter step of the mass term $\mathcal{U}^{(M)}(\Delta t) = e^{-iH_M\Delta t}$ acts on a register of fermions $\{|n_{x,\alpha}\rangle\}$, with the particle-number operator $n_{x,\alpha} = \psi^\dagger_{x,\alpha}\psi_{x,\alpha}$ diagonal. Hence, the mass term acts as

$$\mathcal{U}^{(M)}\left[\otimes_{x,\alpha}|n_{x,\alpha}\rangle\right] = \otimes_{x,\alpha}\left[e^{-i\Delta t M(-1)^{x_1+x_2}n_{x,\alpha}}\,|n_{x,\alpha}\rangle\right]\ . \tag{1.24}$$

This equation means that the mass term decomposes into a product of local phase gates, such that

$$\mathcal{U}^{(M)}_{x,\alpha} = e^{-i\Delta t M(-1)^{x_1+x_2}\psi^\dagger_{x,\alpha}\psi_{x,\alpha}}\ . \tag{1.25}$$

Regarding the hopping term H_J, it includes multiple three-body terms that couple the gauge field with the matter fields. According to Refs. [132, 150, 199], one can decompose $\mathcal{U}^{(J)} = e^{-iH_J\Delta t}$ introducing operator

$$\mathcal{V}_{x|\ell} = \sum_{k\in\mathcal{G}}|k\rangle\langle k|\otimes e^{\sum_{\alpha,\beta}\log[D(k)]_{\alpha,\beta}\psi^\dagger_{x,\alpha}\psi_{x,\beta}}\ , \tag{1.26}$$

which acts on the Hilbert space spanned by the site x and a neighboring link ℓ. The sum runs over all the group elements $k \in \mathcal{G}$, and the log denotes the matrix logarithm. Since D is unitary, $\mathcal{V}$ is unitary as well, so an anti-Hermitian logarithm exists, i.e., $\left(\log\left[D(k)\right]_{\alpha\beta}\psi^{\dagger}_{x,\alpha}\psi_{x,\beta}\right)^{\dagger} = -\log\left[D(k)\right]_{\beta\alpha}\psi^{\dagger}_{x,\beta}\psi_{x,\alpha}$. By using the Baker–Campbell–Hausdorff formula, one can prove the following identities

$$\mathcal{V}^{\dagger}_{x|\ell}\sum_{\alpha}\left(\psi^{\dagger}_{x,\alpha}U_{\ell,\alpha\beta}\right)\mathcal{V}_{x|\ell} = \psi^{\dagger}_{x,\beta}\ , \tag{1.27}$$

$$\mathcal{V}^{\dagger}_{x|\ell}\sum_{\beta}\left(U^{\dagger}_{\ell,\alpha\beta}\psi_{x,\beta}\right)\mathcal{V}_{x|\ell} = \psi_{x,\alpha}\ . \tag{1.28}$$

The key observation is that $V_{x|\ell}$, defined in Eq. (1.26), acts as a unitary rotation that entangles the matter field at site x with the gauge field on the neighboring link ℓ. Equations (1.27) and (1.28) show that conjugating the combination $\psi^{\dagger}_{x,\alpha}U_{\ell,\alpha\beta}$ and $U_{\ell,\alpha\beta}\psi_{x,\beta}$ by $V_{x|\ell}$ effectively strips the parallel transporter away, leaving behind a bare fermionic operator. In other words, $V_{x|\ell}$ performs a basis change in which the dressed matter field—the fermion together with the gauge flux it carries—is mapped onto an undressed one. As a consequence, the three-body interaction $\psi^{\dagger}_{x,\alpha}U_{\ell,\alpha\beta}\psi_{x',\beta}$, which simultaneously acts on the matter at x, the gauge field on the link ℓ, and the matter at x', can be reformulated as a sequence of two-body terms as follows:

$$\mathcal{V}^{\dagger}_{x|\ell}\left[\sum_{\alpha,\beta}\left(\psi^{\dagger}_{x,\alpha}U_{\ell,\alpha\beta}\psi_{x',\beta} + \text{H.c.}\right)\right]\mathcal{V}_{x|\ell} = \sum_{\alpha}\psi^{\dagger}_{x,\alpha}\psi_{x',\alpha}\ , \tag{1.29}$$

which permits the writing of the hopping term in the real-time evolution as

$$\mathcal{U}^{J} = \prod_{\langle xlx'\rangle}\left\{\mathcal{V}_{x|\ell}\mathcal{U}^{(t)}_{xx'}\mathcal{V}^{\dagger}_{x|\ell}\right\}\ , \tag{1.30}$$

$$\mathcal{U}^{(t)}_{xx'} = e^{-i\Delta t s_{xx'}\sum_{\alpha}\left(\psi^{\dagger}_{x,\alpha}\psi_{x',\alpha}+\text{H.c}\right)}\ . \tag{1.31}$$

1.2.3 Why discrete groups

Given that the gauge groups of the Standard Model are continuous, the ultimate goal of Hamiltonian simulation of QCD must confront the discretization problem, i.e., the encoding of continuous degrees of freedom of the Lie group into a finite Hilbert space. There are several possible approaches to address this issue: (i) truncating in the representation space [63, 94–97], that gives reliable results in the strong coupling regime only; (ii) quantum link models [98–101], at the price of losing the unitarity of the parallel transporter operator U, a non-trivial requirement for an efficient quantum circuit implementation of the magnetic term; (iii) reformulating the theory on a new basis, like a dual basis [62, 102–105] or a $q-$deformed gauge theory [106]; (iv) discrete gauge symmetries, with the idea of studying discrete group theories [73, 107–109, 113, 200]. These models share many features with topologically ordered

2D systems [153, 201–206] and were instrumental in achieving the first quantum simulations of 2D dynamical string-breaking phenomena [82, 93, 207].

The discrete group approach is particularly applied to discrete subgroups of Lie groups to approximate their corresponding continuous parent groups. The well-studied approximation of $U(1)$ with $\mathbb{Z}_N$ falls into this category, and it was already explored in the early Euclidean LGT era [208, 209]. In recent years, an extensive literature has been produced to study the implementation of quantum simulation of LGTs using subgroups of $SU(2)$ and $SU(3)$. In Refs. [109, 110], primitive gates are introduced for the crystal-like subgroups of $SU(2)$, the binary tetrahedral $\mathbb{BT}$ and the binary octahedral $\mathbb{BO}$. The smallest non-Abelian discrete subgroup of $SU(2)$, the quaternion group Q_8, was investigated in Ref. [73]. Regarding $SU(3)$, the gauge group of QCD, the primitive gates for two of its crystal-like subgroups, $\Sigma(36 \times 3)$ and $\Sigma(72 \times 3)$, are exposed in Refs. [111, 112].

However, the use of a discrete subgroup to approximate the parent theory requires particular attention. In general, to perform lattice calculations, the lattice spacing a is fixed as a function of the coupling g, i.e., $a = a(g)$, and the continuous limit $a \to 0$ is reached for $g^2 \to 0$, which is the weak-coupling regime. On the one hand, using a finite a introduces discrepancies with the continuum limit, but the errors are polynomial in a if the simulation is in the *scaling regime*, where $a < a_s(g_s)$. On the other hand, it has been shown that discrete subgroups approximation corresponds to continuous groups broken by a Higgs mechanism. As a consequence, discrete subgroups properly approximate the continuous group above a *freeze-out* lattice spacing a_f, i.e., above a coupling g_f. For $a > a_f$, the gauge links are "frozen" to the identity. Thus, the parent theory can be approximated with discrete subgroups for $a_f < a < a_s$, or $g_f < g < g_s$. Classical Monte Carlo calculations show that, among the aforementioned crystal-like subgroups, only the $\mathbb{BO}$ group satisfies $g_f < g < g_s$ [110]. Hence, quantum simulations of $\mathbb{BT}$, $\Sigma(36 \times 3)$ and $\Sigma(72 \times 3)$ require, to approximate the parent theory, an improved Hamiltonian [109, 111, 112]. For example, one could implement a Hamiltonian that has improved discretization errors of $\mathcal{O}(a^4)$ compared to the usual Kogut–Susskind Hamiltonian derived from the Wilson action, which has a discretization error of $\mathcal{O}(a^2)$ [210]. Other approaches use modified Hamiltonians to approximate the parent group in a larger coupling window [211–213].

Beyond their role as approximations to continuous gauge groups, discrete gauge groups are of independent theoretical interest. In the Abelian case, $\mathbb{Z}_N$ gauge theories are deeply connected to topologically ordered phases of matter—most notably the toric code [214] and its generalizations via string-net condensation [215]—and provide natural benchmarks for quantum error correction protocols, where the structure of gauge symmetries and anyonic excitations are intimately related [3, 216]. The exactly solvable $\mathbb{Z}_2$ case underpins the toric code and surface code family of quantum error-correcting codes, and its ground state realizes a paradigmatic example of $\mathbb{Z}_2$ topological order and quantum spin liquid physics [3, 217]. Already within the Abelian setting, moving beyond $\mathbb{Z}_2$ reveals substantially richer structure: the $\mathbb{Z}_3$

toric code hosts parafermion defects and a charge conjugation symmetry with no $\mathbb{Z}_2$ analog, recently demonstrated experimentally on a trapped-ion processor [218]. Discrete non-Abelian groups represent the natural next step in this hierarchy, combining the tractability of finite group structures with the richer phenomenology of non-commuting symmetries; their quantum double models [219] host non-Abelian anyons whose braiding statistics underlie proposals for topological quantum computation [214, 220].

1.3 Dihedral groups

Among discrete non-Abelian models, the dihedral gauge groups D_N provide one of the easiest scenarios, which has led to promising proposals for their quantum simulation [72, 134, 151]. The group D_N is the symmetry group of a regular polygon with N edges. Its group elements can be distinguished into N rotations and N reflections, so the order of D_N is $2N$. D_N is the extension of $\mathbb{Z}_N$ by $\mathbb{Z}_2$, giving $D_N \cong \mathbb{Z}_N \rtimes \mathbb{Z}_2$. The most studied dihedral LGTs are based on D_3 or D_4. The first is the smallest non-Abelian group formed by the 6 symmetries of an equilateral triangle, and the second represents the 8 symmetries of the square[1]. D_4 LGTs have been studied for several toy models, thanks to the optimal encoding of the gauge field in a register of 3 qubits ($2^3 = 8$) [150]. Moreover, an efficient way to implement primitive gates for D_{2^N} is known [221], and D_4 is the smallest non-Abelian D_{2N} group.

Another important feature relevant to this thesis is that the quantum double model $\mathcal{D}(D_3)$, based on the group $D_3 \cong S_3$, hosts non-Abelian topological order whose anyonic excitations enable universal topological quantum computation, supplementing braiding with anyon measurements and auxiliary states [214, 222, 223]. This places D_3 at a particularly attractive sweet spot: it is the smallest non-Abelian group whose quantum double supports universal quantum computation [154, 155], while remaining simple enough to be prepared via finite-depth adaptive circuits on near-term hardware. Non-Abelian topological order has recently been experimentally realized on trapped-ion processors for D_4 [153] and D_3 [224].

A possible presentation for dihedral groups D_N in terms of two generators s and r (which can be considered respectively as a reflection and a rotation by $2\pi/N$ in a 2-dimensional plane) is the following

$$D_N = \langle s, r | s^2 = r^N = e,\ srs = r^{-1} \rangle \ , \tag{1.32}$$

where e denotes the identity element.
The faithful unitary representation for s and r reads

$$D^\tau(s) = \begin{bmatrix} 0 & 1 \\ 1 & 0 \end{bmatrix}, \ D^\tau(r) = \begin{bmatrix} e^{2\pi i/N} & 0 \\ 0 & e^{-2\pi i/N} \end{bmatrix} \ , \tag{1.33}$$

[1] D_N is non-Abelian for $N \geq 3$. D_2 is the Abelian Klein group, while D_1 corresponds to $\mathbb{Z}_2$

where with τ we denote the faithful irreducible representation described by the two matrices $D^\tau(s)$ and $D^\tau(r)$. The rotation r can also be expressed in the sine and cosine representation [149]. However, in this thesis, we use the exponential one.

Conjugacy classes

Two elements of a group $a, b \in \mathcal{G}$ are called conjugate if there exists a group element $g \in \mathcal{G}$, such that $a = gbg^{-1}$. Since conjugacy defines an equivalence relation, the group factorizes into conjugacy classes, each of which contains mutually conjugate group elements. In the case of the dihedral group, we can also express D_N in terms of group elements

$$D_N = \{\mathbb{1}, r, r^2, \dots, r^{N-1}, s, sr, sr^2, \dots, sr^{N-1}\} \ , \tag{1.34}$$

which makes it easier to understand that the structure of conjugacy classes depends on whether N is even or odd. In particular,

$$\begin{aligned} D_{N_{\text{even}}} =& \{\mathbb{1}\} \cup \{r, r^{-1}\} \cup \{r^2, r^{-2}\} \cup \dots \\ & \cdots \cup \{r^{N/2-1}, r^{-N/2+1}\} \cup \{r^{N/2}\} \\ & \cup \{s, sr^2, sr^4, \dots, sr^{N-2}\} \cup \{sr, sr^3, \dots, sr^{N-1}\} \ , \end{aligned} \tag{1.35}$$

and

$$\begin{aligned} D_{N_{\text{odd}}} =& \{\mathbb{1}\} \cup \{r, r^{-1}\} \cup \{r^2, r^{-2}\} \cup \dots \\ & \cdots \cup \{r^{(N-1)/2}, r^{-(N-1)/2}\} \\ & \cup \{s, sr, sr^2, sr^3, sr^4, \dots, sr^{N-2}, sr^{N-1}\} \ . \end{aligned} \tag{1.36}$$

Conj. classes	rotations, size 1	rotations, size 1	reflections
N even	$\{e\}$ $\{r^{N/2}\}$	$\frac{N}{2} - 1$ classes	$\{sr^{2i} : \ 0 \leq i \leq N/2 - 1\}$ and $\{sr^{2i+1} : \ 0 \leq i \leq N/2 - 1\}$
N odd	$\{e\}$	$\frac{N-1}{2}$ classes	$\{sr^i : \ 0 \leq i \leq N - 1\}$

Table 1.1: Number and size of conjugacy classes for D_N with N even or odd. It is specified whether the conjugacy classes take rotation or reflection group elements.

Table 1.1 schematizes the number, the size, and the type of the conjugacy classes for D_N. This discrepancy between even and odd N is a direct consequence of $D_{N_{\text{even}}}$ having a $\mathbb{Z}_2$ center, which is precisely $\{\mathbb{1}, r^{N/2}\}$. Each element of the center builds its own conjugacy class by definition. In Section 3.3, we show how the different conjugacy-class structures of even- and odd-N dihedral groups are crucial for determining the fusion rules of irreducible representations.

Irreducible representations

In finite groups, the number of conjugacy classes is equal to the number of irreducible representations. This means that D_N has in total $N/2+3$ for even N and $(N+3)/2$ for odd N inequivalent irreps. Furthermore, the cardinality of the group is connected to the dimensions of the irreps

$$\sum_j \dim^2(j) = |\mathcal{G}|. \tag{1.37}$$

For dihedral groups, each representation is either one- or two-dimensional. For even N, there are always 4 one-dimensional irreps, and for odd N, there are always 2 of them. The number and the dimensionality of irreps for an arbitrary D_N group are sketched in Table 1.2.

	num 1-d irreps	num 2-d irreps	Tot num of irreps
N even	4	$N/2-1$	$N/2+3$
N odd	2	$(N-1)/2$	$(N+3)/2$

Table 1.2: Number of irreducible representations in D_N depending on N.

The one-dimensional irreps of D_N are 2 for odd N and 4 for even N. In both cases, we have the trivial representation e that maps all the group elements to 1 and the parity representation p that maps the rotations to 1 and the reflections to -1. For even N, in addition, p_1 maps r to -1 and s to 1, while p_2 maps r to -1 and s to -1. Hence, the following scheme holds

$$\begin{array}{cccc} \forall D_N & \forall D_N & \forall D_{2N} & \forall D_{2N} \\ e: r \mapsto 1 & p: r \mapsto 1 & p_1: r \mapsto -1 & p_2: r \mapsto -1\ . \\ s \mapsto 1 & s \mapsto -1 & s \mapsto 1 & s \mapsto -1 \end{array} \tag{1.38}$$

The two-dimensional irreps of D_N can be characterized (up to an isomorphism) as follows. Let $\omega = e^{2\pi i/N}$ and $h \in \{1,\dots,N/2-1\}$ for N even and $h \in \{1,\dots,(N-1)/2\}$ for N odd. The irreducible representation τ_h of the group elements is given as follows:

$$D^{\tau_h}(r^k) = \begin{pmatrix} \omega^{hk} & 0 \\ 0 & \omega^{-hk} \end{pmatrix}, \quad D^{\tau_h}(sr^k) = \begin{pmatrix} 0 & \omega^{-hk} \\ \omega^{hk} & 0 \end{pmatrix}\ . \tag{1.39}$$

Note that for $h = 1$ we obtain the faithful representation generated by the elements in Eq. (1.33).

From Eq. (1.38) and (1.39), it is possible to write the generalized character table for D_N with N odd or even. The two tables are shown in Table 1.3 and Table 1.4, where C_k denotes the conjugacy class $C_k = \{r^k, r^{-k}\}$, $C_s = \{sr^i :\ 0 \le i \le N-1\}$, $C_s^+ = \{sr^{2i} :\ 0 \le i \le N/2-1\}$, $C_s^- = \{sr^{2i+1} :\ 0 \le i \le N/2-1\}$, and $|C|$ is

the cardinality of the conjugacy class. For convenience, we report in Tab. 1.5 and Tab. 1.6 the character table of D_3 and D_4, the groups on which the LGTs studied in the next chapters are based.

	$\{e\}$	$C_k, \quad k = 1, \dots, \frac{N-1}{2}$	C_s
$\lvert C\rvert$	1	2	N
e	1	1	1
p	1	1	-1
$\tau_h, \quad h = 1, \dots, \frac{N-1}{2}$	2	$2\cos\left(\frac{2\pi hk}{N}\right)$	0

Table 1.3: Character table of D_N for odd N. The group has order $2N$ and $(N+3)/2$ conjugacy classes.

	$\{e\}$	$\{r^{N/2}\}$	$C_k, \quad k = 1, \dots, \frac{N}{2} - 1$	C_s^+	C_s^-
$\lvert C\rvert$	1	1	2	$N/2$	$N/2$
e	1	1	1	1	1
p	1	1	1	-1	-1
p_1	1	$(-1)^{N/2}$	$(-1)^k$	1	-1
p_2	1	$(-1)^{N/2}$	$(-1)^k$	-1	1
$\tau_h, \quad h = 1, \dots, \frac{N}{2} - 1$	2	$2(-1)^h$	$2\cos\left(\frac{2\pi hk}{N}\right)$	0	0

Table 1.4: Character table of D_N for even N. The group has order $2N$ and $N/2+3$ conjugacy classes.

	$\{e\}$	$\{r, r^2\}$	$\{s, sr, sr^2\}$
e	1	1	1
p	1	1	-1
τ	2	-1	0

Table 1.5: Character table of D_3.

1.4 Operators and Hamiltonian terms in D_N theories

In this section, we specialize the lattice gauge theory framework to pure-gauge LGTs based on dihedral groups D_N, the main topic of this thesis. We write explicit matrix representations of the Hamiltonian terms and of the relevant operators for a general D_N, and we specify them to D_3 and D_4 where needed.

Parallel transporter. The parallel transporter U^j_{mn}, defined in Eq. (1.11), is diagonal in the group element basis. Specializing to D_N in the fundamental representa-

	$\{e\}$	$\{r^{N/2}\}$	$\{r, r^3\}$	$\{s, sr^2\}$	$\{sr, sr^3\}$
e	1	1	1	1	1
p	1	1	1	-1	-1
p_1	1	1	-1	1	-1
p_2	1	1	-1	-1	1
τ	2	-2	0	0	0

Table 1.6: Character table of D_4.

tion τ and using the standard ordering of the $2N$ group elements $\{e, r, r^2, \ldots, r^{N-1}, s, sr, \ldots, sr^{N-1}\}$, it reads

$$U_{mn} = \begin{bmatrix} D_{mn}(e) & & & & & \\ & D_{mn}(r) & & & & \\ & & D_{mn}(r^2) & & & \\ & & & \ddots & & \\ & & & & D_{mn}(sr^{N-1}) \end{bmatrix}, \tag{1.40}$$

where we omit the representation index when it equals τ. In the irrep (electric) basis, U^{τ}_{mn} is no longer diagonal: its action on a state in the representation j produces a new state in a representation allowed by the fusion rule $\tau \otimes j$, a point that will be central in Chapter 3. The change of basis between the two representations is given by the group Fourier transform of Eq. (1.9).

Electric term. The electric Hamiltonian in Eq. (1.14) decomposes as a direct sum of single-link terms,

$$H_E = \bigoplus_{\ell} H_E^{(\ell)}, \tag{1.41}$$

each of which is diagonal in the electric basis with entries determined by the irrep label j and multiplicity $\dim(j)^2$. For D_3 and D_4, the single-link electric Hamiltonians read

$$H^{(\ell)}_{E,D_3} = g^2 \mathrm{diag}\Big(\alpha_e,\ \alpha_p,\ \alpha_\tau,\ \alpha_\tau,\ \alpha_\tau,\ \alpha_\tau\Big), \tag{1.42}$$

$$H^{(\ell)}_{E,D_4} = g^2 \mathrm{diag}\Big(\alpha_e,\ \alpha_p,\ \alpha_{p_1},\ \alpha_{p_2},\ \alpha_\tau,\ \alpha_\tau,\ \alpha_\tau,\ \alpha_\tau\Big). \tag{1.43}$$

Magnetic term. Each plaquette operator in the magnetic Hamiltonian of Eq. (1.16) is a four-body term built from the product of four parallel transporter operators U^{τ}_{mn}. The eigenvalues of the plaquette operator, however, only depend on the trace of the elements of the gauge group in the fundamental representation τ, i.e., the character $\chi^{\tau}(g)$. For D_N groups, the character of a rotation is $\chi^{\tau}(r^i) = 2\cos(2\pi i/N)$, while the character of any reflection vanishes, $\chi^{\tau}(sr^i) = 0$, as can be read off the character tables Tabs. 1.3 and 1.4. This structure determines the magnetic flux spectrum: plaquettes threaded by the trivial flux $\mathbb{1}$ carry the lowest energy, rotational fluxes

r^i are distinguished by their character, and all reflections are degenerate at zero character.

The trace gate $\mathfrak{U}_{\mathrm{Tr}}(\phi)$, with $\phi = \frac{1}{g^2}\Delta t$, which implements the time evolution of the magnetic Hamiltonian as described in Fig. 1.2, is diagonal in the group element basis. For a general D_N group, it takes the form

$$\mathfrak{U}_{\mathrm{Tr}}(\phi) = \mathrm{diag}\Big(e^{-i2\phi},\ e^{-i2\cos\left(\frac{2\pi}{N}\right)\phi},\ e^{-i2\cos\left(\frac{4\pi}{N}\right)\phi},\ \ldots,\ e^{-i2\cos\left(\frac{2\pi}{N}\right)\phi},\ \underbrace{1,\ \ldots,\ 1}_{N}\Big)\,, \tag{1.44}$$

where the first N entries correspond to the rotations and the last N to the reflections.

Mass term. Even though the results of this thesis mainly concern the pure-gauge Hamiltonian, it is useful to discuss the mass term and the structure of the matter field, as they provide a more complete picture of how gauge transformations are built and how they act on the different degrees of freedom. In D_N groups, the faithful irreducible representation τ is two-dimensional, as shown in Eq. (1.39). Consequently, a gauge field in the electric basis carries two internal indices and is labeled as $|jmn\rangle$, where m and n run over the rows and columns of the representation matrices. The two-dimensionality of τ also dictates the structure of the matter sector: fermionic matter transforming under τ comes in two colors, $|r\rangle$ and $|g\rangle$ (*red* and *green*).

The local basis of a matter field on site n in a D_N theory is spanned by $|0\rangle, |r\rangle, |g\rangle, |d\rangle$, where $|0\rangle$ denotes an empty site, $|r\rangle$ and $|g\rangle$ denote singly occupied states with red and green color, respectively, and $|d\rangle$ denotes double occupation, i.e., both color components populated. $|0\rangle$ transforms as the trivial representation, $|r\rangle$ and $|g\rangle$ transform according to the internal indices of the fundamental representation τ, and $|d\rangle$ transforms as the parity representation. On the anti-matter sites, $|d\rangle$ is associated with the physical vacuum of the Dirac sea, so it transforms as the trivial representation, while $|0\rangle$ transforms as the parity representation. Hence, the mass term in Eq. (1.17) in the Hamiltonian reads

$$H_M = M\sum_n (-1)^n \psi_a^\dagger(n)\psi_a(n) = M\sum_n (-1)^n \begin{bmatrix} 0 & & & \\ & 1 & & \\ & & 1 & \\ & & & 2 \end{bmatrix}. \tag{1.45}$$

Transformations in D_N. We now show how the different representations transform under the symmetry operators $\theta_h^{L(R)}$ and θ_h^Q. For D_N, symmetries with $h = r, s$ give all the information necessary to characterize the gauge sectors and the gauge-invariant states, because transformations with respect to all the other group elements can be obtained by multiplying those two generators of the group. θ_h operators act as permutation matrices[2] in the group element basis, but they are much more informative in the irrep basis. In general, under a transformation with respect to the

[2] In the case of D_3, they act as the complete permutation set, since $D_3 = S_3$.

group element s, θ_s, the color charge swaps, i.e., $r \leftrightarrow g$, while the transformation $\theta_r^{L(R)}$ gives a phase depending on the irrep it acts on and its internal left (right) index. Applying the same operators to states in 1−dimensional representation, instead, gives a $\pm$ sign depending on the mapping in Eq. (1.38). In the end, we can summarize how the transformations work as

$$\begin{aligned}
&\theta_r^{L(R)}\,|e\rangle = |e\rangle \ , \quad \theta_r^{L(R)}\,|p\rangle = |p\rangle \ , \quad \theta_r^{L(R)}\,|p_1\rangle = -\,|p_1\rangle \ , \quad \theta_r^{L(R)}\,|p_2\rangle = -\,|p_2\rangle \ , \\
&\theta_s^{L(R)}\,|e\rangle = |e\rangle \ , \quad \theta_s^{L(R)}\,|p\rangle = -\,|p\rangle \ , \quad \theta_s^{L(R)}\,|p_1\rangle = |p_1\rangle \ , \quad \theta_s^{L(R)}\,|p_2\rangle = -\,|p_2\rangle \ ,
\end{aligned} \tag{1.46}$$

for the 1−dimensional representations, where $|p_1\rangle$ and $|p_2\rangle$ only exist for D_N with even N, and

$$\begin{aligned}
&\theta_r^{L}\,|\tau_h r n\rangle = \mathrm{e}^{2\pi i h/N}\,|\tau_h r n\rangle \ , \qquad \theta_r^{L}\,|\tau_h g n\rangle = \mathrm{e}^{-2\pi i h/N}\,|\tau_h g n\rangle \ , \quad \theta_s^{L}\,|\tau_h r n\rangle = |\tau_h g n\rangle \ , \\
&\theta_r^{R}\,|\tau_h m r\rangle = \mathrm{e}^{-2\pi i h/N}\,|\tau_h m r\rangle \ , \qquad \theta_r^{R}\,|\tau_h m g\rangle = \mathrm{e}^{2\pi i h/N}\,|\tau_h m g\rangle \ , \quad \theta_s^{R}\,|\tau_h m r\rangle = |\tau_h m g\rangle \ ,
\end{aligned} \tag{1.47}$$

for the 2−dimensional representations.

In Ref. [149], the authors show that one can define the transformation operators on the matter fields as

$$\theta_g^{Q,j} = \mathrm{e}^{\psi_a^\dagger \log\left(D^j_{ab}(g)\right)\psi_b} \det\left(D^j(g)^{-1}\right)^n \ , \tag{1.48}$$

where the exponent n takes into account the parity of the site, i.e., if it is a matter or an anti-matter site, and j is the fermionic matter representation, which we always fix to the fundamental representation τ.

For D_N groups, it holds that

$$\theta_r^Q = \begin{bmatrix} 1 & & & \\ & \mathrm{e}^{2\pi i/N} & & \\ & & \mathrm{e}^{-2\pi i/N} & \\ & & & 1 \end{bmatrix} \ , \quad \theta_s^Q = (-1)^n \begin{bmatrix} 1 & & & \\ & 0 & 1 & \\ & 1 & 0 & \\ & & & -1 \end{bmatrix} \ . \tag{1.49}$$

The first equation indicates that the transformation on the matter field gives the same phases of the left transformations in Eq. (1.47), as the charge of the single fermion was going out of the site n. The second equation indicates that, on a matter site, under θ_s^Q, the empty state remains unchanged, while the double-occupied state takes a -1 phase. On single-occupied sites, the transformation flips the color of the particle.

1.5 Qudit platforms for LGTs

In the context of quantum hardware, *qudit* devices [115], where each fundamental unit of quantum information possesses more than two levels ($d > 2$), represent a

promising platform in the noisy intermediate-scale quantum (NISQ) era [114]. Several platforms have been developed to perform qudit-based computation: trapped ions [116–118], transmons [119–126], Rydberg arrays [127], photonic circuits [128], ultra-cold atomic mixture [129], and superconducting radio-frequency (SRF) cavities [130, 131]. Their main advantage lies in the compact encoding of large local Hilbert spaces: operations that would require multiple entangling gates on a qubit register can be implemented as single-qudit gates, significantly reducing the circuit depth and the associated error rate. Since two-qubit entangling gates currently represent the primary source of hardware noise, this reduction is particularly valuable for near-term devices.

Hence, LGTs represent a natural framework to test and explore the advantages of *qudit* devices. An elementary information unit with d levels is particularly useful for the efficient encoding of groups of order $|\mathcal{G}| > 2$, in particular when $2 < |\mathcal{G}| \leq d$ [225]. This enables the implementation of physically local terms using single qudit gates. The interest of the implementation of LGTs on qudits is due to the significant reduction in the circuit depth and the increase in the fidelity, both for one-body [109] and multi-body terms [73] in the Hamiltonian. The general framework developed for LGTs on qubit digital quantum simulators, shown in Sec. 1.2, has already been expanded for qudit quantum hardware [73, 109, 132]. Furthermore, seminal proof-of-principle experiments on a truncated $U(1)$ group showcased the promising potential of a compact encoding of the gauge degrees of freedom [136]. The hardware used in this protocol is the trapped-ion qudit setup of Ref. [116], which can handle qudits with $d \leq 7$. On the same hardware several experiments have been proposed: the implementation on qudits of the minimal truncation of $SU(2)$ in Ref. [133]; the proposal of digital qudit quantum circuits for scattering processes in a $U(1)$ quantum link lattice gauge theory in Ref. [226]; the implementation of the time-evolution on a simple non-Abelian model based on the group D_3 [161], which will be the topic of Chapter 5.

We can now show where and how qudits represent a possible advantage when compared with qubits. On qubit hardware, the Quantum Fourier Transform (QFT) — required at every Trotter step to rotate between the group-element and the irrep bases — becomes a sequence of entangling gates whose efficient implementation is not known in general. Substantial effort has been devoted to finding optimal QFT circuits for physically relevant non-Abelian groups [227]. As a concrete example, the optimal implementation of the QFT for D_4 requires two entangling gates per link [221], so that a single Trotter step on a lattice of L links incurs $2 \times 2 \times L = 4L$ entangling gates.

On qudit hardware, instead, the QFT reduces to a single-qudit gate as soon as $d \geq |\mathcal{G}|$, since the change of basis between the magnetic and the electric bases requires no entanglement between different link registers. The difficulty due to the magnetic term, instead, remains: its implementation requires the control-multiplication gate $\mathfrak{U}_\times$, the only two-qudit unitary needed for the time evolution. Since $\mathfrak{U}_X = \sum_{k\in\mathcal{G}}(|k\rangle\langle k| \otimes \Theta_k^L)$, each control-multiplication $\mathfrak{U}_X$ gate in Fig. 1.2 applies $|\mathcal{G}|$ dif-

ferent control-operations on the target register depending on the state of the control qudit (one of which, corresponding to the identity, is trivial). In Ref. [73], this decomposition is written as

$$\mathfrak{U}_X = \sum_{k\in\mathcal{G}} (|k\rangle\langle k| \otimes \Theta_k^L) = \prod_{k\in\mathcal{G}} C_{\theta(k)}(k) \ , \tag{1.50}$$

which means that when the control qudit is in the $|k\rangle$ state, the unitary operation $\theta(k)$ is performed on the target qudit. Hence, in terms of elementary operations, a single control-multiplication decomposes into a sequence of $|\mathcal{G}|-1$ control-permutations, each acting on a well-defined pair of group elements. Despite this cost, the overall gate count and the achievable fidelity remain substantially more favorable on qudit devices than on qubit ones. In Ref. [73], the advantage of implementing the multiplication gate on qudits instead of qubits is analyzed for $\mathbb{Q}_8$, the quaternion group that is a non-Abelian subgroup of $SU(2)$ with cardinality 8. In particular, the authors estimate a reachable fidelity of 99.6% for qudits versus 21.4% for qubits.

Regarding the time evolution of the hopping term in Eq. (1.30), the entangling gates $\mathcal{V}_{x|\ell} = \sum_{k\in\mathcal{G}} |k\rangle\langle k| \otimes e^{\sum_{\alpha,\beta} \log[D(k)]_{\alpha,\beta} \psi^\dagger_{x,\alpha}\psi_{x,\beta}}$ can be decomposed as product of control-operations [132]

$$\mathcal{V}_{x|\ell} = \prod_{g\in\mathcal{G}} C^{\ell\to x}_{V_x(g)}(g) \ , \tag{1.51}$$

where

$$C^{\ell\to x}_{V_x(g)}(g) = |g\rangle_\ell\langle g| \otimes V_x(g) + \sum_{g'\neq g} |g'\rangle_\ell\langle g'| \otimes \mathbb{1} \tag{1.52}$$

are control-unitary gates, where the control qudit is on the gauge field, and the target qudit is on the matter field, on which the unitary gate $V_x(g) = e^{\sum_{\alpha,\beta} \log[D(k)]_{\alpha,\beta} \psi^\dagger_{x,\alpha}\psi_{x,\beta}}$ is performed.

For the hopping term, qudit hardware offers an advantage over qubit implementations as well. The gate $V_x(g)$ acts on the matter field, whose Hilbert space has dimension $2^{\dim(\tau)}$, where τ is the fundamental irrep, with Lie groups, or a faithful irrep, with discrete groups. On qubit hardware, encoding such a register requires $\dim(\tau)$ qubits, and $V_x(g)$ decomposes into a sequence of multi-qubit entangling gates. On a qudit device with $d \geq 2^{\dim(\tau)}$, the same operation reduces to a single-qudit gate, and the controlled version $C^{\ell\to x}_{V_x(g)}$ then requires a single two-qudit entangling gate per group element $g \in \mathcal{G}$.

Armed with these tools, in the following chapters we will explore some features of dihedral lattice gauge theories (Chapters 2 and 3), analyzing some possible methods to implement error mitigation in the quantum simulation of discrete non-Abelian lattice gauge theories (Chapters 4 and 5).

Part I

Physics of dihedral Lattice Gauge Theories

Chapter 2

Lattice Gauge Theories with D_N

In this chapter, we characterize gauge invariant sectors for D_N, specifying their number, and comparing them with the sectors in an Abelian LGT with $\mathbb{Z}_2$. We also give an example with D_3 to show the dimension of the gauge invariant sectors with respect to the full Hilbert space. After that, we introduce a gauge-fixed ladder model, we derive the Hamiltonian on the gauge-fixed basis, and we use it to study the crossover between the magnetic and the electric regime, and the energy gap. By exploiting the possibility to study larger systems by Exact Diagonalization (ED), we also study the quantum resources to simulate such a system [158], and the integrability of the model, a first step toward a better understanding of the thermalization of non-Abelian LGTs with discrete groups [228].

2.1 Sectors in $\mathbb{Z}_2$ and D_N LGTs

Looking at the gauge invariant sectors, there is an important difference when we study non-Abelian rather than Abelian theories.

In Abelian theories, all the gauge operators commute, i.e., $\left[\Theta_{h,n}, \Theta_{g,n'}\right] = 0,\ \forall\, h, g \in \mathcal{G},\ \forall n, n'$. Hence, all the $\Theta_{h,n}$ operators can be simultaneously diagonalized, and the total Hilbert space $\mathcal{H}_{\text{tot}}$ can be decomposed as a direct sum of all the possible gauge sectors defined by the set of gauge charges $\{\alpha_{h,n}\},\ \forall h \in \mathcal{G}, n$,

$$\mathcal{H}_{\text{tot}} = \bigoplus_{\{\alpha_{h,n}\}} \mathcal{H}_{\{\alpha_{h,n}\}} \ . \tag{2.1}$$

Hence, each state belongs to a sector.

In non-Abelian theories, on the contrary, gauge operators on the same site, in general, do not commute, i.e., $[\Theta_{h,n}, \Theta_{g,n}] \neq 0,\ \forall\ h, g \in \mathcal{G},\ g \neq h$. The consequence is that a generic state in $\mathcal{H}_{\text{tot}}$ is not a simultaneous eigenstate of all the $\Theta_{h,n}$, and it does not belong to any gauge sector. So, the gauge invariant subspaces defined by all the possible $\{\alpha_{h,n}\}$ sets do not complete the total Hilbert space.

2.1.1 Gauge sectors in $\mathbb{Z}_2$ LGTs

As an Abelian example, we introduce the 1+1d lattice of N sites and $N-1$ links that we will study in Chapter 4. The gauge group of the theory is $\mathbb{Z}_2$, and we consider dynamical fermionic matter to have a non-trivial dynamics [81, 89, 229]. The Hamiltonian $H_{\mathbb{Z}_2} = H_J + H_f + H_m$ is the sum of three contributions

$$H_J = J \sum_n \left(\psi_n^\dagger \tau^x_{n,n+1} \psi_{n+1} + \text{H.c} \right) , \tag{2.2a}$$

$$H_f = f \sum_n \tau^z_{n,n+1} , \tag{2.2b}$$

$$H_m = \frac{M}{2} \sum_n (-1)^n \sigma^z_n . \tag{2.2c}$$

The fermionic operators ψ_n act on the site of the lattice and represent the dynamical charges, while the Pauli operators $\tau^\alpha_{n,n+1}$ are the $\mathbb{Z}_2$ gauge field operators acting on the link between sites n and $n+1$. H_J describes a nearest-neighbor particle hopping assisted by the gauge field connecting the two sites. H_f is an effective "electric-field" contribution to the Hamiltonian and H_m is the staggered mass of fermionic degrees of freedom, which are interpreted as particles on even sites and antiparticles on odd ones. We consider a system with open boundary conditions.

The Hamiltonian $H_{\mathbb{Z}_2}$ commutes with the set of local symmetry operators

$$\Theta_n = -\tau^z_{n-1,n} \sigma^z_n \tau^z_{n,n+1} , \tag{2.3}$$

(see Eq. (3.3)). Thus, the Hilbert space is split into subsectors labeled by the eigenvalues of Θ_n, i.e., an array of conserved local charges $\{\alpha_n\}_{n=0,\dots,N-1}$, with $\alpha_n = -1, 1$. In the model we are considering, the dimension of the Hilbert space, the number of the gauge sectors, and their dimension are sketched in Table 2.1.

Both the sites and the links have a local Hilbert space spanned by two possible states, so the dimension of the total Hilbert space is 2, the cardinality of $\mathbb{Z}_2$, elevated to the sum of sites (N) and links ($N-1$). Since the local gauge charge on each site can assume two possible values, ± 1, the number of sectors is 2^N, and thus the dimension of each gauge sector is 2^{N-1}. An equivalent way to visualize it is to consider every possible configuration of the gauge fields. Then, the associated gauge-invariant state is uniquely determined by the gauge charges, i.e., the possible presence of dynamical matter on the sites. Hence, the dimension of the local Hilbert space of each sector is 2^{N-1}, because, once we fix the state of all the links, the matter fields just indicate in which sector the state is.

2.1.2 Gauge sectors in D_N LGTs

It is worth understanding what happens and how to characterize the gauge sectors in D_N theories. Since a gauge sector is defined by the set of gauge charges $\{\alpha_{h,n}\}$, it is important to list the possible values $\alpha_{h,n}$ can take depending on the group element

$\dim(\mathcal{H}_{\text{tot}})$	num of sectors	dim of each sector
$2^N 2^{N-1}$	2^N	2^{N-1}

Table 2.1: Dimension of the total Hilbert space, number of sectors, and dimension of each sector for the model described by the $\mathbb{Z}_2$ Hamiltonian in Eq. (2.2). Note that the dimension of the total Hilbert space is equal to the sum of the dimensions of all the possible sectors, as described by Eq. (2.1). Hence, every state belongs to a gauge-invariant subspace.

h. The most instructive property is that, even though α_h can in principle take any unitary value, only real values ± 1 can define gauge invariant sectors.

Indeed, to be invariant under Θ_s transformations, each state in $2-$dimensional representations must be a superposition of both colors. This ensures the invariance under Θ_s transformations, but at the same time requires that the multiplication of the phases given by the Θ_r transformation must compute to 1. This is reminiscent of the confinement mechanism in non-Abelian lattice gauge theories: physical states must be color-neutral singlets, consistently with the principle that isolated color-charged particles are not observed in nature [230].

As an example, consider a site n on a $1+1$d lattice, and we see how to write a gauge invariant state on the link going into n from the left, the site n, and the link going out of n on the right, such that the symmetry operators are $\Theta_h = \theta_h^R \theta_h^Q \theta_h^L$. From Eqs. (1.46) and (1.47), we can easily see that $|e, 0, e\rangle$, i.e., the state with the trivial representation on both the links and the empty occupation on the site n, is gauge invariant with $\alpha_r = \alpha_s = 1$. Now, if we excite the left link to the fundamental representation τ, we have to create a superposition of the two internal indices to get a state invariant under Θ_s, i.e., $|\psi\rangle = \frac{1}{\sqrt{2}}(|\tau mr, 0, e\rangle + |\tau mg, 0, e\rangle)$. However, this state is not invariant under the Θ_r transformation, because

$$\Theta_r |\psi\rangle = \left(\mathrm{e}^{-2\pi i/N} |\tau mr, 0, e\rangle + \mathrm{e}^{2\pi i/N} |\tau mg, 0, e\rangle\right)/\sqrt{2} \,. \tag{2.4}$$

So, to ensure the gauge invariance under Θ_r, we have to suppress the two phases with phases of the opposite sign, like

$$\begin{aligned} |\psi_1\rangle &= \left(|\tau mr, 0, \tau rn\rangle + |\tau mg, 0, \tau gn\rangle\right)/\sqrt{2} \,, \text{ or} \\ |\psi_2\rangle &= \left(|\tau mr, r, e\rangle + |\tau mg, g, e\rangle\right)/\sqrt{2} \,. \end{aligned} \tag{2.5}$$

In conclusion, although Θ_r operators have complex phase eigenvalues, the charge α_n defining the gauge sectors can only be real. Hence, the number of sectors depends on the different distinct real eigenvalues of $\theta_r^{L(R)}$ and $\theta_s^{L(R)}$ in Eq. (1.46), and this gives two distinct cases for D_N with N even or N odd, as shown in Tab. 2.2.

Regarding the dimension of the gauge sectors, the computation is not as straightforward as in the $\mathbb{Z}_2$. In Ref. [200], the authors give a useful equation to compute the

D_N	num of sectors
N even	$(4^{N_{\text{sites}}})$
N odd	$(2^{N_{\text{sites}}})$

Table 2.2: Number of sectors for D_N LGTs with N even and N odd. The difference is due to the possibility, only for N even, that Θ_r symmetries can have gauge charge $\alpha_r = -1$ and not only $\alpha_r = 1$, as happens for N odd. In both cases, the gauge charge associated with Θ_s can be $\alpha_s = \pm 1$.

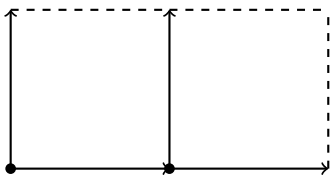

Figure 2.1: Lattice geometry consisting of 4 links and 2 vertices, used to characterized the sectors of a D_3 LGT, as reported in Tab. 2.3.

dimension of the physical Hilbert space for pure-gauge LGTs with discrete groups,

$$\dim(\mathcal{H}_{\text{phys}}) = \sum_C \left(\frac{|\mathcal{G}|}{|C|}\right)^{L-V} , \tag{2.6}$$

where $|C|$ is the cardinality of the conjugacy class C, L is the number of links in the lattice and V is the number of vertices. However, Eq. (2.6) only holds for the neutral sector.

As an example, we can introduce the lattice geometry, shown in Fig. 2.1 and studied in Chapter 5 with D_3 as a gauge group. Here, we are particularly interested in the number of links, $L = 4$, and sites, $V = 2$, such that $L - V = 2$. Looking at the conjugacy classes of D_3 in Tab. 1.5, it is easy to compute that $\dim(\mathcal{H}_{\text{phys}}) = 49$. This is the dimension of the neutral sector, which is only one out of the four sectors we can identify in the system, as reported in Tab. 2.2 for N odd. Here, the sectors are only characterized by the gauge charges $(\alpha_{s,n1}, \alpha_{s,n2})$. A numerical analysis of the Hamiltonian gave the dimensionalities reported in Tab. 2.3.

	$\mathcal{H}_{\text{tot}}$	$(1,1)$	$(1,-1)$	$(-1,1)$	$(-1,-1)$
dim	$6^4 = 1296$	49	41	41	49

Table 2.3: List of the sectors and their dimension in pure-gauge LGT of 2 plaquettes with Periodic Boundary Conditions, consisting of 4 links and 2 sites, with D_3 as gauge group.

2.2 Gauge-fixed ladder: derivation

In this section, we introduce the so-called ladder geometry, which is a one-dimensional chain of plaquettes. This geometry is the minimal system that permits the interplay between the magnetic and the electric terms of the Hamiltonian. In full $2+1d$ geometry, the system quickly becomes intractable with classical computation because of the exponential scaling.

On the contrary, the ladder is not a proper 2-dimensional system. Indeed, in the continuous limit, for the lattice spacing $a \to 0$, the direction of development of the ladder becomes a real physical finite length, while the other spatial dimension is squeezed, and the ladder becomes a 1-dimensional string of plaquettes. However, its more controllable dimension makes it interesting and useful for several case studies, such as for proposals of quantum simulations of simple intermediate systems, and for the possibility of using methods to further simplify the theory. In this last direction, one method is represented by the gauge fixing, which is introduced in the following, while a second possibility is the use of Tensor Networks, which are accessible thanks to the "quasi-$(2+1)$" dimension of the ladder. These two options are not mutually exclusive.

The goal of this section is to reduce the original gauge theory to an effective one-dimensional ladder model by fixing the gauge. This allows for the exact diagonalization and for the investigation of larger systems.

2.2.1 Gauge-fixing procedure

We define N_ℓ as the number of links in the ladder and L as the number of rungs, or the length of the ladder. We start from the Hamiltonian H on the ladder system, whose Hilbert space is $\mathcal{H} = \text{span}\{\otimes_\ell |g_\ell\rangle\,,\ g_\ell \in \mathcal{G}\}$ in the group element basis. Two basis states $|\vec{g}\rangle$ and $|\vec{g}'\rangle$ belong to the same gauge orbit if there exists a set of group elements $\{h_n\}$ such that $\prod_n \Theta_n(h_n)\,|\vec{g}\rangle = |\vec{g}'\rangle$. The gauge orbit of $|\vec{g}\rangle$ is therefore the set

$$\mathcal{O}_{\vec{g}} = \left\{ \prod_n \Theta_n(h_n)\,|\vec{g}\rangle \ \ \forall\ \{h_n \in \mathcal{G}\} \right\}. \tag{2.7}$$

Since $[H, \Theta_n(h)] = 0$ for all n, h, if $|\vec{g}'\rangle = U\,|\vec{g}\rangle$ and $|\vec{h}'\rangle = U\,|\vec{h}\rangle$ for the same gauge transformation U, then $\langle\vec{g}'|\,H\,|\vec{h}'\rangle = \langle\vec{g}|\,H\,|\vec{h}\rangle$. This redundancy of information, typical of LGTs, can be reduced by fixing some of the gauge fields, as shown in the following.

Thanks to the geometry of the system, we can apply a gauge-fixing over all the links on the legs of the ladder, such that they are fixed to the identity. We start from a ladder as the one depicted in Fig. 2.2(a). We denote the $n-$th site with $v_{n,\sigma}$, where $\sigma = \uparrow, \downarrow$ indicates if the vertex is on the top or the bottom leg. We label the links on the left of the $n-$th site with $|g_{n,\sigma}\rangle$, and the rungs, i.e., the vertical links, with $|g_n\rangle$. To proceed with the gauge-fixing, we exploit the Gauss law over each site

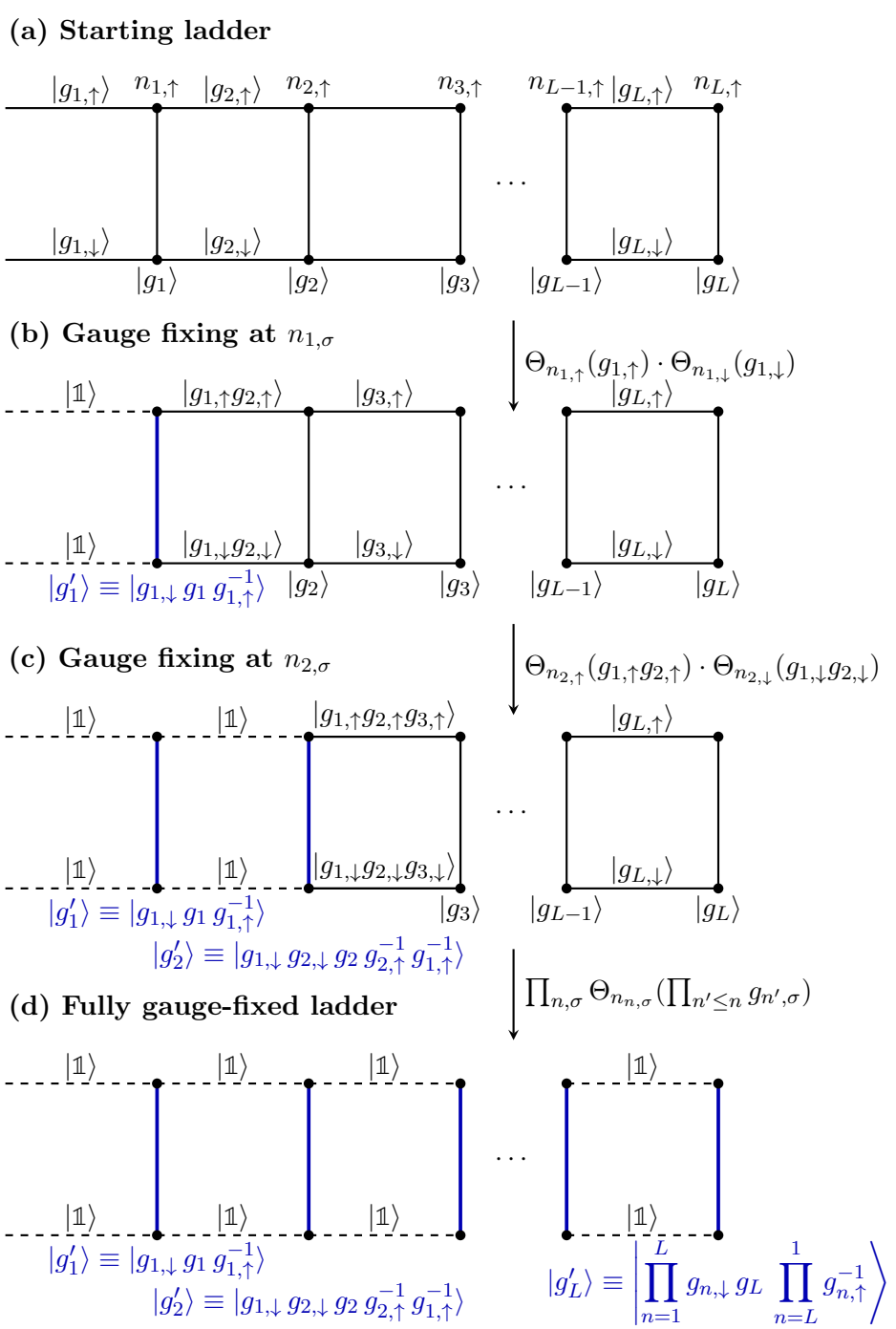

Figure 2.2: (a) The starting ladder. Each link has the state associated with its Hilbert space labeled in the group element basis. (b) The ladder after the gauge fixing on the sites $n_{1,\uparrow}$ and $n_{1,\downarrow}$. The identity is fixed on the first two legs on the left, and the modified rung state $|g'_1\rangle$ is redefined accordingly. (c) The ladder after the gauge fixing on the sites $n_{2,\uparrow}$ and $n_{2,\downarrow}$. (d) The ladder is completely gauge-fixed, after the transformation in Eq. (2.10), that gives the basis in Eq. (2.11).

n to fix the link connecting n and $n-1$ to the identity. For this reason, to fully solve the gauge redundancy, we add a pair of extra links on the left of the ladder.

For instance, if we take the state of the first rung and the two left attached links, i.e., $|g_{1,\downarrow}, g_1, g_{1,\uparrow}\rangle$, the gauge fixing applies a gauge transformation of the site $n_{1,\sigma}$ with respect to the group element $g_{1,\sigma}$, with $\sigma = \uparrow, \downarrow$. So, we can write the first step of the gauge-fixing as

$$\Theta_{n_{1,\uparrow}}(g_{1,\uparrow})\Theta_{n_{1,\downarrow}}(g_{1,\downarrow})\,|g_{1\downarrow}, g_1, g_{1\uparrow}\rangle = |\mathbb{1}, g_{1\downarrow}g_1 g_{1\uparrow}^{-1}, \mathbb{1}\rangle \ . \tag{2.8}$$

We have fixed the two legs to the identity, changing the state of the rung, which is the only degree of freedom. However, by writing explicitly the action of the transformation on the sites, $\Theta_{n_i,\uparrow(\downarrow)} = \theta^{R}_{n,\uparrow(\downarrow)}\,\theta^{R(L)}_{n}\,\theta^{L}_{n+1,\uparrow(\downarrow)}$, we see that the second-leftmost legs are also changed:

$$\Theta_{g_{1,\uparrow},n_{1,\uparrow}}\Theta_{g_{1,\downarrow},n_{1,\downarrow}}\,|g_{2\downarrow}, g_2, g_{2\uparrow}\rangle = |g_{1\downarrow}g_{2\downarrow}, g_2, g_{1\uparrow}g_{2\uparrow}\rangle \ . \tag{2.9}$$

The resulting ladder, after this first step, is depicted in Fig. 2.2(b).

Hence, in the next step of the gauge-fixing, the transformation will be with respect to the product $|g_{1,\sigma}g_{2,\sigma}\rangle$, as shown in Fig. 2.2(c), and the corresponding string will spread on all the rungs up to the end of the ladder, as shown in Fig. 2.2(d).

The total gauge-fixing procedure can be written as

$$|\vec{g}\rangle \to |\vec{g}_r\rangle = \prod_{n,\sigma}\Theta_{n,\sigma}\left(\prod_{n'\leq n} g_{n',\sigma}\right)|\vec{g}\rangle \ . \tag{2.10}$$

As a result, we get an effective basis that has non-trivial components only on the rungs, as shown in Ref. [231],

$$\begin{aligned} &|g_n\rangle \to |\prod_{n'=1}^{n} g_{n'\downarrow}g_n \prod_{n'=n}^{1} g^{-1}_{n'\uparrow}\rangle \equiv |g'_n\rangle = |g_r\rangle \ , \\ &|g_{n,\sigma}\rangle \to |\mathbb{1}\rangle \ . \end{aligned} \tag{2.11}$$

It is now possible to rewrite the action of the magnetic and electric terms of the Hamiltonian in the new gauge-fixed basis, given by Eq. (2.11). Each plaquette product in the magnetic term simplifies from a 4−body term to a 2− body term. Since the two links on the legs are fixed to the identity, the non-trivial product is given by the two rungs, as shown in the following

$$H_B = \frac{1}{g^2}\sum_p \Re\left(\mathrm{Tr}(U_{p1}U_{p2}U^{\dagger}_{p3}U^{\dagger}_{p4})\right) \to H_B^{\mathrm{gf}} = \frac{1}{g^2}\sum_{r=1}^{N-1}\Re\left(\mathrm{Tr}(U^{\dagger}_{r}U_{r+1})\right) \ , \tag{2.12}$$

where the sum is over all the rungs r.

Regarding the electric term, we have to take into account two different kinds of contributions: the ones on the rungs and the ones on the legs. For convenience, we derive them in two distinct subsections.

2.2.2 Rung contribution

In the following, we examine the effect of the gauge-fixing transformation on the matrix elements of H_E, the electric Hamiltonian. The gauge-fixing is implemented by the unitary transformation

$$U_g = \prod_{n,\sigma} \Theta_{n,\sigma} \left(\prod_{n' \leq n} g_{n',\sigma} \right) , \tag{2.13}$$

where $\sigma \in \{\uparrow, \downarrow\}$ labels the two legs. The matrix element of H_E in the gauge-fixed basis becomes

$$\langle \vec{g} | H_E | \vec{h} \rangle \;\rightarrow\; \langle \vec{g} | U_g^\dagger U_g H_E U_h^\dagger U_h | \vec{h} \rangle = \langle \vec{g}_r | U_g H_E \, U_h^\dagger | \vec{h}_r \rangle . \tag{2.14}$$

Since $H_E = \bigoplus_\ell H_E^{(\ell)}$ is a direct sum of single-link terms, we focus on the term acting on rung w, which connects the sites $x, \uparrow$ and $x, \downarrow$, denoted $H_{E,w}$. We define the string

$$\tilde{g}_{n,\sigma} \equiv \prod_{n' \leq n} g_{n',\sigma} . \tag{2.15}$$

The action of $H_{E,w}$ on the gauge-fixed basis is given by

$$H_{E,w} \;\longrightarrow\; \langle \vec{g}_r | U_g H_{E,w} \, U_h^\dagger | \vec{h}_r \rangle = \prod_{n,\sigma} \Theta_{n,\sigma}(\tilde{g}_{n,\sigma}) \; H_{E,w} \; \prod_{n',\sigma} \Theta_{n',\sigma}(\tilde{h}^{-1}_{n',\sigma}) \; . \tag{2.16}$$

Since $H_{E,w}$ acts locally on the rung w only, the factors $\Theta_{n,\sigma}$ with $n, \sigma \neq x, \sigma$ commute with $H_{E,w}$, and the product $\Theta_{n,\sigma}(\tilde{g}_{n,\sigma})\Theta_{n',\sigma}(\tilde{h}^{-1}_{n',\sigma})$ gives $\delta_{\tilde{g}_{n,\sigma}, \tilde{h}_{n',\sigma}}$ for all $\ell \neq w$. Indeed, in the matrix element between gauge-fixed states, the condition that these factors yield a non-zero contribution forces $\tilde{g}_{n,\sigma} = \tilde{h}_{n,\sigma}$ for all $n, \sigma \neq x, \sigma$. We are therefore left with

$$\begin{aligned} &\langle \vec{g}_r | U_g H_{E,w} \, U_h^\dagger | \vec{h}_r \rangle = \\ &\qquad \langle \vec{g}_r | \left(\prod_{\ell \neq w, (\sigma)} \delta_{\tilde{g}_{n,\sigma}, \tilde{h}_{n',\sigma}} \right) \Theta_{w,\uparrow}(\tilde{g}_{w,\uparrow}) \, \Theta_{w,\downarrow}(\tilde{g}_{w,\downarrow}) \, H_{E,w}^{(1)} \, \Theta_{w,\uparrow}(\tilde{h}^{-1}_{w,\uparrow}) \, \Theta_{w,\downarrow}(\tilde{h}^{-1}_{w,\downarrow}) \, | \vec{h}_r \rangle \end{aligned} \tag{2.17}$$

Using the expression for the single-link electric Hamiltonian,

$$H_{E,\ell}^{(1)} = g^2 \sum_j \frac{\dim(j)}{|\mathcal{G}|} \, \alpha_j \sum_g \chi^j(g) \, \theta_\ell^L(g) \; , \tag{2.18}$$

we can write explicitly the matrix element on the links variable where the action is not trivial per se, i.e., on the rung w and the 4 links connected to it:

$$\begin{aligned}\langle \vec{g}_r | U_g H_{E,w} \, U_h^\dagger | \vec{h}_r \rangle =& g^2 \sum_j \frac{\dim(j)}{|\mathcal{G}|} \, \alpha_j \sum_g \chi^j(g) \\ & \prod_\sigma \langle \mathbb{1}_{w,\sigma} | \, \theta^R_{w,\sigma}(\tilde{g}_{w,\sigma}) \theta^R_{w,\sigma}(\tilde{h}^{-1}_{w,\sigma}) \, | \mathbb{1}_{w,\sigma} \rangle \\ & \prod_\sigma \langle \mathbb{1}_{w+1,\sigma} | \, \theta^L_{w+1,\sigma}(\tilde{g}_{w,\sigma}) \theta^L_{w+1,\sigma}(\tilde{h}^{-1}_{w,\sigma}) \, | \mathbb{1}_{w+1,\sigma} \rangle \\ & \langle g_w | \, \theta^L_w(\tilde{g}_{w,\downarrow}) \theta^L_w(g) \theta^L_w(\tilde{h}^{-1}_{w,\downarrow}) \theta^R(\tilde{g}_{w,\uparrow}) \theta^R_w(\tilde{h}^{-1}_{w,\uparrow}) \, | h_w \rangle \ . \end{aligned} \tag{2.19}$$

The matrix elements over the four legs give a non-zero contribution only when $\tilde{g}_{w,\sigma} = \tilde{h}_{w,\sigma}$. This condition gives a contribution $\delta_{\tilde{g}_{w,\sigma},\tilde{h}_{w,\sigma}}$, which we can use to simplify the fourth row of the equation. So, the matrix element in the gauge-fixed basis is limited to the action over the rung w, where the product $\delta_{\tilde{g}_{w,\uparrow},\tilde{h}_{w,\uparrow}} \theta^R(\tilde{g}_{w,\uparrow}) \theta^R_w(\tilde{h}^{-1}_{w,\uparrow}) = \mathbb{1}$, and then we get

$$\langle \vec{g}_r | U_g H_{E,w} \, U_h^\dagger | \vec{h}_r \rangle = g^2 \sum_j \frac{\dim(j)}{|\mathcal{G}|} \, \alpha_j \sum_g \chi^j(g) \, \langle g_w | \, \theta^L_w(\tilde{g}_{w,\downarrow}) \theta^L_w(g) \theta^L_w(\tilde{g}^{-1}_{w,\downarrow}) \, | h_w \rangle \ , \tag{2.20}$$

but since $\theta^L_w(\tilde{g}_{w,\downarrow}) \theta^L_w(g) \theta^L_w(\tilde{g}^{-1}_{w,\downarrow}) = \theta^L_w(\tilde{g}_{w,\downarrow} \, g \, \tilde{g}^{-1}_{w,\downarrow})$ is the conjugate of g, we get $\chi^j\left(\tilde{g}_{w,\uparrow} \, g \, \tilde{g}^{-1}_{w,\uparrow}\right) = \chi^j(g)$, because characters are class functions. The matrix element of $H_{E,w}$ in the gauge-fixed basis therefore yields the same contribution as the original rung electric term, confirming that the rung electric Hamiltonian is unchanged by the gauge-fixing procedure:

$$\langle \vec{g}_r | \, U_g H_{E,w} \, U_h^\dagger \, | \vec{h}_r \rangle = g^2 \sum_j \frac{\dim(j)}{|\mathcal{G}|} \, \alpha_j \sum_g \chi^j(g) \, \langle g_w | \, \theta^L_w(g) \, | h_w \rangle \ . \tag{2.21}$$

2.2.3 Leg contribution

In this subsection, we consider the contribution to the gauge-fixed electric Hamiltonian from a leg link. We focus on the link connecting vertices $w-1$ and w on leg σ, which we denote w_σ. Following the same structure as in the rung case, the gauge-fixed matrix element is

$$\langle \vec{g}_r | \, U_g \, H_{E,w_\sigma} \, U_h^\dagger \, | \vec{h}_r \rangle = \langle \vec{g}_r | \left(\prod_{n,\sigma} \Theta_{n,\sigma}(\tilde{g}_{n,\sigma}) \right) H_{E,w_\sigma} \left(\prod_{n',\sigma} \Theta_{n',\sigma}(\tilde{h}^{-1}_{n',\sigma}) \right) | \vec{h}_r \rangle \, , \tag{2.22}$$

where all the leg links are gauge-fixed to $|\mathbb{1}\rangle$. For all links at positions $n < w$, the matrix element $\langle \vec{g}_r | \, U_g \, H_{E,w_\sigma} \, U_h^\dagger \, | \vec{h}_r \rangle$ gives $\delta_{\tilde{g}_{n,\sigma},\tilde{h}_{n,\sigma}}$ as in the rung case, constraining

$\tilde{g}_{n,\sigma} = \tilde{h}_{n,\sigma}$ for $n < w$. We are left with the action on w_σ and on links at positions $n \geq w$.

We also write for convenience $H^{(1)}_{E,w_\sigma} = g^2 \sum_j \frac{\dim(j)}{|\mathcal{G}|} \alpha_j \sum_g \chi^j(g)\, \theta^L_{w_\sigma}(g)$. In the following, we fix $\sigma = \downarrow$ for simplicity, but the equivalent procedure also works for $\sigma = \uparrow$. The consequence is that we get $\delta_{\tilde{g}_{n,\uparrow},\tilde{h}_{n,\uparrow}}$ also on the links on the top leg.

$$\langle \vec{g}_r |\, U_g\, H_{E,w,\downarrow}\, U_h^\dagger \,| \vec{h}_r \rangle = g^2 \sum_j \frac{\dim j}{|\mathcal{G}|} \alpha_j \sum_g \chi^j(g) \tag{2.23}$$
$$\langle \vec{g}_r | \prod_{n,n'<w} \delta_{\tilde{g}_{n,(\sigma)},\tilde{h}_{n',(\sigma)}} \prod_{n,n'\geq w} \delta_{\tilde{g}_{n,\uparrow},\tilde{h}_{n',\uparrow}} \Theta_{n,\downarrow}(\tilde{g}_{n,\downarrow}) \theta^L_{w,\downarrow}(g) \Theta_{n',\downarrow}(\tilde{h}^{-1}_{n',\downarrow}) \,| \vec{h}_r \rangle \ .$$

Now we focus on the product on the links w and $w,\downarrow$, where the non-trivial operators are $\theta^L_{w,\downarrow}$. We make explicit the first two terms of the product, when $n = n' = w$, such that we get

$$\prod_{n,n'\geq w} \Theta_{n,\downarrow}(\tilde{g}_{n,\downarrow}) \theta^L_{w,\downarrow}(g) \Theta_{n',\downarrow}(\tilde{h}^{-1}_{n',\downarrow}) = \theta^R_{w,\downarrow}(\tilde{g}_{w,\downarrow}) \theta^L_{w,\downarrow}(g) \theta^R_{w,\downarrow}(\tilde{h}^{-1}_{w,\downarrow}) \theta^L_w(\tilde{g}_{w,\downarrow}) \theta^L_w(\tilde{h}^{-1}_{w,\downarrow})$$
$$\prod_{n,n'\geq w+1} \Theta_{n,\downarrow}(\tilde{g}_{n,\downarrow}) \theta^L_{w+1,\downarrow}(\tilde{g}_{w,\downarrow}) \theta^L_{w+1,\downarrow}(\tilde{h}^{-1}_{w,\downarrow}) \Theta_{n',\downarrow}(\tilde{h}^{-1}_{n',\downarrow}) \ . \tag{2.24}$$

On the link $w,\downarrow$, we get the matrix element $\langle \mathbb{1} |\, \theta^R_{w,\downarrow}(\tilde{g}_{w,\downarrow} \tilde{h}^{-1}_{w,\downarrow}) \theta^L_{w,\downarrow}(g) \,| \mathbb{1} \rangle$, which only gives non-zero contribution for $g = \tilde{f}_{w,\downarrow}$, where $\tilde{f}_{w,\downarrow} = \tilde{g}_{w,\downarrow} \tilde{h}^{-1}_{w,\downarrow}$.

Hence,

$$\begin{aligned}
&\prod_{n,n'\geq w} \Theta_{n,\downarrow}(\tilde{g}_{n,\downarrow}) \theta^L_{w,\downarrow}(g) \Theta_{n',\downarrow}(\tilde{h}^{-1}_{n',\downarrow}) = \\
&\quad = \delta_{\tilde{f}_{w,\downarrow},g} \theta^L_w(\tilde{f}_{w,\downarrow}) \prod_{n,n'\geq w+1} \Theta_{n,\downarrow}(\tilde{g}_{n,\downarrow}) \theta^L_{w+1,\downarrow}(\tilde{f}_{w,\downarrow}) \Theta_{n',\downarrow}(\tilde{h}^{-1}_{n',\downarrow}) = \\
&\quad = \theta^L_w(g) \prod_{n,n'\geq w+1} \Theta_{n,\downarrow}(\tilde{g}_{n,\downarrow}) \theta^L_{w+1,\downarrow}(g) \Theta_{n',\downarrow}(\tilde{h}^{-1}_{n',\downarrow}) \ .
\end{aligned} \tag{2.25}$$

So, the gauge-fixing procedure forces the electric field localized on the leg w_σ to spread over the rung on the right and the leg $(w+1)_\sigma$.

Now, we can repeat the same procedure on the link $w+1,\downarrow$, and so on. The final result is that the operator on the link $w,\downarrow$ spreads over all the rungs $r \geq w$,

$$\langle \vec{g}_r |\, U_g\, H_{E,w_\sigma}\, U_h^\dagger \,| \vec{h}_r \rangle = g^2 \sum_j \frac{\dim(j)}{|\mathcal{G}|}\, \alpha_j \sum_g \chi^j(g) \prod_{r\geq w} \theta^R_r(g) \ . \tag{2.26}$$

Summing over all leg positions w on both legs, and noting that characters are class functions so θ^R and θ^L give the same contribution, the total leg electric Hamiltonian in the gauge-fixed basis is

$$H^{\text{leg}}_E = 2g^2 \sum_r \sum_j \frac{\dim(j)}{|\mathcal{G}|}\, \alpha_j \sum_g \chi^j(g) \prod_{r'\geq r} \theta^L_{r'}(g) \ , \tag{2.27}$$

where the factor of 2 accounts for both legs $\sigma = \uparrow, \downarrow$.

Hence, while the encoding of the rung terms remains the same as the original model, the electric Hamiltonian on the leg terms is responsible for a series of non-local string terms.

2.3 Gauge-fixed ladder: physics

Summing all three contributions to the Hamiltonian derived in the previous section, we can then write the full gauge-fixed Hamiltonian that only acts on the rung degrees of freedom.

$$H_{\text{rung}} = g^2 \sum_r \sum_J \alpha_J \frac{\dim(J)}{|\mathcal{G}|} \chi^J(h) \theta_r^L + 2g^2 \sum_i \sum_J \sum_h \alpha_J \frac{\dim(J)}{|\mathcal{G}|} \chi^J(h) \prod_{r' \geq r} \theta_{r'}^L(h) - \frac{1}{2g^2} \sum_r \left(\text{Tr}[U_r^\dagger U_{r+1}] + \text{H.c.} \right) . \tag{2.28}$$

The main advantage of this Hamiltonian is that we reduced the number of degrees of freedom of the original ladder by two-thirds, so we can use Exact Diagonalization (ED) methods to study the system up to a larger dimension.

In the following, we use the gauge group D_3 to test the Hamiltonian in Eq. (2.28), to show the interplay between the electric energy and the magnetic energy as a function of the coupling, and to characterize the transition between the weak- and the strong-coupling regimes.

2.3.1 Cross-over and magnetic-electric interplay

In full $(2+1)d$ geometries, discrete LGTs are expected to undergo a phase transition between a confined phase at strong coupling and a deconfined topologically-ordered phase at weak coupling [152, 153, 155, 201, 232]. On a ladder, however, the edges induce an effective electric field that prevents a phase transition at finite g [233, 234]. Instead, the coupling drives a crossover between two smoothly-connected regimes that minimize either the electric or the magnetic energy. In Fig. 2.3(a-b), the magnetic and the electric energy densities are depicted for different rungs. To keep the quantities comparable, we show the magnetic energy per plaquette and the electric energy per link. Even if the crossover between the two regimes is already visible, it is revealed more clearly by looking at the expectation value of $\langle H_E \rangle / (g^2 N_\ell)$ and of the plaquette operator

$$\langle B_p \rangle = -g^2 \frac{\langle H_B \rangle}{N_{\text{pl}}} . \tag{2.29}$$

These two quantities are independent of the coupling g^2, and their behaviour, reported in Fig. 2.3(c-d), is useful to describe the ground state phenomenology of the D_3 gauge-fixed LGTs in Eq. (2.28). We set the electric energies associated with irreps as $\alpha_e = -1,\ \alpha_p = 1,\ \alpha_\tau = 0$.

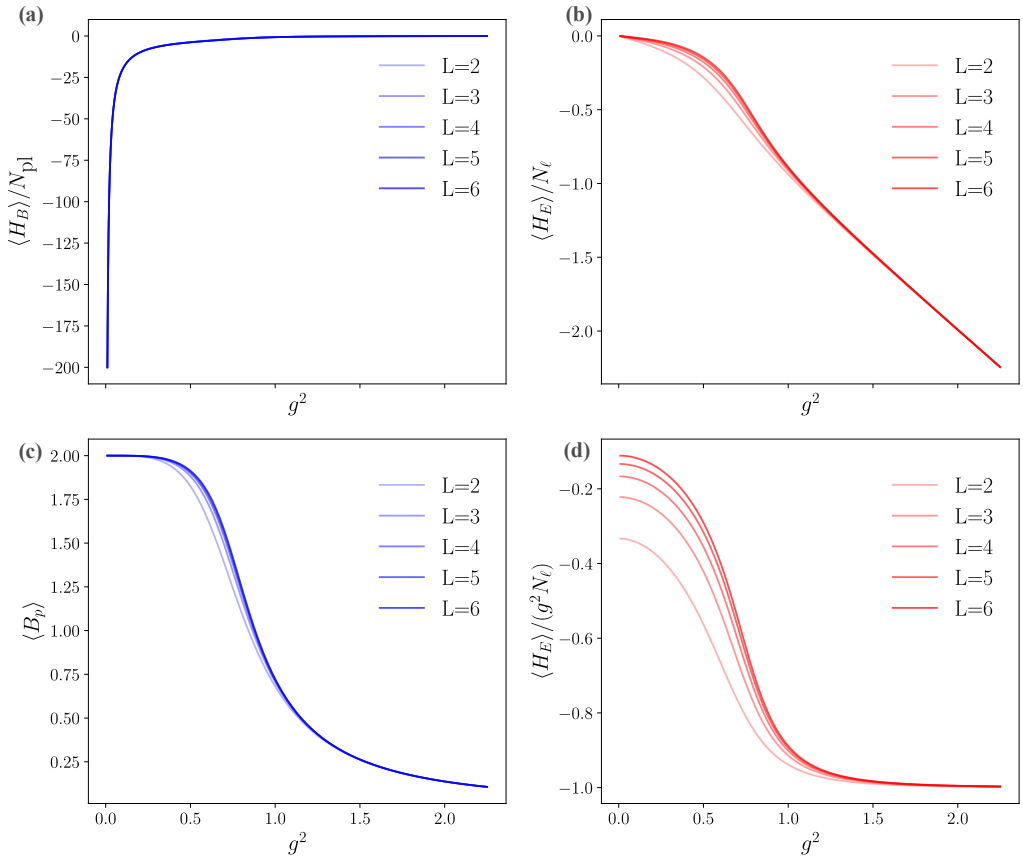

Figure 2.3: (a) Ground state magnetic energy per plaquette and (b) electric energy per link, for different numbers of rungs L. (c) Plaquette operator and (d) electric energy density, independent of g^2, of the ground state for D_3 LGT on a ladder. The results are almost independent of the number of rungs (increasing for darker shades) for the plaquette operator. The plaquette expectation value $\langle B_p \rangle \sim 2$ at $g^2 \to 0$ corresponds to a trivial magnetic flux. The offset in the electric energy densities depends on the presence of the two extra legs that, in the ground state, are in the trivial representation.

In the computation of the data shown in Fig. 2.3(c), we used Eq. (2.29) to get the data from the expectation value of the magnetic Hamiltonian. $\langle B_p \rangle$ is dominant in the weak coupling regime, $g^2 \to 0$, where it converges towards a finite value depending on the character of the identity in the fundamental representation, $\chi^\tau(\mathbb{1}) = 2$. Physically, this value is associated with the absence of magnetic vortices and with the deconfined phase, which on a ladder is reduced to the point $g^2 = 0$. Moreover, in the electric basis, the ground state in the weak coupling regime has, for each link, uniform population in each irrep basis state. For the α values we set, the electric energy

density would be suppressed, with a value of $\langle \frac{H_E}{g^2 N_\ell} \rangle (g \to 0) = \sum_J \alpha_J \frac{\dim(J)^2}{|\mathcal{G}|} \ll 1$. However, this is not what happens in the ladder geometry in Fig. 2.2, since for $g^2 \to 0$ the electric energy density reaches an offset. The reason lies in the two extra legs we added to fully solve the gauge degeneracy: the extra legs do not participate in any plaquette operator, and in the ground state they take the energy of the trivial representation. So, the offset of the electric energy density in Fig. 2.3(d) is $\frac{2}{N_\ell}\alpha_e$, where $N_\ell = 3L$ is the number of links in the original system.

At strong coupling, $g^2 \gg 1$, the magnetic term vanishes, indicating a phase dominated by electric order. Each link in the ground state, here, is in the trivial representation, which corresponds to a uniform superposition of the group elements in the magnetic basis, i.e., $|\psi\rangle_{\text{GS}}\,(g^2 \gg 1) = \frac{1}{\sqrt{|\mathcal{G}|^L}} \sum_{g_1,\ldots,g_L \in \mathcal{G}} |g_1, \ldots, g_L\rangle$. The uniform superposition suppresses the trace of the plaquette products, which indeed approaches 0 in Fig. 2.3(c) at strong coupling, and so it suppresses the magnetic term. The electric energy, instead, is dominant at $g \gg 1$, converging toward a value that depends on the energy associated with the trivial representation, such that $\langle H_E \rangle (g \gg 1) = g^2 N_\ell \alpha_e$.

2.3.2 Energy gaps and global gauge transformations

It is interesting to investigate what happens to the energy gap of this system. Since it does not display a phase transition but a cross-over, we do not expect a gap that reduces to 0 around a critical value for the coupling g. To proceed, we have to take into account that the system still retains a global D_3 gauge symmetry, so that each energy eigenstate transforms as one of the *irreps* of the group. This induces a $|D_3| = 6$-fold degeneracy in the ground state at $g^2 = 0$. Global symmetries can be written as

$$\Theta^{L(R)}_{h,\text{ global}} = \prod_\ell \theta^{L(R)}_{h,i} \ . \tag{2.30}$$

At finite coupling, the ground state $|e_0\rangle$ transforms trivially under the global symmetry, $|e_1\rangle \ldots |e_4\rangle$ transform as the fundamental representation, and $|e_5\rangle$ transforms as the parity representation. Thus, the relevant energy gap is between the ground state E_0 and the first excited state belonging to the same symmetry sector, which is E_6.

In Fig. 2.4, we depict the gap of the D_3 theory. The energy gap $E_6 - E_0$ decreases with system size in the crossover regime but converges quickly to a finite minimum value, which occurs around a level crossing between different symmetry sectors. This behavior illustrates the absence of a phase transition in the thermodynamic limit, but rather the magnetic and electric regimes remain smoothly connected. [1]

[1] Numerically, in Fig. 2.4 E_6 and E_5, the energy associated with e_5, present a crossing around the minimum reached by $(E_6 - E_0)$. For these reasons, from the threshold indicated by the crossing, we computed $(E_6 - E_0)$ using the data from E_5 instead of the ones from E_6.

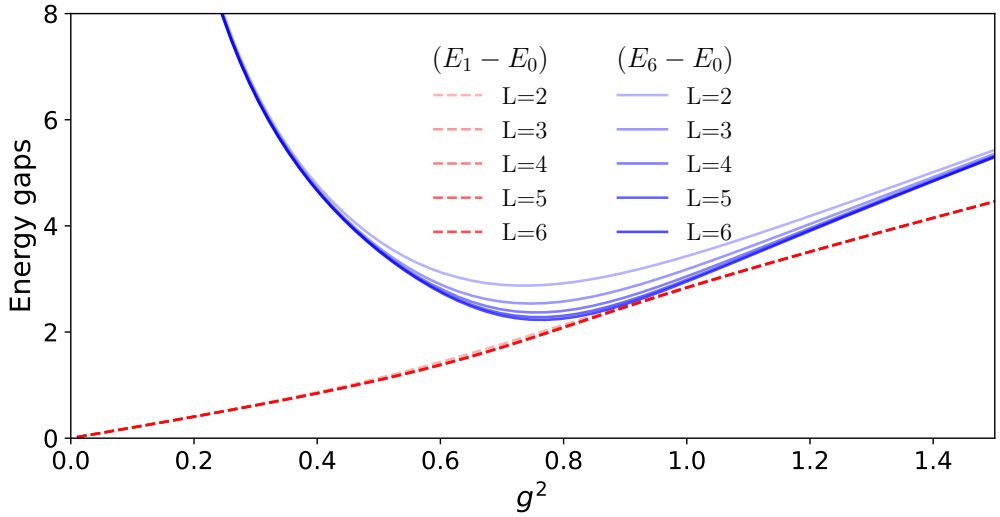

Figure 2.4: Energy gaps vs coupling g^2 for D_3 rung system, depending on the system size L, i.e., the number of rungs in the ladder. Solid lines indicate the gap with the first excited states belonging to the same symmetry sector $(E_6 - E_0)$ of the ground state, while dashed lines point to the manifold that transforms non-trivially under the global D_3 symmetry and becomes degenerate with the ground state at $g^2 = 0$ $(E_1 - E_0)$. The gap $E_6 - E_0$ converging to a finite value different from 0 indicates the lack of a phase transition but rather a smooth crossover between the electric and magnetic regimes.

2.3.3 Quantum resources in the D_3 gauge-fixed model

In hardware devoted to quantum computation, it is possible to select different sets of quantum gates to perform universal quantum computing. One of these sets is the one based on the Clifford group, which can be generated by the Hadamard gate H, the phase gate S, and the $C-NOT$ gate, as listed in the following.

$$H = \frac{1}{\sqrt{2}}\begin{bmatrix} 1 & 1 \\ 1 & -1 \end{bmatrix}, \quad S = \begin{bmatrix} 1 & 0 \\ 0 & i \end{bmatrix}, \quad C-NOT = \begin{bmatrix} 1 & 0 & 0 & 0 \\ 0 & 1 & 0 & 0 \\ 0 & 0 & 0 & 1 \\ 0 & 0 & 1 & 0 \end{bmatrix}. \tag{2.31}$$

However, Clifford gates are not sufficient to perform universal quantum computation. Indeed, quantum states generated by Clifford circuits alone—the so-called *stabilizer states*—can be efficiently simulated on a classical computer despite carrying arbitrarily large entanglement, as established by the Gottesman–Knill theorem [235, 236]. To go beyond classical simulability and reach universal quantum computation, one must supplement Clifford circuits with non-Clifford resources, typically the T-gate,

$$T = \begin{bmatrix} 1 & 0 \\ 0 & \mathrm{e}^{\frac{\pi}{4}i} \end{bmatrix}, \tag{2.32}$$

which injects the so-called *magic* into the computation. Nonstabilizerness is the resource-theoretic quantification of this property: it measures how far a quantum state is from the set of stabilizer states, and thus how many T-gates are needed to prepare it [237, 238]. Crucially, nonstabilizerness is independent from entanglement — a state can be highly entangled yet classically simulable (as is the case for stabilizer states), or weakly entangled yet rich in nonstabilizerness.

This complementarity makes nonstabilizerness a valuable diagnostic for identifying which physical regimes of a quantum many-body system are genuinely hard to simulate, beyond what entanglement alone can reveal. Indeed, the study of nonstabilizerness in quantum many-body systems has grown significantly, driven by its relevance both as a diagnostic of quantum complexity and as a resource for fault-tolerant quantum computation [238–241]. New methods to efficiently compute it in large many-body systems have been developed, both based on tensor network techniques [242–244] and on Monte Carlo sampling [245].

Its application to lattice gauge theories is still in its early stages: a pioneering study connected nonstabilizerness to criticality in gauge models using Pauli-Markov chains [245], and a more recent investigation in a $(1+1)$D $U(1)$ theory showed that, unlike entanglement, nonstabilizerness has no direct relation to the presence of critical points, but its derivatives display discontinuities across them [246]. More broadly, nonstabilizerness has been investigated in a variety of strongly correlated and chaotic systems, including hybrid quantum circuits [247], spin models [248], the Sachdev–Ye–Kitaev model [249], nuclear structure [250], and the neutrino sector [251].

The gauge-fixed Hamiltonian in Eq. (2.28) allows for an efficient numerical study of the D_3 LGT on the ladder. In Ref. [158], we analyzed the ground state of this model in terms of two complementary measures of quantum complexity: the Generalized Geometric Measure (GGM) G_2 and the Stabilizer Rényi Entropy (SRE) $\mathcal{M}_2$.

The GGM quantifies genuine multipartite entanglement as the distance between a quantum state $|\psi\rangle$ and the set of 2-separable product states [252, 253],

$$G_2(|\psi\rangle) = 1 - \max_{A:B} (\lambda_{A:B}^{\max})^2 \ , \tag{2.33}$$

where $\lambda_{A:B}^{\max}$ is the largest Schmidt coefficient across all bipartitions $A : B$. Its maximum possible value is $G_2^{\max} = 1 - 1/d$, where d is the local Hilbert space dimension. From a practical standpoint, G_2 provides a lower bound on the number of entangling gates required to prepare the state on a quantum device.

The SRE $\mathcal{M}_2$ represents one possible measurement of the nonstabilizerness [254]. A large $\mathcal{M}_2$ indicates that the state is far from any stabilizer state and thus requires a large number of T-gates to be prepared. It is defined as

$$\mathcal{M}_2(|\psi\rangle) = -\log \sum_{\mathcal{P}\in\mathcal{P}_L} \frac{|\langle\psi|\mathcal{P}|\psi\rangle|^4}{d^L} \ , \tag{2.34}$$

where the sum runs over the full set of generalized Pauli strings $\mathcal{P}_L$ for a system of L qudits of local dimension d. $\mathcal{M}_2$ vanishes if and only if $|\psi\rangle$ is a stabilizer state.

The behavior of both quantities can be understood directly from the structure of the gauge-fixed Hamiltonian. In the strong-coupling limit $g^2 \gg 1$, the ground state is a product state with every rung in the trivial irrep e, corresponding to a uniform superposition of group elements on each link,

$$|\mathrm{GS}\rangle_{g^2\gg 1} = \bigotimes_i |e\rangle_i \ . \tag{2.35}$$

This state has no entanglement and vanishing SRE, as it is a stabilizer state. In the weak-coupling limit $g^2 \ll 1$, the magnetic term dominates, and the ground state takes the form of a generalized GHZ state in the group element basis, where all rungs are locked together. While this state displays maximal multipartite entanglement, with G_2 approaching $1 - 1/d$, it is also a stabilizer state, so $\mathcal{M}_2$ vanishes in this limit as well.

As a consequence, the most interesting region is around the crossover between the two limits, where G_2 and $\mathcal{M}_2$ are both nonzero, as shown in Fig. 2.5, and where the electric and magnetic terms compete. In this region, G_2 displays a peak whose derivative coincides with the maximum of $\mathcal{M}_2$, indicating that the onset of nonstabilizerness is correlated with the fastest change in multipartite entanglement. This is also the region where the energy gap shown in Fig. 2.4 reaches its minimum.

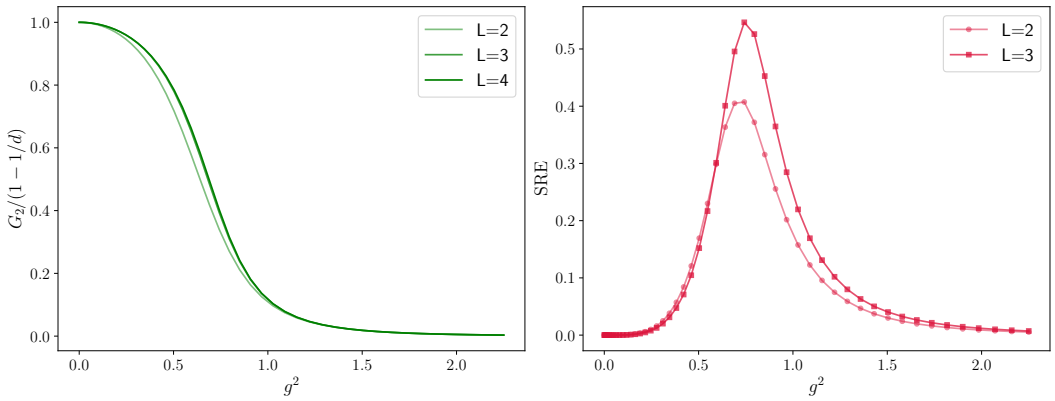

Figure 2.5: Generalized Geometric Measure G_2 (left) and Stabilizer Rényi Entropy $\mathcal{M}_2$ (right) for the ground state of the D_3 gauge-fixed Hamiltonian in Eq. (2.28), as a function of the coupling g^2, for different system sizes L. G_2 is normalized by its maximum possible value $G_2^{\max} = 1 - 1/d$, with $d = 6$, and $\mathcal{M}_2$ is shown as a density per rung. Both quantities vanish in the strong-coupling ($g^2 \gg 1$) and weak-coupling ($g^2 \ll 1$) limits, where the ground state is a product state and a generalized GHZ state, respectively, both of which are stabilizer states. The resources are concentrated in the crossover regime, where the electric and magnetic terms compete. The GGM converges quickly with system size — already $L = 3$ and $L = 4$ are nearly indistinguishable.

2.3.4 Eigenstate Thermalization Hypothesis

A fundamental open question in quantum many-body physics concerns how isolated systems, evolving unitarily and therefore reversibly, can nonetheless exhibit thermal behavior at late times [255, 256]. The Eigenstate Thermalization Hypothesis (ETH) [257–260] provides a compelling resolution: in non-integrable (chaotic) systems, the expectation value of a local observable $\hat{O}$ in an individual energy eigenstate $|n\rangle$ already coincides, up to exponentially small corrections, with the microcanonical prediction at the corresponding energy. More precisely, the ETH ansatz states that the matrix elements of $\mathcal{O}$ in the energy eigenbasis take the form

$$\mathcal{O}_{mn} \;=\; \mathcal{O}(\bar{E})\,\delta_{mn} \;+\; e^{-S(\bar{E})/2}\, f_{\mathcal{O}}(\bar{E},\omega)\, R_{mn}\,, \tag{2.36}$$

where $\bar{E} = (E_m + E_n)/2$, $\omega = E_n - E_m$, $S(\bar{E})$ is the thermodynamic entropy, $\mathcal{O}(\bar{E})$ and $f_{\mathcal{O}}(\bar{E},\omega)$ are smooth functions of their arguments, and R_{mn} is a random variable with zero mean and unit variance. The diagonal part ensures that single-eigenstate expectation values reproduce the thermal average, while the exponential suppression of the off-diagonal part guarantees that temporal fluctuations vanish in the thermodynamic limit.

Although the ETH has been extensively verified in spin chains and fermionic/-bosonic lattice models [261–264], gauge theories remain largely unexplored in this

context. Classical simulations have established that non-Abelian gauge theories are classically chaotic [265], suggesting that the ETH should hold; however, an explicit quantum-level demonstration has been lacking.

A further conceptual difficulty arises when the system possesses a non-Abelian symmetry. The standard ETH ansatz (2.36) relies on two ingredients that non-Abelian symmetries can spoil: (i) the Hamiltonian is assumed non-degenerate, and (ii) the system is prepared in a microcanonical subspace, i.e., a joint eigenspace of all conserved charges. When the conserved charges do not commute—as is the case for the components $S_{a=x,y,z}$ of a total spin in an SU(2)-symmetric system—they share no eigenbasis, so microcanonical subspaces may not exist in the usual sense.

To resolve this tension, in Ref. [266], a *non-Abelian ETH* was proposed. The key idea is to apply the ETH not to the full matrix elements, but to the *reduced* matrix elements $\langle\alpha\|T^{(k)}\|\alpha'\rangle$, such that the ETH ansatz is modified as follows:

$$\langle\alpha\|T^{(k)}\|\alpha'\rangle \;=\; \mathcal{T}^{(k)}(\bar{E},\bar{S})\,\delta_{\alpha\alpha'} \;+\; e^{-S_{\rm th}(\bar{E},\bar{S})/2}\,f_\nu^{(k)}(\bar{E},\bar{S},\omega)\,R_{\alpha\alpha'}\,, \tag{2.37}$$

where $\bar{S} = (s_\alpha + s_{\alpha'})/2$ and $\nu = s_\alpha - s_{\alpha'}$ are the average and difference of the total spin quantum numbers, while the other symbols retain their meaning from Eq. (2.36). Numerical evidence supporting the non-Abelian ETH ansatz (2.37) has been recently provided for SU(2)-symmetric Heisenberg chains in Ref. [267].

The gauge-fixed D_3 ladder model introduced in Sec. 2.2 provides a minimal yet non-trivial arena for investigating both the standard and non-Abelian aspects of the ETH in a gauge theory, since its finite Hilbert space per link allows exact diagonalization without truncation of the gauge degrees of freedom. The convenience of the gauge-fixing is particularly clear now: in the full theory, the dimension of the gauge-invariant sectors is dramatically smaller than the dimension of $\mathcal{H}_{\rm tot}$, as shown in Tab. 2.3. Since to study the thermalization of a non-Abelian theory we need to solve all the degeneracies inside one single sector, and the fundamental tool is the exact diagonalization, a full ladder would be hardly tractable, or it would have too poor statistics.

The rest of this section is adapted from the Master's thesis work of Marco Vaia [228], which we co-supervised, where we characterized a proper symmetry sector in the gauge-fixed non-Abelian ladder for the study of the ETH. Another non-Abelian system, based on the truncation of a $1+1$−d gauge theory with $SU(2)$ with dynamical fermions, has been studied in Ref. [268].

In the gauge-fixed Hamiltonian (2.28), the plaquette operator $\mathrm{Tr}[U_r^\dagger U_{r+1}] + \mathrm{H.c.}$ couples neighboring rungs through the character of the fundamental representation evaluated on the group element $h_r = g_r^{-1} g_{r+1}$. Because characters are class functions, group elements belonging to the same conjugacy class of D_3 produce the same eigenvalue of the plaquette operator, leading to exact degeneracies in the energy spectrum. This is problematic for spectral diagnostics of quantum chaos—such as the nearest-neighbor level spacing distribution (NNSD)—where spurious degeneracies from symmetry considerations must be fully resolved before meaningful statistics can be extracted.

To lift these conjugacy-class degeneracies, one follows the construction introduced for non-Abelian gauge-flux ladders in Ref. [231]. A unitary matrix $C \in U(d_\tau)$, with $d_\tau = \dim(\tau)$, is inserted in the plaquette interaction, replacing it with the *chiral* form

$$H_B^{(C)} \;=\; -\frac{1}{2g^2}\sum_r \Big[\mathrm{Tr}\big(U_r^{\tau\,\dagger}\, C\, U_{r+1}^{\tau}\big) + \mathrm{H.c.}\Big]\,. \tag{2.38}$$

In the group element basis, a two-rung product state $|g_r\rangle \otimes |g_{r+1}\rangle$ is an eigenstate of this operator with eigenvalue $m_g = \mathrm{Tr}[D^\tau(h_r)\, C]$, where $h_r = g_r^{-1} g_{r+1}$ is the flux in the r-th plaquette. For C proportional to the identity, m_g reduces to the character $\chi^\tau(h_r)$, which is constant on conjugacy classes and therefore degenerate. A generic unitary C, instead, can assign distinct values of m_g to every group element, provided the condition

$$\mathrm{Re}\big(\mathrm{Tr}[C\, D^\tau(g)]\big) \;\neq\; \mathrm{Re}\big(\mathrm{Tr}[C\, D^\tau(h)]\big) \qquad \forall\, g \neq h \in D_3 \tag{2.39}$$

is satisfied [231]. Physically, C plays the role of a classical background gauge field that selects a preferred direction in the internal (color) space, in analogy with the chiral phase $e^{i\phi}$ in the chiral Potts model. Following Eq. (1.10), under a left global gauge transformation $\Theta^L_{g,\mathrm{global}} = \prod_r \theta^L_{g,r}$, the operator in Eq. (2.38) remains invariant, whereas the right global transformation $\Theta^R_{g,\mathrm{global}} = \prod_r \theta_g(r)^R$ is explicitly broken whenever C is not proportional to the identity [231]. This symmetry reduction further decreases the number of conserved quantities and is essential for driving the system away from integrability.

A specific choice satisfying condition (2.39) is [231]

$$C_0 = \frac{e^{-i\pi/4}}{\sqrt{2}}\left(\mathbb{I} + \frac{i}{\sqrt{3}}\,\sigma_x + \frac{i}{\sqrt{3}}\,\sigma_y - \frac{i}{\sqrt{3}}\,\sigma_z\right), \tag{2.40}$$

yielding a fully non-degenerate spectrum of flux eigenvalues $\{m_g\} = \{-2,\, 0,\, 2,\, 2/\sqrt{3},\, 1 - 1/\sqrt{3},\, -1 - 1/\sqrt{3}\}$ for the six elements of D_3. To study the crossover between the integrable regime (corresponding to $C \propto \mathbb{I}$, where conjugacy-class degeneracies and the right global gauge symmetry are restored) and the fully chaotic regime, one parametrizes

$$C(\varepsilon) = \frac{e^{-i\pi/4}}{\sqrt{2}}\left[\mathbb{I} + \frac{i\varepsilon}{\sqrt{3}}\big(\sigma_x + \sigma_y - \sigma_z\big)\right], \tag{2.41}$$

so that $\varepsilon \to 0$ recovers a matrix proportional to the identity (restoring integrability), while $\varepsilon = 1$ corresponds to the fully chiral choice C_0.

A standard diagnostic to distinguish chaotic from integrable quantum dynamics is the NNSD of the energy spectrum. In chaotic systems, Random Matrix Theory (RMT) predicts that the spacings follow the Wigner–Dyson distribution (specifically, the Gaussian Orthogonal Ensemble, GOE, for time-reversal-invariant systems), which exhibits characteristic level repulsion: $P(\omega) \to 0$ as $\omega \to 0$. In integrable systems, by contrast, energy levels are uncorrelated and follow Poisson statistics, $P(\omega) = e^{-\omega}$ [269, 270].

Before computing the NNSD, the raw spectrum must be *unfolded* to remove the global variation in the density of states and isolate the universal fluctuations. One first fits a smooth approximation $\rho(E)$ to the density of eigenvalues, and then maps each eigenvalue E_n to the unfolded value

$$\widetilde{E}_n = \int_{-\infty}^{E_n} \rho(E')\, dE' \,. \tag{2.42}$$

The unfolded energies $\widetilde{E}_n = \widetilde{N}(E_n)$ have, by construction, a uniform mean level density, so that the nearest-neighbor spacings $\omega_n = \widetilde{E}_{n+1} - \widetilde{E}_n$ can be directly compared with the theoretical distributions. As an alternative to the NNSD, one can bypass the unfolding procedure entirely by considering the ratio of consecutive level spacings [271, 272],

$$r_n = \frac{\min(\omega_n,\, \omega_{n-1})}{\max(\omega_n,\, \omega_{n-1})} \,, \tag{2.43}$$

whose mean value $\langle r \rangle$ takes the universal values $\langle r \rangle_{\text{Poisson}} \approx 0.386$ and $\langle r \rangle_{\text{GOE}} \approx 0.536$ [272].

To apply these diagnostics, the Hilbert space must first be restricted to a single symmetry sector, so that level repulsion is not masked by accidental crossings between states of different quantum numbers. In the D_3 ladder model, we have already selected one gauge sector by the gauge-fixing, and we have already broken the degeneracy on the magnetic flux. The only relevant symmetry left is geometrical, and is the vertical inversion $\mathcal{I}$, which maps $|g\rangle \to |g^{-1}\rangle$ on every rung and commutes with the Hamiltonian. Within the largest parity sector, we performed exact diagonalization for ladders of $N = 3, 4, 5$ rungs (with coupling $g^2 = 1$ and $C = C_0$) and found NNSD and gap-ratio distributions in excellent agreement with the GOE prediction [228].

Crucially, by tuning ε in Eq. (2.41), one can follow the crossover from integrability to chaos. Figure 2.6 shows the NNSD at six values of ε for $N = 5$. At $\varepsilon = 0.01$, the distribution is close to Poissonian, consistent with the near-integrability of the model when C is close to the identity. As ε increases, the distribution smoothly evolves toward the Wigner–Dyson form, and by $\varepsilon \approx 0.1$ the agreement with GOE is already convincing. The mean gap ratio $\langle r \rangle$ saturates to the GOE value for $\varepsilon \gtrsim 0.5$ and the critical ε at which integrability holds decreases with system size, suggesting that the near-integrable window shrinks to zero in the thermodynamic limit [228].

These spectral results establish the chaotic nature of the D_3 gauge-fixed model in the presence of the chiral perturbation and constitute a necessary prerequisite for the ETH to hold. The full verification of the ETH ansatz (2.36)—including the analysis of diagonal and off-diagonal matrix elements of local observables, the spectral function $f_{\mathcal{O}}(\bar{E}, \omega)$, entanglement entropy, and the real-time thermalization dynamics after quantum quenches—is presented in Ref. [228], to which we refer for further details. The physics of this system, including the precise characterization of the integrable-to-chaotic crossover and its implications for non-Abelian gauge dynamics, is still under active investigation.

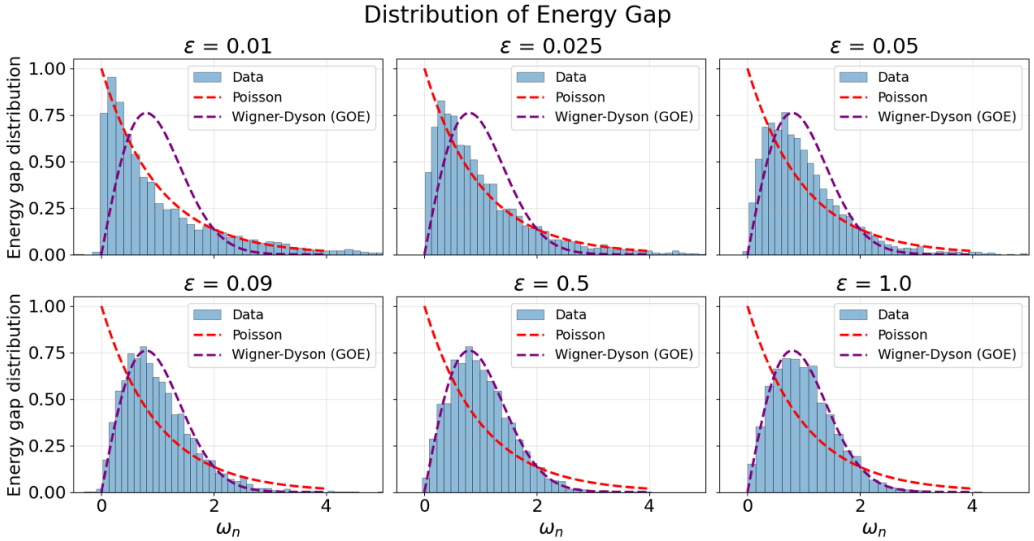

Figure 2.6: Distribution of nearest-neighbor level spacings $\{\omega_n\}$ for the D_3 gauge-fixed ladder ($N = 5$ rungs, largest parity sector) at six values of the chiral parameter ε in Eq. (2.41). At small ε the system displays Poisson statistics (dashed red), while for $\varepsilon \gtrsim 0.1$ the distribution transitions to the Wigner–Dyson (GOE) form (dashed purple), signaling quantum chaos. Taken from Ref. [228].

These results indicate that the gauge-fixed D3 ladder provides a minimal non-Abelian setting where ETH can be investigated without truncations.

2.4 Summary and Outlook

In this chapter, we characterized the gauge-invariant sectors of D_N LGTs, and we compared them with the simpler Abelian case of $\mathbb{Z}_2$. A key feature of non-Abelian LGTs is that the union of all gauge-invariant sectors does not span the full Hilbert space— in contrast to what happens in Abelian theories—, reflecting the richer internal structure of the gauge group. As a consequence, the study of gauge invariant sectors is numerically harder than in the Abelian case, requiring the development of other strategies to reduce the computational cost of the study of these systems.

In order to study the interplay between electric and magnetic degrees of freedom and enable efficient numerical investigations, we introduced the gauge-fixed flux ladder model [231]. This construction maps the original theory to an effective one-dimensional system with non-local string interactions, significantly reducing the effective Hilbert space dimension while preserving the essential physics.

Focusing on the D_3 case, we used this model to explore several physical properties. We have shown that, in a ladder geometry, the system does not exhibit a sharp phase transition between electric and magnetic regimes, but rather a smooth

crossover. This behavior is further supported by the analysis of quantum resource measures, such as nonstabilizerness and the Generalized Geometric Measure, which peak in the crossover region. We also performed a preliminary investigation of integrability, as a first step toward understanding the thermalization properties of the model.

A central open question concerns whether these systems satisfy the Eigenstate Thermalization Hypothesis and whether non-thermal features, such as quantum many-body scars, may arise. Addressing these aspects represents a natural and promising direction for future work.

Chapter 3

String breaking in D_N

3.1 Introduction and string-breaking by pair production

As already stressed in this thesis, the non-perturbative regime of non-Abelian gauge theories remains one of the key open problems in theoretical physics. Hamiltonian simulations of LGTs, both classical and quantum, offer a promising route to address such phenomena beyond the reach of Euclidean Monte Carlo methods. Yet, it remains unclear how deeply non-perturbative phenomena, such as confinement and string-breaking, are imprinted into discrete-group models and how they relate to the phenomenology of more complex theories such as QCD. In this chapter, we address this question by studying string-breaking and gluelump formation in pure-gauge D_N LGTs using tensor network simulations.

String formation is probably the most studied consequence of confinement [230]. Two color charges in representation τ in the vacuum, for example, would be connected by an electric flux in the representation τ to preserve the gauge invariance at each point of the space. If we consider dynamical matter and we imagine distancing the two charges, we find a competition between the electric and the mass term in the Hamiltonian, H_E and H_M, respectively (see Eq. (1.14) and (1.17)).

If we increase the length of the string above a certain threshold distance R^* in lattice spacing units, then the string breaks. Indeed, it is less expensive to produce a new pair of particles from the vacuum than to spend energy in the excitation of the electric flux, as depicted in Fig. 3.1. The condition for the *string-breaking by pair production* can be identified as follows

$$(R^* - 2)g^2\alpha_\tau > 2m \ , \tag{3.1}$$

where $g^2\alpha_\tau$ is the electric energy associated with one link in the lattice in the irrep τ, and $2m$ is the rest energy of the two particles produced from the vacuum.

In the following, we show that the confinement of static charges at strong coupling in dihedral groups D_N is intimately connected to the presence of a $\mathbb{Z}_2$ center.

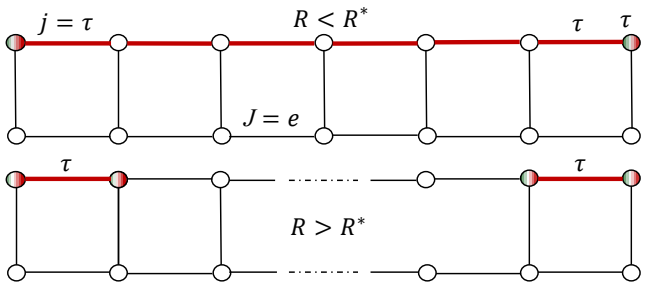

Figure 3.1: Qualitative ground-state configurations at strong coupling of non-Abelian LGTs, on a ladder, in the presence of dynamical matter on the corners. The string in the fundamental representation τ breaks when the charge separation $R > R^*$, with R^* defined in Eq. (3.1). In this case, depicted in the bottom ladder, the production of two particles and the formation of two mesons is energetically favourable, and the string flux is broken.

For N even, the group center is $\mathbb{Z}_2$ and a non-Abelian electric flux string connects—and confines—static probe charges over arbitrary distances. Conversely, when N is odd, the center is trivial and the string breaks *without matter production*, because gluon clouds screen the charges, forming bound states known in QCD as *gluelumps* [230], see Fig. 3.2(a-b) for a graphical representation.

The minimal setup to observe this drastically different behavior between even and odd N is a ladder geometry [231, 233, 234, 273], which combines both magnetic and electric field terms in a tractable 1D setting. In the following, we present tensor-network simulations of pure D_N LGTs, analyzing the different strong-coupling behaviors of D_3 and D_4 symmetry groups. A scaling analysis of the size of the D_3 gluelumps with the coupling strength allows for a precise characterization of the continuum limit, where they retain a finite interaction range. Our work demonstrates how discrete non-Abelian groups—even of small order—represent an ideal testbed to study the interplay between confinement, center symmetry, and fusion rules.

3.2 Model and local symmetries

We consider a D_N pure-gauge theory in a ladder geometry, where each link hosts a Hilbert space $\mathcal{H}_{\text{link}} = \{|h\rangle\,,\ h \in D_N\}$, with lattice spacing a. To test confinement, we add two static color charges on the edges of the upper leg. Figure 3.2 sketches the model and the relevant gauge-invariant configurations. As described in Chapter 1, the pure-gauge Kogut–Susskind Hamiltonian $H = H_B + H_E$ consists of two parts, the electric (see Eq. (1.14) and Eq. (1.15)) and the magnetic (see Eq. (1.16)) contribution. The pure-gauge Hamiltonian is then written as

$$H = H_E + H_B = \frac{c\hbar}{a} g^2 \sum_{\ell \in \text{links}} \sum_{j;m,n} \alpha_j \hat{P}^j_\ell - \frac{c\hbar}{a g^2} \sum_p \Re[\text{Tr}(U^j_{p_1} U^j_{p_2} U^{j\dagger}_{p_3} U^{j\dagger}_{p_4})]\ , \qquad (3.2)$$

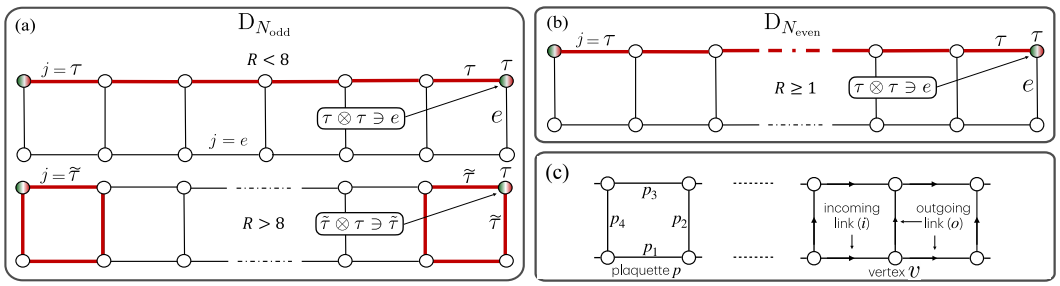

Figure 3.2: (a) Ground-state configurations at strong coupling of $D_{N_{\text{odd}}}$ LGTs on a ladder with static color charges on the corners. The string in the fundamental representation τ breaks when the charge separation R, in lattice units, is greater than 8, making the anti-fundamental $\tilde{\tau}-$glueballs energetically favourable. The charge-glueball configuration, named gluelump, is gauge-invariant due to the screening fusion rule of Eq. (3.8). (b) In $D_{N_{\text{even}}}$, the GS at strong coupling always comprises the shortest τ-string connecting the charged corners, since there is no equivalent to the screening fusion rule. (c) Ordering of links in a plaquette operator and highlighting of incoming and outgoing links associated with a vertex of the directed lattice.

where g^2 is the dimensionless coupling constant, $\sum_\ell$ is the direct sum of one-body terms diagonal in the irreps, and $U^j_{p_i}$ is the group connection in the $j-$th irrep acting on the $i-$th link of the $p-$th plaquette (see Fig. 3.2c). Hereafter, we consider the connection in the two-dimensional fundamental irrep $j = \tau$. We consider the rescaling (canonical) transformation $H \to H' = \frac{a}{c\hbar}H$ to work in dimensionless, natural units for the energy, which, however, may still carry a scaling dimension with the lattice spacing a. In these units, $g^2\alpha_j$ is the electric energy of the $j-$th irrep and $\hat{P}^j_\ell$ the corresponding projector on the $\ell-$th link.

The presence of two static charges does not affect the dynamics of the pure-gauge Hamiltonian in Eq. (3.2). Indeed, the hopping term is suppressed, and the mass term would just contribute to the energy with a constant. Physically, the two static charges can be seen as a background charge on the two vertices.

Considering the local gauge transformations $\Theta_{h,n}$, $h \in D_N$, the presence of the static charges on the sites v' introduces the matter transformation term, which does not appear in pure-gauge vertices. Hence, the transformations on the vertices read as

$$\begin{aligned}\Theta_{h,v} &= \prod_o \theta^L_{h,o} \prod_i \theta^R_{h,i} \ , \text{ for pure-gauge vertices, and} \\ \Theta_{h,v'} &= \prod_o \theta^L_{h,o} \prod_i \theta^R_{h,i}\theta^Q_{v'} \ , \text{ in the presence of a static charge.}\end{aligned} \tag{3.3}$$

Gauge-invariant states in the neutral sector satisfy $\Theta_{h,v}\,|\psi_{\text{phys}}\rangle = |\psi_{\text{phys}}\rangle\,, \forall h, v$. These constraints dictate which combinations of electric field configurations can

appear on the links surrounding the vertex v. In particular, they determine how the irreducible representations surrounding a vertex can fuse, the so-called "*fusion rules*" [274], see Appendix A for details.

3.3 Fusion rules of D_N and screening fusion rule

Finite groups allow for computing the Clebsch–Gordan (CG) coefficients, the mathematical object that describes how two irreps fuse into a third one, and therefore, the fusion rules of representations, through their characters. In the following, we exploit the simple structure of D_N groups to get an analytic calculation of fusion rules, in terms of the decomposition of an arbitrary representation into irreducible ones.

The number and the dimensions of the irreducible representations in D_N are reported in Table 1.2. Here, we repeat for convenience how to characterize the two-dimensional irreducible representations for D_N.

Let $\omega = e^{2\pi i/N}$ and $h \in \{1, \dots, N/2-1\}$ for N even and $h \in \{1, \dots, (N-1)/2\}$ for N odd. The two-dimensional irreducible representation τ_h of the group elements is given as follows:

$$D^{\tau_h}(r^k) = \begin{pmatrix} \omega^{hk} & 0 \\ 0 & \omega^{-hk} \end{pmatrix}, \quad D^{\tau_h}(sr^k) = \begin{pmatrix} 0 & \omega^{-hk} \\ \omega^{hk} & 0 \end{pmatrix} . \tag{3.4}$$

Here, we have chosen the form of the irreps, for which $\overline{\tau_h}(g)$ and $\tau_h(g^{-1})$ are equivalent up to reordering. Therefore, we can drop the conjugation when dealing with fusion rules. The characters are then

$$\begin{aligned} &\chi_{\tau_h}(sr^k) = \chi_\tau(sr^k) = 0 \ , \\ &\chi_{\tau_h}(\mathbb{1}) = \chi_\tau(\mathbb{1}) = 2 \ , \\ &\chi_{\tau_h}(r^k) = 2\cos\left(\frac{2\pi hk}{N}\right) . \end{aligned} \tag{3.5}$$

In the following, we denote the fundamental representation $\tau_{h=1}$ simply as τ.

By the great orthogonality theorem for finite groups, each representation J of $\mathcal{G}$ can be written as a direct sum over irreducible representations

$$J = \bigoplus_{j \text{ irrep}} j^{\otimes a_j} , \tag{3.6}$$

where a_j is the multiplicity of the j-th irreducible representation. The multiplicity can be calculated by referring to the characters of the group in each irrep as follows

$$a_j = (\chi_j, \chi_J) := \frac{1}{|\mathcal{G}|} \sum_{g \in \mathcal{G}} \overline{\chi_j(g)} \chi_J(g) \equiv \frac{1}{|\mathcal{G}|} \sum_C |C| \overline{\chi_j(C)} \chi_J(C) \ , \tag{3.7}$$

where $\chi_J(g)$ is the character of element g in J and $\chi_j(g)$ is its character in j. The bar denotes the complex conjugation. The second equality holds due to the fact that characters are invariant over conjugacy classes, labeled by C.

Definition: screening fusion rule

We define the screening fusion rule as follows:

$$\exists \text{ irrep } j \mid \quad j \otimes \tau \ni j \ , \tag{3.8}$$

where j is a non-Abelian irrep ($\dim(j) > 1$). This rule means that the gauge field in the irrep j is not changed as it flows through a fundamental charge in the τ representation. In D_N groups, Eq. (3.8) can be satisfied by the faithful anti-fundamental irrep $j = \tilde{\tau}$ and the associated CG coefficients are determined by the group center. For odd N, the center is trivial—the identity element $\{\mathbb{1}\}$—and the CG coefficient is one. For even N, the center is $\mathbb{Z}_2$ and the CG coefficient is zero.

We now want to demonstrate that the fusion rule in Eq. (3.8) holds for odd N but not for even N, and that this difference in the value of the CG coefficient associated with the screening fusion rule is due to the presence, or not, of a non-trivial center. The center Z of a group $\mathcal{G}$ is an Abelian subgroup that commutes with every other element of $\mathcal{G}$, i.e., $Z = \{h \in \mathcal{G} : \ \forall\ g \in \mathcal{G},\ hg = gh\}$. Z is also a normal subgroup, meaning that $ghg^{-1} \in Z\ \forall\ g \in \mathcal{G},\ h \in Z$.

Since the D_N characters are real, thus invariant under conjugation, Eq. (3.8) can be rewritten as $\tau_h \otimes \tau_h \ni \tau$. That is, we aim to show that the decomposition of $J = \tau_h \otimes \tau_h$ as per Eq. (3.6) into a direct sum yields the multiplicities associated with the fundamental irrep as $a_\tau = 0$ for N even, while $a_\tau = 1$ is possible for N odd.

To prove the above statement, we consider the more general case $J = \tau_h^{\otimes l}$, where l is even. To find the multiplicities a_τ, we need to compute the inner product

$$(\chi_\tau, \chi_{\tau_h^{\otimes l}}) = \frac{1}{|D_N|} \sum_C |C| \overline{\chi_{\tau_h}(C)}^{\,l} \chi_\tau(C) \ , \tag{3.9}$$

where we used the fact that $\chi_{\tau_h^{\otimes l}} = \chi_{\tau_h}^l$.

Let us begin with N even. In this case, the inner product becomes

$$\begin{aligned} |D_N|(\chi_\tau, \chi_{\tau_h^{\otimes l}}) =& \chi_\tau(\mathbb{1})\chi_{\tau_h}^l(\mathbb{1}) + \chi_\tau(r^{N/2})\chi_{\tau_h}^l(r^{N/2}) \\ &+2 \sum_{k=1}^{N/2-1} \chi_\tau(r^k)\chi_{\tau_h}^l(r^k) + (N/2)\chi_\tau(s)\chi_{\tau_h}^l(s) + (N/2)\chi_\tau(sr)\chi_{\tau_h}^l(sr) \ . \end{aligned} \tag{3.10}$$

Substituting the value of the characters of Eq. (3.5) into Eq. (3.10), one gets

$$|D_N|(\chi_\tau, \chi_{\tau_h^{\otimes l}}) = 2^{l+1} + 2^{l+1}(-1)^{hl+1} + 2^{l+2} \sum_{k=1}^{N/2-1} \cos^l\left(\frac{2\pi hk}{N}\right) \cos\left(\frac{2\pi k}{N}\right) \ . \tag{3.11}$$

The second term has an overall negative sign, since l is even, and cancels exactly the first term. These two contributions are associated with the conjugacy classes of the

$\mathbb{Z}_2$ center $Z = \{\mathbb{1}, r^{N/2}\}$. The third term can be shown to be identically zero for all allowed h. Here, we need to look at two different cases separately. If $N/2-1$ is even, then the number of summands in the sum is even, and they cancel pairwise. For $N/2-1$ odd, the number of summands in the sum is odd, and all but one summand cancel pairwise. The remaining summand, corresponding to $k = N/4$, is, however, zero, since $\cos(\pi/2) = 0$ and therefore the sum vanishes also in this case. Overall, for N even, the coefficient $a_\tau = 0$.

When N is odd, the π rotation is not a group element, and the contribution from the identity conjugate class will not be canceled. The inner product becomes

$$|D_N|(\chi_\tau, \chi_{\tau_h^{\otimes l}}) = \chi_\tau(\mathbb{1})\chi^l_{\tau_h}(\mathbb{1}) + 2\sum_{k=1}^{(N-1)/2} \chi_\tau(r^k)\chi^l_{\tau_h}(r^k) + N\chi_\tau(s)\chi^l_{\tau_h}(s)\ . \quad (3.12)$$

Substituting the character values yields

$$|D_N|(\chi_\tau, \chi_{\tau_h^{\otimes l}}) = 2^{l+1} + 2^{l+2}\sum_{k=1}^{(N-1)/2} \cos^l\left(\frac{2\pi hk}{N}\right)\cos\left(\frac{2\pi k}{N}\right)\ . \quad (3.13)$$

We need to evaluate the second term in the last equation and show that there are h and l for which the inner product is not zero. For example, in the case of $N = 3$, so the group D_3, for $l = 2$, and $h = 1$ (i.e., the only two-dimensional, irrep $\tau_{h=1} \equiv \tau$) it holds

$$|D_3|(\chi_\tau, \chi_{\tau^{\otimes l}}) = 2^{2+1} + 2^{2+2}\left(-\frac{1}{8}\right) = 6\ , \quad (3.14)$$

and therefore $a_\tau = (\chi_\tau, \chi_{\tau^{\otimes 2}}) = 1$.

For odd $N > 3$, the fundamental representation τ does not satisfy Eq. (3.8) any longer —$(\chi_\tau, \chi_{\tau^{\otimes 2}}) = 0$— while the faithful representation with the largest $h = (N-1)/2$ does. This is the anti-fundamental representation, denoted by $\tilde{\tau}$. Indeed, setting $h = (N-1)/2$ and $l = 2$ in Eq. (3.13) leads to

$$(\chi_\tau, \chi_{\tilde{\tau}^{\otimes 2}}) = 1 \quad (3.15)$$

for all odd N. This means that the state on a charged vertex, where two semilinks are in the $\tilde{\tau}$ representation, is gauge invariant, satisfying the screening fusion rule of Eq. (3.8).

In summary, for N even, we have $\tau_h \otimes \tau_h \not\ni \tau$. In contrast, for N odd, $\tau_h \otimes \tau_h = \cdots \oplus \tau$ when $h = (N-1)/2$. Hence, when two copies of a non-Abelian representation for N odd mix, the result can be in the fundamental representation, while this is not the case for N even. The fusion rules of D_3 and D_4, the simplest odd and even groups respectively, are summarized in Fig. 3.3.

Similar calculations suggest that $\tilde{\tau}$-gluelumps are dynamically connected to the τ-flux string connecting the two static charges. To show that, one has to evaluate

Figure 3.3: Graphic comparison of the fusion rules of D_3 (left) and D_4 (right). Arrows indicate nonvanishing Clebsch–Gordan coefficients. For D_3, the fundamental representation τ has a non-vanishing Clebsch–Gordan coefficient with itself, while for D_4, only terms connecting τ with the one-dimensional representations are finite.

the following inner product

$$|D_N|(\chi_\tau^{\otimes l+1}, \chi_{\tilde{\tau}}) = 2^{l+2} + 2^{l+3} \sum_{k=1}^{(N-1)/2} \cos\left(\frac{\pi k(N-1)}{N}\right) \cos^{l+1}\left(\frac{2\pi k}{N}\right) . \tag{3.16}$$

The smallest integer l, for which the inner product $(\chi_\tau^{\otimes l+1}, \chi_{\tilde{\tau}})$ is one, is

$$l = \begin{cases} 0, & N = 3 \\ \frac{N-3}{2}, & N > 3 \, . \end{cases} \tag{3.17}$$

Physically, it implies that we need to apply the group connection U^τ, as part of plaquette operators, $l(N)$ times, to transit from the fundamental string to the $\tilde{\tau}$ loops—the dynamical string-breaking becomes a process of higher order as N increases, making it non-perturbative in the limit of odd $N \to \infty$.

Whether the screening fusion rule in Eq. (3.8) holds has profound consequences for the physics of dihedral LGTs. Consider color charges that transform as the fundamental irrep of the group τ. Then, in $D_{N_{\text{odd}}}$ groups, the screening fusion rule allows them to be simultaneously the source and the sink of electric flux lines in the anti-fundamental representation $\tilde{\tau}$. At strong coupling and large distances, we thus expect static charges to be screened by the glueballs pinned at the charge positions.

Bound states of this kind are known in QCD as *gluelumps* [230], and their formation is connected to a string-breaking phenomenon *without matter production*. Gluelumps are not a gauge-invariant configuration for $D_{N_{\text{even}}}$ groups, where Eq. (3.8) does not hold and a pair of static charges *must* be connected by a τ-flux string. These different gauge-invariant configurations are sketched in Fig. 3.2(a-b).

3.4 Rishon formalism

To study the properties of the gluelumps at different couplings, we perform Tensor Network simulations of D_3 and D_4 LGTs in the rishon formalism. This approach reformulates the gauge theory in terms of a local dressed-site basis, which enables an efficient DMRG implementation by making the non-Abelian Gauss's law explicit at the level of individual vertices. In Sec. 3.4.1, we construct the local gauge-invariant basis by splitting each link into two semilinks (rishons) and projecting onto the physical subspace at each vertex. In Sec. 3.4.2, we express the electric and magnetic terms of the Hamiltonian in this dressed basis, together with the selection rules that enforce the matching between adjacent semilinks.

3.4.1 Local dressed basis in rishon formalism

We proceed with a reformulation of the D_N lattice gauge theory in a local dressed sites basis, which allows for efficient Tensor Network implementation [95, 97, 133, 187, 190]. We solve the non-Abelian Gauss's law on each vertex of the lattice by splitting each link into two halves, each attached to its adjacent vertex. This procedure can be reversed once the so-called selection rules are imposed on semilinks that correspond to the same link.

In the electric basis, the parallel transporter U_{ab}, in the fundamental representation τ, can be expressed as [149]

$$\begin{aligned}
&\langle j_1; m_1, n_1 |\, U_{ab} \,| j_2; m_2, n_2 \rangle = \\
&= \sqrt{\frac{\dim(j_2)}{\dim(j_1)}} \langle j_2, m_2; \tau, a | j_1, m_1 \rangle^* \langle j_2, n_2; \tau, b | j_1, n_1 \rangle \\
&= \sqrt{\dim(j_1)\dim(j_2)} \begin{pmatrix} j_2 & \tau & \bar{j}_1 \\ m_2 & a & \bar{m}_1 \end{pmatrix}^* \begin{pmatrix} j_2 & \tau & \bar{j}_1 \\ n_2 & b & \bar{n}_1 \end{pmatrix} \\
&= \langle \tau, a; \bar{j}_1, \bar{m}_1 | \bar{j}_2, \bar{m}_2 \rangle^* \langle j_2, n_2; \tau, b | j_1, n_1 \rangle \ ,
\end{aligned} \tag{3.18}$$

where we explicitly express the fusion rules via the Clebsch–Gordan coefficients, or $3J$-symbols. We can also explicitly carry out the calculations and get [149]

$$\langle j_1; m_1, n_1 |\, U_{ab} \,| j_2; m_2, n_2 \rangle = \frac{\sqrt{\dim(j_1)\dim(j_2)}}{|\mathcal{G}|} \sum_{g \in \mathcal{G}} D^{\tau}_{ab}(g) D^{j_1 *}_{m_1 n_1}(g) D^{j_2}_{m_2 n_2}(g) \ , \tag{3.19}$$

with $D^{j}_{\alpha\beta}(g)$ denoting the matrix elements of the group element g in the irreducible representation j. Equation (3.18) shows that the group connection fuses separately the two indices of multi-dimensional representations; for instance, the n_2 and m_2 enter two different Clebsch–Gordan coefficients. Therefore, each link can be split into left and right semilinks, such that $|j, m_L, m_R\rangle = |j_1, m_L\rangle \otimes |j_2, m_R\rangle\, \delta_{j_1,j_2} \delta_{j,j_1}$, where δ_{j_1,j_2} fixes the same representation on the two semilinks. Then, the parallel

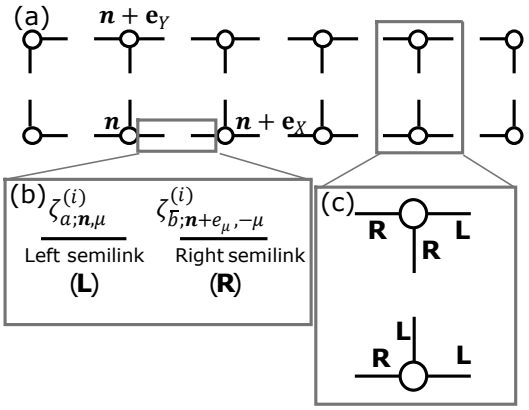

Figure 3.4: (a) Sketch of the ladder geometry. (b) Splitting of a gauge field living on a link into two rishon operators. (c) Dressed sites of the ladder consisting of three semilinks. Sites on the upper legs have two ingoing (R) and one outgoing (L) semilinks, while sites on the lower legs have the opposite.

transporter can be split into rishon operators [68, 96, 275], distinctly acting on the left or the right semilink Hilbert space (see Fig. 3.4(b)),

$$U_{ab;\mathbf{n},\mathbf{n}+\mathbf{e}_\mu} = \sum_i \zeta^{(i)}_{a;\mathbf{n},\mu} \zeta^{(i)\dagger}_{\bar{b};\mathbf{n}+\mathbf{e}_\mu,-\mu} \ , \tag{3.20}$$

where the index i labels different rishon modes. We make explicit the action of the parallel transporter connecting the sites $\mathbf{n}$ and $\mathbf{n}+\mathbf{e}_\mu$ ($\mu = \mathrm{x},\mathrm{y}$), and the tensor product is projected onto the space where left and right rishons are in the same irrep. The label $\pm\mu$ indicates the position, with respect to the site n, of the semilink the rishon operator acts on. Splitting U_{ab} gives the possibility to define gauge transformations and the Hamiltonian in terms of dressed sites, i.e., a site $\mathbf{n}$ with the attached semilinks.

Once split on the rishon spaces, the action of $\theta_g^{L(R)}$ operators (defined in Eq. (1.2)) is non-trivial only on the outgoing (ingoing) semilink:

$$\theta_g^L = \Lambda_g^L \otimes \mathbb{1}_d \ , \quad \theta_g^R = \mathbb{1}_d \otimes \Lambda_g^R \ , \tag{3.21}$$

with $\mathbb{1}_d$ the identity acting on the d-dimensional rishon space. On a ladder, gauge transformations on a vertex are given by the product of three Λ transformations. This indicates that for a given dressed site, i.e., the vertex and the three semilinks, a gauge invariant basis can be obtained by removing states that transform non-trivially under the product of Λ transformations. Due to the choice of orientation of the links, one has to differentiate between upper and lower vertices on the ladder, as well as between the different edges. As one can see in Fig. 3.4(c), the lower dressed sites are constructed by taking the tensor product of one right (R) and two left (L) semilinks, and the upper dressed sites by two right (R) and one left (L) semilink.

In the following, we write the operators and the transformations aforementioned for the D_3 case. We label the representation basis for D_3 as $\{|0\rangle, |p\rangle, |rr\rangle, |rg\rangle, |gr\rangle, |gg\rangle\}$, where $|0\rangle$ indicates the trivial representation, $|p\rangle$ the parity, and the states in the fundamental representation $|\tau ab\rangle$ are labeled by expressing internal indices (colors) as "red" and "green". Thus, the parallel transporter U_{ab} reads

$$U_{ab} = \left(\begin{array}{c|c|cccc} 0 & & \frac{1}{\sqrt{2}}d_{rr} & \frac{1}{\sqrt{2}}d_{rg} & \frac{1}{\sqrt{2}}d_{gr} & \frac{1}{\sqrt{2}}d_{gg} \\ \hline & 0 & \frac{1}{\sqrt{2}}d_{rr} & \frac{-1}{\sqrt{2}}d_{rg} & \frac{-1}{\sqrt{2}}d_{gr} & \frac{1}{\sqrt{2}}d_{gg} \\ \hline \frac{1}{\sqrt{2}}d_{gg} & \frac{1}{\sqrt{2}}d_{gg} & & & & d_{rr} \\ \frac{1}{\sqrt{2}}d_{gr} & \frac{-1}{\sqrt{2}}d_{gr} & & & d_{rg} & \\ \frac{1}{\sqrt{2}}d_{rg} & \frac{-1}{\sqrt{2}}d_{rg} & & d_{gr} & & \\ \frac{1}{\sqrt{2}}d_{rr} & \frac{1}{\sqrt{2}}d_{rr} & d_{gg} & & & \end{array}\right), \tag{3.22}$$

where $d_{\alpha\beta} = \delta_{a\alpha}\delta_{b\beta}$. Importantly, U_{ab} is not block-off diagonal: this implies that acting with the parallel transporter on a link in the fundamental representation τ can still result in the same irrep. In Fig. 3.3, the arrows depict non-vanishing CG coefficients. Since for D_3 we have 3 fluxes (between different representations), we need to formulate three rishon modes, one for each flux. By reducing the representation basis to the left and right semilink basis, $\{|0\rangle, |p\rangle, |r\rangle, |g\rangle\}$, one can check that the following rishon operators satisfy Eq. (3.20) in the decomposition of the parallel transporter of Eq. (3.22):

$$\zeta_a^{(1)} = 2^{-\frac{1}{4}} \left(\begin{array}{c|c|cc} 0 & & \delta_{ar} & \delta_{ag} \\ \hline & 0 & 0 & 0 \\ \hline \delta_{ag} & 0 & 0 & \\ \delta_{ar} & 0 & & 0 \end{array}\right), \quad \zeta_a^{(2)} = 2^{-\frac{1}{4}} \left(\begin{array}{c|c|cc} 0 & & 0 & 0 \\ \hline & 0 & \delta_{ar} & -\delta_{ag} \\ \hline 0 & \delta_{ag} & 0 & \\ 0 & -\delta_{ar} & & 0 \end{array}\right), \tag{3.23}$$

$$\zeta_a^{(3)} = \left(\begin{array}{c|c|cc} 0 & & 0 & 0 \\ \hline & 0 & 0 & 0 \\ \hline 0 & 0 & 0 & \delta_{ar} \\ 0 & 0 & \delta_{ag} & 0 \end{array}\right).$$

To construct the gauge-invariant dressed sites, we need to first describe how the gauge transformations act on the rishons. It is sufficient to consider the transformations $\theta_r^{L(R)}$ and $\theta_s^{L(R)}$, with respect to the group elements r and s[1], respectively,

[1] the non-trivial rotation of $2\pi/3$ and the reflection

since all other transformations of D_N can be written as products of their powers,

$$\theta_r^L = \left(\begin{array}{c|c|ccccc} 1 & & & & & & \\ \hline & 1 & & & & & \\ \hline & & \omega & & & & \\ & & & \omega & & & \\ & & & & \omega^{-1} & & \\ & & & & & \omega^{-1} & \end{array}\right), \quad \theta_s^L = \left(\begin{array}{c|c|cccc} 1 & & & & & \\ \hline & -1 & & & & \\ \hline & & 0 & & 1 & \\ & & & 0 & & 1 \\ & & 1 & & 0 & \\ & & & 1 & & 0 \end{array}\right),$$

$$\theta_r^R = \left(\begin{array}{c|c|ccccc} 1 & & & & & & \\ \hline & 1 & & & & & \\ \hline & & \omega^{-1} & & & & \\ & & & \omega & & & \\ & & & & \omega^{-1} & & \\ & & & & & \omega & \end{array}\right), \quad \theta_s^R = \left(\begin{array}{c|c|cccc} 1 & & & & & \\ \hline & -1 & & & & \\ \hline & & 0 & 1 & & \\ & & 1 & 0 & & \\ & & & & 0 & 1 \\ & & & & 1 & 0 \end{array}\right), \tag{3.24}$$

where $\omega = \exp(2\pi i/3)$. In the 4-dimensional rishon basis $\{|0\rangle, |p\rangle, |r\rangle, |g\rangle\}$, the transformations in Eq. (3.24) read

$$\Lambda_r^L = \left(\begin{array}{c|c|cc} 1 & & & \\ \hline & 1 & & \\ \hline & & \omega & \\ & & & \omega^{-1} \end{array}\right), \quad \Lambda_r^R = \left(\begin{array}{c|c|cc} 1 & & & \\ \hline & 1 & & \\ \hline & & \omega^{-1} & \\ & & & \omega \end{array}\right),$$

$$\Lambda_s^L = \left(\begin{array}{c|c|cc} 1 & & & \\ \hline & -1 & & \\ \hline & & 0 & 1 \\ & & 1 & 0 \end{array}\right) = \Lambda_s^R \,. \tag{3.25}$$

On the upper and lower dressed sites, the transformations read

$$\begin{aligned} \Lambda_{r/s}^{\text{up}} &= \Lambda_{r/s}^R \otimes \Lambda_{r/s}^R \otimes \Lambda_{r/s}^L \,, \\ \Lambda_{r/s}^{\text{down}} &= \Lambda_{r/s}^R \otimes \Lambda_{r/s}^L \otimes \Lambda_{r/s}^L \,, \end{aligned} \tag{3.26}$$

while for the four corners, the transformation laws are

$$\begin{aligned} \Lambda_{r/s}^{\text{up,left}} &= \Lambda_{r/s}^R \otimes \Lambda_{r/s}^L \,, \quad \Lambda_{r/s}^{\text{up,right}} = \Lambda_{r/s}^R \otimes \Lambda_{r/s}^R \,, \\ \Lambda_{r/s}^{\text{down,left}} &= \Lambda_{r/s}^L \otimes \Lambda_{r/s}^L \,, \quad \Lambda_{r/s}^{\text{down,right}} = \Lambda_{r/s}^R \otimes \Lambda_{r/s}^L \,. \end{aligned} \tag{3.27}$$

The local gauge-invariant states in the neutral sector are constructed by projecting the semilinks attached to a vertex on the eigenspace of the gauge transformation operators from Eq. (3.26) and Eq. (3.27) with eigenvalue 1:

$$\Lambda_r \Lambda_s \, |\psi_{\text{phys}}\rangle = |\psi_{\text{phys}}\rangle \,. \tag{3.28}$$

The order of projection with respect to the group elements is not important, as long as the physical space is the common eigenspace with real eigenvalues.

In the presence of charges, physical states on the vertices are constructed by taking the tensor product of the attached semilinks and the four-dimensional Hilbert space of the charge (charges being in the fundamental representation),

$$\Lambda_r \theta^{\psi}_r \Lambda_s \theta^{\psi}_s \left|\psi_{\text{phys}}\right\rangle = \left|\psi_{\text{phys}}\right\rangle \ , \tag{3.29}$$

where we defined the transformation laws for the matter to be the same as for the left rishons, Eq. (3.25), as already discussed as a consequence of Eq. (1.49).

In D_3, in the charge-neutral sector, the gauge-invariant basis for the dressed sites at any vertex within the ladder is 11-dimensional. On the upper leg, labeling the semilinks to the left of the vertex, below the vertex, and to the right of the vertex sequentially, the basis states can be written as

$$\begin{aligned}
&|1\rangle = |0,0,0\rangle \quad |2\rangle = \frac{|r,0,r\rangle + |g,0,g\rangle}{\sqrt{2}} \\
&|3\rangle = \frac{|0,r,r\rangle + |0,g,g\rangle}{\sqrt{2}} \quad |4\rangle = \frac{|r,g,0\rangle + |g,r,0\rangle}{\sqrt{2}} \\
&|5\rangle = \frac{|r,r,g\rangle + |g,g,r\rangle}{\sqrt{2}} \quad |6\rangle = \frac{|r,p,r\rangle - |g,p,g\rangle}{\sqrt{2}} \\
&|7\rangle = \frac{|p,r,r\rangle - |p,g,g\rangle}{\sqrt{2}} \quad |8\rangle = \frac{|r,g,p\rangle - |g,r,p\rangle}{\sqrt{2}} \\
&|9\rangle = |p,p,0\rangle \quad |10\rangle = |p,0,p\rangle \quad |11\rangle = |0,p,p\rangle \ .
\end{aligned} \tag{3.30}$$

For the dressed sites on the lower leg, the gauge-invariant basis can be obtained by conjugating the colored central fields $r \leftrightarrow g$ in Eq. (3.30).

The procedure of projecting on the gauge invariant subspace on each vertex can also be used for D_4, which gives a local gauge-invariant dimension of 28 for each dressed site. On the corners, the dressed local dimension is, for D_3, 5 with static charges and 3 without, while for D_4 it is 8 and 5, respectively.

3.4.2 Hamiltonian in the rishon basis

We proceed with projecting the Hamiltonian on the gauge-invariant dressed basis constructed above. Each semilink contributes with half the electric field energy. Thus, the electric Hamiltonian in Eq. (1.14), which is diagonal in the representation basis, can be reformulated as

$$H_E = \frac{c\hbar}{a} g^2 \sum_{sl \in \text{semilinks}} \sum_j \frac{\alpha_j}{2} \hat{P}^j_{sl} \ . \tag{3.31}$$

By considering the semilinks attached to each vertex, it is possible to express the electric Hamiltonian in terms of dressed sites

$$H_E = \sum_n H^{(1)}_{E,\mathbf{n}} \ , \tag{3.32}$$

where $H_E^{(1)}$ is the electric Hamiltonian acting on the single dressed sites. In D_3, in the 11-dimensional dressed basis in Eq. (3.30), its diagonal entries are the following:

$$\begin{aligned} H_E^{(1)} = \frac{c\hbar}{a}\frac{g^2}{2}\mathrm{diag}(&3\alpha_0,\ 2\alpha_\tau+\alpha_0,\ 2\alpha_\tau+\alpha_0,\ 2\alpha_\tau+\alpha_0,\\ &3\alpha_\tau,\ 2\alpha_\tau+\alpha_p,\ 2\alpha_\tau+\alpha_p,\ 2\alpha_\tau+\alpha_p,\ 2\alpha_p+\alpha_0,\\ &2\alpha_p+\alpha_0,\ 2\alpha_p+\alpha_0)\ . \end{aligned} \tag{3.33}$$

In our numerical simulations, we set the electric energy coefficients α_{j_i} as follows

$$\alpha_0 = 0,\ \alpha_\tau = 1,\ \alpha_p = 10\ . \tag{3.34}$$

The plaquette operator can be projected on the gauge-invariant dressed basis by employing the rishon formulation of the group connection:

$$\begin{aligned} &\sum_{a,b,c,d} \Re(U^{ab}_{\mathbf{n},\mathbf{n}+\mathbf{e}_\mathrm{x}} U^{bc}_{\mathbf{n}+\mathbf{e}_\mathrm{x},\mathbf{n}+\mathbf{e}_\mathrm{x}+\mathbf{e}_\mathrm{y}} U^{\dagger cd}_{\mathbf{n}+\mathbf{e}_\mathrm{y},\mathbf{n}+\mathbf{e}_\mathrm{x}+\mathbf{e}_\mathrm{y}} U^{\dagger da}_{\mathbf{n},\mathbf{n}+\mathbf{e}_\mathrm{y}})\\ &= \left(\sum_i \zeta^{(i)}_{a;\mathbf{n},\mathrm{x}} \zeta^{(i)\dagger}_{\bar{b};\mathbf{n}+\mathbf{e}_\mathrm{x},-\mathrm{x}}\right)\left(\sum_i \zeta^{(i)}_{b;\mathbf{n}+\mathbf{e}_\mathrm{x},\mathrm{y}} \zeta^{(i)\dagger}_{\bar{c};\mathbf{n}+\mathbf{e}_\mathrm{x}+\mathbf{e}_\mathrm{y},-\mathrm{y}}\right)\\ &\times \left(\sum_i \zeta^{(i)}_{\bar{c};\mathbf{n}+\mathbf{e}_\mathrm{x}+\mathbf{e}_\mathrm{y},-\mathrm{x}} \zeta^{(i)\dagger}_{d;\mathbf{n}+\mathbf{e}_\mathrm{y},\mathrm{x}}\right)\left(\sum_i \zeta^{(i)}_{\bar{d};\mathbf{n}+\mathbf{e}_\mathrm{y},-\mathrm{y}} \zeta^{(i)\dagger}_{a;\mathbf{n},\mathrm{y}}\right). \end{aligned} \tag{3.35}$$

By reordering and regrouping the rishons, we can write down the plaquette in the following form:

$$\begin{aligned} &\sum_{a,b,c,d} \Re(U^{ab}_{\mathbf{n},\mathbf{n}+\mathbf{e}_\mathrm{x}} U^{bc}_{\mathbf{n}+\mathbf{e}_\mathrm{x},\mathbf{n}+\mathbf{e}_\mathrm{x}+\mathbf{e}_\mathrm{y}} U^{\dagger cd}_{\mathbf{n}+\mathbf{e}_\mathrm{y},\mathbf{n}+\mathbf{e}_\mathrm{x}+\mathbf{e}_\mathrm{y}} U^{\dagger da}_{\mathbf{n},\mathbf{n}+\mathbf{e}_\mathrm{y}}) =\\ &\sum_{i,j,k,l=1}^{3} C^{li}_{\mathbf{n},\mathrm{x},\mathrm{y}} C^{ij}_{\mathbf{n}+\mathbf{e}_\mathrm{x},\mathrm{y},-\mathrm{x}} C^{jk}_{\mathbf{n}+\mathbf{e}_\mathrm{x}+\mathbf{e}_\mathrm{y},-\mathrm{x},-\mathrm{y}} C^{kl}_{\mathbf{n}+\mathbf{e}_\mathrm{y},-\mathrm{y},\mathrm{x}}\ , \end{aligned} \tag{3.36}$$

where we defined the gauge-invariant corner operators as

$$C^{ij}_{\mathbf{n},\mu_1,\mu_2} \equiv \sum_a \zeta^{i}_{a;\mathbf{n},\mu_1} \zeta^{j\dagger}_{a;\mathbf{n},\mu_2}\ , \tag{3.37}$$

with $a \to \bar{a}$ when $\mu = -\mathrm{x},\ -\mathrm{y}$. The corner operators act per construction on the semilinks attached to the vertex on which they are defined. Furthermore, since they are gauge-invariant per construction (summation over color indices), the projection of the gauge-invariant subspace is rather trivial. Therefore, we can write the magnetic part of the Hamiltonian in the dressed site as

$$H_B = -\frac{1}{ag^2} \sum_{\mathbf{n};i,j,k,l} C^{li}_{\mathbf{n},\mathrm{x},\mathrm{y}} C^{ij}_{\mathbf{n}+\mathbf{e}_\mathrm{x},\mathrm{y},-\mathrm{x}} C^{jk}_{\mathbf{n}+\mathbf{e}_\mathrm{x}+\mathbf{e}_\mathrm{y},-\mathrm{x},-\mathrm{y}} C^{kl}_{\mathbf{n}+\mathbf{e}_\mathrm{y},-\mathrm{y},\mathrm{x}}\ , \tag{3.38}$$

where the summation is performed over the sites $(\mathbf{n})$ and rishon indices (i,j,k,l).

The non-Abelian Gauss's law is already satisfied in the construction of the dressed basis in Eq. (3.30). However, the splitting $|j, m_L, m_R\rangle = |j_1, m_L\rangle \otimes |j_2, m_R\rangle \, \delta_{j_1,j_2} \delta_{j,j_1}$ introduces constraints between adjacent dressed sites, since the left and right semilink representation of each link must be the same. In the effective Hamiltonian implemented in the DMRG, we add the following Abelian selection rules:

$$\begin{aligned} (\hat{D}^R_{\mathbf{n}} \hat{D}^L_{\mathbf{n}+\mathbf{e}_\mathrm{x}} - 1) \, |\psi_\mathrm{phys}\rangle = 0 \ \forall \mathbf{n} \ , \\ (\hat{D}^C_{\mathbf{n}} \hat{D}^{C'}_{\mathbf{n}+\mathbf{e}_\mathrm{y}} - 1) \, |\psi_\mathrm{phys}\rangle = 0 \ \forall \mathbf{n} \ , \end{aligned} \tag{3.39}$$

where the $\hat{D}$ operators are diagonal in the dressed basis space, with entries that depend on the irrep in the left, right, and central semilinks of the dressed site state. We recall that, by construction, $\hat{D}^L$ operators act on the right-most label in the dressed basis in Eq. (3.30), a possible choice for the $\hat{D}$ operators is

$$\begin{aligned} \hat{D}^L_{\mathbf{n}} &= \mathrm{diag}(1, 2, 2, 1, 2, 2, 2, -1, 1, -1, -1) \ , \\ \hat{D}^R_{\mathbf{n}} &= \mathrm{diag}(1, \tfrac{1}{2}, 1, \tfrac{1}{2}, \tfrac{1}{2}, \tfrac{1}{2}, -1, \tfrac{1}{2}, -1, -1, 1) \ , \\ \hat{D}^C_{\mathbf{n}} &= \mathrm{diag}(1, 1, 2, 2, 2, -1, 2, 2, -1, 1, -1) \ , \\ \hat{D}^{C'}_{\mathbf{n}} &= \mathrm{diag}(1, 1, \tfrac{1}{2}, \tfrac{1}{2}, \tfrac{1}{2}, -1, \tfrac{1}{2}, \tfrac{1}{2}, -1, 1, -1) \ , \end{aligned} \tag{3.40}$$

where we assigned arbitrary values to the identity, parity, and fundamental representations, $(1, -1, 2)$ respectively in $\hat{D}^L$ and $\hat{D}^C$, such that Eqs. (3.39) are satisfied only when the two semilinks are in the same irrep.

3.5 DMRG results

To study the properties of the gluelumps at different couplings, we analyze the ground state of D_3 and D_4 LGTs with DMRG. Both groups have a single two-dimensional (fundamental) irrep, so that $\tilde{\tau} = \tau$. We consider the cases in which there are no charges ($q = 0$) and where the upper corners of the ladder are occupied by single static charges ($q = 1$). All simulations are performed using the ITensor [276, 277] Julia library, with maximum MPS bond dimension $\eta = 200$ and cutoff $\epsilon = 10^{-11}$.

Fig. 3.5 shows that the phenomenology of the crossover described in Sec. 2.3.1 appears to be very similar. The electric energy density $\langle H_e \rangle / N_\ell$—with N_ℓ the number of links in the ladder—and the plaquette expectation value $\langle B_p \rangle$, once rescaled by the inverse of their coupling dependence, calculated in D_3 and D_4 LGTs depict a phenomenology that does not depend on the system size (number of rungs $N_r \in [4, 60]$) or on the presence of static charges. For $g^2 \gg 1$, the expectation values of the electric energy at strong coupling correspond to the electric energy of the trivial irrep, while at weak coupling correspond to a weighted average of irreps' electric energies. In this case, because of the values in Eq. (3.34), the weighted averages in the dot-dashed grey line in the top panels in Fig. 3.5, read

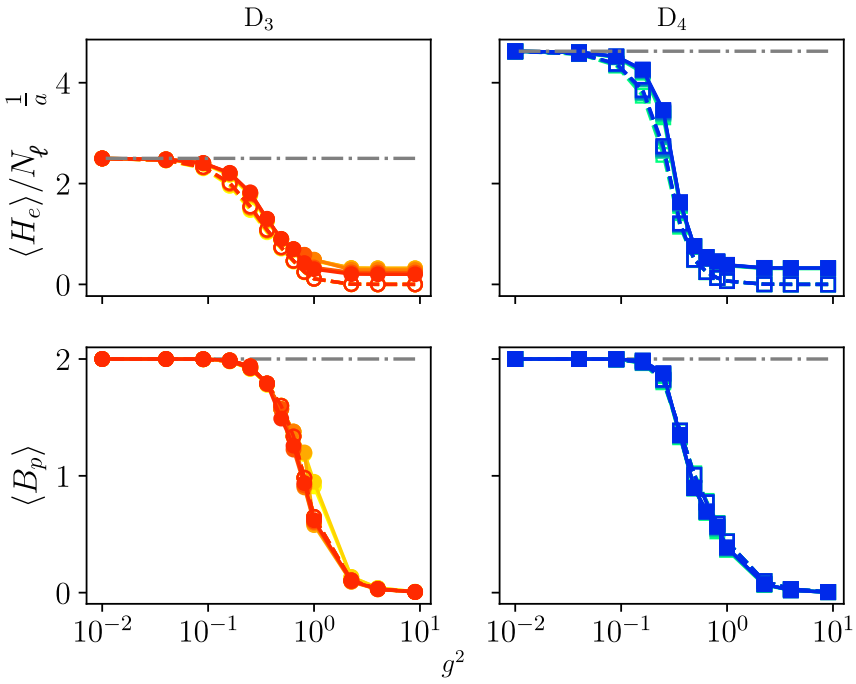

Figure 3.5: Electric (above) and magnetic (bottom) energy density for D_3 and D_4 LGTs on a ladder. Continuous lines with filled markers indicate the presence of two static charges on the upper corners of the ladder, while dashed lines with empty markers stand for the neutral sector. The results are almost independent of the number of rungs ($N_r \in [4, 60]$, increasing for darker colors).

$$\langle \frac{H_E}{g^2 N_\ell} \rangle (g \to 0) = \sum_J \alpha_J \frac{\dim(J)^2}{|\mathcal{G}|} = \begin{cases} \frac{0+1\times4+10}{6} = 2.\bar{3} & \text{for } D_3 \ , \\ \frac{0+1\times4+10+10+10}{8} = 4.25 & \text{for } D_4 \ . \end{cases} \tag{3.41}$$

The effect of glueballs screening the static charges at strong coupling emerges clearly when comparing the string tension

$$\sigma(g, R) = \frac{E_{q=1}(g, R) - E_{q=0}(g, R)}{R} \tag{3.42}$$

for the two groups. $E_{q=1(0)}$ is the ground-state energy with (without) probe charges, and R is their distance. At strong coupling, the dominant contribution to the energy difference is linear with R, and σ is proportional to $g^2(\alpha^\tau - \alpha^e)$. This is, indeed, what happens for D_4, where σ shows no significant size scaling (see Fig. 3.6). Conversely, for D_3 at strong coupling, the string tension decreases linearly as R increases, making the energy difference $E_{q=1} - E_{q=0} = \sigma R$ independent of the charge separation, see inset of Fig. 3.6. This asymptotic value $[E_{q=1}(g, R \to \infty) - E_{q=0}(g, R \to \infty)] = 2M(g)$ can be interpreted as the renormalized contribution to the mass of the two

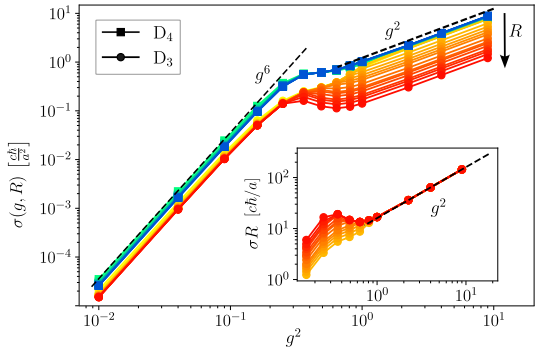

Figure 3.6: String tension as a function of the coupling g^2. We compare different charge separations R, indicated by line shading, for D_3 (warm colours and circles) and D_4 (cold colours and squares). The weak confinement $\sigma \propto g^6$ at $g^2 \lesssim 0.2$ is qualitatively similar for both models. For D_4, the string tension σ is independent of R, indicating the presence of a field string connecting the charges. Instead, for D_3 at strong coupling, the string breaks, indicated by σ decreasing with growing R. The inset shows the energy difference $E_{q=1}(g,R) - E_{q=0}(g,R) = \sigma(g,R)R$ [see Eq. (3.42)]. Its independence of R at strong coupling highlights the mutual screening of the two gluelumps, and $\sigma R = 2M_0(g)$.

	Strong coupling	Weak coupling
D_3	$\min(8,R)g^2$	Rg^6
D_4	Rg^2	Rg^6

Table 3.1: Summary of the scaling of the string energy $R\sigma(g,R)$ consistently with Eq. (3.42) for the two groups and the two regimes considered. R is measured in lattice units a.

gluelumps [2]. Because of the fundamental (trivial) irrep energies in Eq. (3.34), we have $M(g) \simeq M_0(g) = 4g^2$, for $g^2 > 1$.

At weak coupling and short distances, both groups display weak confinement due to the background electric field, analogously to what can be observed in a $\mathbb{Z}_N$ theory [233]. In such a model, second-order perturbation theory predicts the string tension to scale as $\sigma(g,R) \propto g^6$, which matches the behavior of the D_N theories. Table 3.1 summarizes the behaviors of D_3 and D_4 in the two coupling regimes.

The R-dependent crossover between the g^2 and the g^6 scaling in D_3 can be understood in terms of a growing effective size of the dressed particles as g^2 decreases, due to increasing electric-field fluctuations. The spread of the gluelumps along the ladder has a direct effect on their interaction range. To characterize it, we study the

[2]Thanks to the fast convergence of the gluelump mass, we compute it in practice using a fixed large system size accessible to DMRG (here, $R = 59$).

scaling of the distance-dependent potential between two gluelumps,

$$V(g,R) = E_{q=1}(g,R) - E_{q=0}(g,R) - 2M(g)\ . \tag{3.43}$$

When rescaling the distance R, see Fig. 3.7, DMRG data obtained at different g^2 collapse onto a universal behavior of the rescaled potential $V(g, Rg^{\kappa})/M(g)$, with $\kappa = 2.5(1) \simeq \frac{5}{2}$, showing a finite screening length R_s at any nonzero coupling strength. The mass follows $M(g) \simeq \gamma g^{-\upsilon} - M_0(g)$, see inset of Fig. 3.7, with $\upsilon = 5.99(5) \simeq 6$.

These observations convey precious information regarding the continuum limit scaling, which is uniquely defined under a couple of assumptions. First, we request that the physical range r_{phys} of the linear potential well is a finite length in the limit $a \to 0$. This assumption requires the lattice coupling g to obey the scaling

$$g \simeq \left(\zeta \frac{a}{r_{\text{phys}}}\right)^{1/\kappa}, \quad \text{for} \quad a \ll r_{\text{phys}}\,, \tag{3.44}$$

where the dimensionless value $\zeta = 21.2(4)$ is the x-axis location of the knee in Fig. 3.7. According to this argument, since $g \propto a^{1/\kappa}$ and $\kappa > 0$, the continuum limit is located at small g values (as intuitively understood from the lattice extension of the gluelumps increasing with the strength of the plaquette term).

Second, we set the physical quasiparticle excitation energy $\mathcal{E}_{\text{phys}}$, related to one gluelump sitting at the edge, to be finite in the continuum limit. This fixes the scaling dimension of lattice unit energies, as $M \simeq \gamma g^{-\upsilon} \propto a^{-\upsilon/\kappa}$[3], where we fitted $\gamma = 0.19(1)$ in Fig. 3.7(inset). At the same time, $M(g)$ must scale linearly with $\mathcal{E}_{\text{phys}}$ (at fixed r_{phys} and a) and be dimensionless, meaning we can write it as

$$M(g(a)) \simeq \xi \frac{\mathcal{E}_{\text{phys}} r_{\text{phys}}}{c\hbar} \left(\frac{r_{\text{phys}}}{a}\right)^{\upsilon/\kappa}. \tag{3.45}$$

All that is left is to evaluate the dimensionless factor ξ, which, using $M \simeq \gamma g^{-\upsilon}$ and Eq. (3.44), reads

$$\xi = \left(\frac{c\,\hbar}{\mathcal{E}_{\text{phys}}\, r_{\text{phys}}}\right) \frac{\gamma}{\zeta^{\upsilon/\kappa}}. \tag{3.46}$$

Thus, these two assumptions allowed us to perform the energy conversion from lattice to physical units in the continuum limit, similar to a running coupling analysis [278, 279].

Interestingly, the amplitude of the interaction potential V between the two quasiparticles exhibits *the same emergent scaling* as $M(g)$ with g, and therefore with a. This implies that in the continuum limit, this interaction potential will survive and be finite, thus providing measurable elastic scattering amplitudes for the field theory.

[3]Here, we neglect the $M_0 \propto g^2$ contribution assuming it is much smaller than the $\sim g^{-6}$ scaling at weak coupling.

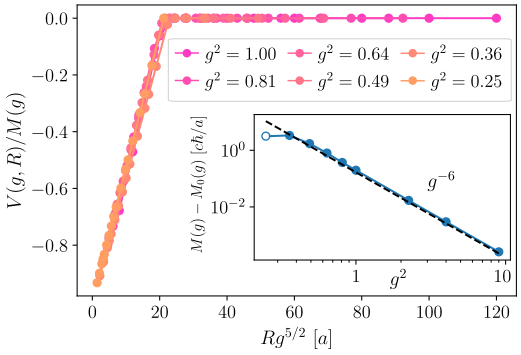

Figure 3.7: Rescaled interaction potential $V(g, Rg^\kappa)$, with $\kappa = 5/2$ as a function of the separation between the two charges. The excellent collapse suggests that the screening distance scales as $R_s \sim g^{-5/2}$. Inset: deviation of the renormalized mass $M(g)$ from the behaviour $M_0(g) = 4g^2$ expected at strong-coupling. The leftmost point corresponds to a coupling strength where R is too small to see the screening effect.

3.6 Comparison with $SU(N)$ LGT

It is instructive to compare dihedral groups with Lie groups like $SU(N)$. For the latter, the nontrivial center prevents the screening fusion rule for the fundamental representation, but not for other representations that have zero N-ality. N-ality is related to the mapping of the center subgroup $\mathbb{Z}_N$ in a given representation of $SU(N)$. Zero N-ality means that the center is mapped into the identity matrix. One such example is the eight-dimensional adjoint irrep of $SU(3)$ (**8**), which fulfills the screening fusion condition. Indeed,

$$\mathbf{3} \otimes \mathbf{8} \ni \mathbf{3} \ , \tag{3.47}$$

that satisfies the screening fusion rule of Eq. (3.8). This allows for color-neutral objects composed by a charge screened by a gluon cloud, the QCD gluelumps [230, 280, 281]. These excitations—although theoretically possible—have not been observed in nature, as their existence would be linked to matter particles transforming as the **8** irrep. Even though gluelumps are not asymptotic states of QCD, they have been extensively studied as lattice objects with a static adjoint source [282–285]. A similar phenomenology also happens in $D_{N_{\text{even}}}$, with $N_{\text{even}} \geq 6$, where two-dimensional non-faithful irreps with zero N-ality do exist. Considering D_6, for example, the fusion rule reads

$$\tau_1 \otimes \tau_2 \ni \tau_1 \ . \tag{3.48}$$

where τ_1 is the fundamental representation of D_6 and τ_2 is the non-faithful two-dimensional representation, such that the group elements in the two representations

are given by

$$D^{\tau_1}(r^k) = \begin{pmatrix} \omega^k & 0 \\ 0 & \omega^{-k} \end{pmatrix}, \quad D^{\tau_1}(sr^k) = \begin{pmatrix} 0 & \omega^{-k} \\ \omega^k & 0 \end{pmatrix},$$
$$D^{\tau_2}(r^k) = \begin{pmatrix} \omega^{2k} & 0 \\ 0 & \omega^{-2k} \end{pmatrix}, \quad D^{\tau_2}(sr^k) = \begin{pmatrix} 0 & \omega^{-2k} \\ \omega^{2k} & 0 \end{pmatrix}, \tag{3.49}$$

where $\omega = e^{\pi i/3}$. Note that τ_2, the non-faithful two-dimensional representation of D_6, reads like the fundamental representation τ of D_3.

Despite the similarities in the construction of the D_N- and the $SU(N)$-gluelumps, there are major differences, once we consider the gauge theory coupled to dynamical matter. In QCD, adjoint matter is associated with composite objects like quark–antiquark pairs. Thus, $SU(N)$ gluelumps can be obtained by producing a quark-antiquark pair from the vacuum, moving either component around an arbitrary closed path, and merging it back to the partner particle. The reverse process would annihilate them. This is not the case, e.g., for the D_3 gauge theory with staggered fermions in the fundamental representation τ. Here, the charge components of gluelumps are subject to a global U(1) symmetry, protecting them from being absorbed in the vacuum, thus making the gluelumps stable particles.

3.7 Summary and outlook

In this chapter, we have investigated the influence of fusion rules on the structure of gauge-invariant states in dihedral LGTs. Only models with $D_{N_{\text{odd}}}$ gauge symmetry allow for the screening of fundamental static charges at strong coupling thanks to the formation of gluelumps, i.e., bound states of a charge and a glueball. Through scaling analysis, we have shown that the interaction range of such objects remains finite in the continuum limit, raising the perspective of studying related scattering phenomena. In $D_{N_{\text{even}}}$, gluelump formation is prevented by a (nontrivial) $\mathbb{Z}_2$ center. Interestingly, the very same property also has a deep impact on local-fermionic-parity conservation when the theory includes dynamical fermions: only when $\mathbb{Z}_2$ is a normal subgroup of the gauge group, one can map the system onto a local Hamiltonian without fermionic degrees of freedom in arbitrary dimensions [97, 134, 149, 190, 286, 287] (see also Appendix B).

The group property supporting the $D_{N_{\text{odd}}}$ gluelumps implies that they remain valid gauge-invariant states in any spatial dimension. The scaling analysis and the spatial structure of the gluon cloud, in contrast, do depend on the ladder geometry. This raises interesting questions about how our findings generalize to larger-dimensional lattices and whether the gluelumps remain stable in the presence of a finite-coupling deconfinement phase transition.

Moreover, these results showcase how pure-gauge D_3 theories already display a string-breaking process without the presence of dynamical charges, making them one

of the simplest models to test quantum- and quantum-inspired simulation protocols for the study of confinement and string-breaking in non-Abelian LGTs.

A natural question that emerges is the competition between the string-breaking by gluelump formation and the string-breaking mediated by the production of dynamical particles, whose condition is reported in Eq. (3.1). The distance in lattice spacing units between two charges must be $R' > 8$ to cause the gluelump formation, while for the string-breaking by pair production we have $R^* > 2(\frac{m}{g^2\alpha_\tau} + 1)$. Comparing R' and R^* indicates when one process is privileged, or it is suppressed by the other one. We expect the gluelump formation to be privileged when $R' < R^*$. Taking the extreme value of $R' = 8$, we get

$$2\left(\frac{m}{g^2\alpha_\tau} + 1\right) > 8, \ \rightarrow \frac{m}{g^2\alpha_\tau} > 3, \ \rightarrow m > 3g^2\alpha_\tau \ . \tag{3.50}$$

In general, we expect the previous condition not to hold in the strong coupling limit, meaning that for $g^2 \gg 1$ the privileged string-breaking mechanism will be the one mediated by pair production. As g^2 decreases, however, the two competing mechanisms—gluelump formation and pair nucleation—may become energetically comparable, and their relative dominance will depend non-trivially on the ratio $m/g^2\alpha_\tau$. Understanding how this competition evolves as a function of the coupling strength, and in particular identifying the crossover regime where neither mechanism dominates, represents a concrete open question for future investigations, both on the ladder and in higher-dimensional geometries.

Part II

Quantum simulation of Lattice Gauge Theories

Chapter 4

Quantum Zeno effect in Abelian LGTs

Generally speaking, until fault-tolerant devices are developed, quantum simulation protocols are prone to imperfections and approximations. In the case of quantum simulation of LGTs, the result may be the breaking of the gauge symmetries, resulting in errors that lead to nonphysical results. The local conserved quantities in LGTs present an intriguing avenue for harnessing these symmetries to implement several error-mitigation strategies [143, 288]. Among the possible approaches, one can modify the Hamiltonian to include energy penalties on unphysical gauge sectors [65, 81, 99, 289–293], design stochastic processes to destroy phase coherence between physical and nonphysical states [294–297], or use the gauge symmetry to improve the data quality in post-selection [81, 82, 85].

A particularly appealing approach in the context of digital quantum simulation is to adapt mid-circuit syndrome measurements, a cornerstone of quantum error-correction and detection algorithms [298], to the context of LGTs, as the local gauge symmetries offer a natural qubit redundancy [299–302]. Previous works on using measurements to stabilize local symmetries have mostly focused on formal fault-tolerant frameworks [295, 296, 299–302], often overlooking realistic quench dynamics and how measurements affect it, or on protecting against purely coherent gauge drifts [81, 99, 288, 293–295], neglecting scenarios with both unitary and dissipative errors.

Here, instead, we deal with both coherent and incoherent gauge-breaking errors within the same framework. We consider the effect on the system dynamics of the interplay of error strength and the measurement frequency, also taking into account the further noise they might introduce. In particular, we study the physics of the dynamical post-selection (DPS) protocol, which consists of the error protection due to the measurement of the gauge charges not only at the end of the time evolution, as happens in the standard post-selection, but in the middle of it.

Our framework is based on the general theory of the interplay between monitoring and unitary dynamics, which introduces a further layer of complexity and can

give rise to intricate many-body dynamics, including, e.g., phase transitions in the entanglement properties [303–307]. One remarkable phenomenon that emerges in this context is the celebrated quantum Zeno (QZ) effect, wherein frequent measurements hamper the quantum dynamics, constraining the system evolution within a limited set of states [308–315]. Understanding and harnessing the QZ effect in a many-body system is currently one of the main challenges in the field of monitored systems and can be key for advancing the capabilities of quantum simulations and quantum information processing, as well as improving our comprehension of open quantum system dynamics [316–325].

We will work mainly through the paradigmatic example of a $1+1$d $\mathbb{Z}_2$ LGT with fermionic matter, where we explore the synergistic relationship between stochastic monitored quantum dynamics, error correcting codes [147, 203, 299, 300, 326], and strong constraints. The reason for that is the simplicity of such a model, which has been previously studied in quantum simulation on superconducting qubits in Ref. [81]. In particular, its small dimensionality makes it possible to study the Liouvillian master equation using Exact Diagonalization. We demonstrate the generality of our findings by also analysing gauge theories with $\mathbb{Z}_3$ and truncated $U(1)$ symmetry. In the next chapter, the measurement of local gauge charges to mitigate errors is applied to the non-Abelian group D_3.

4.1 Dynamical post-selection in digital quantum simulations

In present-day devices, quantum simulations are typically affected by errors that can break the symmetries of the target model. In the spirit of performing real-time evolution, for LGTs, this means that the time evolution couples the physical superselection sector with non-physical subspaces. We denote these subspaces with $\mathcal{H}_{\mathcal{P}}$ and $\mathcal{H}_{\mathcal{Q}}$, respectively. A single Trotter step affected by this *gauge non-invariant* time evolution can be modeled as

$$\rho(t+\Delta t) = \mathcal{E} \circ \mathcal{U}_{\Delta t}[\rho(t)] \ , \tag{4.1}$$

where $\mathcal{U}_{\Delta t}$ generates the desired gauge-invariant dynamics, according to Eq. (1.19), and $\mathcal{E}$ is a generic error channel, typically coupling $\mathcal{H}_P$ and $\mathcal{H}_Q$, as sketched in Fig. 4.1(a). After sufficiently many such time steps, the errors accumulating during the time evolution induce an effective thermalization, and the density matrix will typically approach a steady state.

To preserve the gauge invariance of the system state, we exploit the Gauss' law operators in Eq. (1.1). Since $[H_{\mathrm{PG}}, \Theta_{h,n}] = 0$ for all h, n, applying the gauge-symmetry transformations does not affect the target gauge-invariant dynamics on the physical superselection sector, the neutral sector in the following version of Eq. (1.5),

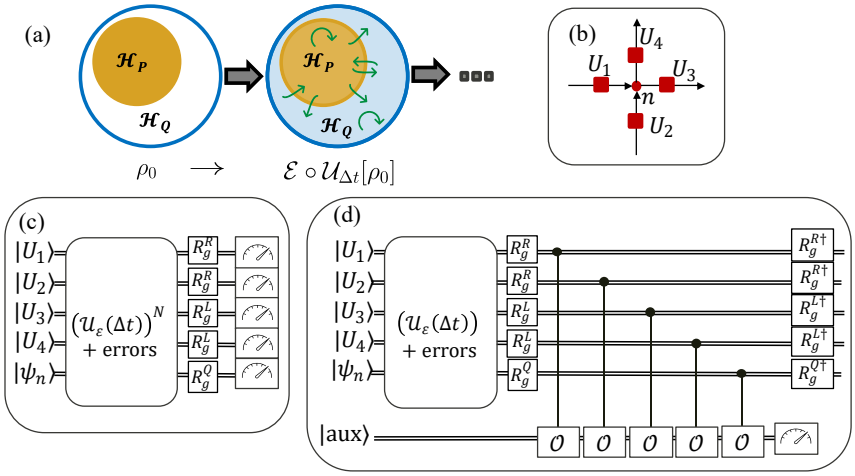

Figure 4.1: (a) Errors in the quantum simulation of an LGT model couple the physical (gauge-invariant) sector $\mathcal{H}_P$ with the rest of the Hilbert space $\mathcal{H}_Q$. (b) A site n and its associated link variables U_i. (c) Standard post-selection: whether a target local symmetry is satisfied or not is checked at the end of the simulation. First, we rotate into the basis that diagonalizes $\Theta_{g,n}$, then projective measurements on the system register can be used to reconstruct the value of the gauge charge $\alpha_{g,n}$. (d) In Dynamical post-selection (DPS), after the change of basis, the index pointing to $\alpha_{g,n}$ is encoded on an auxiliary register. The controlled operators C-$\mathcal{O}$ depend on the group structure. A local measurement on the auxiliary qudit identifies whether the Gauss' law associated with $\Theta_{g,n}$ is satisfied or not, projecting the wave function onto the corresponding subspace (see Eq. (4.5)). Finally, we rotate back into the computational basis. After this building block, another Trotter step, another gauge test, or the measurement of desired observables can follow. In (c-d), double lines identify quantum registers.

$$\Theta_{h,n} |\psi_{\text{phys}}\rangle = |\psi_{\text{phys}}\rangle \ \ \forall h, n \ , \forall \psi_{\text{phys}} \in \mathcal{H}_P \, . \tag{4.2}$$

Employing symmetries is an established tool for detecting and mitigating errors in the outcomes of quantum computations [143, 327–333]. These techniques can become more challenging when coping with LGTs, as one has to verify an extensive number of potentially non-commuting symmetries.

Let us consider a general site on a lattice as shown in Fig. 4.1(b), where the local gauge transformation associated with a group element g in Eq. (1.1) reads

$$\Theta_{g_n} = \theta^R_{g,1} \otimes \theta^R_{g,2} \otimes \theta^L_{g,3} \otimes \theta^L_{g,4} \otimes \theta^Q_g \, . \tag{4.3}$$

The indices $\{1, \dots, 4\}$ label the four links connected to the site n. The vertex operator Θ_{g_n} can be diagonalized by the tensor product of matrices diagonalizing $\Theta^{R(L)}_g$ on each link,

$$R = R^R_{g,1} \otimes R^R_{g,2} \otimes R^L_{g,3} \otimes R^L_{g,4} \otimes R^Q_g \ . \tag{4.4}$$

The simplest idea would be to use this change of basis at the end of the time evolution to check whether the gauge symmetries are still satisfied or not. We denote this scheme, successfully applied for example in Ref. [81] and sketched in Fig. 4.1(c), as standard post-selection. Standard post-selection cannot notice errors that couple the physical sector with itself with a second or higher-order phenomena. Moreover, it includes projective measurements on the system register, potentially losing physical information even if the target symmetry is satisfied and preventing further operations.

In contrast, one of the goals in DPS is to measure the eigenvalue of Θ_{g_n} without causing a complete wavefunction collapse. In the spirit of syndrome/stabilizer measurements [299, 327, 334], we introduce an auxiliary register to encode the information about the symmetry we want to test. This auxiliary register is initialized in the $|0\rangle$ state and the information about $\Theta_{v,g}$ is encoded through the action of four controlled operators C-$\mathcal{O}$, following the basis rotations of Eq. (4.4) to diagonalize Θ_{g_n}, as depicted in Fig. 4.1(c). The specific form of the operator $\mathcal{O}$ depends on the gauge group $\mathcal{G}$ and on the group element g, but it typically acts on the auxiliary register as a controlled permutation of its states. Then, a local measurement yielding the $|0\rangle$ ($|k \neq 0\rangle$) state on the auxiliary register projects the system state onto the subspace that satisfies (does not satisfy) invariance under the target local transformation. Finally, the basis rotation is reversed. Note that a reset of the auxiliary register is not necessary, as the simulation stays in the target sector as long as all auxiliary registers remain in their initial state $|0\rangle$. The outcome of each measurement, instead, can be easily stored in a number of classical registers growing linearly in both N and the circuit depth.

To further understand the result of this procedure, let us consider a situation where the incoherent error channel in Eq. (4.1) is described by probabilistically

occurring unitaries. Such a scenario includes a broad range of errors, such as uncontrolled gate fluctuations. Assuming the state at time t satisfied the non-Abelian Gauss' laws, we can approximate a noisy Trotter step of a single random (unitary) trajectory as

$$\begin{aligned} |\psi(t)\rangle_{\text{sat}} &\longrightarrow \alpha\,|\psi(t+\Delta t)\rangle_{\text{sat}} + \beta\,|\psi\rangle_{\text{np}} \\ &\longrightarrow \alpha\,|\psi(t+\Delta t)\rangle_{\text{sat}} \otimes |0\rangle + \beta\,|\psi\rangle_{\text{np}} \otimes |k\neq 0\rangle \\ &\longrightarrow \begin{cases} |\psi(t+\Delta t)\rangle_{\text{sat}} & \text{with probability } |\alpha|^2 \\ |\psi\rangle_{\text{np}} & \text{with probability } |\beta|^2 \end{cases} , \end{aligned} \tag{4.5}$$

where $|\psi\rangle_{\text{sat}}$ denotes states that satisfy the local symmetry Θ_{g_n} that has been monitored and $|\psi\rangle_{\text{np}}$ denotes non-physical states that violate it. Despite the discretized evolution being deterministic, the outcome of each measurement is stochastic, and so is the collapse of the wavefunction in the physical or the non-physical Hilbert space, with the probability of its outcome depending on the amplitude of the gauge violation. Importantly, we may dilute the measurements, either by measuring only a subset of local charges at each time step or by reducing the frequency of the measurements. This allows for the tuning of the effective protection strength. Finally, at the end of the procedure, we can measure observables of interest or continue the time evolution, since the physical information remains untouched by the DPS when we measure the initial gauge charge.

Crucially, when a gauge violation is measured, i.e., the ancilla state has flipped, the simulation is discarded as it gives a nonphysical contribution to the evaluation of expectation values.

4.2 Model Hamiltonian

To illustrate the interplay between measurements and gauge protection in the simplest way possible, we consider a $1+1$d lattice with open boundary conditions of N sites and $N-1$ links, the gauge group of the theory is $\mathbb{Z}_2$, and we consider dynamical matter to have a non-trivial dynamics [81, 89, 229]. We have already introduced this system in Sec. 2.1.1 to show the partition of the Hilbert space in different sectors in an Abelian theory, so here we will just write the Hamiltonian after a standard Jordan–Wigner transformation, recasting the fermionic matter fields in terms of spin operators:

$$H_J = J \sum_n \left(\sigma_n^+ \tau^x_{n,n+1} \sigma^-_{n+1} + \text{h.c}\right) , \tag{4.6a}$$

$$H_f = f \sum_n \tau^z_{n,n+1} , \tag{4.6b}$$

$$H_m = \frac{M}{2} \sum_n (-1)^n \sigma^z_n . \tag{4.6c}$$

In the place of the fermionic operators in Eq. (2.2), the Pauli operators σ_n^α act on the sites of a 1D lattice and represent the dynamical charges, while the Pauli operators $\tau_{n,n+1}^\alpha$ are still the $\mathbb{Z}_2$ gauge field operators acting on the link between sites n and $n+1$.

We also repeat the set of local symmetry operators the Hamiltonian $H_{\mathbb{Z}_2}$ commutes with:

$$\Theta_n = -\tau_{n-1,n}^z \sigma_n^z \tau_{n,n+1}^z \ , \tag{4.7}$$

(see Eq. (3.3)).

Since we are interested in possible error suppression and correction methods, we consider coherent as well as incoherent sources of errors. For the coherent errors, we choose spin flips of the gauge operators and unassisted tunneling between neighboring matter sites in order to represent typical local errors that may appear in a quantum simulation [90, 91, 293, 335]. The corresponding Hamiltonian is

$$H_{\text{err}} = \lambda_1 \sum_n \tau_{n,n+1}^x + \lambda_2 \sum_n \left(\sigma_n^+ \sigma_{n+1}^- + \text{h.c.}\right) \ , \tag{4.8}$$

where $\lambda_{1(2)}$ is the strength of the corresponding error source. The Hamiltonian H_{err} does not commute with the symmetry generators Θ_n and thus couples sectors with different values of the local charges. The normalized gauge violation

$$\delta g = \frac{1}{2N} \sum_n |\langle \Theta_n \rangle - \alpha_{n,\text{targ}}| \tag{4.9}$$

monitors how far the error Hamiltonian is leading the state away from the target charge sector identified by the set of conserved charges $\alpha_{n,\text{targ}}$. While other error sources can be considered, we do not expect their specific choice to qualitatively change the system dynamics, as long as H_{err} remains local and explicitly breaks the gauge symmetries.

We model incoherent errors as spin flips or phase flips (Pauli errors) randomly occurring during the time evolution. We will denote with p_{err} the probability per qubit per Trotter step that one of these errors affects a quantum simulation. As we are interested in harnessing the Gauss laws to detect and correct gauge-violating errors, we will consider only the Pauli-X channel that explicitly breaks the $\mathbb{Z}_2$ gauge symmetries.

We use the Python library qutip [336, 337] for the numerical analysis of the following sections.

4.3 DPS in $\mathbb{Z}_2$ LGT

To test the results of the DPS in the presence of the noise model in Eq. (4.8), we consider a digital quantum simulation protocol where the state evolves according to a standard first-order Trotter discretization of the time evolution operator $\mathrm{e}^{-iHt} = \left[\mathrm{e}^{-iH\Delta t}\right]^{n_t}$, with $t = \Delta t\, n_t$ being the total evolution time and n_t the number of

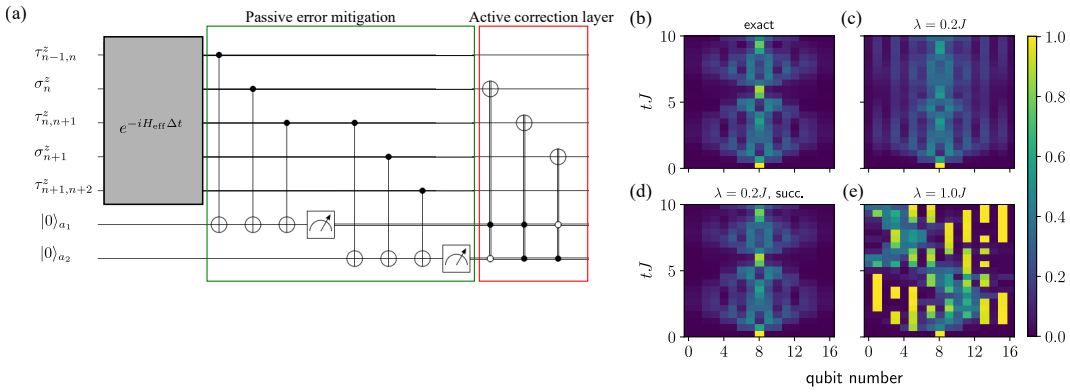

Figure 4.2: (a) Circuit representation of the DPS error mitigation/correction scheme. The gray box is a single Trotter step with an effective non-Hermitian Hamiltonian that includes gauge-breaking terms and, possibly, incoherent spin flips. The results of the measurements on the auxiliary qubits have to be stored in a $N \times n_t$ classical register. The first block after the unitary evolution monitors possible gauge violations, mitigating coherent errors. The active correction layer exerts feedback on the computational qubits based on the measurements on the ancillas, compensating for spin-flip incoherent errors. (b-e) Examples of dynamics affected by gauge-violating errors and measurements of the local gauge charges. The colormap represents the qubit excitation $(1 - \sigma^z_n)/2$ for matter qubits and $(1 - \tau^z_{n,n+1})/2$ for gauge variables. (b) Ideal trotterized dynamics. (c) Dynamics affected by coherent errors with $\lambda = 0.2J$. The deviations from the ideal dynamics are clearly visible. (d) Single trajectory with successful dynamical post-selection in the Zeno regime. The ideal dynamics is restored to an excellent degree. (e) Irregular dynamics due to measurements out of the quantum Zeno regime, where error suppression is no longer possible. All simulations have $L = 17$ qubits ($N = 9$ matter sites), electric coupling $f = 0.5J$ and fermion mass $M = 0$.

Trotter steps. Each element is further decomposed in the product of simpler unitary operators generated by the single terms in the sums in Eqs. (4.6) and (4.8). The addition of incoherent spin flips to the noise is explored in Section 4.6, where we employ a feedback correction mechanism. Since here we are mainly interested in the dynamics due to the use of mid-circuit measurement, we focus on the situation where the only error sources are coherent, with a single parameter $\lambda_1 = \lambda_2 = \lambda$ setting their strength.

To detect and protect against gauge violations arising during the time evolution, we implement the DPS protocol we introduced in Section 4.1.

The DPS circuit is exemplified in the green box of Fig. 4.2(a), where we show the version of the circuit in Fig. 4.1(d) applied to the $\mathbb{Z}_2$ model acting on two neighboring local charges Θ_n and Θ_{n+1}. In the red box, we show the active correction layer tested in Sec. 4.6. In $\mathbb{Z}_2$ LGTs, the change of basis in Eq. (4.4) is not necessary, since the Gauss laws in Eq. (4.7) are already diagonal in the chosen computational basis, while the controlled-operators $C - \mathcal{O}$ in Fig. 4.1(d) consist in the common controlled-Not gates. If all Θ_n are measured at each Trotter step, N auxiliary qubits are needed.

To benchmark the DPS, we test it on a quantum quench corresponding to studying the spreading of an initially localized meson (consisting of a mobile charge and a fixed background charge) [81]. In this scenario, the system is initially prepared with the electric field all polarized in the x direction, and a single mass excitation is set at the center of the chain. This state is then evolved with a standard first-order Trotter discretization of the evolution operator generated by $H = H_{\mathbb{Z}_2} + H_{\text{err}}$ with $\lambda = 0.2J$, $f = 0.5J$, and $M = 0$. We consider a system with $L = 17$ qubits, corresponding to $N = 9$ local charges. This choice corresponds to the deconfined phase of the $\mathbb{Z}_2$ LGT, where we expect the mass defect to spread ballistically in the chain and bounce off the edges, as the chain has open boundary conditions. Indeed, this behavior is clearly visible in Fig. 4.2(b), where we show the local qubit excitation ($\frac{1-\sigma^z}{2}$ for site and $\frac{1-\tau^z}{2}$ for link variables) in such protocol with $\lambda = 0$.

When the coherent error is added, see Fig. 4.2(c), the correlation between matter and gauge variables is visibly smeared out. However, it is recovered completely with a successful application of the DPS protocol, shown in panel (d). On the contrary, in panel (e), we show an application of the DPS that did not succeed, meaning that it did not measure the initial gauge charges at every Trotter step. This generates a non-protected realization, where the measurements project the state onto a random gauge sector, and the dynamics displays a very irregular behavior. In the following, we show how the frequency of the measurements differentiates between two regimes: one where the protection shown in panel (d) is more likely, and the other, dominated by irregular behavior without physical meaning.

4.3.1 Effective Lindblad master equation and quantum Zeno transition

To understand the origin of these two regimes and determine the measurement frequency threshold for gauge protection, it is instructive to look at the continuous-

time limit of the DPS protocol in the ensemble average over many trajectories, and to frame it within the spectral theory of Liouvillians [338]. An important aspect to consider is that the measurements in the DPS protocol are strongly correlated, as they are all performed at the end of a Trotter step. In a continuous-time framework, we require instead independent measurements that do not occur simultaneously. Then, it is possible to describe the effect of the measurements of local charges Θ_n in terms of jump operators in a Lindblad master equation,

$$\dot{\rho} = i[\rho, H] + \frac{1}{2\mathrm{d}\tau} \sum_n \left[\Theta_n \rho \Theta_n^\dagger - \frac{1}{2}\{\Theta_n^\dagger \Theta_n, \rho\} \right] , \tag{4.10}$$

which describes the evolution of the density matrix associated with the ensemble average of the stochastic trajectories originated by the measurement process. For a technical construction of Eq. (4.10), see Appendix C. The time step $\mathrm{d}\tau$ in Eq. (4.10) is the measurement frequency, or the average time between two consecutive measurements of the same local charge. When taking the continuous-time limit, $\Delta t \to 0$, the effective measurement rate $\gamma \equiv \frac{1}{2\mathrm{d}t}$ is kept constant. That is, in this limit, each generator is measured only once during many Trotter steps.

From Eq. (4.10), we can draw a direct connection with previous proposals for gauge protection in analog quantum simulations [294], which used random gauge rotations with vanishing autocorrelation time (white noise dephasing) to implement a master equation of the form of Eq. (4.10),

$$\dot{\rho} = i[\rho, H] + \frac{1}{\gamma} \sum_n \left[\Theta_n \rho \Theta_n^\dagger - \frac{1}{2}\{\Theta_n^\dagger \Theta_n, \rho\} \right] . \tag{4.11}$$

Both error mitigation mechanisms rely on the suppression of coherences between different gauge sectors due to the actions of the Lindblad operators Θ_n in the large γ limit. In the context of measurement-induced dynamics, however, we can interpret Eq. (4.10) as the ensemble average over stochastic quantum trajectories arising from the continuous measurements of the local charges Θ_n. Within this protocol, until a quantum jump occurs, each trajectory evolves as $|\psi(t)\rangle = \exp(-iH_{\mathrm{eff}}t)/\mathcal{N}(t)$, where we defined the effective non-Hermitian Hamiltonian

$$H_{\mathrm{eff}} = H - \frac{i\gamma}{2} \sum_n \Theta_n^\dagger \Theta_n , \tag{4.12}$$

and $\mathcal{N}(t)$ ensures normalization of the quantum state. Stochastic quantum jumps occur with uniform probability in time $\mathrm{d}p = \gamma \Delta t$ and modify the state according to

$$|\psi(t + \Delta t)\rangle = \Theta_n |\psi(t)\rangle \, / \sqrt{\langle \psi(t)| \, \Theta_n^\dagger \Theta_n \, |\psi(t)\rangle} \ . \tag{4.13}$$

The total probability of a quantum jump event is thus $N\gamma dt$, where N is the number of local charges (for the present theory equal to the number of matter sites). The denominator ensures the normalization of the wavefunction; for $\mathbb{Z}_2$ LGT, it is

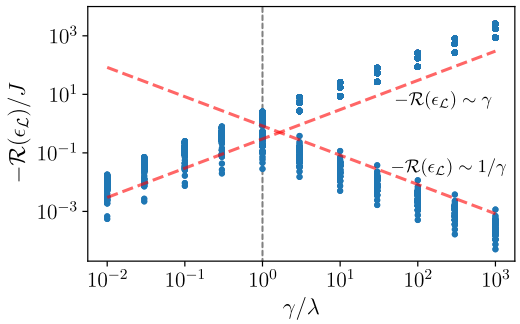

Figure 4.3: Absolute value of the real part of the Liouvillian spectrum for $N = 3$ versus the measurement rate of the local charges, γ, and error strength, $\lambda = 0.3J$. The remaining Hamiltonian parameters are $M = 0$ and $f = 0.5J$. The vertical dashed line is a guide to the eye marking the quantum Zeno transition. After it, two distinct groups of eigenvalues emerge, with opposite $\mathcal{R}(\epsilon_\mathcal{L}) \sim \gamma^{\pm 1}$ highlighted by the dashed red lines. The lower group of eigenvalues (with $\epsilon_\mathcal{L} \sim 1/\gamma$) marks "dark" states that are stabilized by the measurement.

redundant, Θ_n being unitary, but we write it explicitly to keep the notation more general. In this context, $1/\gamma$ is the average time between consecutive jumps. Notice, however, that it is twice as large as the average "waiting" time for the continuous limit of the DPS protocol, where $\mathrm{d}\tau = \frac{1}{2\gamma}$, a hint that the two approaches lead to different unraveling of the same Lindblad equation. Indeed, the measurement procedures are also different: in the DPS protocol, we stroboscopically project the state on the target gauge sector, while in the analog quantum simulation, we monitor the local charges with continuous weak measurements. More details about the quantum trajectory approach are presented in App. C.

Symmetry-protection phase transition From the above and also previous discussions [294], it may appear that the error-mitigation regime emerges continuously for any value of the measurement rate with a protection strength proportional to γ. Instead, we now show that the error-mitigation regime rather appears after a sharp quantum Zeno transition that signals the onset of the protected phase.

This transition is not manifested at the level of the stationary state of the associated Liouvillian operator $\mathcal{L}$, as it is always a trivial infinite-temperature mixed state. Instead, it is revealed in the behavior of the real part of the nonstationary eigenvalues; these are all negative values whose amplitudes determine the decay rates for different eigenstates of $\mathcal{L}$. We plot the real part of the Liouvillian eigenvalues $\epsilon_\mathcal{L}$ in Fig. 4.3; the presence of a quantum Zeno point is signaled by their branching into two groups at $\gamma/\lambda = 1$, marked by the vertical dashed line. In the protected phase, $\gamma > \lambda$, a set of levels decay to zero as $1/\gamma$, consistently with the protection rate observed in Ref. [294]. In the $\gamma \to \infty$ limit, the stochastic dynamics stabilizes these

states that become "dark" with respect to the jump operators. They correspond to all combinations [1] of eigenstates of $\{\Theta_n\}$: indeed, each gauge sector is equally protected by the Liouvillian dynamics, which is insensitive to the initial state. Hence, the dimension of the protected manifold is the same as the full Hilbert space. The jump operators destroy the coherence between states belonging to different sectors, thus preserving the initial configuration of local charges.

Armed with this knowledge, we can look again at the data presented in Fig. 4.2(d-e) to better understand the effect of the local measurements. In both cases, the Trotter step is $\Delta t = 0.5J^{-1}$, but it corresponds to different gauge protection strength depending on the error amplitude λ. In panel (d), $\gamma/\lambda = 1/(2\Delta t\lambda) = 5$, signaling that the protocol is in the protected regime of Fig. 4.3. Indeed, the coherent error is almost perfectly suppressed after each time step, allowing for the reconstruction of the exact dynamics. In panel (e), in contrast, $\gamma/\lambda = 1$, just below the transition to the Zeno phase. Consequently, the dynamics are highly irregular, with no resemblance to the ideal gauge-symmetric behavior.

Further analysis in the presence of noisy measurements, which for now have been supposed to be fault-tolerant, and also for $\mathbb{Z}_3$ and truncated $U(1)$ LGTs are provided in Section 4.4.

4.3.2 Different unravelings for digital and analog gauge protection

A natural question at this point is how the two stochastic processes compare with each other: on the one hand, we have the DPS protocol for discrete-time evolution, and, on the other hand, continuous measurements (or dephasing) of the local charges in an analog quantum-simulation setup. They are rooted in the same Liouvillian dynamics, meaning that the ensemble average is fully equivalent. As we show now, their unravelings in quantum trajectories show profound differences.

These are summarized in Fig. 4.4, where we investigate the same quench dynamics presented before, comparing trajectories for the two gauge protection mechanisms. Figure 4.4(a-b) shows the time evolution of the electric field excitation $1 - \tau^z_{n,n+1}$ averaged over all link degrees of freedom in 100 independent trajectories (faint dashed lines) obtained with the DPS protocol (panel a) and with continuous measurements (panel b). In both plots, we also report the exact evolution (solid blue line) of the average electric field as well as the dynamics in the presence of coherent errors with strength $\lambda = 0.2J$ but no protection (solid orange line).

In Fig. 4.4(a), the stochastic DPS trajectories are clearly split into two groups. During the time evolution, a measurement of one of Gauss' laws may yield the wrong result $\alpha_n \neq \alpha_{n,\text{targ}}$, incurring a gauge violation, and the state is projected into the subspace orthogonal to the target sector. These trajectories are plotted as faint dashed red lines, starting from the time step at which the measurement fails. After the state is projected in the nonphysical sector, each trajectory behaves differently,

[1] Eigenstates of $\mathcal{L}$ must be traceless but for the stationary state that is the only proper density matrix.

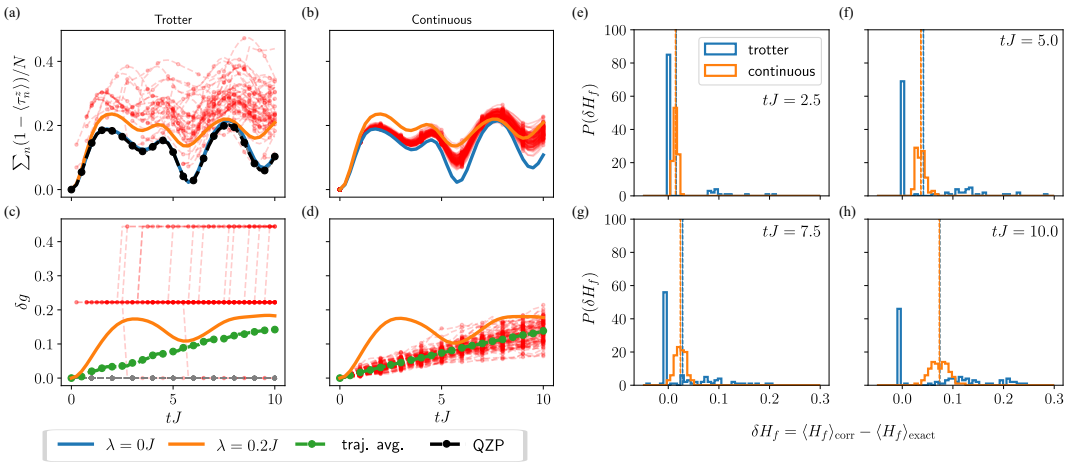

Figure 4.4: (a) Evolution of the average electric field in the deconfined phase, comparing the exact Trotterized dynamics (blue), the coherent error (orange), and 100 trajectories with gauge measurements after each step (dashed lines). Each trajectory is depicted in gray as long as it does not break gauge invariance, and in red from the first time a violation is measured. The grey lines are all perfectly superimposed, and their average (dashed black lines and circles) matches almost perfectly the exact evolution, as a consequence of quantum Zeno protection (QZP). The Trotter step is $\Delta t = 0.25J^{-1}$ (c) Evolution of the gauge violation, same protocols as in panel (a). 47 out of 100 trajectories never incur a gauge violation. (b) and (d) plot the same observables as (a) and (c), respectively, obtained with a standard quantum trajectory unraveling of Eq. (4.10), with a rate $\gamma = \frac{1}{2\mathrm{d}\tau} = 2J$. By comparing panels (c) and (d), it is evident that the trajectory statistics are very different, despite their ensemble average being the same (green circles with dashed line). (e-h) Probability distribution of the error with respect to the exact dynamics in the expectation value of the electric field H_f. We compare the DPS protocol (blue) and the continuous weak measurements (orange). The normalized histograms are extracted from 500 independent trajectories for both protocols. The vertical dashed lines mark the average of the probability distributions. The averages of the two distributions are the same, despite their statistics differing significantly. The physical parameters of the Hamiltonian are $f = 0.5J$, $M = 0$, and $\lambda = 0.2J$. The spin chain has $N = 9$ matter sites (L=17 qubits).

and their average tends to an infinite temperature state. In several instances, however, the state is projected back into the target gauge sector throughout the entire time evolution (faint dashed grey lines). These trajectories perfectly collapse on each other and are, therefore, identical to their average (dashed black line with full circles), which follows the exact dynamics extremely closely.

The trajectory behavior in the continuous time evolution protocol is markedly different, as shown in Fig. 4.4(b). Individual trajectories now are much more concentrated around their ensemble average, which drifts away from the ideal evolution on a timescale $\propto \gamma$ (see App. C.1 for details), consistently also with the behavior of the Liouvillian eigenvalues in the protected phase.

The difference between the two stochastic processes emerges even more clearly when looking at the average gauge violation, defined in Eq. (4.9), along individual trajectories, which we show in Fig. 4.4(c) and (d). For the discrete-time evolution, gauge violation is quantized, as a failed local charge measurement leads to a jump in δg corresponding to a flip of two neighboring generators Θ_n, Θ_{n+1}. When the gauge symmetry is protected, $\delta g = 0$ does not increase (superimposed gray lines). In contrast, in the continuous dynamics, each trajectory displays a similar slow increase of the average gauge violation, without any sharp jumps. Despite their different distributions, however, once we average over the entire ensemble of stochastic dynamics, the mean gauge drift (green lines and circles) is the same. Indeed, the trajectory averages in panels (c) and (d) are very similar [2]. Clearly, in DPS, the average only over trajectories where the error has been successfully suppressed remains totally flat, as no gauge violation occurs. An analog consideration in the continuous-time dynamics is not possible. This difference represents a major advantage of the digital implementation over the analog one, where the discrimination between successful or unsuccessful trajectories is not possible by construction.

To further analyze the contrasting unravelings of the two protocols, we compare the error of the expectation value of the electric field $\langle H_f \rangle$ over 500 trajectories. The result is shown in Fig. 4.4(e-h) for four time snapshots. As already observed, the trajectories for the trotterized dynamics (blue) clearly split into two groups with different behaviors, leading to a bimodal distribution. A single prominent peak corresponds to the simulations in which no gauge violation has occurred yet at time t, while a more irregular and broader part of the distribution describes all those states that have been projected on a space orthogonal to the target sector. As time increases, weight is transferred from the sharp peak to the broad distribution, as more trajectories incur at least one error during the measurement stage. In continuous-time dynamics (orange), instead, the probability distribution remains centered around its average, while its width slowly increases. The means of the two distributions are marked in each panel by a vertical dashed line of color matching that of the corresponding histogram. The two lines are almost superimposed, in-

[2] In the ensemble average, we first compute the gauge violation $\delta g = \sum_n |\langle \Theta_n \rangle - \alpha_n|$ for an individual trajectory and then we average over many stochastic evolutions. Hence, the fact that the two protocols give the same average is not evident a priori.

dicating that the ensemble average of the very different trajectory distributions is, indeed, the same.

4.3.3 DPS survival probability

The clear distinction in DPS between trajectories that have incurred gauge violation and those that have not permits us to postselect on states that reside within the physical subspace. This approach is indeed successfully pursued in current gauge-theory quantum-simulation experiments, albeit only for measurements on the final state [81, 83, 85]. Despite the similarities, the two approaches are not equivalent. In the standard post-selection, as the evolution time increases, we expect the number of trajectories satisfying the gauge symmetry to decrease exponentially in t, thus requiring a larger number of shots to obtain sufficient statistics within the physical subspace. Moreover, a final measurement of the local charges can not identify gauge violations that occurred at earlier times and then compensated for by further errors later on. In DPS, we still expect an exponential decrease in the number of successful runs, but with two important differences with respect to standard post-selection. First, within a successful run, the state can only drift out of the target sector between one measurement and the next one. If those are sufficiently close, we expect the probability of a second-order process that introduces an error through a virtual occupation of a nonphysical sector to be suppressed. Second, the decay rate of the successful trajectories will be dependent on the measurement frequency; in the strongly protected phase, where the quantum Zeno effect takes place, the population of the sector stabilized by the measurements decreases *linearly* in time. For a better quantitative understanding, it thus becomes an important aspect to study the survival probability $P_s(t) = \left\langle \hat{P}_{\text{phys}}(t) \right\rangle$, where $\hat{P}_{\text{phys}} = \bigotimes_n P_n^+$ is the projector onto the physical subspace. Physically, P_s measures the number of trajectories that never incur a gauge violation as a function of time.

As a rough estimate, the error probability for any measurement is of the order $p_{\text{err}} \sim (\lambda \Delta t)^2$, as this is the rate at which other gauge sectors are populated in each Trotter step. Thus, the probability of surviving n_t time steps for a system with N local charges is approximately

$$P_s(t) = (1 - p_{\text{err}})^{N n_t} \simeq \mathrm{e}^{-(\lambda^2 \Delta t) N t}, \tag{4.14}$$

where $t = n_t \Delta t$ is the evolution time. It decreases faster for larger systems and longer evolution times, besides larger error strength, while it benefits from smaller Trotter steps. If Δt is small enough, meaning that the frequency of measurements is faster than the growth rate of the error λ^2, the dynamics reach a quantum Zeno regime where the exponential drift out of the target sector is well approximated by a linear dependence on time $P_s(t) \simeq 1 - (\lambda^2 \Delta t) N t$. The decay rate is also connected to the Zeno timescale, corresponding to the simulation time up to which this linear approximation holds, and we can extract reliable physical information from gauge-invariant trajectories. This Zeno timescale is approximately $t_{\text{Z}} \sim (\lambda^2 \Delta t N)^{-1}$, meaning it increases linearly with the measurement frequency $\gamma = \frac{1}{2\Delta t}$.

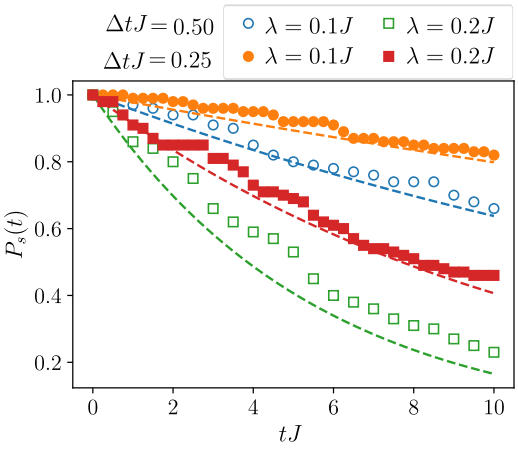

Figure 4.5: Number of trajectories that have not violated gauge invariance as a function of evolution time for different error strengths. Filled markers correspond to simulations with 40 Trotter steps ($\Delta tJ = 0.25$) while empty markers have $n_t = 20$ ($\Delta tJ = 0.5$). The theoretical estimate, Eq. (4.14), for each dataset, is plotted with a dashed line with the same color as the numerical data. For small values of error strength and Trotter step size, the agreement is satisfactory, and the data reproduces an approximate linear dependence at short simulated times.

We plot this figure of merit in Fig. 4.5, for two error strengths ($\lambda = 0.1J$, $0.2J$; circles and squares, respectively) and two different Trotter steps ($n_t = 20$, 40; empty and filled markers, respectively). The success probability is extracted from 100 trajectories for each set of parameters. We find a good agreement between the numerical data and Eq. (4.14) (dashed lines), in particular for small decay rates $\lambda^2 \Delta t$.

In general, an exponential overhead is common to many error-mitigation techniques [143, 339], and DPS makes no exception. Although this eventually limits their applicability on large systems, direct post-selection methods, for instance, have already been successfully applied to study nontrivial dynamics in LGT experiments [81, 82, 85]. Moreover, the accurate estimate of local observables only requires the system to satisfy the gauge symmetries within their light cone, allowing for extracting meaningful physical information also from trajectories that incur a small number of gauge violations. Since changing the monitoring frequency allows for tuning the decay rate in Eq. (4.14), DPS can prove advantageous both in terms of sampling overhead and protection efficiency with respect to direct-post-selection, making it relevant for system sizes comparable with state-of-the-art NISQ devices (~ 100 qubits), provided the mid-circuit measurements are sufficiently accurate. In the next section, we investigate what happens if this is not the case.

4.4 Noisy measurements

Until now, we have assumed that the gates used to encode the local charge on the auxiliary qubits act with arbitrary precision, without introducing further errors or noise. Despite highlighting the quantum Zeno transition more transparently, this is a significant simplification since two-qubit gates are the main noise sources in realistic hardware. Here, we relax this assumption and model imperfect measurements through the action of random Pauli noise any time we couple a physical qubit with the ancilla. Specifically, if we measure $\Theta_n = -\tau^z_{n-1,n}\sigma^z_n\tau^z_{n,n+1}$, we also apply small random rotations around the $\mathbf{x}$ and $\mathbf{z}$ axes on the three involved system qubits, given by

$$U_{R,n}(\boldsymbol{\xi},\boldsymbol{\eta}) = \bigotimes_{k\in\mathrm{supp}(\Theta_n)} \mathrm{e}^{-i\xi_k Z_k}\mathrm{e}^{-i\eta_k X_k} \ . \tag{4.15}$$

k labels the qubits in the support of Θ_n and $Z = \sigma^z$ (τ^z) when k denotes a charge (gauge) degree of freedom, and analogously for X. The angles $(\boldsymbol{\xi},\boldsymbol{\eta})$ of the rotations are drawn from a normal distribution with zero mean and a standard deviation σ that sets the noise level. U_R maintains unitarity of the time evolution on a single trajectory but generates both dephasing and dissipation when we take the ensemble average. We characterize its fidelity through the Hilbert–Schmidt inner product with the identity operator, averaged over noise realizations

$$\mathcal{F} = \overline{(\mathbb{1}, U_R(\boldsymbol{\xi},\boldsymbol{\eta}))_{\mathrm{HS}}} \simeq 1 - 3\sigma^2 \ . \tag{4.16}$$

The effective error rate induced by noisy measurements is the infidelity $1-\mathcal{F}$.

A first nontrivial question regards the fate of the Zeno transition marked by the branching of the Liouvillian eigenvalues. With finite measurement fidelity, the effective Lindblad equation approximately becomes

$$\begin{aligned}\dot\rho = \quad & i[\rho,H] + \gamma\textstyle\sum_n\left[\Theta_n\rho\Theta_n^\dagger - \frac{1}{2}\{\Theta_n^\dagger\Theta_n,\rho\}\right] \\ & +(1-\mathcal{F})\gamma\textstyle\sum_{k=1}^{2N-1}\left[L_k\rho L_k^\dagger - \frac{1}{2}\{L_k^\dagger L_k,\rho\}\right] \ ,\end{aligned} \tag{4.17}$$

where $L_k = X_k, Z_k$ and k runs over all $2N-1$ degrees of freedom. Hence, increasing the measurement frequency also increases the effective error rate. If the eigenvalue branching remains, we expect the presence of an optimal region in the measurement frequency where the Zeno regime still exists. Figure 4.6, which reports the magnitude of the γ dependence of the real part of the Liouvillian eigenvalues for $\lambda = 0.2J$ and $\mathcal{F} = 0.99$, confirms this picture. The branching that signals the onset of the protected phase at $\gamma/\lambda = 1$ is, indeed, still present, but the measurement noise prevents the stabilization of the Zeno effect at large frequencies because of a bundle of eigenvalues growing as $-\mathcal{R}(\epsilon_\mathcal{L}) \propto \gamma$ that "bends" upward the Zeno-protected states. However, a finite range of measurement frequencies remains where the gauge protection from DPS is expected.

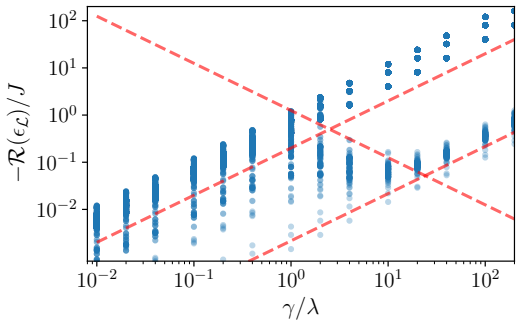

Figure 4.6: Magnitude of the real part of Liouvillian eigenvalues as a function of the ratio γ/λ between the measurement frequency and the coherent error strength, for a measurement fidelity of $\mathcal{F} = 0.99$. There remains an intermediate Zeno-protected phase. It is limited from below ($\gamma/\lambda \sim 1$) as before by the build-up of simulation errors when measurements are rare, and from above ($\gamma/\lambda \sim 10$) by large errors accumulating through the measurements themselves once they become too frequent. Marker opacity reflects the density of states, and the dashed lines are guides to the eyes to highlight the three competing behaviors.

To confirm this prediction, we simulate the dynamics of a chain of $N = 7$ charge sites (13 qubits) with the same quantum quench protocol as described in Sec. 4.3 and varying measurement frequency. In practice, we fix the total evolution time $t_f J = 20$ and the Trotter step $\Delta t J = 0.25$, but we dilute the measurements. We denote with Δt_m the time interval between consecutive measurement layers, such that the monitoring frequency becomes $\gamma = \frac{1}{2\Delta t_m}$. We take Δt_m as an integer multiple of the Trotter step Δt.

Figures 4.7 (a) and (b) report the relative error of the electric field Hamiltonian at two time slices $tJ = 10$ (a) and $tJ = 20$ (b), averaged over successful DPS trajectories out of 800 independent runs. We compare ideal measurements ($\mathcal{F} = 1$, circles) with noisy ones ($\mathcal{F} = 0.99$, squares) and a direct post-selection performed only at the end of the run (horizontal dashed line). The latter corresponds to a measurement period of $\Delta t_m = tJ$. When the measurements are perfect, increasing their frequency first leads to worse performances with respect to direct post-selection. After the Zeno transition ($2\Delta t_m \lambda \simeq 1$), the error starts decreasing and, eventually, DPS performs better than direct post-selection. Noisy measurements do not significantly alter this picture. The fluctuations, however, markedly increase for larger measurement frequencies as the accumulated errors tend to diffuse the trajectories around their average while, at the same time, reducing the number of successful ones. Hence, even if sometimes the noisy measurements lead to better results than ideal DPS in the mean values, the large standard deviations do not make this behavior relevant. At small Δt_m, noise overshadows the Zeno effect and the error starts growing again.

The survival probability also reflects the presence of the Zeno transition and its

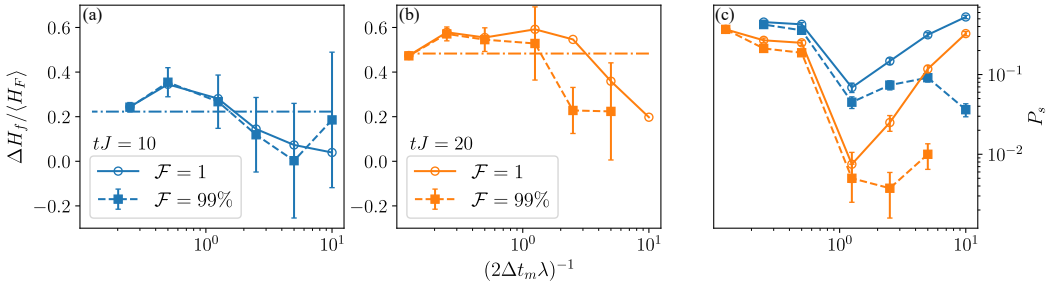

Figure 4.7: Relative error of the electric Hamiltonian at times $tJ = 10$ (a) and $tJ = 20$ (b) for DPS applied with varying measurement intervals Δt_m and both ideal ($\mathcal{F} = 1$, empy circles) and imperfect ($\mathcal{F} = 0.99$, filled squares) measurements. We compare the data with a post-selection procedure only at the end of the simulation with no intermediate monitoring (horizontal dashed line). At sufficiently large measurement frequencies, DPS improves on top of direct post-selection even with noisy measurement circuits. (c) Survival probability as a function of the measurement frequency. A dip appears in correspondence with the Zeno transition, with a worse recovery for finite infidelity $1 - \mathcal{F}$. Data for $tJ = 20$ and the shortest (noisy) measurement period $\Delta t_m = \Delta t$ is missing because no physical DPS trajectory was found. Simulation parameters: $N = 7$, $\Delta tJ = 0.25$, $f = 0.5J$, $\lambda = 0.2J$.

persistence at a finite error rate in the measurements, as is visible from Fig. 4.7(c). It shows the survival fraction corresponding to the data in panels (a) and (b) as a function of the measurement frequency. At the Zeno critical point, P_s has a clear dip followed by a sharp increase that surpasses the ratio of trajectories retained by direct post-selection (leftmost points). The noisy measurements affect P_s in the Zeno regime, reducing the number of trajectories that can be used for reconstructing the target dynamics. In particular, the survival probability in Eq. (4.14) is modified with an effective error rate that grows with $(1 - \mathcal{F})$

$$P_s(t) \simeq \mathrm{e}^{-[\lambda^2 \Delta t_m + (1-\mathcal{F})/\Delta t_m] N t}. \tag{4.18}$$

Importantly, now it is no longer possible to arbitrarily reduce the exponential decay rate of P_s by making more frequent measurements, but one has to balance the benefit of the Zeno-like stabilization with the additional noise.

To summarize, imperfect measurements have two main effects: first, they induce an effective relaxation within the target gauge sector, reducing the quality of the reconstructed dynamics. Second, the fraction of successful DPS trajectories decreases due to the higher error rate. Thus, while it is no longer possible to arbitrarily improve the gauge protection by increasing the measurement density, an optimal frequency range exists close to the quantum Zeno transition where mid-circuit measurements still provide the desired mitigation against coherent errors. In this regime, our protocol leads to a better approximation of the target dynamics than standard

post-selection, as it suppresses multiple gauge violations that combine in a gauge-invariant error. The existence of the optimal region in the measurement frequency depicted in 4.7 does not depend on the gauge group, as shown in the next section.

4.5 Effective Liouvillian spectrum in $\mathbb{Z}_3$ and $U(1)$ gauge groups

In this section, we extend the investigation of the Liouvillian spectrum associated with the continuous-time limit of the DPS protection protocol to LGTs in one spatial dimension with $\mathbb{Z}_3$ and $U(1)$ symmetries. For both, the structure of the Hamiltonian is the same as Eq. (4.6), but the operators acting on the gauge degrees of freedom and the local charges need to be changed to take into account the larger groups.

$\mathbb{Z}_3$ group

A LGT with a discrete $\mathbb{Z}_N$ gauge group is a generalization of the simpler model analyzed in the main text. We consider generalized Pauli matrices (clock operators) satisfying the algebra

$$Q^N = P^N = \mathbb{1} \ , \tag{4.19a}$$

$$QP = PQe^{i\frac{2\pi}{N}} \ , \tag{4.19b}$$

$$Q|m\rangle = e^{i\frac{2\pi}{N}m}|m\rangle \ . \tag{4.19c}$$

Here, we focus on $N = 3$. After a Jordan–Wigner transformation on the fermions (matter sites), the Hamiltonian (4.6) then becomes

$$H_{\mathbb{Z}_3} = J\sum_n \left(\sigma_n^+ P_{n,n+1}\sigma_{n+1}^- + \text{h.c}\right) + \frac{f}{2}\sum_n (Q_{n,n+1} + Q_{n,n+1}^\dagger) + \frac{M}{2}\sum_n (-1)^n \sigma_n^z \ .$$

The gauge transformations are [149]

$$\Theta_n = Q_{n-1,n}Q_{n,n+1}^\dagger e^{-i\frac{\pi}{3}(1+\sigma_n^z)} \tag{4.20}$$

and their eigenvalues are the cubic roots of unity $\alpha_n = e^{i\frac{2\pi}{3}m}$, with $m = 0, 1, 2$.

Truncated $U(1)$

$U(1)$ is the gauge group of quantum electrodynamics [16], making it one of the most popular targets for quantum simulations of LGT. Since $U(1)$ is a continuous group, we need to truncate it to map it to the discrete degrees of freedom of quantum hardware. Here, we adopt the quantum-link-model formulation for the gauge fields [16, 98]. In practice, we consider the operators S^z and U acting on the links, such that

$$S^z|m\rangle = m|m\rangle \ \text{ with } m = -S, -S+1, \ldots, S \ , \tag{4.21}$$

and

$$U\,|m\rangle = |m+1\rangle \;\text{ if } m < S\;. \tag{4.22}$$

Using Kogut–Susskind staggered fermions, followed by a Jordan–Wigner transformation to hard-core bosons, the Hamiltonian of the theory is

$$H_{U(1)} = J\sum_n \left(\sigma_n^+ U_{n,n+1}\sigma_{n+1}^- + \text{h.c}\right) + f\sum_n \left(S_{n,n+1}^z\right)^2 + \frac{M}{2}\sum_n (-1)^n \sigma_n^z\;,$$

while the local Gauss' law generators read

$$\Theta_n = S_{n,n+1}^z - S_{n-1,n}^z - \frac{1}{2}((-1)^n + \sigma_n^z)\;. \tag{4.23}$$

The physical subspace is the one with $\Theta_n = 0$ and the $(-1)^n$ factor takes into account the different values of the charge on even and odd sites. We truncate the gauge fields to $S = 1$, meaning that the electric field can take three different values on each link. The Hilbert space is, therefore, the same as the $\mathbb{Z}_3$ LGT, but the local symmetries and the constraints they impose are different.

Liouvillian spectrum

Following the gauge-symmetry-violating Hamiltonian used in the main text, here we consider two sources for coherent errors, rotations of the gauge fields and unassisted hopping between matter sites. The latter is independent of the gauge group and is identical to the one in the error Hamiltonian in Eq. (4.8). On-site electric field rotations take the form $(P_{n,n+1} + P_{n,n+1}^\dagger)$ for $\mathbb{Z}_3$ and $(U_{n,n+1} + U_{n,n+1}^\dagger)$ for $U(1)$.

To investigate the presence of a quantum Zeno transition, we consider an effective Lindbladian where the unitary evolution is given by the model Hamiltonian and the coherent error terms with a strength λ, while the collapse operators correspond to the local charges in Eqs. (4.20) and (4.23). Measuring the generators of gauge transformations for larger groups is technically more complicated than the simple stabilizer of the $\mathbb{Z}_2$ group. A circuit implementation can be found, for instance, in Ref. [299]. We also consider the situation in which the measurements of the local charges have finite fidelity, by adding further on-site dissipative noise with a rate $\gamma(1-\mathcal{F})$, where γ is the measurement frequency and $\mathcal{F}$ their average fidelity. Figure 4.8 summarizes our results: the appearance of the quantum Zeno phase in the Liouvillian spectrum, see panels (a-d), is qualitatively similar to what we observed in Sec. 4.3 for both $\mathbb{Z}_3$ and $U(1)$ groups, even though the critical measurement frequency slightly changes. The Zeno phase survives also with finite measurement fidelity (here $\mathcal{F} = 0.99$) on a finite range of γ, as observed for the $\mathbb{Z}_2$ LGT model. When looking at a specific example of gauge-invariant dynamics one wishes to recover, the effect of the measurements is again similar to what we observed for the $\mathbb{Z}_2$ model. We report an instance for the $\mathbb{Z}_3$ group in panels (e-g) of Fig. 4.8, where a dramatic improvement in the Zeno phase becomes clear with respect to the bare evolution subject to coherent errors.

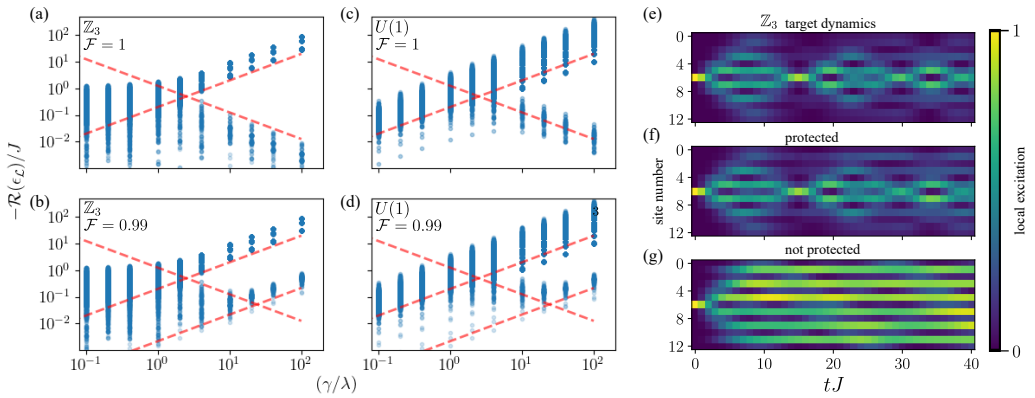

Figure 4.8: (a-d): Liouvillian spectrum as a function of the measurement frequency in the presence of unitary errors for the $\mathbb{Z}_3$ (a-b) and $U(1)$ (c-d) gauge groups. The branching in the spectrum signals the onset of the quantum Zeno phase that protects gauge invariance and survives also for finite measurement fidelity, see panels (b) and (d). The opacity of the markers reflects the density of states. (e-g): example of dynamics in the deconfined phase of a 1+1d $\mathbb{Z}_3$ LGT model. The Zeno protection with $\gamma = 20\lambda$ (f) recovers the target dynamics (e), while it is almost completely lost (g) without it. Simulation parameters: $f = 0.5J$, $M = 0.1J$, $\lambda = 0.2J$. In panels (a-d) the chain consists of $N = 3$ matter sites, while in panels (e-f) $N = 7$.

4.6 Error correction

As we have seen in Sec. 4.3, reading out the violations of gauge symmetry at each time step suppresses errors due to a quantum Zeno effect. In addition, it also opens up the possibility to actively correct the measured errors. This active correction scheme is represented by the full circuit sketched in Fig. 4.2(a). Its implementation requires on-chip feedback during the quantum algorithm. Such a feature is currently actively researched due to its importance for general error correction and is expected to become available in the next generation of quantum chips [340–342]. We will see below that one can exploit it for significantly improving the quality of gauge theory quantum-simulation data, without the requirement for full error correction capabilities.

First, we test the correction capabilities on a bit-flip (Pauli-X) channel, where we only consider the incoherent errors that the local charge measurements can correct without resorting to more sophisticated QEC protocols [300, 302]. For simplicity, here we resort again to ideal measurements. Alternatively, one could consider a larger error rate incorporating the effect of the two-qubit gates used in the coupling with the ancillas. We model the bit-flip error by assuming that, during each Trotter step, an incoherent spin flip can occur on any qubit with probability p_{err}. These errors can be detected by local charge measurements by comparing them with the known target sector [299, 327], using the same circuit as sketched in Fig. 4.2(a).

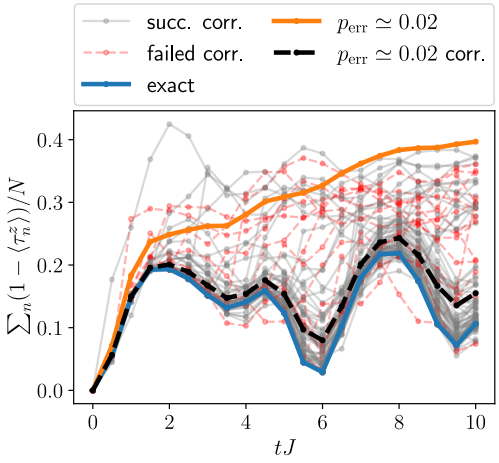

Figure 4.9: Example of error correction effectiveness with a pure bit-flip error channel. The orange solid line reports the uncorrected expectation value averaged over 100 noisy runs. The dashed black line is the average over the successfully corrected trajectories (faint grey lines), while we discard the trajectories where the error correction can not be applied unambiguously (faint dashed red lines). The corrected result gets very close to the exact data (blue solid line).

Then, we apply the reverse bit-flip operation and correct the error depending on which gauge symmetries have been violated. This procedure works unambiguously only when the error probability is sufficiently small such that the probability of two errors occurring in the same Trotter step is negligible. Indeed, when two bit-flips affect neighboring local charges, a simple measurement can not determine which qubits were affected by the dissipation errors. In our numerics, when errors with ambiguous detection happen, we discard the run and do not use it to compute the expectation values of observables of interest.

We report an example of the correction scheme in Fig. 4.9, where we compare the exact dynamics (solid blue line), the average over 100 noisy trajectories (solid orange line), and the average over successfully corrected trajectories (dashed black lines). The gauge symmetry protection is not as effective as the dynamical post-selection in the presence of coherent error sources (see Fig. 4.4(a) for comparison). However, it is able to recover the exact dynamics qualitatively. This feature is noteworthy, considering the different types of noise (here: incoherent dissipation) and the completely deviating behavior of the average of the noisy trajectories.

When looking at individual quantum trajectories, however, it is apparently no longer possible to qualitatively distinguish those that have been unambiguously corrected (grey) and those that have not (dashed red). Indeed, while there is a bundle of corrected trajectories that closely follow the exact dynamics, there are some in which the correction is apparently applied with success, but they result in an irregular behavior similar to those where the correction can not be performed. These originate

when two neighboring gauge symmetries are violated by two independent spin flips on the matter sites instead of a flip of the gauge field, which is more probable and therefore implicitly assumed in the correction scheme. This situation occurs with a smaller probability than single bit-flips, hence the average is dominated by the group of trajectories where the correction is successful. As time increases, more trajectories will incur such non-detectable double spin-flips, reducing the effectiveness of this error correction scheme for long evolution times.

Hence, it is clear that estimating the probability of non-detectable errors is of great importance in verifying the effectiveness of the correction scheme. For instance, let us consider Θ_n and Θ_{n+1}, which involve 5 qubits; if errors affect two of them, the correction protocol fails. Given the error probability $p_{\rm err} \ll 1$ on a single qubit, the probability of having two errors in the same Trotter step affecting spins belonging either to Θ_n or Θ_{n+1} approximately reads

$$p_2 = p_{\rm err}^2 (1-p_{\rm err})^{L-2} 6(N-1) \ , \tag{4.24}$$

where L is the total number of qubits (matter and gauge sites), while N is the number of matter sites. The factor $6(N-1)$ is the number of qubit pairs where errors can occur and affect two consecutive local charges. In this estimate, we neglect the effect of the boundaries. Neglecting the possibility that three or more consecutive errors happen in the same Trotter step, the probability that a simulation fails due to these non-correctable errors is, therefore, $1 - P_{\rm corr} = 1 - (1-p_2)^{n_t}$. For the data presented in Fig. 4.9, where $p_{\rm err} = 0.02$, $L = 17$, and $n_t = 20$, this estimate gives a total error probability at the end of the time evolution of $P_{\rm err} = 1 - P_{\rm corr} \simeq 0.25$. This estimate is compatible with the numerical data: out of 100 trajectories, 16 are discarded because of ambiguous errors (dashed red lines), and 15 lead to wrong results because of nondetectable double errors (outlier grey lines).

To appreciate the effectiveness of the correction scheme, we compare it to the survival rate of a noisy evolution, where after n_t Trotter steps the probability that no incoherent bit-flip affected the dynamics is $P_{\rm succ} = (1-p_{\rm err})^{L n_t}$. The ratio between the two success probabilities is

$$\frac{P_{\rm corr}}{P_{\rm succ}} = \left[\frac{1 - p_{\rm err}^2 (1-p_{\rm err})^{L-2} 6(N-1)}{(1-p_{\rm err})^L} \right]^{n_t} \ . \tag{4.25}$$

Assuming that $p_{\rm err} < 1/L$ is small, a first-order expansion of the error rate per Trotter step leads to

$$\frac{P_{\rm corr}}{P_{\rm succ}} \sim (1 + L p_{\rm err})^{n_t} \ . \tag{4.26}$$

The error correction scheme gives an *exponential* protection as n_t increases, with respect to the bare noisy evolution, with a larger ratio for larger error probabilities.

Finally, let us combine the two types of error sources we discussed so far, i.e., local incoherent spin flips and the coherent error driven by the Hamiltonian in Eq. (4.8).

Now, enforcing gauge protection becomes more complicated as ancilla measurements detect both incoherent spin flips and coherent gauge drift, but cannot discriminate between them. A correction with a further bit flip is attempted in both cases, but it successfully compensates only the former. Correlated coherent errors cannot be inverted, indeed, by a single local bit-flip. The suppression of the coherent gauge drift, therefore, relies on the "passive" protection offered by the quantum Zeno effect through frequent measurements alone.

We adopt the same protocol as discussed so far, with both DPS and bit-flip correction, on top of which we implement a simple post-selection of the corrected trajectories. To eliminate automatically those instances where the correction failed, we exclude the erratic trajectories far from the exact dynamics. First, we evaluate the mean and standard deviation (std) of an observable, the electric Hamiltonian H_f, for instance, using all the simulations in which the gauge violation has been corrected. Then, we exclude all the data that wander sufficiently far from the average, assuming they are affected by undetectable errors. From the remaining trajectories, we extract a new ensemble average and variance. We iterate this procedure twice, first by excluding data that differ more than one standard deviation from the average, then those that differ more than two *updated* std from the new mean. It is important to remark that this post-processing may fail in actual experiments, as it requires an accurate estimate of the expectation value of an observable on a single trajectory. Nevertheless, its success suggests that more refined clustering methods might produce similar effects on data collected with projective measurements on the computational basis.

Figure 4.10 exemplifies the effectiveness of this method; while the DPS with EC already reduces the overall error from the noisy dynamics (dashed black and solid orange lines, respectively), the additional filtering of trajectories leads to excellent protection of the dynamics from both coherent and bit-flip errors (dashed green line). Moreover, the filtering also reduces the dispersion of the trajectories, as indicated by the error bars, selecting only those that follow the exact evolution (solid blue line). While the trajectory variance with DPS is comparable with the electric field shot noise, after the filter, their dispersion is greatly reduced, allowing for a more precise estimate of the expectation value.

A key take-home message is that within the framework of mid-circuit measurements, which naturally occur in any error-correction scheme, both coherent and incoherent errors can be handled. The efficiency of such protocols is limited by the measurement accuracy and the consequent maximum monitoring frequency. Understanding the intricate interplay between these many ingredients is a crucial step to bridge current NISQ devices to the primitive fault-tolerant ones, where the measurement-induced effects and imperfect error detection could still affect the circuit dynamics in nontrivial ways.

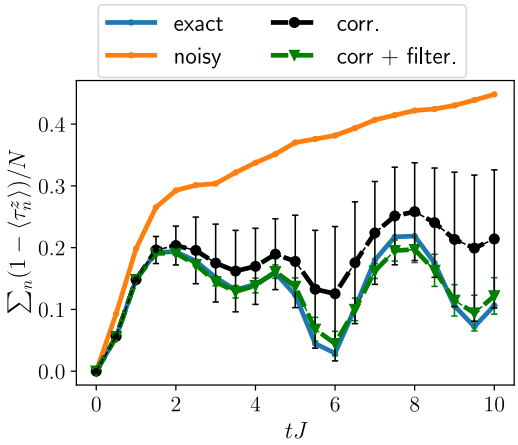

Figure 4.10: Active error correction. The noisy dynamics (solid orange line) deviate significantly from the exact dynamics (solid blue line). The average over corrected trajectories without the additional filter (dashed black line and circles) reach considerably closer to the exact dynamics. An additional filter that iteratively discards outlier trajectories reproduces the exact solution (dashed green line and triangles). The incoherent error probability per Trotter step at each qubit is $p_{\text{err}} = 0.02$ and the coherent error strength is $\lambda = 0.2J$.

4.7 Summary and outlook

In summary, we have proposed a dynamical post-selection protocol (DPS) harnessing passive mid-circuit measurements to both suppress (coherent) and correct (incoherent) violations of local gauge symmetries in quantum simulations of Abelian LGT models. The error mitigation capacity is not continuous in the monitoring frequency but emerges only after a quantum Zeno transition in the spectrum of an associated Liouvillian superoperator, which separates the protected phase from a regime in which the measurements induce a dynamics that quickly thermalizes to an infinite temperature ensemble. Framing our findings within the spectral theory of Liouvillians, we highlight the generality of the Zeno transition with respect to different measurement schemes in digital and analog protocols, showing that this transition is determined by the ratio between the circuit density of local projective measurements [307, 343, 344] of the gauge symmetry generators and the coherent error strength. This framework, based on the quantum Zeno effect, unifies many different proposals that exploit stochastic dynamics to protect the gauge symmetries in both digital and analog quantum simulation protocols, such as random gauge transformations [295], engineered dissipation [294], and syndrome measurements [299]. Crucially, despite the underlying Liouvillian being identical, each protocol results in a different unraveling in quantum trajectories. We exemplified this feature by comparing the stroboscopic projective measurements in a digital quantum simula-

tion (the DPS protocol) with continuous weak measurements of the local charges in a continuous-time setup.

Importantly, noisy measurements do not spoil the gauge protection, although the Zeno-like regime does not hold any longer to arbitrary large monitoring frequency. This holds for all the groups for which we studied the effective Liouvillian spectrum associated with the Zeno transition: $\mathbb{Z}_2$, $\mathbb{Z}_3$, and $U(1)$, the latter truncated to a quantum link model with $S = 1$ [16, 83, 85, 88, 98].

Moreover, we showed that a simple error-correcting scheme harnessing the natural redundancy in LGTs [300] can be easily integrated with DPS circuits.

Though weaker than similar fully error-correcting schemes [300, 302], it is also significantly less demanding as it only requires at most N ancilla qubits for the measurements, instead of auxiliary computational qubits and the associated heavier logical gates. It showcases how coherent and incoherent errors are handled differently within the same quantum circuit: first, frequent measurements suppress the coherent gauge drift, and, second, the active feedback builds upon the measurement results to compensate for incoherent spin-flips. Hence, there is no need to implement further gauge protection schemes to suppress coherent errors, typically also requiring entangling gates, if mid-circuit measurements are sufficiently reliable.

An aspect that we did not consider is the effect of a dephasing error channel. Indeed, we showed that DPS with error correction can suppress both coherent and bit-flip gauge-breaking errors, but it is insensitive to errors not affecting Gauss' laws. A possible approach to refine our proposal is to use qubit redundancy with majority votes to correct dephasing errors and the local charge measurements for bit-flips [300, 302], at the price of implementing more costly error-corrected logical gates. Moreover, in our analysis, we assumed that the error accumulated in each layer of the circuit is proportional to the discretization step Δt. Although this is irrelevant in the DPS scheme, it will likely affect its performance dependence on the number of Trotter steps. When considering the error rates of nonparametric gates, such as CNOT, the Zeno protection will appear only in an optimal window of measurement frequency ranges. This is essentially what emerges when the circuit coupling the ancilla with the computational qubits is noisy, as we have shown in Sec. 4.4, resulting in an imperfect but still effective error suppression. In the future, it will be interesting to perform a thorough analysis with realistic error and noise sources to fully assess the efficiency of DPS in practical scenarios.

Finally, the extension of the DPS to non-Abelian groups, for which the standard post-selection has several disadvantages, is studied and exposed in the next chapter.

Chapter 5

Symmetry verification in non-Abelian LGTs

In the previous chapter, we introduced the so-called dynamical post-selection (DPS) protocol, to check whether the local symmetries characterizing LGTs remain satisfied, and to mitigate the impact of gauge-breaking errors. Another main advantage of DPS is its possible application to non-Abelian LGTs, where the utility of the standard post-selection is significantly reduced. In the case of an Abelian gauge group, indeed, one may simultaneously diagonalize the gauge transformation operators, allowing for the concurrent confirmation of all conservation laws. Runs violating the symmetry at any vertex can then be discarded, and only the symmetry-verified runs are used to calculate the quantities of interest. Hence, the standard post-selection permits one to extract relevant observables that commute with the Abelian gauge symmetry, like electric field strength, particle number, or chiral condensate, without the requirement for additional circuit elements. In non-Abelian LGTs, the standard post-selection does not work because transformations associated with different group elements generally do not commute, preventing one from projectively monitoring the full gauge invariance at once.

In this chapter, we discuss the application of the DPS and of another complementary technique to significantly improve the quality of the acquired data in noisy real-time evolution of non-Abelian symmetries. We will denote the second scheme "post-processed symmetry verification" (PSV), by which expectation values of gauge-invariant operators can be reconstructed through an effective projection on the target superselection sector, and hence recovering a sort of standard post-selection, at least in the results. The effective projection is performed not by a direct projective measurement but by acquiring and post-processing the gauge-noninvariant data on a suitable set of observables. The observables that have to be measured correspond to correlators between the target observable and gauge symmetry operators.

Importantly, here, we will focus on the implementation of DPS and PSV on qudit devices [115, 116, 125, 126, 345], which provide the ideal setting to cope

with the large local Hilbert space of non-Abelian groups. As a benchmark, we test our protocols on the dihedral group D_3, whose small cardinality fits state-of-the-art universal qudit platforms [116].

5.1 Model

In the following, symmetry-verification models will be tested on the time evolution of a 2+1 D pure gauge lattice model with the dihedral D_3 group. The lattice geometry of our toy model consists of 2 plaquettes and 2 vertices with periodic boundary conditions (PBCs), see Fig. 5.1(a), so there are 4 independent link variables. Having order $|D_3| = 6$, it can be encoded exactly in existing qudit processors [116] and thus presents an ideal setting to experimentally investigate the transition between strong- and weak-coupling limits. The full Hilbert space has dimension $\dim(\mathcal{H}) = 6^L = 1296$, for $L = 4$ links but the physical gauge sector space is considerably smaller, with dimension [200] $\dim(\mathcal{H}_\mathcal{P}) = \sum_C \left[\frac{|\mathcal{G}|}{|C|}\right]^{L-V} = 49$. C represents conjugacy classes of the group, and V is the number of vertices.

As already discussed in Sec. 1.3, D_3 has two one-dimensional irreducible representations ($j = e, p$) and one two-dimensional irreducible representation ($j = \tau$). The latter is the only faithful one, i.e., with a unique correspondence between group elements g and matrices $D^\tau(g)$, up to a common unitary transformation. Henceforth, we will work only with $j = \tau$. A possible encoding of the group elements in a qudit with $d \geq 6$ is

$$|g\rangle \Leftarrow D^\tau(g) = \begin{bmatrix} 0 & 1 \\ 1 & 0 \end{bmatrix}^{\lfloor \frac{g}{3} \rfloor} \begin{bmatrix} e^{2\pi i/3} & 0 \\ 0 & e^{-2\pi i/3} \end{bmatrix}^g , \tag{5.1}$$

where $g \in \{0,\ 1, \ldots, 5\}$ and $\lfloor \cdot \rfloor$ denotes the integer part. The two matrices in Eq. (5.1) belong to a faithful irreducible representation $D^\tau(g)$ of the generators s and r of the group, see Eq.(1.33), which represent a reflection and a rotation by an angle $2\pi/3$, respectively.

The pure gauge Hamiltonian reads

$$H_{\mathrm{PG}} = H_B + H_E \ , \tag{5.2}$$

where H_B is the magnetic term (see Eq. (1.16)) and H_E the electric term (see Eq. (1.14)). Because of the lattice geometry of the system and the PBCs, the magnetic term consists of 2 plaquette terms and reads

$$H_B = -\frac{1}{ag^2}\Re\left[\mathrm{Tr}\left(U_0 U_3 U_0^\dagger U_2^\dagger\right) + \mathrm{Tr}\left(U_1 U_2 U_1^\dagger U_3^\dagger\right)\right] \ . \tag{5.3}$$

For the results of this chapter, the electric term has been derived from the transfer matrix associated with the Wilson action of the magnetic term [150], $H_E = -\frac{1}{a}\ln T_E$. The transfer matrix is defined as

$$\langle \mathbf{g}' | \, T_E \, | \mathbf{g} \rangle = \prod_\ell \exp\left\{\frac{1}{g^2}\mathrm{Tr}\left[D^j(g_\ell'^{-1}) D^j(g_\ell)\right]\right\} \ , \tag{5.4}$$

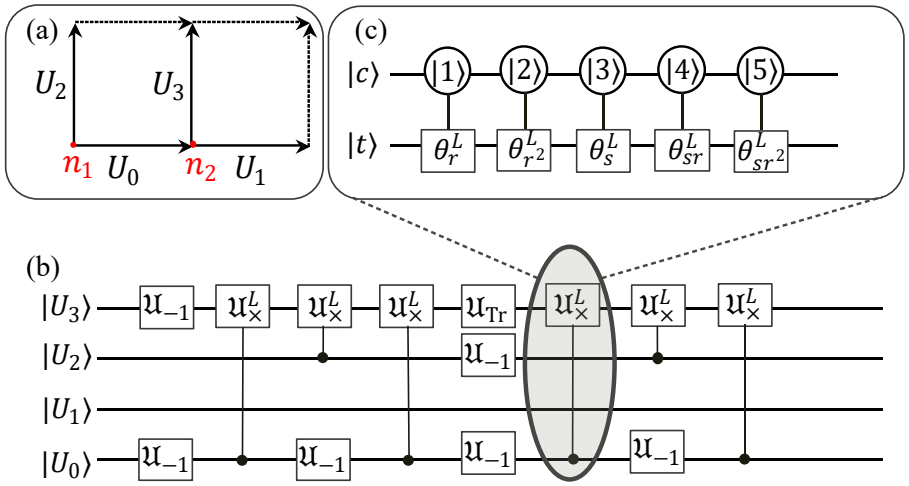

Figure 5.1: (a) The lattice geometry of the toy model studied numerically in this chapter: two plaquettes with Periodic Boundary Conditions, consisting of 2 vertices and 4 links. (b) The quantum circuit implementing the time evolution of the left plaquette term, where every U variable is encoded in a single qudit. The circuit requires control-left-multiplications, while the inversion gates can be absorbed in the multiplication gates as explained in the text. (c) The expansion of one control-left-multiplication operator in terms of a series of single control-permutations. Based on the state of the control qudit $|c\rangle$, left group multiplications are applied to the target qudit $|t\rangle$. Group elements in the target qudit are connected to qudit states by the mapping in Eq. (5.1).

where $|\mathbf{g}\rangle$ and $|\mathbf{g}'\rangle$ are two vectors in the group-element basis for the spatial two-dimensional lattice, and the product runs over all links ℓ. Since the electric Hamiltonian is the sum of one-body terms acting independently on each link, one only needs to compute the transfer matrix for one link and apply the matrix logarithm to get the electric Hamiltonian acting on the single link, $H_E^{(1)} = -\frac{c\hbar}{a} \ln T_E^{(1)}$.

The gauge transformations for the two vertices n_1 and n_2 are

$$\begin{aligned} \Theta_{g,n1} &= \Theta_g^L \otimes \Theta_g^R \otimes \Theta_g^L \Theta_g^R \otimes \mathbb{1}_6 \ , \\ \Theta_{g,n2} &= \Theta_g^R \otimes \Theta_g^L \otimes \mathbb{1}_6 \otimes \Theta_g^L \Theta_g^R \ , \end{aligned} \tag{5.5}$$

where we dropped the link indices as they are identified by the order in the tensor product. The terms $\Theta_g^L \Theta_g^R$ reflect the "double" directionality of the vertical links, which are both ingoing and outgoing from the vertices due to PBCs. However, this modifies neither the eigenvalues of $\Theta_{g,n}$ nor the possibility of diagonalizing them with single-qudit rotations.

The time evolution terms $\mathrm{e}^{-iH_E\Delta t}$ and $\mathrm{e}^{-iH_B\Delta t}$, necessary for the Trotterized evolution, can be implemented similarly to what we have shown in Eq. (1.21) and Eq. (1.22), with some differences due to the use of a qudit-based hardware. The main advantage is represented by the Quantum Fourier Transform. Since its gate becomes a single-qudit gate when $d \geq |\mathcal{G}|$, the necessity of control operations for the change of basis between the magnetic and the electric basis decays, i.e., the Fourier transform of the group $\mathfrak{U}_{\mathrm{QFT},\ell}$ can be implemented just with single-qudit gates. So, since here we use the magnetic basis as the computational one, the electric time evolution on the link ℓ, $\mathfrak{U}_{\mathrm{QFT},\ell}\mathfrak{U}_{\mathrm{ph},\ell}(\alpha_j g^2 \Delta t)\mathfrak{U}_{\mathrm{QFT},\ell}^{-1}$, results control-gate-free.

Regarding the magnetic time evolution, we need to implement a circuit like the one depicted in Fig. 1.2 for each plaquette. In Fig. 5.1(b), we show the quantum circuit implementing the time evolution of the left plaquette in the magnetic term for the lattice geometry in panel (a). Panel (c) shows the implementation of one control-left-multiplication as a series of control-permutations. When the control qudit is in the state corresponding to the group element g, on the target qudit, the left multiplication associated with g is performed. θ_g^L in the group element basis is a permutation matrix, since it encodes how the group element $|h\rangle$ changes under the left multiplication $\theta_g^L |h\rangle = |gh\rangle$. Of the primitive gates necessary for the implementation in panel (b), see Sec.1.2, one can include the inversion gates $\mathfrak{U}_{-1}$ in the control-multiplication gates by performing the θ_g^L permutation when the state of the control qudit is $|g^{-1}\rangle$ [73]. In D_3, this technique only swaps $r \longleftrightarrow r^2$, since every other group element is the inverse of itself.

For example, the left multiplication operator with respect to the group element

r and the trace operator read

$$\Theta^L_{|r\rangle} = \begin{bmatrix} 0 & 0 & 1 & 0 & 0 & 0 \\ 1 & 0 & 0 & 0 & 0 & 0 \\ 0 & 1 & 0 & 0 & 0 & 0 \\ 0 & 0 & 0 & 0 & 1 & 0 \\ 0 & 0 & 0 & 0 & 0 & 1 \\ 0 & 0 & 0 & 1 & 0 & 0 \end{bmatrix} \qquad U_{\mathrm{Tr}}(\phi) = \begin{bmatrix} e^{-2i\phi} & 0 & 0 & 0 & 0 & 0 \\ 0 & e^{i\phi} & 0 & 0 & 0 & 0 \\ 0 & 0 & e^{i\phi} & 0 & 0 & 0 \\ 0 & 0 & 0 & 1 & 0 & 0 \\ 0 & 0 & 0 & 0 & 1 & 0 \\ 0 & 0 & 0 & 0 & 0 & 1 \end{bmatrix}, \tag{5.6}$$

where the phase $\phi = -\frac{1}{g^2}\Delta t$ takes into account the parameters of the simulation, i.e., the coupling and the Trotter step, and the numerical exponents are the traces of the group elements of D_3 in the fundamental representation, see Table 1.5.

5.1.1 Error model

To introduce errors in the simulations and test the gauge protection capability of our protocols, we consider a noise channel generated by random unitaries close to the identity. While this choice maintains unitarity in the time evolution on a single run (trajectory), the ensemble average results in an incoherent error channel.

Several techniques can numerically generate random unitaries close to the identity. Here, we implement a method based on Householder transformations [346]. These are unitary transformations describing the reflection about a hyperplane that contains the origin. The matrix operator describing the Householder reflection defined by its normal vector $\boldsymbol{v}$ reads $\mathcal{R} = \mathbb{1} - 2\boldsymbol{v}\boldsymbol{v}^\dagger$, where $\boldsymbol{v}$ in our case is a random complex vector whose elements are extracted from a normal distribution with unit variance.

To tune how close the random unitary is to the identity, we introduce a diagonal operator $\mathcal{D}$, with normally distributed real elements, such that the final noise term is

$$U_{\mathcal{E}(\gamma)} = \exp(i\mathcal{D}\gamma)\mathcal{R} \ , \tag{5.7}$$

where γ is a dimensionless parameter that determines the noise strength and the average distance of the random unitaries from the identity. The result is a dense unitary random matrix, whose eigenvalues lie on the unit circle in the complex plane. One of them is -1, originating from the Householder reflection. The others are centered around 1 with a width depending on γ. We characterize the average difference between the $U_{\mathcal{E}(\gamma)}$ and the identity through the Hilbert–Schmidt inner product

$$d_{\mathrm{HS}}(\gamma) = \frac{\overline{\langle U_{\mathcal{E}(\gamma)}, \mathbb{1}\rangle_{\mathrm{HS}}}}{\dim\mathcal{H}} = \left(1 - \frac{2}{\dim\mathcal{H}}\right) \mathrm{e}^{-\gamma^2/2} \ . \tag{5.8}$$

Using this ensemble of random unitaries, the noisy discrete-time evolution over a single Trotter step reads

$$U(\Delta t) = U_{\mathcal{E}(\gamma)} \mathrm{e}^{-iH_E\Delta t} \mathrm{e}^{-iH_B\Delta t} \ , \tag{5.9}$$

with $U_{\mathcal{E}(\gamma)}$ being drawn independently for every Trotter step of every trajectory. The ensemble average of Eq. (5.9) constitutes the noisy channel used in the simulated noisy Trotterized evolution of the non-Abelian model.

A realistic estimate for the error rate strongly depends on the individual qudit hardware. Reference [73] also considers a small lattice with a pure gauge theory and a discrete group, where the main sources of error are control-multiplications used to implement the plaquette operators. On a Rydberg-atom qudit simulator, they estimate the achievable fidelity to be 99.6%. Since six of such two-qudit gates are required for each plaquette operator, one can expect the overall fidelity of a single Trotter step to be about 95% for the two-plaquette lattice we have considered in this section. This corresponds to a noise strength $\gamma \sim 0.22$, which is compatible with the regime in which we tested DPS and PSV. At the same time, the bare noisy dynamics quickly relax to a nonphysical steady state, highlighting the necessity of error-mitigation schemes.

5.2 Symmetry verification schemes

5.2.1 Post-processed symmetry verification

As pointed out at the beginning of this chapter, direct post-selection is not accessible for non-Abelian symmetries, as the gauge transformations do not all commute pairwise. Here, we outline an alternative approach that leverages the concept of verifying symmetries in post-processing [327, 329, 331, 332]. It allows for the verification of gauge invariance without a need for additional circuit elements beyond rotations into a suitable basis at the final step, and is based on acquiring data on an increased set of suitable observables from the error-prone gauge-violating dynamics, from which the gauge-invariant part of the desired observable can be reconstructed. Importantly, this approach is valid for any symmetry, Abelian and non-Abelian, as well as local and global.

Generally, the projection of a noisy outcome ρ of a simulation onto the symmetry-preserving subspace, defined by the projector Π_s, is given by

$$\rho_s = \frac{\Pi_\mathrm{s}\rho\Pi_\mathrm{s}}{\mathrm{Tr}[\Pi_\mathrm{s}\rho]}\,. \tag{5.10}$$

By construction, the overlap of ρ_s with the aspired ideal, noise-free outcome $\rho_\mathrm{id} = |\psi\rangle\langle\psi|$ increases as

$$\mathrm{Tr}(\rho_\mathrm{s}\,|\psi\rangle\langle\psi|) = \frac{\mathrm{Tr}[\rho\,|\psi\rangle\langle\psi|]}{\mathrm{Tr}[\Pi_\mathrm{s}\rho]} \geq \mathrm{Tr}[\rho\,|\psi\rangle\langle\psi|]\,. \tag{5.11}$$

The expectation value of an observable O with respect to the symmetry-projected state reads

$$\mathrm{Tr}(O\rho_\mathrm{s}) = \frac{\mathrm{Tr}[O\Pi_\mathrm{s}\rho\Pi_\mathrm{s}]}{\mathrm{Tr}[\Pi_\mathrm{s}\rho]} = \frac{\mathrm{Tr}[O_\mathrm{s}\rho]}{\mathrm{Tr}[\Pi_\mathrm{s}\rho]}\,, \tag{5.12}$$

where $O_\mathrm{s} = \Pi_\mathrm{s} O \Pi_\mathrm{s}$. If $[O, \Pi_\mathrm{s}] = 0$, as is the case for gauge-invariant observables, this expectation value simplifies to

$$\mathrm{Tr}(O\rho_\mathrm{s}) = \frac{\mathrm{Tr}[O\Pi_\mathrm{s}\rho]}{\mathrm{Tr}[\Pi_\mathrm{s}\rho]} \,. \tag{5.13}$$

For a lattice gauge theory with symmetry group $\mathcal{G}$, the symmetry-preserving subspace S is given by invariance under the gauge transformations $\Theta_{g,n} |\psi\rangle = |\psi\rangle$ for all group elements $g \in \mathcal{G}$ and all of the n_v vertices $n \in \mathrm{V}$. In the case of a finite (Abelian or non-Abelian) $\mathcal{G}$, the projector Π_s takes the form

$$\Pi_\mathrm{s} = \prod_{n\in\mathrm{V}} \frac{1}{|\mathcal{G}|} \sum_{g\in\mathcal{G}} \Theta_{g,n} = \frac{1}{|\mathcal{G}|^{n_\mathrm{v}}} \sum_{\mathbf{g}\in\mathcal{G}^{\times n_\mathrm{v}}} \prod_{n\in\mathrm{V}} \Theta_{g_n,n} \,. \tag{5.14}$$

Inserting Eq. (5.14) into Eq. (5.13) and employing the linearity of the trace yields

$$\mathrm{Tr}(O\rho_\mathrm{s}) = \frac{\sum_{\mathbf{g}\in\mathcal{G}^{\times n_\mathrm{v}}} \mathrm{Tr}\left[\rho O \prod_{n\in\mathrm{V}} \Theta_{g_n,n}\right]}{\sum_{\mathbf{g}\in\mathcal{G}^{\times n_\mathrm{v}}} \mathrm{Tr}\left[\rho \prod_{n\in\mathrm{V}} \Theta_{g_n,n}\right]} \,. \tag{5.15}$$

With this, one may perform symmetry verification by post-processing measurement outcomes determined by the individual conservation laws and their correlations with the target observable. That is, the expectation value of any gauge-invariant observable O in the state projected into the symmetry-preserving subspace ρ_s can be obtained from a combination of measurements on the noisy state ρ.

While this approach does not suffer from an exponentially decreasing number of valid shots, as does usual direct post-selection, the decompositions of Eq. (5.15) employ on the order of $|\mathcal{G}|^{n_\mathrm{v}}$ operators. In Sec. 5.3.2, we discuss the resource requirements in more detail. Importantly, implementing this procedure does not require additional circuit elements in the form of ancillas or measurement gates and is not dependent on the commutation relations of the symmetry transformations. To summarize, the action of the PSV protocol is to reconstruct the expectation value of a physical observable over a noisy ensemble of wave functions, or realizations of an experiment or of a circuit. The result consists of an effective projection of the ensemble over the gauge invariant subspace. Hence, PSV can be seen as a method to get an effective standard post-selection, even if it is not available in non-Abelian LGTs.

The circuit for the implementation of PSV for the two-plaquettes model is depicted in Fig. 5.2(a), where the single lines indicate that the quantum information is encoded in qudits.

5.2.2 Dynamical post-selection in D_3 LGT

Here, we show the application of the DPS protocol introduced in Sec. 4.1 to the D_3 LGT of the previous section. The circuit to diagonalize the symmetry operator $\Theta_{g,n1}$ in Eq. (5.5) is depicted in Fig. 5.2(b), where the single lines indicate that each link

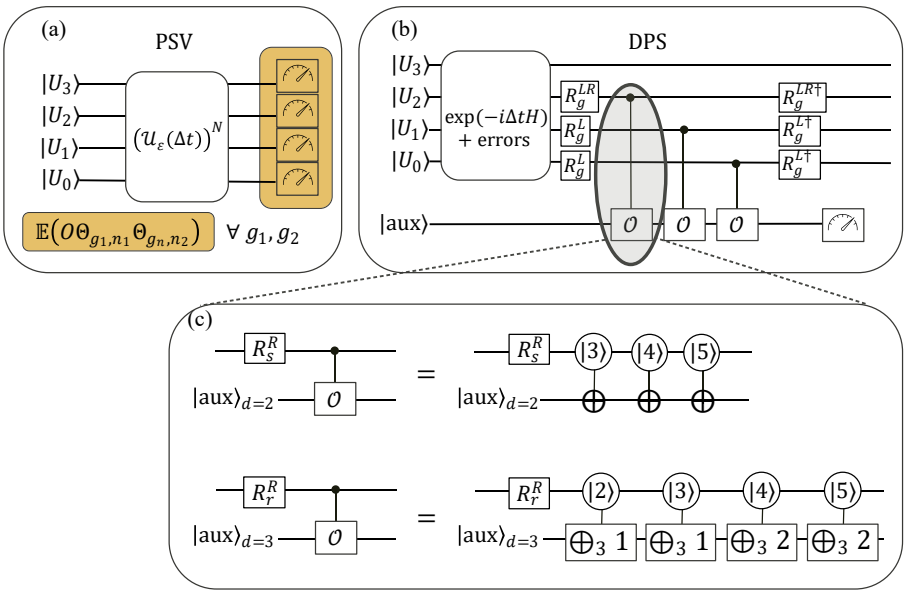

Figure 5.2: (a) PSV post-processes data acquired from different measurement settings in order to reconstruct gauge-invariant observables. Here we show the circuit including all these measurements at the end of an ensemble of noisy evolution for the model of two plaquettes and 4 links. (b) DPS circuit to check whether the $\Theta_{g,n1}$ symmetry in Eq. (5.5) is satisfied or not. (c) A possible implementation of the C-$\mathcal{O}$ after R^R, both for reflections (labeled with s, top circuit) and for rotations (labeled with r, bottom circuit). $d = 2, 3$ defines the dimension of the auxiliary qudit and $\bigoplus_3$ indicates the sum modulo 3 ($\mathbb{Z}_3$ cyclic permutations). We add 1 or 2, depending on the qudit state controlling the operation.

variable is a qudit and not a qubit-based quantum register as depicted in Fig. 4.1(c-d). In particular, the control-operators $C-\mathcal{O}$ are now mixed-dimensional controlled gates, meaning that the control and the target qudits have different dimensions.

The nature of mixed-dimensional controlled operators C-$\mathcal{O}$, as well as the dimension of the auxiliary qudit, depends on the group element we decide to protect. For the reflections $g \in \{3,4,5\}$, the $\Theta_s^{R(L)}$ operators have 2 distinct eigenvalues,

$$\sigma^{R(L)}_{g\in\{3,4,5\}} = \{1,1,1,-1,-1,-1\} \ , \tag{5.16}$$

so a qubit is enough to encode both of them. On the other hand, for non-trivial rotations, $g \in \{1,2\}$, the operators $\Theta_r^{R(L)}$ have 3 distinct eigenvalues,

$$\begin{aligned}\sigma^{R(L)}_{g\in\{1,2\}} = \{1,1,&\exp\{(2\pi i/3)\},\exp\{(2\pi i/3)\},\\ &\exp\{(-2\pi i/3)\},\exp\{(-2\pi i/3)\}\} \ ,\end{aligned} \tag{5.17}$$

meaning we need a qutrit auxiliary register.

Figure 5.2(c) shows a possible way to implement the C-$\mathcal{O}$ operators after the change of basis on the computational qudits. When the protected symmetry is a reflection, we encode the information of its eigenvalues in the auxiliary qudit. This is done by applying a X (NOT) operator when the eigenstate encoded on the controlling qudit has eigenvalue -1. When the protected symmetry is a rotation, its eigenvalues are encoded through a sum modulo 3 on the auxiliary qutrit: we add 1 (2) to the ancilla when the eigenstate encoded on the controlling qudit has eigenvalue $\exp(2\pi i/3)$ ($\exp(-2\pi i/3)$). The choice, however, is not unique, and the order of operators can be arranged as is most convenient. When the operator acting on the link variable is $\Theta_g^L\Theta_g^R$, C-$\mathcal{O}$ operators need two controlled gates since the eigenvalues are $\sigma^{RL}_{g\in\{3,4,5\}} = \{1,1,1,1,-1,-1\}$ and $\sigma^{RL}_{g\in\{1,2\}} = \{1,1,1,1,\exp\{(2\pi i/3)\},\exp\{(-2\pi i/3)\}\}$ for reflections and rotations respectively.

For Abelian groups with a single symmetry generator per vertex, measuring $|0\rangle$ on the auxiliary qudit already implies the output state is locally physical. This is no longer true for non-Abelian groups, and so for D_3. In that case, the building block of Fig. 5.2(b) can be repeated to check for the other symmetry transformations acting at the same vertex. In principle, to obtain a full certification, the gauge transformations at all vertices should be measured. In our numerics below, we cyclically choose only a single transformation at a single vertex in each Trotter step, for which we already find excellent error-mitigation performance. This should not surprise, since from the previous chapter we know that the frequency of mid-circuit measurements is the main factor in the error mitigation mediated by the Zeno effect. Finally, at the end of the procedure, we can measure observables of interest or continue the time evolution.

5.3 Numerical benchmarks on the D_3 model

To illustrate the performance of the two non-Abelian gauge-protection schemes, we simulate the system evolution following a quantum quench. We initialize the system

in a gauge-invariant state by setting every link in the trivial representation $j = e$, the ground state of H_{PG}, Eq. (5.2), in the strong coupling limit ($g \gg 1$). This state is given by a uniform superposition in the group element basis

$$|\psi_0\rangle = \bigotimes_{\ell=1}^{L} \frac{1}{\sqrt{|D_3|}} \sum_{g \in D_3} |g\rangle_\ell \ , \tag{5.18}$$

with L the number of links. The system then evolves according to Eq. (5.9), which includes the randomly drawn unitary operations $U_{\mathcal{E}(\gamma)}$ at each Trotter step, and where the Trotterized electric and magnetic terms are implemented according to Eq. (1.21) and Eq. (1.22), respectively. To monitor the time evolution, we study the expectation value of the left plaquette operator $\mathcal{O}_{P1}$, which corresponds to

$$\langle \mathcal{O}_{P1} \rangle = \langle \mathrm{Re}[\mathrm{Tr}(U_0 U_3 U_0^\dagger U_2^\dagger)] \rangle = -\frac{1}{2} a g^2 \langle H_B \rangle \, . \tag{5.19}$$

Since $\langle H \rangle = \langle H_E \rangle + \langle H_B \rangle = \mathrm{const}$, $\langle \mathcal{O}_{P1} \rangle$ gives information on all terms constituting the Hamiltonian.

Repeating the unitary evolution for M independent trajectories allows us to estimate the ensemble-averaged dynamics subject to decoherence.

We numerically simulate the system dynamics with exact diagonalization in the full Hilbert space of dimension 6^L. The code is available at [347]. In our simulations, we use a fixed Trotter step $\Delta t/a = 0.25$ and different noise strengths γ, and we set $\frac{1}{g^2} = 0.5$ in order to work in a scenario where H_E and H_B compete.

5.3.1 Dynamical post-selection

In this section, we evaluate the power of DPS to restore the desired gauge-invariant evolution of a noisy system. In the protocol we apply here, we protect only a single local symmetry after each noisy Trotter step, alternating vertices and group elements. For the given gauge group and system size, every local symmetry is checked on average every $t^* = 10\Delta t$. Thanks to the threshold ratio between error rate and measurement frequency beyond which the gauge-protection regime is achieved, as shown in the previous chapter, one can expect the measurement frequency chosen here to be effective as long as the error strengths are not too large. For higher γ, instead, one should protect several symmetries after each Trotter step to enter into a Zeno-protected dynamics. In our simulations, the operations of the DPS protocol itself are applied as if they do not introduce further errors, to highlight the physics of DPS.

In Fig. 5.3(a), we plot the results of $M = 5000$ trajectories affected by noise composed of random unitaries with a magnitude $\gamma = 0.2$. DPS follows the exact dynamics closely up to the maximum considered evolution time ($t/a = 25$). The protocol considerably improves over the noisy data, which strongly deviates from the error-free evolution already after $t/a = 3$. Due to the stochastic nature of the error protection protocol, the number of trajectories that preserve all tested gauge

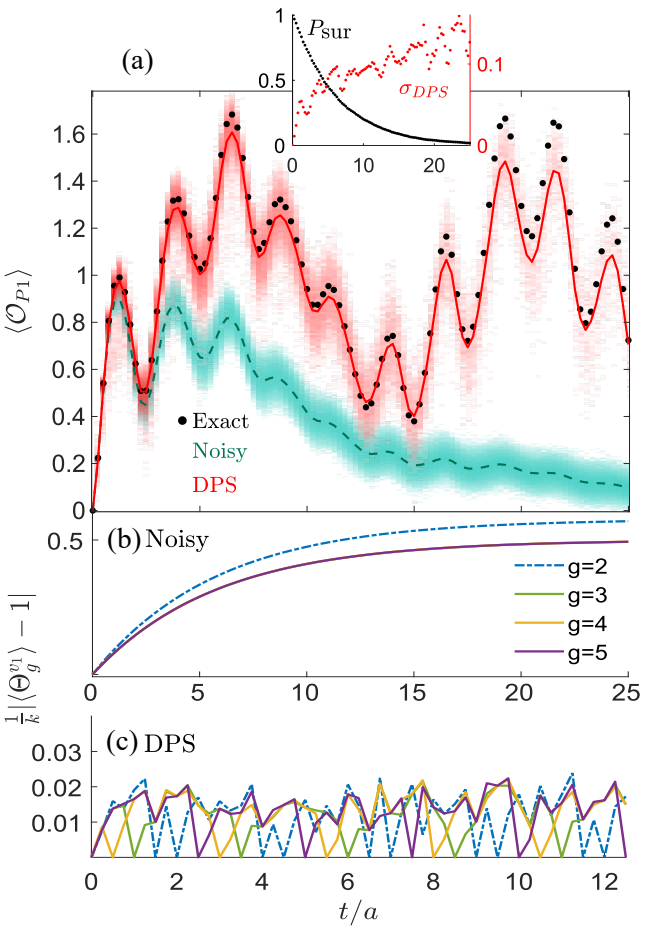

Figure 5.3: (a) Data clouds represent $\langle \mathcal{O}_{P1} \rangle$ at time t/a on individual trajectories for DPS (red) and noisy (green) evolutions. The opacity reflects the fraction of trajectories retained after DPS. Solid lines represent ensemble averages. The DPS ensemble average follows very well the error-free evolution (black dots). In the inset, we show the standard deviation of DPS data (red dots) and the fraction $P_{\rm sur}$ of trajectories that always preserved the gauge symmetries (black dots). (b-c) Gauge violations on vertex n_1 for the average of noisy evolutions without DPS (b) and for a single successful DPS trajectory (c). Reflection terms $g = 3, 4, 5$ (solid lines) do not superimpose on a single noisy trajectory, while their averages do. Rotations are here represented by $g = 2$ (dashed lines). Notably, the violation of a symmetry $\Theta_{g,n}$ can be partially suppressed also when other gauge charges are measured. The system is evolved with $\gamma = 0.2$, $1/g^2 = 0.5$, and $\Delta t/a = 0.25$ for $M = 5000$ trajectories. The x-axis in panel (c) is zoomed in, compared to panels (a) and (b), to improve the readability.

symmetries decreases exponentially in time, as shown by the black dots in the inset of Fig. 5.3(a). Such a decrease is typical also for post-selection protocols based on data taken at the final time, which nevertheless have been used very successfully to restore symmetry-respecting time evolutions in Abelian theories [81, 82, 85]. In the same inset, we plot the point-wise standard deviation of the successfully post-selected trajectories. Importantly, the standard deviation grows only slowly, reaching around 0.1 (about 10% of the mean) at the final considered time.

To better visualize the effect of DPS, one can study the dynamics of the individual symmetry violations, which we define as

$$\mathrm{GV}_{g,n} = \frac{1}{k_g} |\langle \Theta_{g,n} \rangle - 1| \ . \tag{5.20}$$

Here, k_g is a normalization factor depending on g such that $\mathrm{GV} \in [0, 1]$. The Gauss' laws violation allows us to qualitatively compare post-selected and noisy dynamics and to assess the quality of the gauge-protection protocol. Figure 5.3(c) displays the dynamics of $\mathrm{GV}_{g,n1}$ at the first vertex for a trajectory where the local symmetries are always successfully protected. Out of the six possible gauge transformations for each vertex, we can neglect the identity $g = 0$ as it acts trivially. Moreover, we only monitor the violations corresponding to one rotation ($g = 2$), since the $\mathbb{Z}_3$ subgroup of $\frac{2\pi}{3}$ rotations is cyclic, rendering conservation of the associated local symmetries equivalent. As shown in Fig. 5.3(c), the DPS protocol repeatedly suppresses the gauge violations through the auxiliary measurements, and their growth between two successive measurements of the same symmetry operator remains limited. This pattern remains constant even for longer times, although the noisy evolution becomes increasingly decoupled from the exact one. Moreover, gauge violations in Fig. 5.3(c) decrease even when other symmetries are monitored, which indicates that gauge violations of different local charges are correlated. The behaviour is markedly different in the bare noisy dynamics, shown in Fig. 5.3(b). Here, the ensemble-averaged violations increase until they reach a plateau, 0.5 for reflections and $1/\sqrt{3}$ for rotations, corresponding to a fully mixed state[1].

5.3.2 Comparing DPS and PSV

Let us now explicitly compare the error-mitigation capacity of the two protocols described in Sec. 5.2. First, we contrast the protection efficacy of both methods. After that, we discuss the relative scalings, which help in assessing which method may be most suitable for a given platform.

Protection efficacy

In Fig. 5.4(a), we compare the ensemble averages of the two protocols over $M = 5000$ trajectories to the bare noisy evolution, for a high noise strength $\gamma = 0.3$. As above,

[1] The precise asymptotic value depends on the definition in Eq. (5.20), but in general every charge sector is uniformly populated after a characteristic time depending on γ.

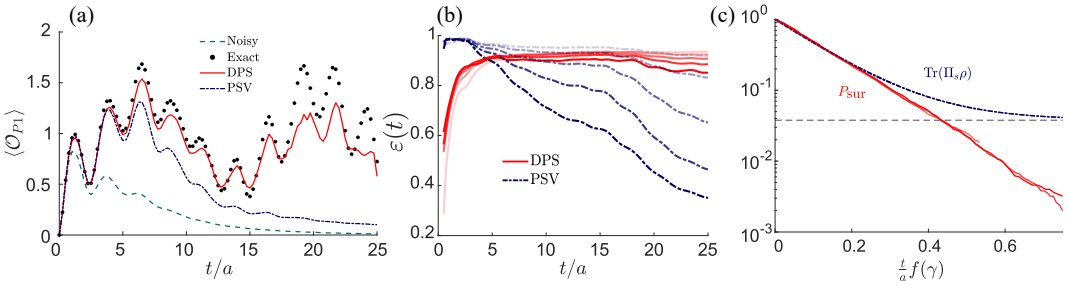

Figure 5.4: (a) Comparison between PSV (dot-dashed blue line) and DPS (solid red line) for relatively strong noise with $\gamma = 0.3$, computed over 5000 trajectories. Both methods significantly improve over the average noisy evolution (dashed green line). PSV follows the exact Trotterized evolution (black dots) quantitatively well up to $t/a \simeq 6$, DPS even up to $t/a \simeq 17.5$. (b) Protection efficacy, defined in Eq. (5.23), versus time, for increasing noise strength $\gamma = \{0.1, 0.15, 0.20, 0.25, 0.3\}$ (light to dark lines). PSV performs better initially, but DPS remains resilient against noise for longer evolution times. (c) The survival probability of DPS trajectories and the gauge-symmetric projection of the density matrix in PSV, describing a signal-to-noise ratio, initially follow the same exponential decay. At late times, PSV reaches the value of the fully mixed density matrix, $\mathcal{H}_P/\mathcal{H}$ (horizontal dashed line). The rescaling $t/a \to \frac{t}{a} f(\gamma)$ collapses the data with different noise strengths. $f(\gamma)$ is defined in Eq. (5.24) and sets the effective error rate. Data for $1/g^2 = 0.5$ and $\Delta t/a = 0.25$.

in the DPS we perform one measurement per Trotter step. In the PSV scheme for the symmetry group $\mathcal{G} = \mathrm{D}_3$ on $n = 2$ vertices, Eq. (5.15) for the gauge-symmetric expectation value reduces to

$$\mathrm{Tr}(O\rho_{\mathrm{s}}) = \frac{\sum_{g_1,g_2\in \mathrm{D}_3} \mathrm{Tr}[\rho O \Theta_{g_1,n_1} \Theta_{g_2,n_2}]}{\sum_{g_1,g_2\in \mathrm{D}_3} \mathrm{Tr}[\rho \Theta_{g_1,n_1} \Theta_{g_2,n_2}]} \,. \tag{5.21}$$

Despite the strong noise, the two protocols produce very similar (and close to ideal) results up to $t/a \sim 6$, a time at which the noisy average has already lost any resemblance to the target dynamics. For $t/a \gtrsim 6$, PSV relaxes towards the infinite-temperature steady state while DPS continues to follow the target dynamics with small deviations until $t/a \sim 17.5$. The cause of this visible difference is that the PSV does not account for multiple gauge violations that combine into a gauge-invariant error. Eventually, DPS also deviates from the exact time evolution, all the while maintaining a rather satisfactory resemblance except for the very latest times we considered. Identifying and suppressing gauge violations already during the dynamics thus enhances the protection efficacy of DPS over PSV. This better error mitigation capacity of DPS comes, however, at the cost of a larger number of entangling gates required for the measurement of the symmetry constraints through the auxiliary qudits. In contrast, PSV just necessitates the addition of a layer of basis rotations at the end of the circuit in order to extract the relevant observables that constitute Eq. (5.21).

To get a better quantitative understanding of how the performances of the two

protocols depend on the noise strength γ, we consider the cumulative error over time

$$\mathcal{E}^*(t) = \sum_{t_n \leq t} |\langle H_B(t_n)\rangle_* - \langle H_B(t_n)\rangle_{\mathrm{id}}| \ , \tag{5.22}$$

where t_n labels the discrete time slices, $\langle H_B\rangle_{\mathrm{id}}$ is the magnetic energy measured after an ideal error-free Trotterized evolution, and the sub-/superscript $* \in \{\mathrm{DPS}, \mathrm{PSV}\}$ represents the use of one of the two methods on top of a noisy evolution. We define the protection efficacy as the normalized difference between cumulative errors with and without gauge protection

$$\varepsilon(t) = 1 - \mathcal{E}^*(t)/\mathcal{E}^{\mathrm{Noisy}}(t) \ . \tag{5.23}$$

When $\varepsilon = 0$, the gauge protection protocol does not improve over the bare noisy evolution, while $\varepsilon = 1$ corresponds to perfect error mitigation matching the error-free dynamics.

We compare the protection efficacy of DPS and PSV in Fig. 5.4(b) for different values of $\gamma \in [0.1, 0.3]$. PSV displays an advantage at short times as it incorporates all gauge transformations *at once*. In contrast, our implementation of DPS only monitors one local symmetry per Trotter step, thus requiring a longer time to properly suppress the gauge violations. On the other hand, DPS is more stable from intermediate to long times, consistent with Fig. 5.4(a), and is less affected by the increasing noise strength. Our results also suggest that increasing the error rate in DPS due to imperfect mid-circuit measurements will not impact its protection efficacy qualitatively, as the algorithm performance is stable from weak to intermediate-strength noise.

Resource requirements

A natural question is whether either of the two methods offers a practical advantage over the other, in situations where they present similar error-mitigation quality. Roughly speaking, PSV is more flexible and can be used in any architecture, whereas DPS seems beneficial in platforms where adequate mid-circuit measurement operations are available. To be able to make more precise statements, it is useful to consider the scaling of both methods.

To implement DPS with full symmetry verification after each Trotter step for n_{v} vertices, one needs at most $|\mathcal{G}|n_t n_{\mathrm{v}}$ single-shot mid-circuit measurements during a single run. Since these measurements concern local operators, those acting on non-neighboring vertices can be parallelized. Hence, the resulting increase in the number of circuit layers does not depend on the system size. The above scaling with $|\mathcal{G}|$ can be further improved by measuring only an optimal generating set of $\mathcal{G}$ (e.g., for D_3, the reflection and the rotation with the smallest angle are already enough to ensure full protection). Further, to circumvent costly mid-circuit readout and reset [348–350], one may also employ an array of ancillas whose measurement is delayed to the

end of the circuit. The additional spatial (auxiliary qudits) and logical resources (two-qudit gates coupling the ancillas to the system) need to be sufficiently precise, as otherwise they would wash out the benefits of gauge protection. In contrast, PSV needs only basis rotations at the end of the simulations to measure the desired operators, making a single run less demanding.

As for any similar mitigation method [143, 339], the present algorithms have a sampling overhead that is exponential in the simulated time, i.e., number of Trotter steps, and system size, which, however, becomes manifest differently in the two protocols: in DPS, the dynamics will eventually be dominated by the proliferation of gauge-violating trajectories, meaning an ever smaller number of runs can be successfully retained as the size and depth of the circuit increases; in comparison, the decreasing weight of the group-symmetric density matrix $\Pi_s\rho$, leading to a small denominator in Eq. (5.15), limits PSV performance.

Focusing on the scaling in the number of Trotter steps at a fixed system size, the survival rate of DPS, i.e., how many trajectories never incur a measurement yielding a "wrong" result, can be estimated assuming that the amplitude β in Eq. (4.5) is $\propto \gamma$. In that case, the error channel populates the gauge-violating sector with a rate $p_{\text{err}} \sim \gamma^2$. More precisely, we found that the error rate is associated with the average Hilbert–Schmidt inner product $\overline{\langle U_{\mathcal{E}(\gamma)}, \mathbb{1}\rangle}_{\text{HS}}$ between the identity (i.e., zero noise) and the random unitaries $U_{\mathcal{E}(\gamma)}$ drawn according to the chosen noise model,

$$p_{\text{err}} \simeq f(\gamma) = 1 - \frac{\overline{\langle U_{\mathcal{E}(\gamma)}, \mathbb{1}\rangle}_{\text{HS}}}{\dim\mathcal{H}} = 1 - \mathrm{e}^{-\frac{\gamma^2}{2}}\left(1 - \frac{2}{\dim\mathcal{H}}\right). \tag{5.24}$$

At the lowest order in γ, indeed $p_{\text{err}} \sim \gamma^2$, while the expression for $\overline{\langle U_{\mathcal{E}(\gamma)}, \mathbb{1}\rangle}_{\text{HS}}$ is given by the error model described in Sec. 5.1.1. The probability of never incurring any gauge violations after $n_t = t/\Delta t$ Trotter steps is therefore

$$P_s(t) = (1 - p_{\text{err}})^{n_t} \sim \mathrm{e}^{-\frac{t}{\Delta t} f(\gamma)} \,. \tag{5.25}$$

In Fig. 5.4(c), we show the survival probability $P_s(t)$ for DPS as well as the weight of the symmetrized density matrix $\mathrm{Tr}[\Pi_s\rho]$ using PSV for $\gamma \in [0.1, 0.3]$. The rescaling $t/a \to \frac{t}{a} f(\gamma)$ suggested by Eq. (5.25) leads to a perfect collapse of the data and highlights that both methods require an exponentially scaling overhead to properly estimate the gauge-invariant expectation values. The main difference between the two protocols is a saturation occurring for PSV at long times, since $\mathrm{Tr}[\Pi_s\rho] \to \dim\mathcal{H}_P/\dim(\mathcal{H})$ as a consequence of the steady state being fully mixed. The time around which $\mathrm{Tr}[\Pi_s\rho]$ deviates from the exponential decay ($\frac{t}{a} f(\gamma) \approx 0.3$ in Fig. 5.4c) coincides with the time around which the reconstructed PSV signal deviates significantly from the ideal data (for $\gamma = 0.3$, $t/a \approx 7$, see Fig. 5.4a).

For PSV, naively we could expect that one would need to construct all expectation values in Eq. (5.15) explicitly, which would imply $2|\mathcal{G}|^{n_v}$ independent measurement settings. The actual cost can be considerably lower. First, a gauge

transformation $\prod_{v\in \mathrm{V}} \Theta_{g_v,v}$ and its correlator with a gauge-invariant observable O may be measured simultaneously. Further, one can employ the group commutation structure to identify groupings of commensurable or related contributions of different group elements in Eq. (5.15), reducing the number of different measurements needed. Generally, the question of how many independent measurements are required may be formalized as finding a minimum clique cover on a graph representing the commutation structure of the operators, which here is given by the commutators within $\mathcal{G}^{\times n_\mathrm{v}}$. In the numerical example of the above section for $n_\mathrm{v} = 2$ vertices and the gauge group $\mathcal{G} = D_3$, this allows one to reduce from the $2 \cdot 6^2 = 72$ individual expectation values appearing in Eq. (5.21) to $4^2 = 16$ cliques of simultaneously measured operators. A further efficiency improvement could be achieved by restricting the full projector to one that only acts in the vicinity of the local observables of interest.

Additionally, one can estimate Eq. (5.15) through a random sampling of the group element combinations $\{g_1, \ldots, g_{n_\mathrm{v}}\}$. For every sample, one simultaneously measures the prescribed gauge transformation operator and its correlator with the gauge-invariant target observable (or cardinality-weighted cliques thereof). Analogous considerations for the qubit case [330–332] reveal such estimators to require a sampling overhead scaling as $\mathrm{Tr}[\Pi_\mathrm{s}\rho]^{-2}$. This overhead can generally be determined by analyzing the increase in the variance of the new estimator compared to the unmitigated, noisy one. The variance of a ratio of expectation values, such as those estimators, is then dominated quadratically by the inverse of the denominator. The decrease of $\mathrm{Tr}[\Pi_\mathrm{s}\rho]$ with circuit depth and system size is governed by the strength of (gauge-invariance breaking) error rates, and therefore the required sampling cost immediately benefits from any quantum hardware developments. In particular, for a given shot budget and error rate, one has a window of simulated time within which controlled sampling of the gauge-invariant expectation value is possible.

As a final remark, the feasibility and quality of the mid-circuit measurements are a fundamental requirement to implement DPS. While qudit hardware is still in a rapidly developing stage and the various platforms have yet to demonstrate their implementation, mid-circuit measurements are routinely used in qubit processors for several purposes, e.g., state preparation [153] or long-range entangling operations [348]. The extension to qudit devices requires some care, as the readout process becomes slower and more delicate because of the many levels involved, but faces no fundamental obstacle. In addition, efficient mid-circuit monitoring of ancilla qubits is a crucial building block for any error-correcting code and, as such, is actively pursued in many platforms aiming towards fault-tolerance.

5.4 Gauge protection on three plaquettes

Any error mitigation technique is expected to become more resource-intensive for increasing system size, as the total error rate typically increases. In this section, we benchmark DPS and PSV for a larger system composed of a ladder with three plaquettes and periodic boundary conditions, consisting of 6 qudits in total, and a

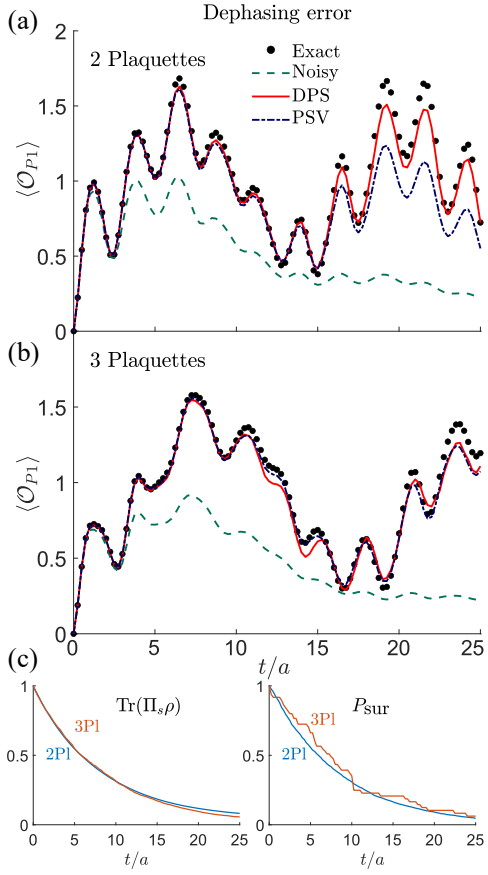

Figure 5.5: Comparison between the exact, noisy, DPS, and PSV time evolution in the presence of dephasing noise for (a) two plaquettes, averaged over 5000 independent trajectories, and (b) three plaquettes, averaged over 145 independent trajectories. (c) At constant local error rate, the weight of the gauge-invariant part of the state for PSV and the survival probability in the case of DPS remain comparable (for DPS, there is still a single measurement per Trotter step). Thus, from 2 to 3 plaquettes, the protection quality of DPS only slightly decreases, due to the reduced measurement density, while maintaining a constant resource cost. For PSV, by contrast, the protection quality even increases, at the cost of 6 times more observables to be measured, and thanks to the smaller ratio between the dimensions of the physical sector and the total Hilbert space. For the two-plaquette system, $\gamma = 0.2$ as previously, while for the three-plaquette system we rescaled to the corresponding $\gamma = 0.245$, as explained in the text.

Hilbert space of dimension 46656. To reduce the memory requirements, we consider a global dephasing noise instead of dense random unitaries. We model the dephasing noise through a Hamiltonian H_{dp} that is diagonal in the group element basis and whose entries are sampled from a normal distribution with vanishing mean and unit variance. H_{dp} is independently drawn at each Trotter step. The noisy discrete-time evolution for a single step then reads

$$U(\Delta t) = \mathrm{e}^{-iH_{\mathrm{dp}}\gamma}\mathrm{e}^{-iH_E\Delta t}\mathrm{e}^{-iH_B\Delta t} \,, \tag{5.26}$$

First, we study the effect of dephasing noise on the target dynamics and the level of gauge protection offered by the two techniques in the two-plaquette ladder investigated in the main text. We show the ensemble average over $M = 5000$ trajectories in Fig. 5.5(a), with noise strength $\gamma = 0.2$ and the same parameters used for the simulations in this chapter ($1/g^2 = 0.5$ and $\Delta t/a = 0.25$). Despite the simpler structure than the dense random unitaries considered in the main text, the noisy dynamics is qualitatively similar. DPS and PSV both yield excellent error mitigation, with the former performing better at longer times, similar to Fig. 5.4(a).

The overall picture continues to hold when considering the larger system with 3 plaquettes, as reported in Fig. 5.5(b), where we again monitor the left plaquette of the lattice. In DPS, we again measure only one local symmetry after each Trotter step so that the overall cost of the mitigation technique does not increase with respect to the two-plaquette model. Remarkably, the reduced measurement density only slightly affects the gauge protection, compared to the smaller system shown in Fig. 5.5(a). For a fair comparison, the noise strength here is rescaled such that the overall error rate $\sim \gamma^2$ is proportional to the system size. Given a small local error probability p_{err}, the error rate per Trotter step for N qudits at first order in p_{err} is given by $\gamma^2 \simeq 1 - (1 - p_{\mathrm{err}})^N \simeq N p_{\mathrm{err}}$. Here, p_{err} reflects the average fault rate per qudit resulting from all gates applied in the implementation of a single Trotter step. When increasing the system size from two to three plaquettes, we assume that this microscopic error rate p_{err} remains fixed. With the number of operations per layer growing linearly with the number of plaquettes, this leads to a corresponding linear increase of the overall infidelity γ^2 for each Trotter step, i.e. $\gamma^2_{3\mathrm{P}} = 3\gamma^2_{2\mathrm{P}}/2$. Because the measurement density is also rescaled down with the same ratio 3/2, the decay of the DPS survival probability behaves similarly in the two cases, as shown in the right panel of Fig. 5.5(c).

Notably, PSV now better approximates the exact time evolution with respect to the data shown for the two-plaquette lattice. This counterintuitive behaviour can be explained by considering the ratio between the dimensions of the physical sector and the total Hilbert space. In the two-plaquette lattice, one has $\frac{\dim\mathcal{H}_{\mathrm{P}}}{\dim\mathcal{H}_{\mathrm{tot}}} = \frac{49}{1296} \simeq 0.0378$, while in the three-plaquette system $\frac{\dim\mathcal{H}_{\mathrm{P}}}{\dim\mathcal{H}_{\mathrm{tot}}} = \frac{251}{46656} \simeq 0.0054$. The smaller fraction reduces the probability of effective gauge-invariant errors originating from two consecutive gauge-violating errors that cancel, which PSV is not able to reveal. Hence, the fraction of noisy states projected into the physical sector retains information about the physical dynamics for a longer time. However, considering the

overhead scaling with the number of vertices discussed in Sec. 5.3.2 suggests DPS could hold a practical advantage if mid-circuit measurements are available with sufficient speed and accuracy. Interestingly, the weight of the symmetrized density matrix $\mathrm{Tr}[\Pi_s \rho]$ also does not display appreciable differences between the two- and three-plaquette ladders, see left panel of Fig. 5.5(c).

5.5 Summary and outlook

In this chapter, we have discussed symmetry-verification frameworks modified to work with quantum simulations of non-Abelian lattice gauge theories in noisy devices, where fault-tolerant computation is beyond reach and error mitigation strategies are essential to extract meaningful physical information. The non-commutative nature of the gauge transformations hinders their simultaneous projective measurement and prevents the use of direct ancilla-free post-selection of experimental runs, requiring a novel approach to protect non-Abelian gauge invariance. Focusing on qudit-based architectures, we have discussed two protocols: the first, termed dynamical post-selection (DPS), preserves gauge invariance through frequent mid-circuit measurements of ancillary qudits encoding the local gauge charges. The second, post-processed symmetry verification (PSV), involves estimating group-symmetrized expectation values by measuring correlations between the target observable and Gauss' law operators.

We have applied these methods to the dihedral group D_3, the smallest discrete non-Abelian group, which allows for an exact encoding on current qudit hardware [116]. Both approaches significantly improve the Trotterized time evolution in the presence of noise. As they offer distinct advantages and face different constraints, these two tools neatly complement each other.

DPS is remarkably resilient against noise, and the measurement strategy can be easily adapted to suit specific needs. For instance, the density of mid-circuit measurements can be tuned according to the system studied and the error channel expected on a specific hardware. The only requirement is that the measurement frequency must be above the quantum Zeno threshold for error mitigation in the system; otherwise, the system would enter an unprotected regime with random dynamics jumping between different gauge sectors, as discussed in Chapter 4. The two-qudit gates used in the DPS circuit also contribute with an additional error rate. Nevertheless, as long as the number of additional two-qudit gates is sufficiently smaller than the ones already required for the Hamiltonian time evolution, this does not constitute a decisive limiting factor. On a qudit-based architecture, one needs $6(|\mathcal{G}| - 1)$ control-permutations per Trotter step per plaquette, using the strategy sketched in Fig. 5.1. In contrast, checking one local symmetry $\Theta_{g,v}$ requires $4(|\mathcal{G}| - n_g)$ control-permutations, where n_g is the number of states that transform trivially under the group element g. For the two-plaquette system considered above, this leads to 60 control-permutations for each Trotter step and 8 (10) for a reflection

(rotation) symmetry check[2]. This advantage shows a promising window of opportunity for future experimental studies on qudit-based hardware during the NISQ era. Moreover, the resource requirements can be mitigated by choosing an optimal subset of group elements for the symmetry measurements: gauge violations on a single vertex v can be fully suppressed by monitoring only a suitably chosen generating set of $\mathcal{G}$, such as the symmetries parametrized by the rotation r and the reflection s.

Conversely, the circuit depth for PSV increases at most by a basis rotation above the "bare" time evolution in order to measure the correlators between the desired observables and symmetry transformation operators. Instead of explicitly measuring all of these individually, a significant reduction of required measurements can be achieved by groupings of commensurable operators and sampling strategies. Moreover, one can restrict the projector to enforce only a local subset of the symmetries. Further, PSV retains the entire ensemble of shots taken, unlike direct post-selection procedures, and therefore does not alter the error channel acting on the circuits; it may thus be readily combined with other error mitigation methods explicitly depending on information about the present error channel.

These results pave the way for experimental investigations of non-Abelian LGTs on qudit-based hardware, where both DPS and PSV can be implemented with resources compatible with near-term devices. Demonstrating their effectiveness on real hardware would represent a concrete step towards reliable quantum simulations of gauge theories beyond the Abelian case, and more broadly towards bridging the gap between current NISQ devices and the fault-tolerant era.

[2]These numbers reflect the fact that each vertex has only three links in our geometry and the trivial subspace for the vertical links has dimension 4 for both reflection and rotations, see Section 5.2.2.

Chapter 6

Conclusions and Outlook

In this thesis, we showed how dihedral lattice gauge theories offer a rich and promising setup for quantum simulations of discrete non-Abelian lattice gauge theories. After introducing the concepts of quantum simulation of LGTs, the structure of dihedral groups, and the framework of LGT simulations on qudit hardware, we studied physical phenomena of dihedral LGTs in Part I, and we explored possible error mitigation protocols for their actual quantum implementation on qudits in Part II.

To start the analysis of the physical phenomena, we characterized the structure of gauge sectors in D_N LGTs, showing that their dimension is dramatically smaller than the dimension of the total Hilbert space. As a consequence, studying physics that requires exact diagonalization of the full Hamiltonian becomes quickly intractable with the system size. This motivates the introduction of the ladder geometry, which allows for a gauge-fixing procedure that reduces the degrees of freedom, such that every state in the gauge-fixed model is gauge-invariant. Yet, the ladder geometry represents the minimal setup to study the interplay between the electric and the magnetic field. We formulated the gauge-fixed model for the gauge group D_3, proceeding with the study of the crossover between electric- and magnetic-dominated regimes. We found that, on a ladder, there is a smooth crossover between the two regimes rather than the sharp phase transition expected in the two-dimensional model. On the same system, we computed quantities related to quantum resources, such as the Generalized Geometric Measure and the Stabilizer Rényi Entropy, finding that the latter is peaked in the region of the crossover. Furthermore, we reformulated the model, introducing a term to resolve the conjugacy-class degeneracies in the magnetic term. This reformulation allowed the study of the integrability of the system, a fundamental step toward the analysis of the Eigenstate Thermalization Hypothesis for a discrete non-Abelian LGT. In particular, we showed that the reformulated theory presents a nearest-neighbor level spacing distribution that fits with a Wigner-Dyson distribution, a hallmark of non-integrable quantum systems.

Maintaining the same ladder geometry, we addressed the phenomenon of string breaking in pure-gauge D_N theories in the presence of static charges. Here, the

algebraic distinction between even and odd N—the presence or absence of a non-trivial $\mathbb{Z}_2$ center—translates into qualitatively different physics, directly affecting the Clebsch–Gordan coefficients. For D_N with N odd, the screening fusion rule allows the formation of gluelumps, charge–glueball bound states that are gauge invariant by virtue of the fusion rules. For D_N with N even, the non-trivial $\mathbb{Z}_2$ center forbids this screening mechanism, and the ground state in the strong coupling regime always consists of the shortest flux-string connecting the charges. We verified this prediction through large-scale DMRG simulations of D_3 and D_4 ladders in the rishon formalism, which enforces the non-Abelian Gauss laws site by site. Our numerics confirm the gluelump picture for D_3, with a string tension that signals a string-breaking mechanism and a rescaling analysis that proves the persistence of the gluelumps in the continuous limit.

We turned then to the problem of mitigating and correcting gauge-breaking errors in the quantum simulation of lattice gauge theories. With the goal of performing a reliable real-time evolution of LGTs, we introduced a dynamical post-selection (DPS) protocol, in which the local gauge charges are measured on auxiliary registers during, rather than at the end of, the Trotterized time evolution. Framing this protocol within the spectral theory of Liouvillian superoperators, we demonstrated that gauge protection does not emerge continuously with the measurement rate γ, but rather sharply, as a quantum Zeno transition at $\gamma \simeq \lambda$, where λ is the gauge-breaking error strength. Above the transition, the dynamics stabilize a manifold of dark states characterized by a well-defined configuration of local gauge charges, while below it the system rapidly thermalizes to an infinite-temperature ensemble. We compared in detail the stroboscopic unraveling realized by the DPS with the continuous measurement unraveling relevant for analog simulations, showing that—despite sharing the same Lindbladian at the level of the ensemble average—the two protocols produce markedly different individual trajectory distributions, with the digital one allowing a clean separation between protected and gauge-violating trajectories that is unavailable in the analog case. We also quantified the robustness of the Zeno protection to imperfect measurements, showing that an optimal finite window of measurement frequencies still persists. We tested the generality of the mechanism on $\mathbb{Z}_2$, $\mathbb{Z}_3$, and truncated $U(1)$ gauge symmetries.
Furthermore, we discussed an active error-correction layer that, exploiting the measurement record, can compensate for incoherent bit-flip errors on top of the passive Zeno protection against coherent drift, achieving good agreement with the exact dynamics in the presence of both coherent and incoherent errors.

Finally, we extended this analysis to the genuinely non-Abelian setting, where standard post-selection loses most of its effectiveness because transformations associated with different group elements do not commute and cannot be diagonalized simultaneously. We tested the DPS protocol and an alternative post-processed symmetry verification (PSV) scheme on a two-plaquette D_3 model with periodic boundary conditions, small enough to be encoded in a handful of state-of-the-art qudit registers yet large enough to exhibit non-trivial dynamics. Our numerical

benchmarks show that DPS delivers a tangible improvement in the reconstructed dynamics already on this minimal setup, while PSV provides an alternative strategy when mid-circuit measurements are not available or prohibitively noisy. We also explored how these ideas scale by studying gauge protection on a three-plaquette geometry, finding no important differences. These results establish DPS and PSV as concrete, near-term-feasible tools for the experimental verification of local non-Abelian symmetries on qudit hardware, and provide a quantitative basis for the design of future experiments.

We now turn to the possible outlooks based on the results discussed in this thesis. As regards the thermalization of non-Abelian lattice gauge theories, the gauge-fixed D_3 ladder represents a minimal but non-trivial setting in which the Eigenstate Thermalization Hypothesis can be tested in discrete non-Abelian lattice gauge theories. This direction has already been explored in a master's thesis that we co-supervised [228], whose results constitute a first step toward a systematic analysis of thermalization in discrete non-Abelian lattice gauge theories. Further, preliminary results show the presence of quantum many-body scars [351–354], a feature that has also been explored in other lattice gauge theories [88, 355–359]. Quantum scar states are accessible in quantum simulators [87, 360–362], and they are at the basis of recent proposals [363–365], as well as of real hardware applications [366–368]. A possible proposal could be to use quantum scars as a benchmark in quantum simulation of real-time evolution, one of the goals in the study of lattice gauge theories. Initializing the real-time evolution as a superposition of two quantum scar states, indeed, would force the system to evolve by rotating inside the initial subspace. When the quantum many-body scars belong to different energy levels E_1 and E_0, one expects to see periodic oscillations in the fidelity with the initial state with a period of $T = \frac{2\pi}{\Delta E}$, where $\Delta E = E_1 - E_0$. The preparation of such initial states is particularly favourable: a characteristic feature of quantum many-body scars is precisely their large overlap with simple, separable states, which allows one to approximately prepare them efficiently even on near-term hardware, without the need for complex state-preparation circuits. Furthermore, the scar trajectory provides a natural cross-check against classical simulations: despite residing in the bulk of the many-body spectrum, scar states are low-entanglement configurations whose dynamics can be tracked by tensor-network methods. This classical benchmarking is a valuable consistency check that can validate the quantum simulation before entering regimes where classical methods become prohibitively expensive.

The study of the string-breaking by the gluelump formation opens the exciting perspective of studying the string-breaking dynamics by initializing a flux-string in a D_3 theory, and by applying real-time evolution Tensor Network methods, such as the time-dependent variational principle, TDVP [369, 370], that has been applied in Refs. [371–374]. Another natural outlook would be to study the scattering of these particles by tensor network simulations, as recently shown in [375–378], as well as the competition with the string-breaking mediated by particle production in intermediate- and weak-coupling regimes. The latter would include the necessity of

implementing dynamical matter in tensor networks [190, 372, 379]. On the quantum simulation side, D_3 offers the exciting possibility of studying string-breaking in the smallest and simplest non-Abelian group without the introduction of dynamical matter, making it the minimal setup for the quantum simulation of non-Abelian string-breaking.

While more reliable quantum devices are still being developed, dihedral LGTs can still be interesting and useful in the near-term platforms, especially when coupled with qudit devices. D_N lattice gauge theories can fit in state-of-the-art qudits thanks to their manageable dimension. In contrast to the crystal-like subgroups of $SU(2)$, which are limited to Q_8, $\mathbb{BT}$, $\mathbb{BO}$, $\mathbb{BI}$ with cardinality, respectively, of 8, 24, 48, 120, D_N can be fine-tuned to every even dimensionality (holding $|D_N| = 2N$), making it a comfortable testbed for qudits with an arbitrary number of internal levels. The simple structure $D_N \cong \mathbb{Z}_N \rtimes \mathbb{Z}_2$ makes it possible to encode D_N group elements on a mixed-dimensional register composed of a qudit with $d = N$ levels and a qubit. As a consequence, D_3 group elements are not only implementable in the current generation of qudits with $d \geq 6$ levels [116, 120], but also in platforms that allow the use of qutrits, as shown in Ref. [224], where the authors used one qubit and one logical qutrit to encode D_3.

An experimental real-time simulation of the electric-magnetic interplay in a pure-gauge non-Abelian model would represent a significant milestone on the path toward quantum-simulating QCD-like dynamics. In the current generation of quantum hardware, implementing error mitigation techniques is still necessary. At the same time, the DPS protocol we studied for D_3 requires too many resources for hardware in which mid-circuit readout remains costly [147]. A minimal experiment implementing the two-plaquette system studied in Chapter 5 could perform a few Trotter steps and then proceed with the measurement of the gauge charges α_{r,n_1}, α_{r,n_2}, α_{s,n_1}, α_{s,n_2} on auxiliary qudits at the end of the simulation only. If all of them are equal to 1, then the system is in the neutral gauge sector, and the measurement of a physical observable is then meaningful. The result would correspond to the ones we computed for the effective projection that we tested, the PSV. Hence, at the price of giving up the Zeno protection, non-trivial error mitigation would still be doable in current devices.

A question that naturally arises at the end of this discussion is whether quantum simulation of lattice gauge theories can be expected to achieve a genuine quantum advantage over classical methods. Intriguingly, this remains an open question. What the past decade has made increasingly clear is that quantum and classical simulation approaches are not isolated from one another, but in dialogue: quantum simulation proposals set new targets that stimulate the development of more powerful classical algorithms, while classical benchmarks validate quantum hardware and identify the regimes where it might eventually surpass them. Tensor network methods, in particular, have benefited enormously from this shared journey, pushing the boundaries of what is classically tractable precisely in response to the challenge posed by quantum simulators. In this light, even a scenario in which the pursuit of quantum advantage

ultimately leads to better classical algorithms should be counted as a success. The goal, after all, is to understand the physics of strongly coupled gauge theories—and a deeper understanding reached by any means is equally valuable.

While awaiting further developments in the interplay we have just described, we hope that the results presented in this thesis can contribute to identifying minimal, physically meaningful models for testing the reliability of near-term quantum hardware on the long road toward quantum simulation of non-Abelian lattice gauge theories.

Appendix A

Gauge transformations, static charges, and fusion rules

This appendix provides the representation-theoretic underpinning of the string-breaking analysis presented in Chapter 3. The goal is to show that the structure of gauge-invariant physical states at the corners of the ladder—in the presence of static charges—is entirely constrained by the Clebsch—Gordan coefficients of the gauge group. We derive the fusion rule that the link representations meeting at a corner vertex must satisfy in order for the resulting state to be gauge invariant, directly establishing the conditions under which gluelump formation is algebraically allowed.

The decomposition in Eq. (3.6) of general representations into irreducible representations has direct implications in the description of the ladder in the presence of static charges at its corners. Let us consider the case of the top left corner in Fig. 3.2(a) of the main text (the static charge at the opposite corner has an analogous behavior). In the presence of a static charge τ, there is a multiplet of physical states $|\Psi_{\text{phys},m}\rangle$ ($m = 1, \dots, \dim(\tau)$) transforming as the τ irreducible representation under the local gauge transformation Θ_{h,v_τ}, where v_τ labels the top left corner,

$$\theta^R_{h,r}\theta^L_{h,l}\,|\Psi_{\text{phys},m}\rangle = \sum_n D^\tau_{n,m}(h)\,|\Psi_{\text{phys},n}\rangle\ , \tag{A.1}$$

where r labels the first rung, l is the first link in the upper leg, and $D^\tau_{n,m}(h)$ is the 2×2 matrix that represents the group element h in the fundamental representation τ. To describe $|\Psi_{\text{phys},m}\rangle$, we consider explicitly its decomposition in terms of the states $|j_i, m_i, n_i\rangle$ of the links $i = r$ and $i = l$ and the state $|\tau, m\rangle$ of the static charge:

$$|\Psi_{\text{phys},m}\rangle = \sum_{j_r,j_l,n_r,m_l} A^{j_r,j_l}_{n_r,n_l}\,|j_r, m_r, n_r\rangle\,|j_l, m_l, n_l\rangle\,|\tau, m\rangle\ . \tag{A.2}$$

The left hand side of Eq. (A.1) becomes equivalent to:

$$\theta^R_{h,r}\theta^L_{h,l} \sum_{j_r,j_l,n_r,m_l} A^{j_r,j_l}_{n_r,n_l} \left|j_r, m_r, n_r\right\rangle \left|j_l, m_l, n_l\right\rangle \left|\tau, m\right\rangle = \tag{A.3}$$

$$\sum_{j_r,j_l,n_r,m_l} A^{j_r,j_l}_{n_r,m_l} D^{j_r}_{n'_r,n_r}(h^{-1}) D^{j_l}_{m_l,m'_l}(h) \times \left|j_r, m_r, n'_r\right\rangle \left|j_l, m'_l, n_l\right\rangle \left|\tau, m\right\rangle \ . \tag{A.4}$$

Based on the Clebsch–Gordan series relation [380],

$$D^{j_r}_{n'_r,n_r}(h^{-1}) D^{\tau}_{m',m}(h^{-1}) = \sum_{I,n,n'} \langle j_r n'_r \tau m' | I n' \rangle \langle I n | j_r n_r \tau m \rangle D^{I}_{n'n}(h^{-1}) \ , \tag{A.5}$$

Eq. (A.3) is equivalent to the right-hand side of Eq. (A.1) only if the coefficients A are of the form [95]

$$A^{j_r,j_l}_{n_r,n_l} = \alpha(j_r, j_l) \left\langle j_r n_r \tau m | j_l m_l \right\rangle \ , \tag{A.6}$$

where α depends on the irreducible representations j_l, j_r only and $\langle j_r n_r \tau m | j_l m_l \rangle$ is the conjugate of a Clebsch–Gordan coefficient. The previous equation states that the ingoing representations j_r and τ must fuse into j_l, such that

$$\tau \otimes j_r \ni j_l \ . \tag{A.7}$$

To realize the gluelump state, it is necessary that both links are in the same irreducible representation and combine with the charge into a group singlet, which is verified for $j_r = j_l = \tilde{\tau}$ and results in Eq. (3.8). An analogous construction holds when we consider a vertex with three links in the bulk of the ladder. In this case, τ is replaced by the irreducible representation characterizing the states of the additional link (see the construction for 2D lattices in Ref. [95]).

To summarize, these results are the algebraic backbone of the screening fusion rule in Chapter 3: the condition Eq. (A.7), and the specific gluelump constraint $j_r = j_l = \tilde{\tau}$, directly determine whether static charges can be screened by gluelumps. As shown in Chapter 3, this is possible for D_N with N odd—where the trivial center permits the necessary Clebsch-–Gordan coupling—but forbidden for N even, explaining the qualitatively different string-breaking physics of D_3 and D_4.

Appendix B

Fermionic parity of the rishons

This appendix addresses a subtle but important aspect of the rishon formalism introduced in Sec. 3.4: whether the rishon operators can be consistently endowed with fermionic statistics when dynamical matter is present.

One important consequence of the trivial center in the $D_{N_{\text{odd}}}$ case is that the gauge group does not preserve local $\mathbb{Z}_2$ parity. The implication of this is that, when coupled to fermionic matter, the $D_{N_{\text{odd}}}$ lattice gauge theory cannot be defermionized, i.e., it can not be mapped onto a local Hamiltonian without fermionic degrees of freedom independently of the dimensionality. Instead, in $D_{N_{\text{even}}}$, the rishons are fermions and they can be combined with fermionic matter to form singlets, which behave as an effective bosonic particle.

Here, we illustrate this general property of dihedral groups on the example of D_3 and D_4—the latter having a $\mathbb{Z}_2$ center, while the former does not. In the $D_{N_{\text{even}}}$ case, the parity operator on a semilink is defined as

$$P = \begin{pmatrix} 1 & & & \\ & 1 & & \\ & & \ddots & \\ & & & -\mathbb{1}_2 \end{pmatrix} . \tag{B.1}$$

D_N only has one- and two-dimensional representations. The former ones carry even parity and the latter ones odd parity.

Similar to what we did above for D_3, from Fig. 3.3 it is possible to count the number of different rishon modes, counting the number of arrows, to reconstruct the

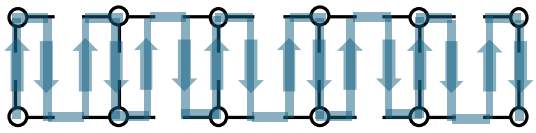

Figure B.1: Sketch of the ladder geometry. The shaded path indicates the order in which we define the fermionic rishon parity.

parallel transporter for D_4. A possible choice for the four rishon operators is

$$\zeta_a^{(1)} = 2^{-\frac{1}{4}} \left(\begin{array}{c|c|c|c|cc} 0 & & & & \delta_{ar} & \delta_{ag} \\ \hline & 0 & & & & \\ \hline & & 0 & & & \\ \hline & & & 0 & & \\ \hline \delta_{ag} & & & & 0 & \\ \delta_{ar} & & & & & 0 \end{array}\right),$$

$$\zeta_a^{(2)} = 2^{-\frac{1}{4}} \left(\begin{array}{c|c|c|c|cc} 0 & & & & & \\ \hline & 0 & & & \delta_{ar} & -\delta_{ag} \\ \hline & & 0 & & & \\ \hline & & & 0 & & \\ \hline & \delta_{ag} & & & 0 & \\ & -\delta_{ar} & & & & 0 \end{array}\right),$$

$$\zeta_a^{(3)} = 2^{-\frac{1}{4}} \left(\begin{array}{c|c|c|c|cc} 0 & & & & & \\ \hline & 0 & & & & \\ \hline & & 0 & & \delta_{ag} & -\delta_{ar} \\ \hline & & & 0 & & \\ \hline & & \delta_{ar} & & 0 & \\ & & -\delta_{ag} & & & 0 \end{array}\right),$$

$$\zeta_a^{(4)} = 2^{-\frac{1}{4}} \left(\begin{array}{c|c|c|c|cc} 0 & & & & & \\ \hline & 0 & & & & \\ \hline & & 0 & & & \\ \hline & & & 0 & \delta_{ag} & \delta_{ar} \\ \hline & & & \delta_{ar} & 0 & \\ & & & \delta_{ag} & & 0 \end{array}\right). \tag{B.2}$$

The rishons formulated in Eq. (B.2) for the D_4 theory anti-commute with P on the same semilink and commute on different semilinks. Therefore, one can define fermionic rishon operators by attaching a Jordan–Wigner-like parity string to the local rishon operators,

$$\zeta^{(i)}_{F;a;\mathbf{n},\mu} = \left(\bigotimes_{(\mathbf{n}',\mu')\in \mathrm{path}} P_{\mathbf{n}',\mu'} \right) \otimes \tilde{\zeta}^{(i)}_{a;\mathbf{n},\mu} \otimes \mathbb{1} \ , \tag{B.3}$$

where we denoted

$$\tilde{\zeta}^{(i)}_{a;\mathbf{n},\mu} = \begin{cases} \zeta^{(i)}_{a;\mathbf{n},\mu} P_{\mathbf{n},\mu} \ , & \text{on left semilinks,} \\ \zeta^{(i)}_{a;\mathbf{n},\mu} \ , & \text{on right semilinks.} \end{cases} \tag{B.4}$$

$$\tag{B.5}$$

In Eq. (B.3), the path, as illustrated in Fig. B.1, is a particular choice of ordering the semilinks on the lattice. The rishons defined as in Eq. (B.3) anti-commute on

different semilinks,

$$\{\tilde{\zeta}^{(i)}_{F,a;\mathbf{n},\mu}, \tilde{\zeta}^{(i)}_{F,a;\mathbf{n}',\mu'}\} = 0 \text{ for } (\mathbf{n},\mu) \neq (\mathbf{n}',\mu')\,, \tag{B.6}$$

and therefore are indeed of fermionic nature. The local rishon operators can simply be replaced by the fermionic ones in the expression for the link operator (Eq. (3.20)):

$$U_{ab;\mathbf{n},\mathbf{n}+\mathbf{e}_\mu} = \sum_i \zeta^{(i)}_{F,a;\mathbf{n},\mu} \zeta^{(i)\dagger}_{F,\bar{b};\mathbf{n}+\mathbf{e}_\mu,-\mu}\,. \tag{B.7}$$

In the presence of dynamical matter fermions, the hopping term in the rishon formulation becomes

$$\begin{aligned} &\psi^\dagger_{a,\mathbf{n}} U_{ab;\mathbf{n},\mathbf{n}+\mathbf{e}_\mu} \psi_{b,\mathbf{n}+\mathbf{e}_\mu} + \text{h.c.} \\ &= \sum_i \psi^\dagger_{a,\mathbf{n}} \zeta^{(i)}_{F,a;\mathbf{n},\mu} \zeta^{(i)\dagger}_{F,\bar{b};\mathbf{n}+\mathbf{e}_\mu,-\mu} \psi_{b,\mathbf{n}+\mathbf{e}_\mu} + \text{H.c.} \end{aligned} \tag{B.8}$$

The right-hand side of the expression above is a product of operators that commute with the fermionic parity on each dressed site and, therefore, can be defermionized.

In the case of the $D_{N_{\text{odd}}}$ gauge theory, the screening fusion rule prevents us from assigning odd parity to the fundamental representation. Regardless of whether we assign even or odd parity to the anti-fundamental representation $\tilde{\tau}$, the product on the left-hand side of Eq. (3.8) is of even parity. Then, the only possibility for the fundamental representation is to be of even parity, rendering some rishons in the decomposition of Eq. (3.20) to be bosonic operators. Therefore, no full defermionization as in the D_4 (or, in general, the $D_{N_{\text{even}}}$) case is possible.

Summarizing, this result has direct consequences for future extensions of the DMRG simulations of Chapter 3 to theories with dynamical matter. For $D_{N_{\text{even}}}$ gauge theories, the full fermionic rishon construction allows for the defermionization, making tensor network methods directly applicable at reduced computational cost. For $D_{N_{\text{odd}}}$ theories such as D_3, the absence of a consistent fermionic assignment means that dynamical matter cannot be incorporated via standard defermionization, as shown in [133], and alternative strategies—such as the use of $\mathbb{Z}_2$ graded tensor networks—would be required.

Appendix C

Lindblad calculation and continuous measurement of local charges

This appendix provides the formal derivation underlying the Lindblad framework used in Chapter 4 to describe and analyse the DPS protocol. Starting from the discrete measurement process introduced in Sec. 4.1, we derive the effective Lindblad master equation governing the ensemble-averaged density matrix, showing how the periodic measurement of local gauge charges maps onto a set of jump operators acting on the system. In the second part, the Sec. C.1, we extend the analysis to the continuous measurement limit, which is the relevant regime for analog quantum simulators, and study the suppression of gauge violations at the level of individual quantum trajectories.

A convenient workaround is to split the time step associated with the measurement frequency Δt in smaller intervals $\Delta t = N_{\text{step}} \mathrm{d}t$ and assume that quantum jumps occur randomly in such finer steps with a probability $\mathrm{d}t/\Delta t$. Hence, Δt becomes the average time in which N charges are measured.

Let us momentarily neglect the unitary evolution; given a state $|\psi(t)\rangle$ of the system at a given time t, the measurement of a local charge G_n leads to

$$|\psi(t+\mathrm{d}t)\rangle = \begin{cases} \frac{P_n^+ |\psi(t)\rangle}{\sqrt{\langle\psi(t)|P_n^+|\psi(t)\rangle}} \text{ with } p_n^+ = \frac{1+\langle G_n\rangle}{2} \,, \\ \frac{P_n^- |\psi(t)\rangle}{\sqrt{\langle\psi(t)|P_n^-|\psi(t)\rangle}} \text{ with } p_n^- = \frac{1-\langle G_n\rangle}{2} \,, \end{cases} \tag{C.1}$$

where, according to the Born rule, $p_n^\pm = \langle\psi(t)| P_n^\pm |\psi(t)\rangle$ is the probability of projecting on either one of the symmetry sectors and $P_n^\pm = \frac{1\pm G_n}{2}$ the corresponding projection operator. The denominators ensure the normalization of the state after a measurement and the expectation values are taken over the state $|\psi(t)\rangle$ [1]. Using

[1] We note that the protocol (C.1) defines a POVM since $\left(P_n^+\right)^\dagger P_n^+ + \left(P_n^-\right)^\dagger P_n^- = 1$ and $p_n^+ + p_n^- =$

Eq. (C.1) and taking into account the probability $\mathrm{d}t/\Delta t$ that a measurement occurs in the interval $\mathrm{d}t$, we can write the evolution of the system density matrix $\rho(t)$ as

$$\begin{aligned}\rho(t+\mathrm{d}t) &= \frac{\mathrm{d}t}{\Delta t}\left[P_n^+\rho(t)P_n^+ + P_n^-\rho(t)P_n^-\right] + \left(1-\frac{\mathrm{d}t}{\Delta t}\right)\rho(t) \\ &= \frac{\mathrm{d}t}{\Delta t}\left[2P_n^+\rho(t)P_n^+ - \{P_n^+,\rho(t)\}\right] - \rho(t)\ , \end{aligned} \tag{C.2}$$

where we used $P_n^- = 1 - P_n^+$. We can now expand at first order $\rho(t+\mathrm{d}t) \simeq \rho(t) + \mathrm{d}t\dot{\rho}(t)$ to derive an effective master equation of the density matrix,

$$\dot{\rho}(t) \simeq \frac{1}{2\Delta t}\left[G_n\rho(t)G_n^\dagger - \frac{1}{2}\{G_n^\dagger G_n,\rho(t)\}\right]\ , \tag{C.3}$$

where we explicitly use the local charge G_n instead of the associated projector. A further simplification for the $\mathbb{Z}_2$ gauge group follows from $G_n^\dagger = G_n$ and $G_n^\dagger G_n = G_n^2 = \mathbb{1}$, but the functional form of Eq. (C.3) makes it clearer that it corresponds to the contribution of a jump operator G_n to a Lindblad master equation. Inserting the unitary part and summing over all local charges, we finally get

$$\dot{\rho} = i[\rho,H] + \frac{1}{2\Delta t}\sum_n\left[G_n\rho G_n^\dagger - \frac{1}{2}\{G_n^\dagger G_n,\rho\}\right]\ , \tag{C.4}$$

which is the Lindblad equation describing the evolution of the density matrix associated with the ensemble average of the stochastic trajectories originated by the measurement process.

C.1 Continuous measurement of local charges

In the following, we give more details on how continuous measurements of the local charges can suppress the gauge violation induced by H_{err} in analog quantum simulations. Our starting point is the Lindblad equation studied in Ref. [294]. In that work, it was shown that adding dephasing terms proportional to the Gauss' law generators leads to a suppression of the gauge-breaking error that scales as $1/\gamma$, where γ is the effective rate determining the strength of the incoherent part of the dynamics. The full Lindblad equation is given by

$$\dot{\rho} = i[\rho,H_0+H_{\mathrm{err}}] + \gamma\sum_n G_n\rho G_n^\dagger - \frac{1}{2}\{G_n^\dagger G_n,\rho\}\ . \tag{C.5}$$

Equation (C.5) describes a "mean" evolution of the density matrix, i.e., it represents an ensemble average over (infinitely) many realizations of the time evolution of the system coupled to some environment through the Lindblad (jump) operators

1. In the expressions for the probabilities and normalizations we also exploited that $\left(P_n^\pm\right)^\dagger P_n^\pm = \left(P_n^\pm\right)^2 = P_n^\pm$

G_n with a common effective rate γ. Hence, a direct solution of Eq. (C.5) only describes the evolution of the expectation values of the observables over a statistical ensemble while it tells us nothing about what happens at individual trajectories of the quantum system or, in other words, at a single experimental realization of such a protocol. In particular, a question we address is whether the gauge violation is suppressed by the action of the jump operators in each simulation or if it emerges only after averaging over many trajectories.

To study the evolution of states, instead of density matrices, under open dynamics, a possibility is to *unravel* the Lindblad equation in quantum trajectories. The first step is to incorporate the second term of the incoherent contribution into an effective non-Hermitian Hamiltonian

$$H_{\text{eff}} = H - \frac{i\gamma}{2} \sum_n G_n^\dagger G_n \ . \tag{C.6}$$

The non-Hermitian part of the effective Hamiltonian causes an effective reduction of the norm of the wavefunction $|\psi(t)\rangle$; at first order in a time step dt, we have that

$$\begin{aligned} \langle \psi(t+\delta t)| \psi(t+\delta t)\rangle &\simeq 1 - \delta t \gamma \sum_n \langle \psi(t)| G_n^\dagger G_n |\psi(t)\rangle \\ &= 1 - \delta p \ , \end{aligned} \tag{C.7}$$

where δt must be chosen such that $\delta p \ll 1$. The latter is then interpreted as the probability that the state undergoes a quantum jump described by

$$|\psi(t+\delta t)\rangle = G_n |\psi(t)\rangle \, / \sqrt{\gamma \langle \psi(t)| G_n^\dagger G_n |\psi(t)\rangle} \ . \tag{C.8}$$

The denominator is used to keep the normalization of the wavefunction. This approach gives rise to stochastic dynamics in which the jump operators, in this case the generators of the local $\mathbb{Z}_2$ symmetry, act at a random time with a probability proportional to their norm and the rate γ on top of a deterministic nonunitary dynamics determined by the Hamiltonian in Eq. (4.12).

Notice that due to the specific form of the jump operators $G_n^\dagger G_n = \mathbb{1}$, the non-Hermitian contribution to the Hamiltonian reduces to a trivial decrease of the state norm $\propto N\delta t\gamma$. Their action in Eq. (C.8), instead, acts trivially only if $|\psi(t)\rangle$ is an eigenstate of G_n; thus, when the jump operators are repeatedly applied to $|\psi(t)\rangle$, they induce dephasing between states belonging to different gauge sectors. This, in turn, suppresses the speed of the population transfer between them caused by the action of H_{err}.

We now focus on the dynamics of individual quantum trajectories, which has not been analyzed previously in the context of dissipative gauge protection. To this end, we consider a chain of $N = 9$ matter sites with OBC ($L = 17$ spins in total) prepared with a single matter defect in the central site $n = 4$. The system is evolved with the Hamiltonian in the deconfined phase ($f = 0.5J$, $M = 0$) and with a coherent error strength $\lambda = 0.3J$. To investigate the error protection effectiveness, we analyze in

Fig. C.1 the evolution of the gauge violation δg [defined in Eq. (4.9)]. We show both the deterministic dynamics affected by the coherent error and the result of the continuous measurement protocol. For the latter, the average over 50 trajectories is plotted as a thick dashed line while individual stochastic dynamics are the fainter ones.

Large measurement rates provide an effective error suppression, although a drift outside the target sector deteriorates the quality of the simulation, requiring a higher measurement rate for reliably reaching a longer total evolution time. The trajectory spread also increases in time, although the data for the weakest rate ($\gamma = \lambda$) suggest that it saturates as soon as equilibrium is approached. Since the steady state of Eq. (C.5) is the infinite-temperature density matrix, irrespective of the rate γ, equilibrium is always characterized by an average gauge violation of $1/2$.

Despite the coherent error of $\lambda = 0.3J$ being rather strong, the dynamics of the gauge violation is entirely dominated by the jump processes. Indeed, if the coherent error alone is active, without gauge protection, a fast gauge violation is generated that then oscillates around an average value dependent on λ. In contrast, gauge protection via measuring the local charges causes a monotonous increase in the average violation. Only at the level of individual trajectories, do some oscillations survive but without any resemblance to the coherent dynamics. In the Zeno regime ($\gamma > \lambda$), the steady increase of the gauge violation happens on a time scale set by the measurement rate γ, consistently with the behavior of the Liouvillian eigenvalues shown in Fig. 4.3. Indeed, if we rescale time as $t \to t\frac{\lambda}{\gamma}$, the curves describing the average gauge violation for different γ in time perfectly collapse on top of each other, as we report in panel (b) of Fig. C.1. A slight violation can be discerned only for the smallest γ considered. When $\gamma < \lambda$, instead, the relaxation rate increases with γ, as seen from the Liouvillian eigenvalues, leading to a fast equilibration to an infinite temperature state characterized by $\langle \delta g \rangle = 0.5$.

To conclude, the Lindblad equation in Eq. (C.4) is the theoretical foundation on which the Zeno transition analysis of Chapter 4 rests: the spectral gap of the associated Liouvillian superoperator, studied in Sec. 4.3.1, directly controls the threshold between the protected and unprotected regimes. The trajectory-level analysis carried out in Sec. C.1 further establishes the comparison between the digital (DPS) and analog (continuous measurement) unravelings in Sec. 4.3.2, showing that—despite sharing the same ensemble-averaged Lindbladian—the two protocols produce qualitatively distinct trajectory distributions, with the digital case allowing a clean separation between gauge-invariant and gauge-violating runs.

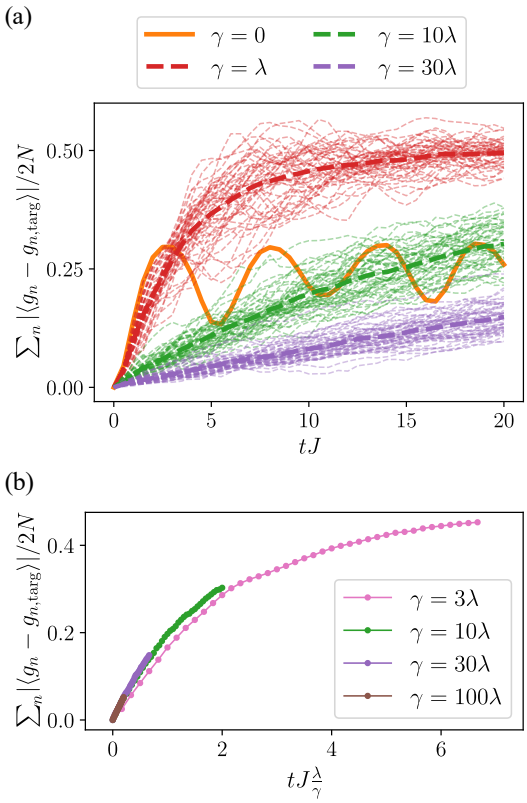

Figure C.1: (a) Evolution of the average violation of the local charges, comparing the coherent error (solid orange line) and the corrected dynamics with different measurement rates (dashed lines). The thick lines represent the average over 50 different trajectories (fainter lines). Individual trajectories remain close to the ensemble average and the gauge violation decreases as $1/\gamma$ in the protected phase ($\gamma > \lambda$). The initial state corresponds to a local charge defect at the center of the chain and the physical parameters are $f = 0.5J$, $M = 0$, and $\lambda = 0.3J$. (b) By plotting the average gauge violation versus the rescaled time $t\lambda/\gamma$, a perfect data collapse is achieved once the system is sufficiently deep in the quantum Zeno regime.

Bibliography

[1] Michael E Peskin. *An Introduction to quantum field theory*. CRC press, 2018 (cit. on p. 1).

[2] John B. Kogut. "An introduction to lattice gauge theory and spin systems". In: *Rev. Mod. Phys.* 51 (4 Oct. 1979), pp. 659–713. DOI: 10.1103/RevModPhys.51.659. URL: https://link.aps.org/doi/10.1103/RevModPhys.51.659 (cit. on p. 1).

[3] Chetan Nayak, Steven H. Simon, Ady Stern, Michael Freedman, and Sankar Das Sarma. "Non-Abelian anyons and topological quantum computation". In: *Rev. Mod. Phys.* 80 (3 Sept. 2008), pp. 1083–1159. DOI: 10.1103/RevModPhys.80.1083. URL: https://link.aps.org/doi/10.1103/RevModPhys.80.1083 (cit. on pp. 1, 16).

[4] Kenneth G. Wilson. "Confinement of quarks". In: *Phys. Rev. D* 10 (8 Oct. 1974), pp. 2445–2459. DOI: 10.1103/PhysRevD.10.2445. URL: https://link.aps.org/doi/10.1103/PhysRevD.10.2445 (cit. on p. 1).

[5] John Kogut and Leonard Susskind. "Hamiltonian formulation of Wilson's lattice gauge theories". In: *Phys. Rev. D* 11 (2 Jan. 1975), pp. 395–408. DOI: 10.1103/PhysRevD.11.395. URL: https://link.aps.org/doi/10.1103/PhysRevD.11.395 (cit. on pp. 1, 7, 12).

[6] A.M. Polyakov. "Quark confinement and topology of gauge theories". In: *Nuclear Physics B* 120.3 (1977), pp. 429–458. ISSN: 0550-3213. DOI: https://doi.org/10.1016/0550-3213(77)90086-4. URL: https://www.sciencedirect.com/science/article/pii/0550321377900864 (cit. on p. 1).

[7] Christof Gattringer and Christian B. Lang. *Quantum chromodynamics on the lattice*. Vol. 788. Berlin: Springer, 2010. ISBN: 978-3-642-01849-7, 978-3-642-01850-3. DOI: 10.1007/978-3-642-01850-3 (cit. on pp. 1, 12).

[8] N. Brambilla et al. "QCD and strongly coupled gauge theories: challenges and perspectives". In: *The European Physical Journal C* 74.10 (Oct. 21, 2014), p. 2981. ISSN: 1434-6052. DOI: 10.1140/epjc/s10052-014-2981-5. URL: https://doi.org/10.1140/epjc/s10052-014-2981-5 (cit. on pp. 1, 12).

[9] Y. Aoki et al. "FLAG review 2024". In: *Phys. Rev. D* 113 (1 Jan. 2026), p. 014508. DOI: 10.1103/nfzp-p5dn. URL: https://link.aps.org/doi/10.1103/nfzp-p5dn (cit. on pp. 1, 12).

[10] Matthias Troyer and Uwe-Jens Wiese. "Computational Complexity and Fundamental Limitations to Fermionic Quantum Monte Carlo Simulations". In: *Phys. Rev. Lett.* 94 (17 May 2005), p. 170201. DOI: 10.1103/PhysRevLett.94.170201. URL: https://link.aps.org/doi/10.1103/PhysRevLett.94.170201 (cit. on pp. 1, 12).

[11] Ettore Vicari and Haralambos Panagopoulos. "θ dependence of SU(N) gauge theories in the presence of a topological term". In: *Physics Reports* 470.3 (2009), pp. 93–150. ISSN: 0370-1573. DOI: https://doi.org/10.1016/j.physrep.2008.10.001. URL: https://www.sciencedirect.com/science/article/pii/S037015730800389X (cit. on p. 1).

[12] Richard P Feynman. "Simulating physics with computers". In: *Feynman and computation*. cRc Press, 2018, pp. 133–153 (cit. on pp. 1, 12).

[13] Erez Zohar, J Ignacio Cirac, and Benni Reznik. "Quantum simulations of lattice gauge theories using ultracold atoms in optical lattices". In: *Reports on Progress in Physics* 79.1 (Dec. 2015), p. 014401. DOI: 10.1088/0034-4885/79/1/014401. URL: https://doi.org/10.1088/0034-4885/79/1/014401 (cit. on pp. 1, 2).

[14] Marcello Dalmonte and Simone Montangero. "Lattice gauge theory simulations in the quantum information era". In: *Contemporary Physics* 57.3 (2016), pp. 388–412. DOI: 10.1080/00107514.2016.1151199. URL: https://doi.org/10.1080/00107514.2016.1151199 (cit. on pp. 1, 2, 12).

[15] Mari Carmen Bañuls et al. "Simulating lattice gauge theories within quantum technologies". In: *The European Physical Journal D* 74.8 (Aug. 2020), p. 165. ISSN: 1434-6079. DOI: 10.1140/epjd/e2020-100571-8. URL: https://doi.org/10.1140/epjd/e2020-100571-8 (cit. on pp. 1, 2, 4, 12).

[16] U.-J. Wiese. "Ultracold quantum gases and lattice systems: quantum simulation of lattice gauge theories". In: *Annalen der Physik* 525.10-11 (2013), pp. 777–796. DOI: https://doi.org/10.1002/andp.201300104. eprint: https://onlinelibrary.wiley.com/doi/pdf/10.1002/andp.201300104. URL: https://onlinelibrary.wiley.com/doi/abs/10.1002/andp.201300104 (cit. on pp. 1, 91, 98).

[17] Philipp Hauke, Fernando M Cucchietti, Luca Tagliacozzo, Ivan Deutsch, and Maciej Lewenstein. "Can one trust quantum simulators?" In: *Reports on Progress in Physics* 75.8 (July 2012), p. 082401. DOI: 10.1088/0034-4885/75/8/082401. URL: https://dx.doi.org/10.1088/0034-4885/75/8/082401 (cit. on p. 1).

[18] Iulia Buluta and Franco Nori. "Quantum Simulators". In: *Science* 326.5949 (2009), pp. 108–111. DOI: 10.1126/science.1177838. eprint: https://www.science.org/doi/pdf/10.1126/science.1177838. URL: https://www.science.org/doi/abs/10.1126/science.1177838 (cit. on p. 1).

[19] J. Ignacio Cirac and Peter Zoller. "Goals and opportunities in quantum simulation". en. In: *Nature Physics* 8.4 (Apr. 2012), pp. 264–266. ISSN: 1745-2481. DOI: 10.1038/nphys2275. URL: https://www.nature.com/articles/nphys2275 (visited on 04/14/2026) (cit. on p. 1).

[20] I. M. Georgescu, S. Ashhab, and Franco Nori. "Quantum simulation". In: *Rev. Mod. Phys.* 86 (1 Mar. 2014), pp. 153–185. DOI: 10.1103/RevModPhys.86.153. URL: https://link.aps.org/doi/10.1103/RevModPhys.86.153 (cit. on p. 1).

[21] Seth Lloyd. "Universal Quantum Simulators". In: *Science* 273.5278 (1996), pp. 1073–1078. DOI: 10.1126/science.273.5278.1073. eprint: https://www.science.org/doi/pdf/10.1126/science.273.5278.1073. URL: https://www.science.org/doi/abs/10.1126/science.273.5278.1073 (cit. on p. 2).

[22] H. F. Trotter. "On the Product of Semi-Groups of Operators". In: *Proceedings of the American Mathematical Society* 10.4 (1959), pp. 545–551. ISSN: 00029939, 10886826. URL: http://www.jstor.org/stable/2033649 (visited on 09/02/2023) (cit. on pp. 2, 13).

[23] M. Suzuki. "Generalized Trotter's Formula and Systematic Approximants of Exponential Operators and Inner Derivations with Applications to Many Body Problems". In: *Commun. Math. Phys.* 51 (1976), pp. 183–190. DOI: 10.1007/BF01609348 (cit. on pp. 2, 13).

[24] J. Q. You and Franco Nori. "Quantum information processing with superconducting qubits in a microwave field". en. In: *Physical Review B* 68.6 (Aug. 2003), p. 064509. ISSN: 0163-1829, 1095-3795. DOI: 10.1103/PhysRevB.68.064509. URL: https://link.aps.org/doi/10.1103/PhysRevB.68.064509 (visited on 04/14/2026) (cit. on p. 2).

[25] Andrew A. Houck, Hakan E. Türeci, and Jens Koch. "On-chip quantum simulation with superconducting circuits". en. In: *Nature Physics* 8.4 (Apr. 2012), pp. 292–299. ISSN: 1745-2481. DOI: 10.1038/nphys2251. URL: https://www.nature.com/articles/nphys2251 (visited on 04/14/2026) (cit. on p. 2).

[26] J. I. Cirac and P. Zoller. "Quantum Computations with Cold Trapped Ions". en. In: *Physical Review Letters* 74.20 (May 1995), pp. 4091–4094. ISSN: 0031-9007, 1079-7114. DOI: 10.1103/PhysRevLett.74.4091. URL: https://link.aps.org/doi/10.1103/PhysRevLett.74.4091 (visited on 04/14/2026) (cit. on p. 2).

[27] R. Blatt and C. F. Roos. “Quantum simulations with trapped ions”. en. In: *Nature Physics* 8.4 (Apr. 2012), pp. 277–284. ISSN: 1745-2481. DOI: 10.1038/nphys2252. URL: https://www.nature.com/articles/nphys2252 (visited on 04/14/2026) (cit. on p. 2).

[28] Bjoern Lekitsch, Sebastian Weidt, Austin G. Fowler, Klaus Mølmer, Simon J. Devitt, Christof Wunderlich, and Winfried K. Hensinger. “Blueprint for a microwave trapped ion quantum computer”. In: *Science Advances* 3.2 (Feb. 2017), e1601540. ISSN: 2375-2548. DOI: 10.1126/sciadv.1601540. URL: https://www.science.org/doi/10.1126/sciadv.1601540 (visited on 04/14/2026) (cit. on p. 2).

[29] J. M. Pino et al. “Demonstration of the trapped-ion quantum CCD computer architecture”. In: *Nature* 592.7853 (Apr. 2021), pp. 209–213. ISSN: 1476-4687. DOI: 10.1038/s41586-021-03318-4. URL: https://doi.org/10.1038/s41586-021-03318-4 (cit. on p. 2).

[30] D. Jaksch and P. Zoller. “The cold atom Hubbard toolbox”. In: *Annals of Physics*. Special Issue 315.1 (Jan. 2005), pp. 52–79. ISSN: 0003-4916. DOI: 10.1016/j.aop.2004.09.010. URL: https://www.sciencedirect.com/science/article/pii/S0003491604001782 (visited on 04/14/2026) (cit. on p. 2).

[31] Immanuel Bloch, Jean Dalibard, and Wilhelm Zwerger. “Many-body physics with ultracold gases”. en. In: *Reviews of Modern Physics* 80.3 (July 2008), pp. 885–964. ISSN: 0034-6861, 1539-0756. DOI: 10.1103/RevModPhys.80.885. URL: https://link.aps.org/doi/10.1103/RevModPhys.80.885 (visited on 04/14/2026) (cit. on p. 2).

[32] Immanuel Bloch, Jean Dalibard, and Sylvain Nascimbène. “Quantum simulations with ultracold quantum gases”. en. In: *Nature Physics* 8.4 (Apr. 2012), pp. 267–276. ISSN: 1745-2481. DOI: 10.1038/nphys2259. URL: https://www.nature.com/articles/nphys2259 (visited on 04/14/2026) (cit. on p. 2).

[33] Antoine Browaeys and Thierry Lahaye. “Many-body physics with individually controlled Rydberg atoms”. en. In: *Nature Physics* 16.2 (Feb. 2020), pp. 132–142. ISSN: 1745-2481. DOI: 10.1038/s41567-019-0733-z. URL: https://www.nature.com/articles/s41567-019-0733-z (visited on 04/14/2026) (cit. on p. 2).

[34] Jeremy L. O’Brien. “Optical Quantum Computing”. en. In: *Science* 318.5856 (Dec. 2007), pp. 1567–1570. ISSN: 0036-8075, 1095-9203. DOI: 10.1126/science.1142892. URL: https://www.science.org/doi/10.1126/science.1142892 (visited on 04/14/2026) (cit. on p. 2).

[35] Alán Aspuru-Guzik and Philip Walther. "Photonic quantum simulators". en. In: *Nature Physics* 8.4 (Apr. 2012), pp. 285–291. ISSN: 1745-2481. DOI: 10.1038/nphys2253. URL: https://www.nature.com/articles/nphys2253 (visited on 04/14/2026) (cit. on p. 2).

[36] Ronald Hanson and David D. Awschalom. "Coherent manipulation of single spins in semiconductors". en. In: *Nature* 453.7198 (June 2008), pp. 1043–1049. ISSN: 1476-4687. DOI: 10.1038/nature07129. URL: https://www.nature.com/articles/nature07129 (visited on 04/14/2026) (cit. on p. 2).

[37] Daniel Loss and David P. DiVincenzo. "Quantum computation with quantum dots". en. In: *Physical Review A* 57.1 (Jan. 1998), pp. 120–126. ISSN: 1050-2947, 1094-1622. DOI: 10.1103/PhysRevA.57.120. URL: https://link.aps.org/doi/10.1103/PhysRevA.57.120 (visited on 04/14/2026) (cit. on p. 2).

[38] Lucas Lamata, Adrian Parra-Rodriguez, Mikel Sanz, and Enrique Solano. "Digital-analog quantum simulations with superconducting circuits". In: *Advances in Physics: X* 3.1 (2018), p. 1457981. DOI: 10.1080/23746149.2018.1457981. URL: https://doi.org/10.1080/23746149.2018.1457981 (cit. on p. 2).

[39] Adrian Parra-Rodriguez, Pavel Lougovski, Lucas Lamata, Enrique Solano, and Mikel Sanz. "Digital-analog quantum computation". In: *Phys. Rev. A* 101 (2 Feb. 2020), p. 022305. DOI: 10.1103/PhysRevA.101.022305. URL: https://link.aps.org/doi/10.1103/PhysRevA.101.022305 (cit. on p. 2).

[40] Zohreh Davoudi, Norbert M. Linke, and Guido Pagano. "Toward simulating quantum field theories with controlled phonon-ion dynamics: A hybrid analog-digital approach". In: *Phys. Rev. Res.* 3 (4 Oct. 2021), p. 043072. DOI: 10.1103/PhysRevResearch.3.043072. URL: https://link.aps.org/doi/10.1103/PhysRevResearch.3.043072 (cit. on p. 2).

[41] Antonio Acín et al. "The quantum technologies roadmap: a European community view". In: *New Journal of Physics* 20.8 (Aug. 2018), p. 080201. DOI: 10.1088/1367-2630/aad1ea. URL: https://doi.org/10.1088/1367-2630/aad1ea (cit. on p. 2).

[42] Ehud Altman et al. "Quantum Simulators: Architectures and Opportunities". In: *PRX Quantum* 2 (1 Feb. 2021), p. 017003. DOI: 10.1103/PRXQuantum.2.017003. URL: https://link.aps.org/doi/10.1103/PRXQuantum.2.017003 (cit. on p. 2).

[43] Frank Arute et al. "Quantum supremacy using a programmable superconducting processor". In: *Nature* 574 (2019), pp. 505–510. DOI: 10.1038/s41586-019-1666-5. arXiv: 1910.11333 [quant-ph] (cit. on p. 2).

[44] Han-Sen Zhong et al. “Quantum computational advantage using photons”. en. In: *Science* 370.6523 (Dec. 2020), pp. 1460–1463. ISSN: 0036-8075, 1095-9203. DOI: 10.1126/science.abe8770. URL: https://www.science.org/doi/10.1126/science.abe8770 (visited on 04/14/2026) (cit. on p. 2).

[45] Yulin Wu et al. “Strong Quantum Computational Advantage Using a Superconducting Quantum Processor”. en. In: *Physical Review Letters* 127.18 (Oct. 2021), p. 180501. ISSN: 0031-9007, 1079-7114. DOI: 10.1103/PhysRevLett.127.180501. URL: https://link.aps.org/doi/10.1103/PhysRevLett.127.180501 (visited on 04/14/2026) (cit. on p. 2).

[46] Han-Sen Zhong et al. “Phase-Programmable Gaussian Boson Sampling Using Stimulated Squeezed Light”. en. In: *Physical Review Letters* 127.18 (Oct. 2021), p. 180502. ISSN: 0031-9007, 1079-7114. DOI: 10.1103/PhysRevLett.127.180502. URL: https://link.aps.org/doi/10.1103/PhysRevLett.127.180502 (visited on 04/14/2026) (cit. on p. 2).

[47] Lars S. Madsen et al. “Quantum computational advantage with a programmable photonic processor”. en. In: *Nature* 606.7912 (June 2022), pp. 75–81. ISSN: 1476-4687. DOI: 10.1038/s41586-022-04725-x. URL: https://www.nature.com/articles/s41586-022-04725-x (visited on 04/14/2026) (cit. on p. 2).

[48] Yu-Hao Deng et al. “Gaussian Boson Sampling with Pseudo-Photon-Number-Resolving Detectors and Quantum Computational Advantage”. In: *Phys. Rev. Lett.* 131 (15 Oct. 2023), p. 150601. DOI: 10.1103/PhysRevLett.131.150601. URL: https://link.aps.org/doi/10.1103/PhysRevLett.131.150601 (cit. on p. 2).

[49] Dongxin Gao et al. “Establishing a New Benchmark in Quantum Computational Advantage with 105-qubit Zuchongzhi 3.0 Processor”. In: *Phys. Rev. Lett.* 134 (9 Mar. 2025), p. 090601. DOI: 10.1103/PhysRevLett.134.090601. URL: https://link.aps.org/doi/10.1103/PhysRevLett.134.090601 (cit. on p. 2).

[50] A. Morvan et al. “Phase transitions in random circuit sampling”. en. In: *Nature* 634.8033 (Oct. 2024), pp. 328–333. ISSN: 1476-4687. DOI: 10.1038/s41586-024-07998-6. URL: https://www.nature.com/articles/s41586-024-07998-6 (visited on 04/14/2026) (cit. on p. 2).

[51] Tim Byrnes and Yoshihisa Yamamoto. “Simulating lattice gauge theories on a quantum computer”. In: *Phys. Rev. A* 73 (2 Feb. 2006), p. 022328. DOI: 10.1103/PhysRevA.73.022328. URL: https://link.aps.org/doi/10.1103/PhysRevA.73.022328 (cit. on p. 2).

[52] Ian C. Cloët et al. *Opportunities for Nuclear Physics & Quantum Information Science*. 2019. arXiv: 1903.05453 [nucl-th]. URL: https://arxiv.org/abs/1903.05453 (cit. on p. 2).

[53] Simon V. Mathis, Guglielmo Mazzola, and Ivano Tavernelli. "Toward scalable simulations of lattice gauge theories on quantum computers". In: *Phys. Rev. D* 102 (9 Nov. 2020), p. 094501. DOI: 10.1103/PhysRevD.102.094501. URL: https://link.aps.org/doi/10.1103/PhysRevD.102.094501 (cit. on p. 2).

[54] Zohreh Davoudi, Indrakshi Raychowdhury, and Andrew Shaw. "Search for efficient formulations for Hamiltonian simulation of non-Abelian lattice gauge theories". In: *Phys. Rev. D* 104 (7 Oct. 2021), p. 074505. DOI: 10.1103/PhysRevD.104.074505. URL: https://link.aps.org/doi/10.1103/PhysRevD.104.074505 (cit. on p. 2).

[55] Natalie Klco, Alessandro Roggero, and Martin J Savage. "Standard model physics and the digital quantum revolution: thoughts about the interface". In: *Reports on Progress in Physics* 85.6 (May 2022), p. 064301. DOI: 10.1088/1361-6633/ac58a4. URL: https://doi.org/10.1088/1361-6633/ac58a4 (cit. on p. 2).

[56] Monika Aidelsburger et al. "Cold atoms meet lattice gauge theory". In: *Philosophical Transactions of the Royal Society A: Mathematical, Physical and Engineering Sciences* 380.2216 (2022), p. 20210064. DOI: 10.1098/rsta.2021.0064. URL: https://royalsocietypublishing.org/doi/abs/10.1098/rsta.2021.0064 (cit. on p. 2).

[57] Christian W. Bauer et al. "Quantum Simulation for High-Energy Physics". In: *PRX Quantum* 4 (2 May 2023), p. 027001. DOI: 10.1103/PRXQuantum.4.027001. URL: https://link.aps.org/doi/10.1103/PRXQuantum.4.027001 (cit. on pp. 2, 12).

[58] A. Mezzacapo, E. Rico, C. Sabín, I. L. Egusquiza, L. Lamata, and E. Solano. "Non-Abelian SU(2) Lattice Gauge Theories in Superconducting Circuits". In: *Phys. Rev. Lett.* 115 (24 Dec. 2015), p. 240502. DOI: 10.1103/PhysRevLett.115.240502. URL: https://link.aps.org/doi/10.1103/PhysRevLett.115.240502 (cit. on p. 2).

[59] P. Hauke, D. Marcos, M. Dalmonte, and P. Zoller. "Quantum Simulation of a Lattice Schwinger Model in a Chain of Trapped Ions". In: *Phys. Rev. X* 3 (4 Nov. 2013), p. 041018. DOI: 10.1103/PhysRevX.3.041018. URL: https://link.aps.org/doi/10.1103/PhysRevX.3.041018 (cit. on p. 2).

[60] Dayou Yang, Gouri Shankar Giri, Michael Johanning, Christof Wunderlich, Peter Zoller, and Philipp Hauke. "Analog quantum simulation of $(1+1)$-dimensional lattice QED with trapped ions". In: *Phys. Rev. A* 94 (5 Nov. 2016), p. 052321. DOI: 10.1103/PhysRevA.94.052321. URL: https://link.aps.org/doi/10.1103/PhysRevA.94.052321 (cit. on p. 2).

[61] Christine Muschik, Markus Heyl, Esteban Martinez, Thomas Monz, Philipp Schindler, Berit Vogell, Marcello Dalmonte, Philipp Hauke, Rainer Blatt, and Peter Zoller. "U(1) Wilson lattice gauge theories in digital quantum simulators". In: *New J. Phys.* 19.10 (2017), p. 103020. DOI: 10.1088/1367-

2630/aa89ab. URL: https://doi.org/10.1088/1367-2630/aa89ab (cit. on p. 2).

[62] D. Paulson et al. "Simulating 2D Effects in Lattice Gauge Theories on a Quantum Computer". In: *PRX Quantum* 2 (3 Aug. 2021), p. 030334. DOI: 10.1103/PRXQuantum.2.030334. URL: https://link.aps.org/doi/10.1103/PRXQuantum.2.030334 (cit. on pp. 2, 15).

[63] Pavel P. Popov, Michael Meth, Maciej Lewestein, Philipp Hauke, Martin Ringbauer, Erez Zohar, and Valentin Kasper. "Variational quantum simulation of U(1) lattice gauge theories with qudit systems". In: *Phys. Rev. Res.* 6 (1 Feb. 2024), p. 013202. DOI: 10.1103/PhysRevResearch.6.013202. URL: https://link.aps.org/doi/10.1103/PhysRevResearch.6.013202 (cit. on pp. 2, 3, 15).

[64] Erez Zohar and Benni Reznik. "Confinement and Lattice Quantum-Electrodynamic Electric Flux Tubes Simulated with Ultracold Atoms". en. In: *Physical Review Letters* 107.27 (Dec. 2011), p. 275301. ISSN: 0031-9007, 1079-7114. DOI: 10.1103/PhysRevLett.107.275301. URL: https://link.aps.org/doi/10.1103/PhysRevLett.107.275301 (visited on 04/15/2026) (cit. on p. 2).

[65] D. Banerjee, M. Dalmonte, M. Müller, E. Rico, P. Stebler, U.-J. Wiese, and P. Zoller. "Atomic Quantum Simulation of Dynamical Gauge Fields Coupled to Fermionic Matter: From String Breaking to Evolution after a Quench". In: *Phys. Rev. Lett.* 109 (17 Oct. 2012), p. 175302. DOI: 10.1103/PhysRevLett.109.175302. URL: https://link.aps.org/doi/10.1103/PhysRevLett.109.175302 (cit. on pp. 2, 73).

[66] Erez Zohar, J. Ignacio Cirac, and Benni Reznik. "Cold-Atom Quantum Simulator for SU(2) Yang-Mills Lattice Gauge Theory". In: *Phys. Rev. Lett.* 110 (12 Mar. 2013), p. 125304. DOI: 10.1103/PhysRevLett.110.125304. URL: https://link.aps.org/doi/10.1103/PhysRevLett.110.125304 (cit. on p. 2).

[67] L. Tagliacozzo, A. Celi, P. Orland, M. W. Mitchell, and M. Lewenstein. "Simulation of non-Abelian gauge theories with optical lattices". en. In: *Nature Communications* 4.1 (Oct. 2013), p. 2615. ISSN: 2041-1723. DOI: 10.1038/ncomms3615. URL: https://www.nature.com/articles/ncomms3615 (visited on 04/15/2026) (cit. on p. 2).

[68] D. Banerjee, M. Bögli, M. Dalmonte, E. Rico, P. Stebler, U.-J. Wiese, and P. Zoller. "Atomic Quantum Simulation of $\mathbf{U}(N)$ and SU(N) Non-Abelian Lattice Gauge Theories". In: *Phys. Rev. Lett.* 110 (12 Mar. 2013), p. 125303. DOI: 10.1103/PhysRevLett.110.125303. URL: https://link.aps.org/doi/10.1103/PhysRevLett.110.125303 (cit. on pp. 2, 59).

[69] L. Tagliacozzo, A. Celi, A. Zamora, and M. Lewenstein. "Optical Abelian lattice gauge theories". In: *Annals of Physics* 330 (2013), pp. 160–191. ISSN: 0003-4916. DOI: https://doi.org/10.1016/j.aop.2012.11.009. URL: https://www.sciencedirect.com/science/article/pii/S0003491612001819 (cit. on p. 2).

[70] V Kasper, F Hebenstreit, F Jendrzejewski, M K Oberthaler, and J Berges. "Implementing quantum electrodynamics with ultracold atomic systems". In: *New Journal of Physics* 19.2 (Feb. 2017), p. 023030. DOI: 10.1088/1367-2630/aa54e0. URL: https://doi.org/10.1088/1367-2630/aa54e0 (cit. on p. 2).

[71] Erez Zohar, Alessandro Farace, Benni Reznik, and J. Ignacio Cirac. "Digital Quantum Simulation of $\mathbb{Z}_2$ Lattice Gauge Theories with Dynamical Fermionic Matter". In: *Phys. Rev. Lett.* 118 (7 Feb. 2017), p. 070501. DOI: 10.1103/PhysRevLett.118.070501. URL: https://link.aps.org/doi/10.1103/PhysRevLett.118.070501 (cit. on p. 2).

[72] Julian Bender, Erez Zohar, Alessandro Farace, and J Ignacio Cirac. "Digital quantum simulation of lattice gauge theories in three spatial dimensions". In: *New Journal of Physics* 20.9 (Sept. 2018), p. 093001. DOI: 10.1088/1367-2630/aadb71. URL: https://doi.org/10.1088/1367-2630/aadb71 (cit. on pp. 2, 3, 17).

[73] Daniel González-Cuadra, Torsten V. Zache, Jose Carrasco, Barbara Kraus, and Peter Zoller. "Hardware Efficient Quantum Simulation of Non-Abelian Gauge Theories with Qudits on Rydberg Platforms". In: *Phys. Rev. Lett.* 129 (16 Oct. 2022), p. 160501. DOI: 10.1103/PhysRevLett.129.160501. URL: https://link.aps.org/doi/10.1103/PhysRevLett.129.160501 (cit. on pp. 2, 3, 15, 16, 24, 25, 102, 104).

[74] Tsafrir Armon, Shachar Ashkenazi, Gerardo García-Moreno, Alejandro González-Tudela, and Erez Zohar. "Photon-Mediated Stroboscopic Quantum Simulation of a $\mathbb{Z}_2$ Lattice Gauge Theory". In: *Phys. Rev. Lett.* 127 (25 Dec. 2021), p. 250501. DOI: 10.1103/PhysRevLett.127.250501. URL: https://link.aps.org/doi/10.1103/PhysRevLett.127.250501 (cit. on p. 2).

[75] N. Klco, E. F. Dumitrescu, A. J. McCaskey, T. D. Morris, R. C. Pooser, M. Sanz, E. Solano, P. Lougovski, and M. J. Savage. "Quantum-classical computation of Schwinger model dynamics using quantum computers". In: *Phys. Rev. A* 98 (3 Sept. 2018), p. 032331. DOI: 10.1103/PhysRevA.98.032331. URL: https://link.aps.org/doi/10.1103/PhysRevA.98.032331 (cit. on p. 2).

[76] Natalie Klco, Martin J. Savage, and Jesse R. Stryker. "SU(2) non-Abelian gauge field theory in one dimension on digital quantum computers". In: *Phys. Rev. D* 101 (7 Apr. 2020), p. 074512. DOI: 10.1103/PhysRevD.101.074512.

URL: https://link.aps.org/doi/10.1103/PhysRevD.101.074512 (cit. on p. 2).

[77] Anthony Ciavarella, Natalie Klco, and Martin J. Savage. "Trailhead for quantum simulation of SU(3) Yang-Mills lattice gauge theory in the local multiplet basis". In: *Phys. Rev. D* 103 (9 May 2021), p. 094501. DOI: 10.1103/PhysRevD.103.094501. URL: https://link.aps.org/doi/10.1103/PhysRevD.103.094501 (cit. on p. 2).

[78] Y. Y. Atas, J. Zhang, R. Lewis, A. Jahanpour, J. F. Haase, and C. A. Muschik. "SU(2) hadrons on a quantum computer via a variational approach". In: *Nat. Comm.* 12.1 (Nov. 2021). ISSN: 2041-1723. DOI: 10.1038/s41467-021-26825-4. URL: http://dx.doi.org/10.1038/s41467-021-26825-4 (cit. on p. 2).

[79] Roland C. Farrell, Ivan A. Chernyshev, Sarah J. M. Powell, Nikita A. Zemlevskiy, Marc Illa, and Martin J. Savage. "Preparations for quantum simulations of quantum chromodynamics in $1+1$ dimensions. I. Axial gauge". In: *Phys. Rev. D* 107 (5 Mar. 2023), p. 054512. DOI: 10.1103/PhysRevD.107.054512. URL: https://link.aps.org/doi/10.1103/PhysRevD.107.054512 (cit. on p. 2).

[80] Zhan Wang et al. "Observation of emergent $\mathbb{Z}_2$ gauge invariance in a superconducting circuit". In: *Phys. Rev. Res.* 4 (2 June 2022), p. L022060. DOI: 10.1103/PhysRevResearch.4.L022060. URL: https://link.aps.org/doi/10.1103/PhysRevResearch.4.L022060 (cit. on p. 2).

[81] Julius Mildenberger, Wojciech Mruczkiewicz, Jad C. Halimeh, Zhang Jiang, and Philipp Hauke. "Confinement in a $\mathbb{Z}_2$ lattice gauge theory on a quantum computer". en. In: *Nature Physics* 21.2 (Feb. 2025), pp. 312–317. ISSN: 1745-2481. DOI: 10.1038/s41567-024-02723-6. URL: https://www.nature.com/articles/s41567-024-02723-6 (visited on 07/01/2025) (cit. on pp. 2, 30, 73, 74, 76, 77, 80, 86, 87, 110).

[82] T. A. Cochran et al. "Visualizing dynamics of charges and strings in $(2+1)$D lattice gauge theories". en. In: *Nature* 642.8067 (June 2025), pp. 315–320. ISSN: 1476-4687. DOI: 10.1038/s41586-025-08999-9. URL: https://www.nature.com/articles/s41586-025-08999-9 (visited on 07/01/2025) (cit. on pp. 2, 16, 73, 87, 110).

[83] Esteban A. Martinez et al. "Real-time dynamics of lattice gauge theories with a few-qubit quantum computer". In: *Nature* 534.7608 (June 2016), pp. 516–519. ISSN: 1476-4687. DOI: 10.1038/nature18318. URL: https://doi.org/10.1038/nature18318 (cit. on pp. 2, 86, 98).

[84] C. Kokail et al. "Self-verifying variational quantum simulation of lattice models". In: *Nature* 569.7756 (May 2019), pp. 355–360. ISSN: 1476-4687. DOI: 10.1038/s41586-019-1177-4. URL: https://doi.org/10.1038/s41586-019-1177-4 (cit. on p. 2).

[85] Nhung H. Nguyen, Minh C. Tran, Yingyue Zhu, Alaina M. Green, C. Huerta Alderete, Zohreh Davoudi, and Norbert M. Linke. "Digital Quantum Simulation of the Schwinger Model and Symmetry Protection with Trapped Ions". In: *PRX Quantum* 3 (2 May 2022), p. 020324. DOI: 10.1103/PRXQuantum.3.020324. URL: https://link.aps.org/doi/10.1103/PRXQuantum.3.020324 (cit. on pp. 2, 73, 86, 87, 98, 110).

[86] Niklas Mueller, Joseph A. Carolan, Andrew Connelly, Zohreh Davoudi, Eugene F. Dumitrescu, and Kübra Yeter-Aydeniz. "Quantum Computation of Dynamical Quantum Phase Transitions and Entanglement Tomography in a Lattice Gauge Theory". In: *PRX Quantum* 4 (3 Aug. 2023), p. 030323. DOI: 10.1103/PRXQuantum.4.030323. URL: https://link.aps.org/doi/10.1103/PRXQuantum.4.030323 (cit. on p. 2).

[87] Hannes Bernien et al. "Probing many-body dynamics on a 51-atom quantum simulator". en. In: *Nature* 551.7682 (Nov. 2017), pp. 579–584. ISSN: 1476-4687. DOI: 10.1038/nature24622. URL: https://www.nature.com/articles/nature24622 (visited on 04/15/2026) (cit. on pp. 2, 121).

[88] Federica M. Surace, Paolo P. Mazza, Giuliano Giudici, Alessio Lerose, Andrea Gambassi, and Marcello Dalmonte. "Lattice Gauge Theories and String Dynamics in Rydberg Atom Quantum Simulators". In: *Phys. Rev. X* 10 (2 May 2020), p. 021041. DOI: 10.1103/PhysRevX.10.021041. URL: https://link.aps.org/doi/10.1103/PhysRevX.10.021041 (cit. on pp. 2, 98, 121).

[89] Christian Schweizer, Fabian Grusdt, Moritz Berngruber, Luca Barbiero, Eugene Demler, Nathan Goldman, Immanuel Bloch, and Monika Aidelsburger. "Floquet approach to $\mathbb{Z}_2$ lattice gauge theories with ultracold atoms in optical lattices". In: *Nature Physics* 15.11 (Nov. 2019), pp. 1168–1173. ISSN: 1745-2481. DOI: 10.1038/s41567-019-0649-7. URL: https://doi.org/10.1038/s41567-019-0649-7 (cit. on pp. 2, 30, 77).

[90] Bing Yang, Hui Sun, Robert Ott, Han-Yi Wang, Torsten V. Zache, Jad C. Halimeh, Zhen-Sheng Yuan, Philipp Hauke, and Jian-Wei Pan. "Observation of gauge invariance in a 71-site Bose–Hubbard quantum simulator". In: *Nature* 587.7834 (Nov. 2020), pp. 392–396. ISSN: 1476-4687. DOI: 10.1038/s41586-020-2910-8. URL: https://doi.org/10.1038/s41586-020-2910-8 (cit. on pp. 2, 78).

[91] Alexander Mil, Torsten V. Zache, Apoorva Hegde, Andy Xia, Rohit P. Bhatt, Markus K. Oberthaler, Philipp Hauke, Jürgen Berges, and Fred Jendrzejewski. "A scalable realization of local U(1) gauge invariance in cold atomic mixtures". In: *Science* 367.6482 (2020), pp. 1128–1130. DOI: 10.1126/science.aaz5312. URL: https://www.science.org/doi/abs/10.1126/science.aaz5312 (cit. on pp. 2, 78).

[92] Zhao-Yu Zhou, Guo-Xian Su, Jad C. Halimeh, Robert Ott, Hui Sun, Philipp Hauke, Bing Yang, Zhen-Sheng Yuan, Jürgen Berges, and Jian-Wei Pan. "Thermalization dynamics of a gauge theory on a quantum simulator". en. In: *Science* 377.6603 (July 2022), pp. 311–314. ISSN: 0036-8075, 1095-9203. DOI: 10.1126/science.abl6277. URL: https://www.science.org/doi/10.1126/science.abl6277 (visited on 04/15/2026) (cit. on p. 2).

[93] Daniel González-Cuadra et al. "Observation of string breaking on a (2+ 1) D Rydberg quantum simulator". In: *Nature* 642 (2025), p. 321. URL: https://doi.org/10.1038/s41586-025-09051-6 (cit. on pp. 2, 16).

[94] L. Tagliacozzo, A. Celi, and M. Lewenstein. "Tensor Networks for Lattice Gauge Theories with Continuous Groups". In: *Phys. Rev. X* 4 (4 Nov. 2014), p. 041024. DOI: 10.1103/PhysRevX.4.041024. URL: https://link.aps.org/doi/10.1103/PhysRevX.4.041024 (cit. on pp. 2, 12, 15).

[95] E. Zohar and M. Burrello. "Building projected entangled pair states with a local gauge symmetry". In: *New J. Phys.* 18.4 (Apr. 2016), p. 043008. DOI: 10.1088/1367-2630/18/4/043008. URL: https://doi.org/10.1088/1367-2630/18/4/043008 (cit. on pp. 2, 12, 15, 58, 126).

[96] P. Silvi, E. Rico, M. Dalmonte, F. Tschirsich, and S. Montangero. "Finite-density phase diagram of a $(1+1)-d$ non-Abelian lattice gauge theory with tensor networks". In: *Quantum* 1 (Apr. 2017), p. 9. ISSN: 2521-327X. DOI: 10.22331/q-2017-04-25-9. URL: https://doi.org/10.22331/q-2017-04-25-9 (cit. on pp. 2, 15, 59).

[97] Timo Felser, Pietro Silvi, Mario Collura, and Simone Montangero. "Two-Dimensional Quantum-Link Lattice Quantum Electrodynamics at Finite Density". In: *Phys. Rev. X* 10 (4 Nov. 2020), p. 041040. DOI: 10.1103/PhysRevX.10.041040. URL: https://link.aps.org/doi/10.1103/PhysRevX.10.041040 (cit. on pp. 2, 12, 15, 58, 69).

[98] S Chandrasekharan and U.-J Wiese. "Quantum link models: A discrete approach to gauge theories". In: *Nuclear Physics B* 492.1 (1997), pp. 455–471. ISSN: 0550-3213. DOI: https://doi.org/10.1016/S0550-3213(97)80041-7. URL: https://www.sciencedirect.com/science/article/pii/S0550321397800417 (cit. on pp. 2, 15, 91, 98).

[99] Jad C Halimeh, Haifeng Lang, and Philipp Hauke. "Gauge protection in non-Abelian lattice gauge theories". In: *New Journal of Physics* 24.3 (Mar. 2022), p. 033015. DOI: 10.1088/1367-2630/ac5564. URL: https://dx.doi.org/10.1088/1367-2630/ac5564 (cit. on pp. 2, 15, 73).

[100] Uwe-Jens Wiese. "From quantum link models to D-theory: a resource efficient framework for the quantum simulation and computation of gauge theories". In: *Philosophical Transactions of the Royal Society A: Mathematical, Physical and Engineering Sciences* 380.2216 (Dec. 2021), p. 20210068. ISSN: 1364-503X. DOI: 10.1098/rsta.2021.0068. eprint: https://royalsocietypublishing.

org/rsta/article-pdf/doi/10.1098/rsta.2021.0068/1322645/rsta.2021.0068.pdf. URL: https://doi.org/10.1098/rsta.2021.0068 (cit. on pp. 2, 15).

[101] Hanqing Liu and Shailesh Chandrasekharan. "Qubit Regularization and Qubit Embedding Algebras". In: *Symmetry* 14.2 (2022). ISSN: 2073-8994. DOI: 10.3390/sym14020305. URL: https://www.mdpi.com/2073-8994/14/2/305 (cit. on pp. 2, 15).

[102] Manu Mathur and T. P. Sreeraj. "Canonical transformations and loop formulation of SU(N) lattice gauge theories". In: *Phys. Rev. D* 92 (12 Dec. 2015), p. 125018. DOI: 10.1103/PhysRevD.92.125018. URL: https://link.aps.org/doi/10.1103/PhysRevD.92.125018 (cit. on pp. 2, 15).

[103] Jan F. Haase, Luca Dellantonio, Alessio Celi, Danny Paulson, Angus Kan, Karl Jansen, and Christine A. Muschik. "A resource efficient approach for quantum and classical simulations of gauge theories in particle physics". In: *Quantum* 5 (Feb. 2021), p. 393. ISSN: 2521-327X. DOI: 10.22331/q-2021-02-04-393. URL: https://doi.org/10.22331/q-2021-02-04-393 (cit. on pp. 2, 15).

[104] Pierpaolo Fontana, Marc Miranda-Riaza, and Alessio Celi. "Efficient Finite-Resource Formulation of Non-Abelian Lattice Gauge Theories beyond One Dimension". In: *Phys. Rev. X* 15 (3 Sept. 2025), p. 031065. DOI: 10.1103/k9p6-c649. URL: https://link.aps.org/doi/10.1103/k9p6-c649 (cit. on pp. 2, 15).

[105] Marc Miranda-Riaza, Pierpaolo Fontana, and Alessio Celi. *Renormalized dual basis for scalable simulations of 2+1D compact quantum electrodynamics*. 2025. arXiv: 2510.18594 [quant-ph]. URL: https://arxiv.org/abs/2510.18594 (cit. on pp. 2, 15).

[106] Torsten V. Zache, Daniel González-Cuadra, and Peter Zoller. "Quantum and Classical Spin-Network Algorithms for q-Deformed Kogut-Susskind Gauge Theories". In: *Phys. Rev. Lett.* 131 (17 Oct. 2023), p. 171902. DOI: 10.1103/PhysRevLett.131.171902. URL: https://link.aps.org/doi/10.1103/PhysRevLett.131.171902 (cit. on pp. 2, 15).

[107] S. Notarnicola, E. Ercolessi, P. Facchi, G. Marmo, S. Pascazio, and F. V. Pepe. "Discrete Abelian gauge theories for quantum simulations of QED". In: *J. Phys. A: Math. Theor.* 48.30 (July 2015), 30FT01. DOI: 10.1088/1751-8113/48/30/30ft01. URL: https://doi.org/10.1088/1751-8113/48/30/30ft01 (cit. on pp. 2, 15).

[108] Elisa Ercolessi, Paolo Facchi, Giuseppe Magnifico, Saverio Pascazio, and Francesco V. Pepe. "Phase transitions in $\mathbb{Z}_n$ gauge models: Towards quantum simulations of the Schwinger-Weyl QED". In: *Phys. Rev. D* 98 (7 Oct. 2018), p. 074503. DOI: 10.1103/PhysRevD.98.074503. URL: https://link.aps.org/doi/10.1103/PhysRevD.98.074503 (cit. on pp. 2, 15).

[109] Erik J. Gustafson, Henry Lamm, Felicity Lovelace, and Damian Musk. "Primitive quantum gates for an SU(2) discrete subgroup: Binary tetrahedral". In: *Phys. Rev. D* 106 (11 Dec. 2022), p. 114501. DOI: 10.1103/PhysRevD.106.114501. URL: https://link.aps.org/doi/10.1103/PhysRevD.106.114501 (cit. on pp. 2, 15, 16, 24).

[110] Erik J. Gustafson, Henry Lamm, and Felicity Lovelace. "Primitive quantum gates for an SU(2) discrete subgroup: Binary octahedral". In: *Phys. Rev. D* 109 (5 Mar. 2024), p. 054503. DOI: 10.1103/PhysRevD.109.054503. URL: https://link.aps.org/doi/10.1103/PhysRevD.109.054503 (cit. on pp. 2, 3, 16).

[111] Erik J. Gustafson, Yao Ji, Henry Lamm, Edison M. Murairi, Sebastian Osorio Perez, and Shuchen Zhu. "Primitive quantum gates for an $SU(3)$ discrete subgroup: $\Sigma(36 \times 3)$". In: *Phys. Rev. D* 110 (3 Aug. 2024), p. 034515. DOI: 10.1103/PhysRevD.110.034515. URL: https://link.aps.org/doi/10.1103/PhysRevD.110.034515 (cit. on pp. 2, 16).

[112] Sebastian Osorio Perez, Edison M. Murairi, Erik J. Gustafson, and Henry Lamm. *Primitive Quantum Gates for an $SU(3)$ Discrete Subgroup: $\Sigma(72\times3)$*. 2025. arXiv: 2511.17437 [hep-lat]. URL: https://arxiv.org/abs/2511.17437 (cit. on pp. 2, 16).

[113] Gabriele Calliari, Robert Ott, Hannes Pichler, and Torsten V. Zache. "Field digitization scaling in a $\mathbb{Z}_N \subset U(1)$ symmetric model". In: *arXiv:2507.22984* (2025). URL: https://arxiv.org/abs/2507.22984 (cit. on pp. 2, 15).

[114] John Preskill. "Quantum Computing in the NISQ era and beyond". In: *Quantum* 2 (Aug. 2018), p. 79. ISSN: 2521-327X. DOI: 10.22331/q-2018-08-06-79. URL: https://doi.org/10.22331/q-2018-08-06-79 (cit. on pp. 3, 24).

[115] Yuchen Wang, Zixuan Hu, Barry C. Sanders, and Sabre Kais. "Qudits and High-Dimensional Quantum Computing". In: *Frontiers in Physics* 8 (2020). ISSN: 2296-424X. DOI: 10.3389/fphy.2020.589504. URL: https://www.frontiersin.org/journals/physics/articles/10.3389/fphy.2020.589504 (cit. on pp. 3, 23, 99).

[116] Martin Ringbauer, Michael Meth, Lukas Postler, Roman Stricker, Rainer Blatt, Philipp Schindler, and Thomas Monz. "A universal qudit quantum processor with trapped ions". In: *Nature Physics* 18.9 (2022), pp. 1053–1057. DOI: https://doi.org/10.1038/s41567-022-01658-0. URL: https://www.nature.com/articles/s41567-022-01658-0#article-info (cit. on pp. 3, 24, 99, 100, 117, 122).

[117] Pei Jiang Low, Brendan White, and Crystal Senko. "Control and readout of a 13-level trapped ion qudit". In: *npj Quantum Information* 11.1 (2025), p. 85. DOI: https://doi.org/10.1038/s41534-025-01031-y. URL: https://www.nature.com/articles/s41534-025-01031-y#citeas (cit. on pp. 3, 24).

[118] Anastasiia S. Nikolaeva et al. "Scalable Improvement of the Generalized Toffoli Gate Realization Using Trapped-Ion-Based Qutrits". In: *Phys. Rev. Lett.* 135 (6 Aug. 2025), p. 060601. DOI: 10.1103/p1z9-6w93. URL: https://link.aps.org/doi/10.1103/p1z9-6w93 (cit. on pp. 3, 24).

[119] Zihao Wang, Rayleigh W. Parker, Elizabeth Champion, and Machiel S. Blok. "High-E_J/E_C transmon qudits with up to 12 levels". In: *Phys. Rev. Appl.* 23 (3 Mar. 2025), p. 034046. DOI: 10.1103/PhysRevApplied.23.034046. URL: https://link.aps.org/doi/10.1103/PhysRevApplied.23.034046 (cit. on pp. 3, 24).

[120] Elizabeth Champion, Zihao Wang, Rayleigh W. Parker, and Machiel S. Blok. "Efficient Control of a Transmon Qudit Using Effective Spin-7/2 Rotations". In: *Phys. Rev. X* 15 (2 June 2025), p. 021096. DOI: 10.1103/vbh4-lysv. URL: https://link.aps.org/doi/10.1103/vbh4-lysv (cit. on pp. 3, 24, 122).

[121] Noah Goss, Samuele Ferracin, Akel Hashim, Arnaud Carignan-Dugas, John Mark Kreikebaum, Ravi K Naik, David I Santiago, and Irfan Siddiqi. "Extending the computational reach of a superconducting qutrit processor". In: *npj Quantum Information* 10.1 (2024), p. 101. DOI: https://doi.org/10.1038/s41534-024-00892-z. URL: https://www.nature.com/articles/s41534-024-00892-z (cit. on pp. 3, 24).

[122] Kai Luo et al. "Experimental Realization of Two Qutrits Gate with Tunable Coupling in Superconducting Circuits". In: *Phys. Rev. Lett.* 130 (3 Jan. 2023), p. 030603. DOI: 10.1103/PhysRevLett.130.030603. URL: https://link.aps.org/doi/10.1103/PhysRevLett.130.030603 (cit. on pp. 3, 24).

[123] Lennart Maximilian Seifert, Ziqian Li, Tanay Roy, David I. Schuster, Frederic T. Chong, and Jonathan M. Baker. "Exploring ququart computation on a transmon using optimal control". In: *Phys. Rev. A* 108 (6 Dec. 2023), p. 062609. DOI: 10.1103/PhysRevA.108.062609. URL: https://link.aps.org/doi/10.1103/PhysRevA.108.062609 (cit. on pp. 3, 24).

[124] Shuxiang Cao, Mustafa Bakr, Giulio Campanaro, Simone D Fasciati, James Wills, Deep Lall, Boris Shteynas, Vivek Chidambaram, Ivan Rungger, and Peter Leek. "Emulating two qubits with a four-level transmon qudit for variational quantum algorithms". In: *Quantum Science and Technology* 9.3 (Apr. 2024), p. 035003. DOI: 10.1088/2058-9565/ad37d4. URL: https://doi.org/10.1088/2058-9565/ad37d4 (cit. on pp. 3, 24).

[125] Pei Liu et al. "Performing SU(d) Operations and Rudimentary Algorithms in a Superconducting Transmon Qudit for $d = 3$ and $d = 4$". In: *Phys. Rev. X* 13 (2 May 2023), p. 021028. DOI: 10.1103/PhysRevX.13.021028. URL: https://link.aps.org/doi/10.1103/PhysRevX.13.021028 (cit. on pp. 3, 24, 99).

[126] Xian Wu, S. L. Tomarken, N. Anders Petersson, L. A. Martinez, Yaniv J. Rosen, and Jonathan L. DuBois. "High-Fidelity Software-Defined Quantum Logic on a Superconducting Qudit". In: *Phys. Rev. Lett.* 125 (17 Oct. 2020), p. 170502. DOI: 10.1103/PhysRevLett.125.170502. URL: https://link.aps.org/doi/10.1103/PhysRevLett.125.170502 (cit. on pp. 3, 24, 99).

[127] Andreas Kruckenhauser, Rick van Bijnen, Torsten V Zache, Marco Di Liberto, and Peter Zoller. "High-dimensional SO(4)-symmetric Rydberg manifolds for quantum simulation". In: *Quantum Science and Technology* 8.1 (Dec. 2022), p. 015020. DOI: 10.1088/2058-9565/aca996. URL: https://doi.org/10.1088/2058-9565/aca996 (cit. on pp. 3, 24).

[128] Yulin Chi, Jieshan Huang, Zhanchuan Zhang, Jun Mao, Zinan Zhou, Xiaojiong Chen, Chonghao Zhai, Jueming Bao, Tianxiang Dai, Huihong Yuan, et al. "A programmable qudit-based quantum processor". In: *Nature communications* 13.1 (2022), p. 1166. DOI: https://doi.org/10.1038/s41467-022-28767-x. URL: https://www.nature.com/articles/s41467-022-28767-x (cit. on pp. 3, 24).

[129] Valentin Kasper, Daniel González-Cuadra, Apoorva Hegde, Andy Xia, Alexandre Dauphin, Felix Huber, Eberhard Tiemann, Maciej Lewenstein, Fred Jendrzejewski, and Philipp Hauke. "Universal quantum computation and quantum error correction with ultracold atomic mixtures". In: *Quantum Science and Technology* 7.1 (Nov. 2021), p. 015008. DOI: 10.1088/2058-9565/ac2d39. URL: https://doi.org/10.1088/2058-9565/ac2d39 (cit. on pp. 3, 24).

[130] Taeyoon Kim et al. *Ultracoherent superconducting cavity-based multiqudit platform with error-resilient control*. 2025. arXiv: 2506.03286 [quant-ph]. URL: https://arxiv.org/abs/2506.03286 (cit. on pp. 3, 24).

[131] Nicholas Bornman, Tanay Roy, Joshua A Job, Namit Anand, Gabriel N Perdue, Silvia Zorzetti, and M Sohaib Alam. "Benchmarking the performance of a high-Q cavity qudit using random unitaries". In: *Quantum Science and Technology* 10.2 (Apr. 2025), p. 025062. DOI: 10.1088/2058-9565/adc47c. URL: https://doi.org/10.1088/2058-9565/adc47c (cit. on pp. 3, 24).

[132] Torsten V. Zache, Daniel González-Cuadra, and Peter Zoller. "Fermion-qudit quantum processors for simulating lattice gauge theories with matter". In: *Quantum* 7 (Oct. 2023), p. 1140. ISSN: 2521-327X. DOI: 10.22331/q-2023-10-16-1140. URL: http://dx.doi.org/10.22331/q-2023-10-16-1140 (cit. on pp. 3, 14, 24, 25).

[133] Giuseppe Calajó, Giuseppe Magnifico, Claire Edmunds, Martin Ringbauer, Simone Montangero, and Pietro Silvi. "Digital Quantum Simulation of a (1+1)D SU(2) Lattice Gauge Theory with Ion Qudits". In: *PRX Quantum* 5 (4 Oct. 2024), p. 040309. DOI: 10.1103/PRXQuantum.5.040309. URL:

https://link.aps.org/doi/10.1103/PRXQuantum.5.040309 (cit. on pp. 3, 24, 58, 129).

[134] Emanuele Gaz, Pavel P. Popov, Guy Pardo, Maciej Lewenstein, Philipp Hauke, and Erez Zohar. "Quantum simulation of non-Abelian lattice gauge theories: A variational approach to $\mathbb{D}_8$ with dynamical matter". In: *Phys. Rev. Res.* 7 (3 July 2025), p. 033012. DOI: 10.1103/l8b6-h5s5. URL: https://link.aps.org/doi/10.1103/l8b6-h5s5 (cit. on pp. 3, 17, 69).

[135] Jacky Jiang, Natalie Klco, and Olivia Di Matteo. "Non-Abelian dynamics on a cube: Improving quantum compilation through qudit-based simulations". In: *Phys. Rev. D* 112 (7 Oct. 2025), p. 074512. DOI: 10.1103/rrmd-fqx6. URL: https://link.aps.org/doi/10.1103/rrmd-fqx6 (cit. on p. 3).

[136] Michael Meth et al. "Simulating two-dimensional lattice gauge theories on a qudit quantum computer". In: *Nature Physics* 21.4 (Apr. 2025), pp. 570–576. ISSN: 1745-2481. DOI: 10.1038/s41567-025-02797-w. URL: https://doi.org/10.1038/s41567-025-02797-w (cit. on pp. 3, 24).

[137] W. G. Unruh. "Maintaining coherence in quantum computers". In: *Phys. Rev. A* 51 (2 Feb. 1995), pp. 992–997. DOI: 10.1103/PhysRevA.51.992. URL: https://link.aps.org/doi/10.1103/PhysRevA.51.992 (cit. on p. 3).

[138] Peter W. Shor. "Scheme for reducing decoherence in quantum computer memory". In: *Phys. Rev. A* 52 (4 Oct. 1995), R2493–R2496. DOI: 10.1103/PhysRevA.52.R2493. URL: https://link.aps.org/doi/10.1103/PhysRevA.52.R2493 (cit. on p. 3).

[139] P.W. Shor. "Fault-tolerant quantum computation". In: *Proceedings of 37th Conference on Foundations of Computer Science*. 1996, pp. 56–65. DOI: 10.1109/SFCS.1996.548464 (cit. on p. 3).

[140] A. M. Steane. "Error Correcting Codes in Quantum Theory". In: *Phys. Rev. Lett.* 77 (5 July 1996), pp. 793–797. DOI: 10.1103/PhysRevLett.77.793. URL: https://link.aps.org/doi/10.1103/PhysRevLett.77.793 (cit. on p. 3).

[141] A. R. Calderbank and Peter W. Shor. "Good quantum error-correcting codes exist". In: *Phys. Rev. A* 54 (2 Aug. 1996), pp. 1098–1105. DOI: 10.1103/PhysRevA.54.1098. URL: https://link.aps.org/doi/10.1103/PhysRevA.54.1098 (cit. on p. 3).

[142] Daniel Gottesman. "Theory of fault-tolerant quantum computation". In: *Phys. Rev. A* 57 (1 Jan. 1998), pp. 127–137. DOI: 10.1103/PhysRevA.57.127. URL: https://link.aps.org/doi/10.1103/PhysRevA.57.127 (cit. on p. 3).

[143] Zhenyu Cai, Ryan Babbush, Simon C. Benjamin, Suguru Endo, William J. Huggins, Ying Li, Jarrod R. McClean, and Thomas E. O'Brien. "Quantum error mitigation". In: *Rev. Mod. Phys.* 95 (4 Dec. 2023), p. 045005. DOI: 10.1103/RevModPhys.95.045005. URL: https://link.aps.org/doi/10.1103/RevModPhys.95.045005 (cit. on pp. 3, 73, 76, 87, 113).

[144] V. V. Sivak et al. “Real-time quantum error correction beyond break-even”. en. In: *Nature* 616.7955 (Apr. 2023), pp. 50–55. ISSN: 1476-4687. DOI: 10.1038/s41586-023-05782-6. URL: https://www.nature.com/articles/s41586-023-05782-6 (visited on 04/15/2026) (cit. on p. 3).

[145] Zhongchu Ni et al. “Beating the break-even point with a discrete-variable-encoded logical qubit”. en. In: *Nature* 616.7955 (Apr. 2023), pp. 56–60. ISSN: 1476-4687. DOI: 10.1038/s41586-023-05784-4. URL: https://www.nature.com/articles/s41586-023-05784-4 (visited on 04/15/2026) (cit. on p. 3).

[146] Rajeev Acharya et al. “Suppressing quantum errors by scaling a surface code logical qubit”. en. In: *Nature* 614.7949 (Feb. 2023), pp. 676–681. ISSN: 1476-4687. DOI: 10.1038/s41586-022-05434-1. URL: https://www.nature.com/articles/s41586-022-05434-1 (visited on 04/15/2026) (cit. on p. 3).

[147] Dolev Bluvstein et al. “Logical quantum processor based on reconfigurable atom arrays”. en. In: *Nature* 626.7997 (Feb. 2024), pp. 58–65. ISSN: 1476-4687. DOI: 10.1038/s41586-023-06927-3. URL: https://www.nature.com/articles/s41586-023-06927-3 (visited on 04/15/2026) (cit. on pp. 3, 74, 122).

[148] Rajeev Acharya et al. “Quantum error correction below the surface code threshold”. en. In: *Nature* 638.8052 (Feb. 2025), pp. 920–926. ISSN: 1476-4687. DOI: 10.1038/s41586-024-08449-y. URL: https://www.nature.com/articles/s41586-024-08449-y (visited on 04/15/2026) (cit. on p. 3).

[149] Erez Zohar and Michele Burrello. “Formulation of lattice gauge theories for quantum simulations”. In: *Phys. Rev. D* 91 (5 Mar. 2015), p. 054506. DOI: 10.1103/PhysRevD.91.054506. URL: https://link.aps.org/doi/10.1103/PhysRevD.91.054506 (cit. on pp. 3, 7, 9, 10, 18, 23, 58, 69, 91).

[150] Henry Lamm, Scott Lawrence, and Yukari Yamauchi. “General methods for digital quantum simulation of gauge theories”. In: *Phys. Rev. D* 100 (3 Aug. 2019), p. 034518. DOI: 10.1103/PhysRevD.100.034518. URL: https://link.aps.org/doi/10.1103/PhysRevD.100.034518 (cit. on pp. 3, 9, 13, 14, 17, 100).

[151] Fromm Michael, Philipsen Owe, and Christopher Winterowd. “Dihedral lattice gauge theories on a quantum annealer”. In: *EPJ Quantum Technology* 10 (Aug. 2023). DOI: 10.1140/epjqt/s40507-023-00188-9. URL: https://doi.org/10.1140/epjqt/s40507-023-00188-9 (cit. on pp. 3, 17).

[152] Nathanan Tantivasadakarn, Ruben Verresen, and Ashvin Vishwanath. “Shortest Route to Non-Abelian Topological Order on a Quantum Processor”. In: *Phys. Rev. Lett.* 131 (6 Aug. 2023), p. 060405. DOI: 10.1103/PhysRevLett.131.060405. URL: https://link.aps.org/doi/10.1103/PhysRevLett.131.060405 (cit. on pp. 3, 39).

[153] Mohsin Iqbal et al. "Non-Abelian topological order and anyons on a trapped-ion processor". In: *Nature* 626.7999 (Feb. 2024), pp. 505–511. ISSN: 1476-4687. DOI: 10.1038/s41586-023-06934-4. URL: https://doi.org/10.1038/s41586-023-06934-4 (cit. on pp. 3, 16, 17, 39, 114).

[154] Liyuan Chen, Yuanjie Ren, Ruihua Fan, and Arthur Jaffe. "A universal circuit set using the S 3 quantum double". In: *npj Quantum Information* 11.1 (2025), p. 112. URL: https://www.nature.com/articles/s41534-025-01063-4 (cit. on pp. 3, 17).

[155] Chiu Fan Bowen Lo, Anasuya Lyons, Ruben Verresen, Ashvin Vishwanath, and Nathanan Tantivasadakarn. *Universal Quantum Computation with the S_3 Quantum Double: A Pedagogical Exposition*. 2025. arXiv: 2502.14974 [quant-ph]. URL: https://arxiv.org/abs/2502.14974 (cit. on pp. 3, 17, 39).

[156] Mari Carmen Bañuls and Krzysztof Cichy. "Review on novel methods for lattice gauge theories". In: *Reports on Progress in Physics* 83.2 (Jan. 2020), p. 024401. DOI: 10.1088/1361-6633/ab6311. URL: https://doi.org/10.1088/1361-6633/ab6311 (cit. on p. 4).

[157] Giuseppe Magnifico, Giovanni Cataldi, Marco Rigobello, Peter Majcen, Daniel Jaschke, Pietro Silvi, and Simone Montangero. "Tensor networks for lattice gauge theories beyond one dimension". en. In: *Communications Physics* 8.1 (Aug. 2025), p. 322. ISSN: 2399-3650. DOI: 10.1038/s42005-025-02125-x. URL: https://www.nature.com/articles/s42005-025-02125-x (visited on 04/14/2026) (cit. on pp. 4, 12).

[158] Gopal Chandra Santra, Julius Mildenberger, Edoardo Ballini, Alberto Bottarelli, Matteo M. Wauters, and Philipp Hauke. *Quantum Resources in Non-Abelian Lattice Gauge Theories: Nonstabilizerness, Multipartite Entanglement, and Fermionic Non-Gaussianity*. 2025. arXiv: 2510.07385 [quant-ph]. URL: https://arxiv.org/abs/2510.07385 (cit. on pp. 5, 29, 44).

[159] Pavel P. Popov, Edoardo Ballini, Alberto Bottarelli, Michele Burrello, Pietro Silvi, Matteo M. Wauters, and Philipp Hauke. *When the center matters: color screening and gluelumps in dihedral lattice gauge theories*. 2025. arXiv: 2512.00152 [hep-lat]. URL: https://arxiv.org/abs/2512.00152 (cit. on p. 5).

[160] Matteo M. Wauters, Edoardo Ballini, Alberto Biella, and Philipp Hauke. "Symmetry-protection Zeno phase transition in monitored lattice gauge theories". In: *Phys. Rev. B* 111 (9 Mar. 2025), p. 094315. DOI: 10.1103/PhysRevB.111.094315. URL: https://link.aps.org/doi/10.1103/PhysRevB.111.094315 (cit. on p. 5).

[161] Edoardo Ballini, Julius Mildenberger, Matteo M Wauters, and Philipp Hauke. "Symmetry verification for noisy quantum simulations of non-Abelian lattice gauge theories". In: *Quantum* 9 (2025), p. 1802. URL: https://quantum-journal.org/papers/q-2025-07-22-1802/ (cit. on pp. 6, 24).

[162] Edoardo Ballini, Giuseppe Clemente, Massimo D'Elia, Lorenzo Maio, and Kevin Zambello. "Quantum computation of thermal averages for a non-Abelian D_4 lattice gauge theory via quantum Metropolis sampling". In: *Phys. Rev. D* 109 (3 Feb. 2024), p. 034510. DOI: 10.1103/PhysRevD.109.034510. URL: https://link.aps.org/doi/10.1103/PhysRevD.109.034510 (cit. on p. 6).

[163] Erez Zohar. "Quantum simulation of lattice gauge theories in more than one space dimension-requirements, challenges and methods". In: *Philosophical Transactions of the Royal Society A: Mathematical, Physical and Engineering Sciences* 380.2216 (2022), p. 20210069. DOI: 10.1098/rsta.2021.0069. URL: https://royalsocietypublishing.org/doi/abs/10.1098/rsta.2021.0069 (cit. on pp. 8, 12).

[164] Jean-Pierre Serre et al. *Linear representations of finite groups*. Vol. 42. New York: Springer, 1977. DOI: https://doi.org/10.1007/978-1-4684-9458-7 (cit. on p. 9).

[165] John B. Kogut. "The lattice gauge theory approach to quantum chromodynamics". In: *Rev. Mod. Phys.* 55 (3 July 1983), pp. 775–836. DOI: 10.1103/RevModPhys.55.775. URL: https://link.aps.org/doi/10.1103/RevModPhys.55.775 (cit. on pp. 11, 12).

[166] Heinz J. Rothe. *Lattice Gauge Theories : An Introduction (Fourth Edition)*. Vol. 43. World Scientific Publishing Company, 2012. ISBN: 978-981-4365-87-1, 978-981-4365-85-7. DOI: 10.1142/8229 (cit. on p. 11).

[167] Leonard Susskind. "Lattice fermions". In: *Phys. Rev. D* 16 (10 Nov. 1977), pp. 3031–3039. DOI: 10.1103/PhysRevD.16.3031. URL: https://link.aps.org/doi/10.1103/PhysRevD.16.3031 (cit. on p. 11).

[168] H.B. Nielsen and M. Ninomiya. "A no-go theorem for regularizing chiral fermions". In: *Physics Letters B* 105.2 (1981), pp. 219–223. ISSN: 0370-2693. DOI: https://doi.org/10.1016/0370-2693(81)91026-1. URL: https://www.sciencedirect.com/science/article/pii/0370269381910261 (cit. on p. 11).

[169] Claudio Rebbi. *Lattice gauge theories and Monte Carlo simulations*. World scientific, 1983 (cit. on p. 12).

[170] Michael Creutz, Laurence Jacobs, and Claudio Rebbi. "Monte Carlo computations in lattice gauge theories". In: *Physics Reports* 95.4 (1983), pp. 201–282. ISSN: 0370-1573. DOI: https://doi.org/10.1016/0370-1573(83)90016-9. URL: https://www.sciencedirect.com/science/article/pii/0370157383900169 (cit. on p. 12).

[171] Gert Aarts et al. "Phase Transitions in Particle Physics: Results and Perspectives from Lattice Quantum Chromo-Dynamics". In: *Progress in Particle and Nuclear Physics* 133 (2023), p. 104070. ISSN: 0146-6410. DOI: https://doi.org/10.1016/j.ppnp.2023.104070. URL: https://www.sciencedirect.com/science/article/pii/S0146641023000510 (cit. on p. 12).

[172] Philippe de Forcrand. *Simulating QCD at finite density*. 2010. arXiv: 1005.0539 [hep-lat]. URL: https://arxiv.org/abs/1005.0539 (cit. on p. 12).

[173] Keitaro Nagata. "Finite-density lattice QCD and sign problem: Current status and open problems". In: *Progress in Particle and Nuclear Physics* 127 (2022), p. 103991. ISSN: 0146-6410. DOI: https://doi.org/10.1016/j.ppnp.2022.103991. URL: https://www.sciencedirect.com/science/article/pii/S0146641022000497 (cit. on p. 12).

[174] Christian W. Bauer, Zohreh Davoudi, Natalie Klco, and Martin J. Savage. "Quantum simulation of fundamental particles and forces". en. In: *Nature Reviews Physics* 5.7 (July 2023), pp. 420–432. ISSN: 2522-5820. DOI: 10.1038/s42254-023-00599-8. URL: https://www.nature.com/articles/s42254-023-00599-8 (visited on 04/18/2026) (cit. on p. 12).

[175] P. Silvi, E. Rico, T. Calarco, and S. Montangero. "Lattice gauge tensor networks". In: *New J. Phys.* 16.10 (Oct. 2014), p. 103015. DOI: 10.1088/1367-2630/16/10/103015. URL: https://doi.org/10.1088/1367-2630/16/10/103015 (cit. on p. 12).

[176] Román Orús. "Tensor networks for complex quantum systems". en. In: *Nature Reviews Physics* 1.9 (Sept. 2019), pp. 538–550. ISSN: 2522-5820. DOI: 10.1038/s42254-019-0086-7. URL: https://www.nature.com/articles/s42254-019-0086-7 (visited on 04/14/2026) (cit. on p. 12).

[177] Pietro Silvi, Ferdinand Tschirsich, Matthias Gerster, Johannes Jünemann, Daniel Jaschke, Matteo Rizzi, and Simone Montangero. "The Tensor Networks Anthology: Simulation techniques for many-body quantum lattice systems". In: *SciPost Phys. Lect. Notes* (2019), p. 8. DOI: 10.21468/SciPostPhysLectNotes.8. URL: https://scipost.org/10.21468/SciPostPhysLectNotes.8 (cit. on p. 12).

[178] J. Ignacio Cirac, David Pérez-García, Norbert Schuch, and Frank Verstraete. "Matrix product states and projected entangled pair states: Concepts, symmetries, theorems". In: *Rev. Mod. Phys.* 93 (4 Dec. 2021), p. 045003. DOI: 10.1103/RevModPhys.93.045003. URL: https://link.aps.org/doi/10.1103/RevModPhys.93.045003 (cit. on p. 12).

[179] F. Verstraete and J. I. Cirac. *Renormalization algorithms for Quantum-Many Body Systems in two and higher dimensions*. 2004. arXiv: cond-mat/0407066 [cond-mat.str-el]. URL: https://arxiv.org/abs/cond-mat/0407066 (cit. on p. 12).

[180] Román Orús. "A practical introduction to tensor networks: Matrix product states and projected entangled pair states". In: *Annals of Physics* 349 (2014), pp. 117–158. ISSN: 0003-4916. DOI: https://doi.org/10.1016/j.aop.2014.06.013. URL: https://www.sciencedirect.com/science/article/pii/S0003491614001596 (cit. on p. 12).

[181] Mari Carmen Bañuls and Krzysztof Cichy. "Review on novel methods for lattice gauge theories". In: *Reports on Progress in Physics* 83.2 (Jan. 2020), p. 024401. DOI: 10.1088/1361-6633/ab6311. URL: https://doi.org/10.1088/1361-6633/ab6311 (cit. on p. 12).

[182] Alberto Di Meglio et al. "Quantum Computing for High-Energy Physics: State of the Art and Challenges". In: *PRX Quantum* 5 (3 Aug. 2024), p. 037001. DOI: 10.1103/PRXQuantum.5.037001. URL: https://link.aps.org/doi/10.1103/PRXQuantum.5.037001 (cit. on p. 12).

[183] L. Tagliacozzo and G. Vidal. "Entanglement renormalization and gauge symmetry". In: *Phys. Rev. B* 83 (11 Mar. 2011), p. 115127. DOI: 10.1103/PhysRevB.83.115127. URL: https://link.aps.org/doi/10.1103/PhysRevB.83.115127 (cit. on p. 13).

[184] Jutho Haegeman, Karel Van Acoleyen, Norbert Schuch, J. Ignacio Cirac, and Frank Verstraete. "Gauging Quantum States: From Global to Local Symmetries in Many-Body Systems". In: *Phys. Rev. X* 5 (1 Feb. 2015), p. 011024. DOI: 10.1103/PhysRevX.5.011024. URL: https://link.aps.org/doi/10.1103/PhysRevX.5.011024 (cit. on p. 13).

[185] K. Zapp and R. Orús. "Tensor network simulation of QED on infinite lattices: Learning from (1+1) d, and prospects for (2+1) d". In: *Phys. Rev. D* 95 (11 June 2017), p. 114508. DOI: 10.1103/PhysRevD.95.114508. URL: https://link.aps.org/doi/10.1103/PhysRevD.95.114508 (cit. on p. 13).

[186] D. Robaina, M. C. Bañuls, and J. I. Cirac. "Simulating (2 + 1)D $\mathbb{Z}_3$ Lattice Gauge Theory with an Infinite Projected Entangled-Pair State". In: *Phys. Rev. Lett.* 126 (5 Feb. 2021), p. 050401. DOI: 10.1103/PhysRevLett.126.050401. URL: https://link.aps.org/doi/10.1103/PhysRevLett.126.050401 (cit. on p. 13).

[187] Giuseppe Magnifico, Timo Felser, Pietro Silvi, and Simone Montangero. "Lattice quantum electrodynamics in (3+ 1)-dimensions at finite density with tensor networks". In: *Nature communications* 12.1 (2021), p. 3600 (cit. on pp. 13, 58).

[188] Patrick Emonts, Ariel Kelman, Umberto Borla, Sergej Moroz, Snir Gazit, and Erez Zohar. "Finding the ground state of a lattice gauge theory with fermionic tensor networks: A 2 + 1D $\mathbb{Z}_2$ demonstration". In: *Phys. Rev. D* 107 (1 Jan. 2023), p. 014505. DOI: 10.1103/PhysRevD.107.014505. URL: https://link.aps.org/doi/10.1103/PhysRevD.107.014505 (cit. on p. 13).

[189] Patrick Emonts and Erez Zohar. "Fermionic Gaussian projected entangled pair states in 3 + 1D: Rotations and relativistic limits". In: *Phys. Rev. D* 108 (1 July 2023), p. 014514. DOI: 10.1103/PhysRevD.108.014514. URL: https://link.aps.org/doi/10.1103/PhysRevD.108.014514 (cit. on p. 13).

[190] Giovanni Cataldi, Giuseppe Magnifico, Pietro Silvi, and Simone Montangero. "Simulating (2 + 1)D SU(2) Yang-Mills lattice gauge theory at finite density with tensor networks". In: *Phys. Rev. Res.* 6 (3 July 2024), p. 033057. DOI: 10.1103/PhysRevResearch.6.033057. URL: https://link.aps.org/doi/10.1103/PhysRevResearch.6.033057 (cit. on pp. 13, 58, 69, 122).

[191] Atis Yosprakob and Kouichi Okunishi. "Tensor Renormalization Group Study of the 3D SU(2) and SU(3) Gauge Theories with the Reduced Tensor Network Formulation". In: *Progress of Theoretical and Experimental Physics* 2025.3 (Feb. 2025), 033B06. ISSN: 2050-3911. DOI: 10.1093/ptep/ptaf028. eprint: https://academic.oup.com/ptep/article-pdf/2025/3/033B06/61934624/ptaf028.pdf. URL: https://doi.org/10.1093/ptep/ptaf028 (cit. on p. 13).

[192] Muhammad Asaduzzaman, Simon Catterall, Yannick Meurice, Ryo Sakai, and Goksu Can Toga. "Tensor network representation of non-abelian gauge theory coupled to reduced staggered fermions". en. In: *Journal of High Energy Physics* 2024.5 (May 2024), p. 195. ISSN: 1029-8479. DOI: 10.1007/JHEP05(2024)195. URL: https://doi.org/10.1007/JHEP05(2024)195 (visited on 04/14/2026) (cit. on p. 13).

[193] Pietro Silvi, Yannick Sauer, Ferdinand Tschirsich, and Simone Montangero. "Tensor network simulation of an SU(3) lattice gauge theory in 1D". In: *Phys. Rev. D* 100 (7 Oct. 2019), p. 074512. DOI: 10.1103/PhysRevD.100.074512. URL: https://link.aps.org/doi/10.1103/PhysRevD.100.074512 (cit. on p. 13).

[194] Marco Rigobello, Giuseppe Magnifico, Pietro Silvi, and Simone Montangero. *Hadrons in (1+1)D Hamiltonian hardcore lattice QCD*. 2023. arXiv: 2308.04488 [hep-lat]. URL: https://arxiv.org/abs/2308.04488 (cit. on p. 13).

[195] Anthony N. Ciavarella and Christian W. Bauer. "Quantum Simulation of SU(3) Lattice Yang-Mills Theory at Leading Order in Large-N_c Expansion". In: *Phys. Rev. Lett.* 133 (11 Sept. 2024), p. 111901. DOI: 10.1103/PhysRevLett.133.111901. URL: https://link.aps.org/doi/10.1103/PhysRevLett.133.111901 (cit. on p. 13).

[196] Tomoya Hayata and Yoshimasa Hidaka. "Floquet evolution of the q-deformed $SU(3)_1$ Yang-Mills theory on a two-leg ladder". In: *Phys. Rev. D* 111 (3 Feb. 2025), p. 034513. DOI: 10.1103/PhysRevD.111.034513. URL: https://link.aps.org/doi/10.1103/PhysRevD.111.034513 (cit. on p. 13).

[197] Steven R. White. "Density matrix formulation for quantum renormalization groups". In: *Phys. Rev. Lett.* 69 (19 Nov. 1992), pp. 2863–2866. DOI: 10.1103/PhysRevLett.69.2863. URL: https://link.aps.org/doi/10.1103/PhysRevLett.69.2863 (cit. on p. 13).

[198] Markus Heyl, Philipp Hauke, and Peter Zoller. "Quantum localization bounds Trotter errors in digital quantum simulation". In: *Science Advances* 5.4 (2019), eaau8342. DOI: 10.1126/sciadv.aau8342. eprint: https://www.science.org/doi/pdf/10.1126/sciadv.aau8342. URL: https://www.science.org/doi/abs/10.1126/sciadv.aau8342 (cit. on p. 13).

[199] Erez Zohar, Alessandro Farace, Benni Reznik, and J. Ignacio Cirac. "Digital lattice gauge theories". In: *Phys. Rev. A* 95 (2 Feb. 2017), p. 023604. DOI: 10.1103/PhysRevA.95.023604. URL: https://link.aps.org/doi/10.1103/PhysRevA.95.023604 (cit. on p. 14).

[200] A. Mariani, S. Pradhan, and E. Ercolessi. "Hamiltonians and gauge-invariant Hilbert space for lattice Yang-Mills-like theories with finite gauge group". In: *Phys. Rev. D* 107 (11 June 2023), p. 114513. DOI: 10.1103/PhysRevD.107.114513. URL: https://link.aps.org/doi/10.1103/PhysRevD.107.114513 (cit. on pp. 15, 31, 100).

[201] Alexei Kitaev. "Topological quantum codes and anyons". In: *Proceedings of Symposia in Applied Mathematics*. Vol. 58. 2002, pp. 267–272. URL: https://userpages.cs.umbc.edu/lomonaco/ams/lecturenotes/Kitaev.pdf (cit. on pp. 16, 39).

[202] G. Semeghini et al. "Probing topological spin liquids on a programmable quantum simulator". In: *Science* 374.6572 (2021), pp. 1242–1247. DOI: 10.1126/science.abi8794. URL: https://www.science.org/doi/abs/10.1126/science.abi8794 (cit. on p. 16).

[203] K. J. Satzinger et al. "Realizing topologically ordered states on a quantum processor". In: *Science* 374.6572 (2021), pp. 1237–1241. DOI: 10.1126/science.abi8378. URL: https://www.science.org/doi/abs/10.1126/science.abi8378 (cit. on pp. 16, 74).

[204] T. I. Andersen et al. "Non-Abelian braiding of graph vertices in a superconducting processor". In: *Nature* 618.7964 (June 2023), pp. 264–269. ISSN: 1476-4687. DOI: 10.1038/s41586-023-05954-4. URL: https://doi.org/10.1038/s41586-023-05954-4 (cit. on p. 16).

[205] Shibo Xu et al. "Digital Simulation of Projective Non-Abelian Anyons with 68 Superconducting Qubits". In: *Chin. Phys. Lett.* 40.6 (June 2023), p. 060301. ISSN: 0256-307X. DOI: 10.1088/0256-307X/40/6/060301 (cit. on p. 16).

[206] Shibo Xu et al. "Non-Abelian braiding of Fibonacci anyons with a superconducting processor". In: *Nature Physics* 20.9 (Sept. 1, 2024), pp. 1469–1475. ISSN: 1745-2481. DOI: 10.1038/s41567-024-02529-6. URL: https://doi.org/10.1038/s41567-024-02529-6 (cit. on p. 16).

[207] Jesús Cobos, Joana Fraxanet, César Benito, Francesco di Marcantonio, Pedro Rivero, Kornél Kapás, Miklós Antal Werner, Örs Legeza, Alejandro Bermudez, and Enrique Rico. *Real-Time Dynamics in a (2+1)-D Gauge Theory: The Stringy Nature on a Superconducting Quantum Simulator*. 2025. arXiv: 2507.08088 [quant-ph]. URL: https://arxiv.org/abs/2507.08088 (cit. on p. 16).

[208] Michael Creutz, Laurence Jacobs, and Claudio Rebbi. "Monte Carlo study of Abelian lattice gauge theories". In: *Phys. Rev. D* 20 (8 Oct. 1979), pp. 1915–1922. DOI: 10.1103/PhysRevD.20.1915. URL: https://link.aps.org/doi/10.1103/PhysRevD.20.1915 (cit. on p. 16).

[209] Michael Creutz and Masanori Okawa. "Generalized actions in Zp lattice gauge theory". In: *Nuclear Physics B* 220.2 (1983), pp. 149–166. ISSN: 0550-3213. DOI: https://doi.org/10.1016/0550-3213(83)90220-1. URL: https://www.sciencedirect.com/science/article/pii/0550321383902201 (cit. on p. 16).

[210] Marcela Carena, Henry Lamm, Ying-Ying Li, and Wanqiang Liu. "Improved Hamiltonians for Quantum Simulations of Gauge Theories". In: *Phys. Rev. Lett.* 129 (5 July 2022), p. 051601. DOI: 10.1103/PhysRevLett.129.051601. URL: https://link.aps.org/doi/10.1103/PhysRevLett.129.051601 (cit. on p. 16).

[211] Andrei Alexandru, Paulo F. Bedaque, Siddhartha Harmalkar, Henry Lamm, Scott Lawrence, and Neill C. Warrington. "Gluon field digitization for quantum computers". In: *Phys. Rev. D* 100 (11 Dec. 2019), p. 114501. DOI: 10.1103/PhysRevD.100.114501. URL: https://link.aps.org/doi/10.1103/PhysRevD.100.114501 (cit. on p. 16).

[212] Yao Ji, Henry Lamm, and Shuchen Zhu. "Gluon field digitization via group space decimation for quantum computers". In: *Phys. Rev. D* 102 (11 Dec. 2020), p. 114513. DOI: 10.1103/PhysRevD.102.114513. URL: https://link.aps.org/doi/10.1103/PhysRevD.102.114513 (cit. on p. 16).

[213] Andrei Alexandru, Paulo F. Bedaque, Ruairí Brett, and Henry Lamm. "Spectrum of digitized QCD: Glueballs in a $S(1080)$ gauge theory". In: *Phys. Rev. D* 105 (11 June 2022), p. 114508. DOI: 10.1103/PhysRevD.105.114508. URL: https://link.aps.org/doi/10.1103/PhysRevD.105.114508 (cit. on p. 16).

[214] A.Yu. Kitaev. "Fault-tolerant quantum computation by anyons". In: *Annals of Physics* 303.1 (2003), pp. 2–30. ISSN: 0003-4916. DOI: https://doi.org/10.1016/S0003-4916(02)00018-0. URL: https://www.sciencedirect.com/science/article/pii/S0003491602000180 (cit. on pp. 16, 17).

[215] Michael A. Levin and Xiao-Gang Wen. "String-net condensation: A physical mechanism for topological phases". en. In: *Physical Review B* 71.4 (Jan. 2005), p. 045110. ISSN: 1098-0121, 1550-235X. DOI: 10.1103/PhysRevB.71.045110. URL: https://link.aps.org/doi/10.1103/PhysRevB.71.045110 (visited on 04/23/2026) (cit. on p. 16).

[216] Eric Dennis, Alexei Kitaev, Andrew Landahl, and John Preskill. "Topological quantum memory". In: *Journal of Mathematical Physics* 43.9 (Sept. 2002), pp. 4452–4505. ISSN: 0022-2488. DOI: 10.1063/1.1499754. eprint: https://pubs.aip.org/aip/jmp/article-pdf/43/9/4452/19183135/4452_1_online.pdf. URL: https://doi.org/10.1063/1.1499754 (cit. on p. 16).

[217] Lucile Savary and Leon Balents. "Quantum spin liquids: a review". In: *Reports on Progress in Physics* 80.1 (Nov. 2016), p. 016502. DOI: 10.1088/0034-4885/80/1/016502. URL: https://doi.org/10.1088/0034-4885/80/1/016502 (cit. on p. 16).

[218] Mohsin Iqbal et al. "Qutrit toric code and parafermions in trapped ions". en. In: *Nature Communications* 16.1 (July 2025), p. 6301. ISSN: 2041-1723. DOI: 10.1038/s41467-025-61391-z. URL: https://www.nature.com/articles/s41467-025-61391-z (visited on 04/23/2026) (cit. on p. 17).

[219] Robbert Dijkgraaf and Edward Witten. "Topological gauge theories and group cohomology". en. In: *Communications in Mathematical Physics* 129.2 (Apr. 1990), pp. 393–429. ISSN: 1432-0916. DOI: 10.1007/BF02096988. URL: https://doi.org/10.1007/BF02096988 (visited on 04/23/2026) (cit. on p. 17).

[220] Michael H. Freedman, Michael Larsen, and Zhenghan Wang. "A Modular Functor Which is Universal¶for Quantum Computation". en. In: *Communications in Mathematical Physics* 227.3 (June 2002), pp. 605–622. ISSN: 1432-0916. DOI: 10.1007/s002200200645. URL: https://doi.org/10.1007/s002200200645 (visited on 04/23/2026) (cit. on p. 17).

[221] M. Sohaib Alam, Stuart Hadfield, Henry Lamm, and Andy C. Y. Li. "Primitive quantum gates for dihedral gauge theories". In: *Physical Review D* 105 (11 June 2022), p. 114501. DOI: 10.1103/PhysRevD.105.114501. URL: https://link.aps.org/doi/10.1103/PhysRevD.105.114501 (cit. on pp. 17, 24).

[222] Carlos Mochon. "Anyons from nonsolvable finite groups are sufficient for universal quantum computation". In: *Phys. Rev. A* 67 (2 Feb. 2003), p. 022315. DOI: 10.1103/PhysRevA.67.022315. URL: https://link.aps.org/doi/10.1103/PhysRevA.67.022315 (cit. on p. 17).

[223] Carlos Mochon. "Anyon computers with smaller groups". In: *Phys. Rev. A* 69 (3 Mar. 2004), p. 032306. DOI: 10.1103/PhysRevA.69.032306. URL: https://link.aps.org/doi/10.1103/PhysRevA.69.032306 (cit. on p. 17).

[224] Chiu Fan Bowen Lo et al. *Universal Topological Gates from Braiding and Fusing Anyons on Quantum Hardware*. 2026. arXiv: 2601.20956 [quant-ph]. URL: https://arxiv.org/abs/2601.20956 (cit. on pp. 17, 122).

[225] Doga Murat Kürkçüoglu, Henry Lamm, and Andrea Maestri. *Qudit Gate Decomposition Dependence for Lattice Gauge Theories*. 2024. arXiv: 2410.16414 [quant-ph]. URL: https://arxiv.org/abs/2410.16414 (cit. on p. 24).

[226] Rohan Joshi, Jan C. Louw, Michael Meth, Jesse J. Osborne, Kevin Mato, Guo-Xian Su, Martin Ringbauer, and Jad C. Halimeh. *Probing Hadron Scattering in Lattice Gauge Theories on Qudit Quantum Computers*. 2025. arXiv: 2507.12614 [quant-ph]. URL: https://arxiv.org/abs/2507.12614 (cit. on p. 24).

[227] Edison M. Murairi, M. Sohaib Alam, Henry Lamm, Stuart Hadfield, and Erik Gustafson. "Highly-efficient quantum Fourier transformations for certain non-Abelian groups". In: *Phys. Rev. D* 110 (7 Oct. 2024), p. 074501. DOI: 10.1103/PhysRevD.110.074501. URL: https://link.aps.org/doi/10.1103/PhysRevD.110.074501 (cit. on p. 24).

[228] Marco Vaia. "Integrability and Thermalization in a Discrete non-Abelian Lattice Gauge Theory". Master's thesis. Università di Trento, 2025 (cit. on pp. 29, 46, 48, 49, 121).

[229] Jad C. Halimeh, Valentin Kasper, and Philipp Hauke. *Fate of Lattice Gauge Theories Under Decoherence*. 2020. arXiv: 2009.07848 [cond-mat.quant-gas] (cit. on pp. 30, 77).

[230] J. Greensite. "The confinement problem in lattice gauge theory". In: *Progr. Part. Nucl. Phys.* 51.1 (2003), pp. 1–83. ISSN: 0146-6410. DOI: https://doi.org/10.1016/S0146-6410(03)90012-3. URL: https://www.sciencedirect.com/science/article/pii/S0146641003900123 (cit. on pp. 31, 51, 52, 57, 68).

[231] Morten I. K. Munk, Asbjørn Rasmussen, and Michele Burrello. "Dyonic zero-energy modes". In: *Phys. Rev. B* 98 (24 Dec. 2018), p. 245135. DOI: 10.1103/PhysRevB.98.245135. URL: https://link.aps.org/doi/10.1103/PhysRevB.98.245135 (cit. on pp. 35, 47, 49, 52).

[232] Eduardo Fradkin and Stephen H. Shenker. "Phase diagrams of lattice gauge theories with Higgs fields". In: *Phys. Rev. D* 19 (12 June 1979), pp. 3682–3697. DOI: 10.1103/PhysRevD.19.3682. URL: https://link.aps.org/doi/10.1103/PhysRevD.19.3682 (cit. on p. 39).

[233] J. Nyhegn, C.-M. Chung, and M. Burrello. "$\mathbb{Z}_N$ lattice gauge theory in a ladder geometry". In: *Phys. Rev. Research* 3 (1 Feb. 2021), p. 013133. DOI: 10.1103/PhysRevResearch.3.013133. URL: https://link.aps.org/doi/10.1103/PhysRevResearch.3.013133 (cit. on pp. 39, 52, 66).

[234] S. Pradhan, A. Maroncelli, and E. Ercolessi. "Discrete Abelian lattice gauge theories on a ladder and their dualities with quantum clock models". In: *Phys. Rev. B* 109 (6 Feb. 2024), p. 064410. DOI: 10.1103/PhysRevB.109.064410. URL: https://link.aps.org/doi/10.1103/PhysRevB.109.064410 (cit. on pp. 39, 52).

[235] Daniel Gottesman. "The Heisenberg representation of quantum computers". In: *arXiv preprint quant-ph/9807006* (1998). URL: https://arxiv.org/abs/quant-ph/9807006 (cit. on p. 43).

[236] Scott Aaronson and Daniel Gottesman. "Improved simulation of stabilizer circuits". In: *Phys. Rev. A* 70 (5 Nov. 2004), p. 052328. DOI: 10.1103/PhysRevA.70.052328. URL: https://link.aps.org/doi/10.1103/PhysRevA.70.052328 (cit. on p. 43).

[237] Sergey Bravyi and Alexei Kitaev. "Universal quantum computation with ideal Clifford gates and noisy ancillas". In: *Phys. Rev. A* 71 (2 Feb. 2005), p. 022316. DOI: 10.1103/PhysRevA.71.022316. URL: https://link.aps.org/doi/10.1103/PhysRevA.71.022316 (cit. on p. 43).

[238] Zi-Wen Liu and Andreas Winter. "Many-Body Quantum Magic". In: *PRX Quantum* 3 (2 May 2022), p. 020333. DOI: 10.1103/PRXQuantum.3.020333. URL: https://link.aps.org/doi/10.1103/PRXQuantum.3.020333 (cit. on p. 43).

[239] David Gross, Sepehr Nezami, and Michael Walter. "Schur–Weyl Duality for the Clifford Group with Applications: Property Testing, a Robust Hudson Theorem, and de Finetti Representations". In: *Commun. Math. Phys.* 385.3 (2021), pp. 1325–1393. URL: https://doi.org/10.1007/s00220-021-04118-7 (cit. on p. 43).

[240] Tobias Haug and Lorenzo Piroli. "Stabilizer entropies and nonstabilizerness monotones". In: *Quantum* 7 (2023), p. 1092. DOI: 10.22331/q-2023-08-28-1092. URL: https://doi.org/10.22331/q-2023-08-28-1092 (cit. on p. 43).

[241] Xhek Turkeshi, Anatoly Dymarsky, and Piotr Sierant. "Pauli spectrum and nonstabilizerness of typical quantum many-body states". In: *Phys. Rev. B* 111 (5 Feb. 2025), p. 054301. DOI: 10.1103/PhysRevB.111.054301. URL: https://link.aps.org/doi/10.1103/PhysRevB.111.054301 (cit. on p. 43).

[242] Poetri Sonya Tarabunga, Emanuele Tirrito, Mari Carmen Bañuls, and Marcello Dalmonte. "Nonstabilizerness via Matrix Product States in the Pauli Basis". In: *Phys. Rev. Lett.* 133 (1 July 2024), p. 010601. DOI: 10.1103/PhysRevLett.133.010601. URL: https://link.aps.org/doi/10.1103/PhysRevLett.133.010601 (cit. on p. 43).

[243] Emanuele Tirrito, Poetri Sonya Tarabunga, Gugliemo Lami, Titas Chanda, Lorenzo Leone, Salvatore F. E. Oliviero, Marcello Dalmonte, Mario Collura, and Alioscia Hamma. "Quantifying nonstabilizerness through entanglement spectrum flatness". In: *Phys. Rev. A* 109 (4 Apr. 2024), p. L040401. DOI: 10.1103/PhysRevA.109.L040401. URL: https://link.aps.org/doi/10.1103/PhysRevA.109.L040401 (cit. on p. 43).

[244] M. Frau, P. S. Tarabunga, M. Collura, M. Dalmonte, and E. Tirrito. "Nonstabilizerness versus entanglement in matrix product states". In: *Phys. Rev. B* 110 (4 July 2024), p. 045101. DOI: 10.1103/PhysRevB.110.045101. URL: https://link.aps.org/doi/10.1103/PhysRevB.110.045101 (cit. on p. 43).

[245] Poetri Sonya Tarabunga, Emanuele Tirrito, Titas Chanda, and Marcello Dalmonte. "Many-Body Magic Via Pauli-Markov Chains—From Criticality to Gauge Theories". In: *PRX Quantum* 4 (4 Oct. 2023), p. 040317. DOI: 10.1103/PRXQuantum.4.040317. URL: https://link.aps.org/doi/10.1103/PRXQuantum.4.040317 (cit. on p. 43).

[246] Pedro R. Nicácio Falcão, Poetri Sonya Tarabunga, Martina Frau, Emanuele Tirrito, Jakub Zakrzewski, and Marcello Dalmonte. "Nonstabilizerness in U(1) lattice gauge theory". In: *Phys. Rev. B* 111 (8 Feb. 2025), p. L081102. DOI: 10.1103/PhysRevB.111.L081102. URL: https://link.aps.org/doi/10.1103/PhysRevB.111.L081102 (cit. on p. 43).

[247] Gerald E. Fux, Emanuele Tirrito, Marcello Dalmonte, and Rosario Fazio. "Entanglement – nonstabilizerness separation in hybrid quantum circuits". In: *Phys. Rev. Res.* 6 (4 Oct. 2024), p. L042030. DOI: 10.1103/PhysRevResearch.6.L042030. URL: https://link.aps.org/doi/10.1103/PhysRevResearch.6.L042030 (cit. on p. 43).

[248] Michele Viscardi, Marcello Dalmonte, Alioscia Hamma, and Emanuele Tirrito. "Interplay of entanglement structures and stabilizer entropy in spin models". In: *arXiv:2503.08620* (2025). URL: https://arxiv.org/abs/2503.08620 (cit. on p. 43).

[249] Barbara Jasser, Jovan Odavic, and Alioscia Hamma. "Stabilizer Entropy and entanglement complexity in the Sachdev-Ye-Kitaev model". In: *arXiv:2502.03093* (2025). URL: https://arxiv.org/abs/2502.03093 (cit. on p. 43).

[250] Florian Brökemeier, S. Momme Hengstenberg, James W. T. Keeble, Caroline E. P. Robin, Federico Rocco, and Martin J. Savage. "Quantum magic and multipartite entanglement in the structure of nuclei". In: *Phys. Rev. C* 111 (3 Mar. 2025), p. 034317. DOI: 10.1103/PhysRevC.111.034317. URL: https://link.aps.org/doi/10.1103/PhysRevC.111.034317 (cit. on p. 43).

[251] Ivan Chernyshev, Caroline E. P. Robin, and Martin J. Savage. "Quantum magic and computational complexity in the neutrino sector". In: *Phys. Rev. Res.* 7 (2 June 2025), p. 023228. DOI: 10.1103/PhysRevResearch.7.023228. URL: https://link.aps.org/doi/10.1103/PhysRevResearch.7.023228 (cit. on p. 43).

[252] Tzu-Chieh Wei and Paul M. Goldbart. "Geometric measure of entanglement and applications to bipartite and multipartite quantum states". In: *Phys. Rev. A* 68 (4 Oct. 2003), p. 042307. DOI: 10.1103/PhysRevA.68.042307. URL: https://link.aps.org/doi/10.1103/PhysRevA.68.042307 (cit. on p. 44).

[253] Aditi Sen(De) and Ujjwal Sen. "Channel capacities versus entanglement measures in multiparty quantum states". In: *Phys. Rev. A* 81 (1 Jan. 2010), p. 012308. DOI: 10.1103/PhysRevA.81.012308. URL: https://link.aps.org/doi/10.1103/PhysRevA.81.012308 (cit. on p. 44).

[254] Lorenzo Leone, Salvatore F. E. Oliviero, and Alioscia Hamma. "Stabilizer Rényi Entropy". In: *Phys. Rev. Lett.* 128 (5 Feb. 2022), p. 050402. DOI: 10.1103/PhysRevLett.128.050402. URL: https://link.aps.org/doi/10.1103/PhysRevLett.128.050402 (cit. on p. 44).

[255] John von Neumann. "Beweis des Ergodensatzes und des H-Theorems in der neuen Mechanik". In: *Zeitschrift für Physik* 57 (1929), pp. 30–70. DOI: 10.1140/epjh/e2010-00008-5. URL: https://link.springer.com/article/10.1007/BF01339852#citeas (cit. on p. 45).

[256] Luca D'Alessio, Yariv Kafri, Anatoli Polkovnikov, and Marcos Rigol. "From quantum chaos and eigenstate thermalization to statistical mechanics and thermodynamics". In: *Advances in Physics* 65.3 (2016), pp. 239–362. DOI: 10.1080/00018732.2016.1198134. eprint: https://doi.org/10.1080/00018732.2016.1198134. URL: https://doi.org/10.1080/00018732.2016.1198134 (cit. on p. 45).

[257] J. M. Deutsch. "Quantum statistical mechanics in a closed system". In: *Phys. Rev. A* 43 (4 Feb. 1991), pp. 2046–2049. DOI: 10.1103/PhysRevA.43.2046. URL: https://link.aps.org/doi/10.1103/PhysRevA.43.2046 (cit. on p. 45).

[258] Mark Srednicki. "Chaos and quantum thermalization". In: *Phys. Rev. E* 50 (2 Aug. 1994), pp. 888–901. DOI: 10.1103/PhysRevE.50.888. URL: https://link.aps.org/doi/10.1103/PhysRevE.50.888 (cit. on p. 45).

[259] Mark Srednicki. "The approach to thermal equilibrium in quantized chaotic systems". In: *Journal of Physics A: Mathematical and General* 32.7 (Feb. 1999), p. 1163. DOI: 10.1088/0305-4470/32/7/007. URL: https://doi.org/10.1088/0305-4470/32/7/007 (cit. on p. 45).

[260] Marcos Rigol, Vanja Dunjko, and Maxim Olshanii. "Thermalization and its mechanism for generic isolated quantum systems". In: *Nature* 452 (2008), pp. 854–858. DOI: 10.1038/nature06838. URL: https://www.nature.com/articles/nature06838 (cit. on p. 45).

[261] R. V. Jensen and R. Shankar. "Statistical Behavior in Deterministic Quantum Systems with Few Degrees of Freedom". In: *Phys. Rev. Lett.* 54 (17 Apr. 1985), pp. 1879–1882. DOI: 10.1103/PhysRevLett.54.1879. URL: https://link.aps.org/doi/10.1103/PhysRevLett.54.1879 (cit. on p. 45).

[262] Marcos Rigol, Vanja Dunjko, Vladimir Yurovsky, and Maxim Olshanii. "Relaxation in a Completely Integrable Many-Body Quantum System: An Ab Initio Study of the Dynamics of the Highly Excited States of 1D Lattice Hard-Core Bosons". In: *Phys. Rev. Lett.* 98 (5 Feb. 2007), p. 050405. DOI: 10.1103/PhysRevLett.98.050405. URL: https://link.aps.org/doi/10.1103/PhysRevLett.98.050405 (cit. on p. 45).

[263] Marcos Rigol. "Quantum quenches and thermalization in one-dimensional fermionic systems". In: *Phys. Rev. A* 80 (5 Nov. 2009), p. 053607. DOI: 10.1103/PhysRevA.80.053607. URL: https://link.aps.org/doi/10.1103/PhysRevA.80.053607 (cit. on p. 45).

[264] R. Steinigeweg, J. Herbrych, and P. Prelov šek. "Eigenstate thermalization within isolated spin-chain systems". In: *Phys. Rev. E* 87 (1 Jan. 2013), p. 012118. DOI: 10.1103/PhysRevE.87.012118. URL: https://link.aps.org/doi/10.1103/PhysRevE.87.012118 (cit. on p. 45).

[265] Berndt Müller and Atanas Trayanov. "Deterministic chaos in non-Abelian lattice gauge theory". In: *Phys. Rev. Lett.* 68 (23 June 1992), pp. 3387–3390. DOI: 10.1103/PhysRevLett.68.3387. URL: https://link.aps.org/doi/10.1103/PhysRevLett.68.3387 (cit. on p. 46).

[266] Chaitanya Murthy, Arman Babakhani, Fernando Iniguez, Mark Srednicki, and Nicole Yunger Halpern. "Non-Abelian Eigenstate Thermalization Hypothesis". In: *Phys. Rev. Lett.* 130 (14 Apr. 2023), p. 140402. DOI: 10.1103/PhysRevLett.130.140402. URL: https://link.aps.org/doi/10.1103/PhysRevLett.130.140402 (cit. on p. 46).

[267] Aleksander Lasek, Jae Dong Noh, Jade LeSchack, and Nicole Yunger Halpern. *Numerical evidence for the non-Abelian eigenstate thermalization hypothesis*. 2024. arXiv: 2412.07838 [quant-ph]. URL: https://arxiv.org/abs/2412.07838 (cit. on p. 46).

[268] Diptarka Das, Lukas Ebner, Saurabh V. Kadam, Indrakshi Raychowdhury, Andreas Schäfer, and Xiaojun Yao. *Eigenstate Thermalization in 1+1-Dimensional SU(2) Lattice Gauge Theory Coupled with Dynamical Fermions*. 2025. arXiv: 2509.18269 [hep-th]. URL: https://arxiv.org/abs/2509.18269 (cit. on p. 46).

[269] O. Bohigas, M. J. Giannoni, and C. Schmit. "Characterization of Chaotic Quantum Spectra and Universality of Level Fluctuation Laws". In: *Phys. Rev. Lett.* 52 (1 Jan. 1984), pp. 1–4. DOI: 10.1103/PhysRevLett.52.1. URL: https://link.aps.org/doi/10.1103/PhysRevLett.52.1 (cit. on p. 47).

[270] Michael Victor Berry and M. Tabor. "Level clustering in the regular spectrum". In: *Proceedings of the Royal Society of London. A. Mathematical and Physical Sciences* 356.1686 (Sept. 1977), pp. 375–394. ISSN: 0080-4630. DOI: 10.1098/rspa.1977.0140. eprint: https://royalsocietypublishing.org/rspa/article-pdf/356/1686/375/62525/rspa.1977.0140.pdf. URL: https://doi.org/10.1098/rspa.1977.0140 (cit. on p. 47).

[271] Vadim Oganesyan and David A. Huse. "Localization of interacting fermions at high temperature". In: *Phys. Rev. B* 75 (15 Apr. 2007), p. 155111. DOI: 10.1103/PhysRevB.75.155111. URL: https://link.aps.org/doi/10.1103/PhysRevB.75.155111 (cit. on p. 48).

[272] Y. Y. Atas, E. Bogomolny, O. Giraud, and G. Roux. "Distribution of the Ratio of Consecutive Level Spacings in Random Matrix Ensembles". In: *Phys. Rev. Lett.* 110 (8 Feb. 2013), p. 084101. DOI: 10.1103/PhysRevLett.110.084101. URL: https://link.aps.org/doi/10.1103/PhysRevLett.110.084101 (cit. on p. 48).

[273] Victor V. Albert, David Aasen, Wenqing Xu, Wenjie Ji, Jason Alicea, and John Preskill. *Spin chains, defects, and quantum wires for the quantum-double edge*. 2021. arXiv: 2111.12096 [cond-mat.str-el]. URL: https://arxiv.org/abs/2111.12096 (cit. on p. 52).

[274] Steven H. Simon. *Topological Quantum*. Oxford University Press, Sept. 2023. ISBN: 9780198886723. DOI: 10.1093/oso/9780198886723.001.0001. URL: https://doi.org/10.1093/oso/9780198886723.001.0001 (cit. on p. 54).

[275] R. Brower, S. Chandrasekharan, and U.-J. Wiese. "QCD as a quantum link model". In: *Phys. Rev. D* 60 (9 Sept. 1999), p. 094502. DOI: 10.1103/PhysRevD.60.094502. URL: https://link.aps.org/doi/10.1103/PhysRevD.60.094502 (cit. on p. 59).

[276] Matthew Fishman, Steven R. White, and E. Miles Stoudenmire. "The ITensor Software Library for Tensor Network Calculations". In: *SciPost Phys. Codebases* (2022), p. 4. DOI: 10.21468/SciPostPhysCodeb.4. URL: https://scipost.org/10.21468/SciPostPhysCodeb.4 (cit. on p. 64).

[277] Matthew Fishman, Steven R. White, and E. Miles Stoudenmire. "Codebase release 0.3 for ITensor". In: *SciPost Phys. Codebases* (2022), 4–r0.3. DOI: 10.21468/SciPostPhysCodeb.4-r0.3. URL: https://scipost.org/10.21468/SciPostPhysCodeb.4-r0.3 (cit. on p. 64).

[278] Giuseppe Clemente, Arianna Crippa, and Karl Jansen. "Strategies for the determination of the running coupling of (2 + 1)-dimensional QED with quantum computing". In: *Phys. Rev. D* 106 (11 Dec. 2022), p. 114511. DOI: 10.1103/PhysRevD.106.114511. URL: https://link.aps.org/doi/10.1103/PhysRevD.106.114511 (cit. on p. 67).

[279] Arianna Crippa, Simone Romiti, Lena Funcke, Karl Jansen, Stefan Kühn, Paolo Stornati, and Carsten Urbach. "Towards determining the (2+1)-dimensional quantum electrodynamics running coupling with Monte Carlo and quantum computing methods". In: *Communications Physics* 8.1 (Sept. 11, 2025), p. 367. ISSN: 2399-3650. DOI: 10.1038/s42005-025-02243-6. URL: https://doi.org/10.1038/s42005-025-02243-6 (cit. on p. 67).

[280] N. A. Campbell, I. H. Jorysz, and C. Michael. "The adjoint source potential in SU(3) lattice gauge theory". In: *Physics Letters B* 167.1 (Jan. 1986), pp. 91–93. ISSN: 0370-2693. DOI: 10.1016/0370-2693(86)90552-6. URL: https://www.sciencedirect.com/science/article/pii/0370269386905526 (visited on 04/19/2026) (cit. on p. 68).

[281] Slavo Kratochvila and Philippe de Forcrand. "Observing string breaking with Wilson loops". In: *Nuclear Physics B* 671 (2003), pp. 103–132. ISSN: 0550-3213. DOI: https://doi.org/10.1016/j.nuclphysb.2003.08.014. URL: https://www.sciencedirect.com/science/article/pii/S0550321303006916 (cit. on p. 68).

[282] M. Foster and C. Michael. "Hadrons with a heavy color-adjoint particle". en. In: *Physical Review D* 59.9 (Apr. 1999), p. 094509. ISSN: 0556-2821, 1089-4918. DOI: 10.1103/PhysRevD.59.094509. URL: https://link.aps.org/doi/10.1103/PhysRevD.59.094509 (visited on 04/19/2026) (cit. on p. 68).

[283] Gunnar S. Bali and Antonio Pineda. "QCD phenomenology of static sources and gluonic excitations at short distances". In: *Phys. Rev. D* 69 (9 May 2004), p. 094001. DOI: 10.1103/PhysRevD.69.094001. URL: https://link.aps.org/doi/10.1103/PhysRevD.69.094001 (cit. on p. 68).

[284] Kristen Marsh and Randy Lewis. "Lattice QCD study of generalized gluelumps". en. In: *Physical Review D* 89.1 (Jan. 2014), p. 014502. ISSN: 1550-7998, 1550-2368. DOI: 10.1103/PhysRevD.89.014502. URL: https://link.aps.org/doi/10.1103/PhysRevD.89.014502 (visited on 04/19/2026) (cit. on p. 68).

[285] Jannis Herr, Carolin Schlosser, and Marc Wagner. "Gluelump masses and mass splittings from SU(3) lattice gauge theory". In: *Phys. Rev. D* 109 (3 Feb. 2024), p. 034516. DOI: 10.1103/PhysRevD.109.034516. URL: https://link.aps.org/doi/10.1103/PhysRevD.109.034516 (cit. on p. 68).

[286] Erez Zohar and J. Ignacio Cirac. "Eliminating fermionic matter fields in lattice gauge theories". In: *Phys. Rev. B* 98 (7 Aug. 2018), p. 075119. DOI: 10.1103/PhysRevB.98.075119. URL: https://link.aps.org/doi/10.1103/PhysRevB.98.075119 (cit. on p. 69).

[287] Erez Zohar and J. Ignacio Cirac. "Removing staggered fermionic matter in $U(N)$ and $SU(N)$ lattice gauge theories". In: *Phys. Rev. D* 99 (11 June 2019), p. 114511. DOI: 10.1103/PhysRevD.99.114511. URL: https://link.aps.org/doi/10.1103/PhysRevD.99.114511 (cit. on p. 69).

[288] Jad C. Halimeh and Philipp Hauke. *Stabilizing Gauge Theories in Quantum Simulators: A Brief Review*. 2022. arXiv: 2204.13709 [cond-mat.quant-gas] (cit. on p. 73).

[289] Erez Zohar, J. Ignacio Cirac, and Benni Reznik. "Simulating Compact Quantum Electrodynamics with Ultracold Atoms: Probing Confinement and Nonperturbative Effects". In: *Phys. Rev. Lett.* 109 (12 Sept. 2012), p. 125302. DOI: 10.1103/PhysRevLett.109.125302. URL: https://link.aps.org/doi/10.1103/PhysRevLett.109.125302 (cit. on p. 73).

[290] Yoshihito Kuno, Kenichi Kasamatsu, Yoshiro Takahashi, Ikuo Ichinose, and Tetsuo Matsui. "Real-time dynamics and proposal for feasible experiments of lattice gauge–Higgs model simulated by cold atoms". In: *New Journal of Physics* 17.6 (June 2015), p. 063005. DOI: 10.1088/1367-2630/17/6/063005. URL: https://dx.doi.org/10.1088/1367-2630/17/6/063005 (cit. on p. 73).

[291] Omjyoti Dutta, Luca Tagliacozzo, Maciej Lewenstein, and Jakub Zakrzewski. "Toolbox for Abelian lattice gauge theories with synthetic matter". In: *Phys. Rev. A* 95 (5 May 2017), p. 053608. DOI: 10.1103/PhysRevA.95.053608. URL: https://link.aps.org/doi/10.1103/PhysRevA.95.053608 (cit. on p. 73).

[292] Jad C. Halimeh and Philipp Hauke. "Reliability of Lattice Gauge Theories". In: *Phys. Rev. Lett.* 125 (3 July 2020), p. 030503. DOI: 10.1103/PhysRevLett.125.030503. URL: https://link.aps.org/doi/10.1103/PhysRevLett.125.030503 (cit. on p. 73).

[293] Jad C. Halimeh, Haifeng Lang, Julius Mildenberger, Zhang Jiang, and Philipp Hauke. "Gauge-Symmetry Protection Using Single-Body Terms". In: *PRX Quantum* 2 (4 Oct. 2021), p. 040311. DOI: 10.1103/PRXQuantum.2.040311. URL: https://link.aps.org/doi/10.1103/PRXQuantum.2.040311 (cit. on pp. 73, 78).

[294] K. Stannigel, P. Hauke, D. Marcos, M. Hafezi, S. Diehl, M. Dalmonte, and P. Zoller. "Constrained Dynamics via the Zeno Effect in Quantum Simulation: Implementing Non-Abelian Lattice Gauge Theories with Cold Atoms". In: *Phys. Rev. Lett.* 112 (12 Mar. 2014), p. 120406. DOI: 10.1103/PhysRevLett.112.120406. URL: https://link.aps.org/doi/10.1103/PhysRevLett.112.120406 (cit. on pp. 73, 81, 82, 97, 132).

[295] Henry Lamm, Scott Lawrence, and Yukari Yamauchi. *Suppressing Coherent Gauge Drift in Quantum Simulations*. 2020. DOI: https://doi.org/10.48550/arXiv.2005.12688. arXiv: 2005.12688. URL: https://arxiv.org/abs/2005.12688 (cit. on pp. 73, 97).

[296] Valentin Kasper, Torsten V. Zache, Fred Jendrzejewski, Maciej Lewenstein, and Erez Zohar. "Non-Abelian gauge invariance from dynamical decoupling". In: *Phys. Rev. D* 107 (1 Jan. 2023), p. 014506. DOI: 10.1103/PhysRevD.107.014506. URL: https://link.aps.org/doi/10.1103/PhysRevD.107.014506 (cit. on p. 73).

[297] Carter Ball and Thomas D. Cohen. "Zeno effect suppression of gauge drift in quantum simulations". In: *Phys. Rev. A* 110 (2 Aug. 2024), p. 022417. DOI: 10.1103/PhysRevA.110.022417. URL: https://link.aps.org/doi/10.1103/PhysRevA.110.022417 (cit. on p. 73).

[298] Simon J Devitt, William J Munro, and Kae Nemoto. "Quantum error correction for beginners". In: *Reports on Progress in Physics* 76.7 (June 2013), p. 076001. DOI: 10.1088/0034-4885/76/7/076001. URL: https://dx.doi.org/10.1088/0034-4885/76/7/076001 (cit. on p. 73).

[299] Jesse R. Stryker. "Oracles for Gauss's law on digital quantum computers". In: *Phys. Rev. A* 99 (4 Apr. 2019), p. 042301. DOI: 10.1103/PhysRevA.99.042301. URL: https://link.aps.org/doi/10.1103/PhysRevA.99.042301 (cit. on pp. 73, 74, 76, 92, 93, 97).

[300] Abhishek Rajput, Alessandro Roggero, and Nathan Wiebe. "Quantum error correction with gauge symmetries". In: *npj Quantum Information* 9.1 (Apr. 2023), p. 41. ISSN: 2056-6387. DOI: 10.1038/s41534-023-00706-8. URL: https://doi.org/10.1038/s41534-023-00706-8 (cit. on pp. 73, 74, 93, 98).

[301] Indrakshi Raychowdhury and Jesse R. Stryker. "Solving Gauss's law on digital quantum computers with loop-string-hadron digitization". In: *Phys. Rev. Res.* 2 (3 July 2020), p. 033039. DOI: 10.1103/PhysRevResearch.2.033039. URL: https://link.aps.org/doi/10.1103/PhysRevResearch.2.033039 (cit. on p. 73).

[302] L. Spagnoli, A. Roggero, and N. Wiebe. "Fault-tolerant simulation of Lattice Gauge Theories with gauge covariant codes". In: *Quantum* 10 (Jan. 2026), p. 1968. ISSN: 2521-327X. DOI: 10.22331/q-2026-01-16-1968. URL: https://doi.org/10.22331/q-2026-01-16-1968 (cit. on pp. 73, 93, 98).

[303] Xiangyu Cao, Antoine Tilloy, and Andrea De Luca. "Entanglement in a fermion chain under continuous monitoring". In: *SciPost Phys.* 7 (2019), p. 024. DOI: 10.21468/SciPostPhys.7.2.024. URL: https://scipost.org/10.21468/SciPostPhys.7.2.024 (cit. on p. 74).

[304] O. Alberton, M. Buchhold, and S. Diehl. "Entanglement Transition in a Monitored Free-Fermion Chain: From Extended Criticality to Area Law". In: *Phys. Rev. Lett.* 126 (17 Apr. 2021), p. 170602. DOI: 10.1103/PhysRevLett.126.170602. URL: https://link.aps.org/doi/10.1103/PhysRevLett.126.170602 (cit. on p. 74).

[305] Xhek Turkeshi, Alberto Biella, Rosario Fazio, Marcello Dalmonte, and Marco Schiró. "Measurement-induced entanglement transitions in the quantum Ising chain: From infinite to zero clicks". In: *Phys. Rev. B* 103 (22 June 2021), p. 224210. DOI: 10.1103/PhysRevB.103.224210. URL: https://link.aps.org/doi/10.1103/PhysRevB.103.224210 (cit. on p. 74).

[306] Giulia Piccitto, Angelo Russomanno, and Davide Rossini. "Entanglement transitions in the quantum Ising chain: A comparison between different unravelings of the same Lindbladian". In: *Phys. Rev. B* 105 (6 Feb. 2022), p. 064305. DOI: 10.1103/PhysRevB.105.064305. URL: https://link.aps.org/doi/10.1103/PhysRevB.105.064305 (cit. on p. 74).

[307] Emanuele Tirrito, Alessandro Santini, Rosario Fazio, and Mario Collura. "Full counting statistics as probe of measurement-induced transitions in the quantum Ising chain". In: *SciPost Phys.* 15 (2023), p. 096. DOI: 10.21468/SciPostPhys.15.3.096. URL: https://scipost.org/10.21468/SciPostPhys.15.3.096 (cit. on pp. 74, 97).

[308] B. Misra and E. C. G. Sudarshan. "The Zeno's paradox in quantum theory". In: *Journal of Mathematical Physics* 18.4 (1977), pp. 756–763. DOI: 10.1063/1.523304. eprint: https://doi.org/10.1063/1.523304. URL: https://doi.org/10.1063/1.523304 (cit. on p. 74).

[309] Asher Peres. "Zeno paradox in quantum theory". In: *American Journal of Physics* 48.11 (1980), pp. 931–932. DOI: 10.1119/1.12204. eprint: https://doi.org/10.1119/1.12204. URL: https://doi.org/10.1119/1.12204 (cit. on p. 74).

[310] Wayne M. Itano, D. J. Heinzen, J. J. Bollinger, and D. J. Wineland. "Quantum Zeno effect". In: *Phys. Rev. A* 41 (5 Mar. 1990), pp. 2295–2300. DOI: 10.1103/PhysRevA.41.2295. URL: https://link.aps.org/doi/10.1103/PhysRevA.41.2295 (cit. on p. 74).

[311] P. Facchi, V. Gorini, G. Marmo, S. Pascazio, and E.C.G. Sudarshan. "Quantum Zeno dynamics". In: *Physics Letters A* 275.1 (2000), pp. 12–19. ISSN: 0375-9601. DOI: https://doi.org/10.1016/S0375-9601(00)00566-1. URL: https://www.sciencedirect.com/science/article/pii/S0375960100005661 (cit. on p. 74).

[312] P. Facchi, H. Nakazato, and S. Pascazio. "From the Quantum Zeno to the Inverse Quantum Zeno Effect". In: *Phys. Rev. Lett.* 86 (13 Mar. 2001), pp. 2699–2703. DOI: 10.1103/PhysRevLett.86.2699. URL: https://link.aps.org/doi/10.1103/PhysRevLett.86.2699 (cit. on p. 74).

[313] P. Facchi and S. Pascazio. "Quantum Zeno Subspaces". In: *Phys. Rev. Lett.* 89 (8 Aug. 2002), p. 080401. DOI: 10.1103/PhysRevLett.89.080401. URL: https://link.aps.org/doi/10.1103/PhysRevLett.89.080401 (cit. on p. 74).

[314] Adrien Signoles, Adrien Facon, Dorian Grosso, Igor Dotsenko, Serge Haroche, Jean-Michel Raimond, Michel Brune, and Sébastien Gleyzes. "Confined quantum Zeno dynamics of a watched atomic arrow". In: *Nature Physics* 10.10 (2014), pp. 715–719. DOI: 10.1038/nphys3076. URL: https://doi.org/10.1038/nphys3076 (cit. on p. 74).

[315] Kyrylo Snizhko, Parveen Kumar, and Alessandro Romito. "Quantum Zeno effect appears in stages". In: *Phys. Rev. Research* 2 (3 Sept. 2020), p. 033512. DOI: 10.1103/PhysRevResearch.2.033512. URL: https://link.aps.org/doi/10.1103/PhysRevResearch.2.033512 (cit. on p. 74).

[316] N. Syassen, D. M. Bauer, M. Lettner, T. Volz, D. Dietze, J. J. García-Ripoll, J. I. Cirac, G. Rempe, and S. Dürr. "Strong Dissipation Inhibits Losses and Induces Correlations in Cold Molecular Gases". In: *Science* 320.5881 (2008), pp. 1329–1331. ISSN: 0036-8075. DOI: 10.1126/science.1155309. eprint: https://science.sciencemag.org/content/320/5881/1329.full.pdf. URL: https://science.sciencemag.org/content/320/5881/1329 (cit. on p. 74).

[317] Y. S. Patil, S. Chakram, and M. Vengalattore. "Measurement-Induced Localization of an Ultracold Lattice Gas". In: *Phys. Rev. Lett.* 115 (14 Oct. 2015), p. 140402. DOI: 10.1103/PhysRevLett.115.140402. URL: https://link.aps.org/doi/10.1103/PhysRevLett.115.140402 (cit. on p. 74).

[318] Heinrich Fröml, Alessio Chiocchetta, Corinna Kollath, and Sebastian Diehl. "Fluctuation-Induced Quantum Zeno Effect". In: *Phys. Rev. Lett.* 122 (4 Feb. 2019), p. 040402. DOI: 10.1103/PhysRevLett.122.040402. URL: https://link.aps.org/doi/10.1103/PhysRevLett.122.040402 (cit. on p. 74).

[319] Heinrich Fröml, Christopher Muckel, Corinna Kollath, Alessio Chiocchetta, and Sebastian Diehl. "Ultracold quantum wires with localized losses: Many-body quantum Zeno effect". In: *Phys. Rev. B* 101 (14 Apr. 2020), p. 144301. DOI: 10.1103/PhysRevB.101.144301. URL: https://link.aps.org/doi/10.1103/PhysRevB.101.144301 (cit. on p. 74).

[320] Alberto Biella and Marco Schiró. "Many-Body Quantum Zeno Effect and Measurement-Induced Subradiance Transition". In: *Quantum* 5 (Aug. 2021), p. 528. ISSN: 2521-327X. DOI: 10.22331/q-2021-08-19-528. URL: https://doi.org/10.22331/q-2021-08-19-528 (cit. on p. 74).

[321] Kenneth Choi, Dean Lee, Joey Bonitati, Zhengrong Qian, and Jacob Watkins. "Rodeo Algorithm for Quantum Computing". In: *Phys. Rev. Lett.* 127 (4 July 2021), p. 040505. DOI: 10.1103/PhysRevLett.127.040505. URL: https://link.aps.org/doi/10.1103/PhysRevLett.127.040505 (cit. on p. 74).

[322] Lorenzo Rosso, Alberto Biella, Jacopo De Nardis, and Leonardo Mazza. "Dynamical theory for one-dimensional fermions with strong two-body losses: Universal non-Hermitian Zeno physics and spin-charge separation". In: *Phys. Rev. A* 107 (1 Jan. 2023), p. 013303. DOI: 10.1103/PhysRevA.107.013303. URL: https://link.aps.org/doi/10.1103/PhysRevA.107.013303 (cit. on p. 74).

[323] Lorenzo Rosso, Alberto Biella, and Leonardo Mazza. "The one-dimensional Bose gas with strong two-body losses: the effect of the harmonic confinement". In: *SciPost Phys.* 12 (2022), p. 044. DOI: 10.21468/SciPostPhys.12.1.044. URL: https://scipost.org/10.21468/SciPostPhys.12.1.044 (cit. on p. 74).

[324] Lorenzo Rosso, Leonardo Mazza, and Alberto Biella. "Eightfold way to dark states in SU(3) cold gases with two-body losses". In: *Phys. Rev. A* 105 (5 May 2022), p. L051302. DOI: 10.1103/PhysRevA.105.L051302. URL: https://link.aps.org/doi/10.1103/PhysRevA.105.L051302 (cit. on p. 74).

[325] Jeff Maki, Lorenzo Rosso, Leonardo Mazza, and Alberto Biella. *Loss induced collective mode in one-dimensional Bose gases*. 2024. arXiv: 2402.05824 [cond-mat.quant-gas] (cit. on p. 74).

[326] Rajeev Acharya et al. "Suppressing quantum errors by scaling a surface code logical qubit". In: *Nature* 614.7949 (Feb. 2023), pp. 676–681. ISSN: 1476-4687. DOI: 10.1038/s41586-022-05434-1. URL: https://doi.org/10.1038/s41586-022-05434-1 (cit. on p. 74).

[327] X. Bonet-Monroig, R. Sagastizabal, M. Singh, and T. E. O'Brien. "Low-cost error mitigation by symmetry verification". In: *Phys. Rev. A* 98 (6 Dec. 2018), p. 062339. DOI: 10.1103/PhysRevA.98.062339. URL: https://link.aps.org/doi/10.1103/PhysRevA.98.062339 (cit. on pp. 76, 93, 104).

[328] Sam McArdle, Xiao Yuan, and Simon Benjamin. "Error-Mitigated Digital Quantum Simulation". In: *Phys. Rev. Lett.* 122 (18 May 2019), p. 180501. DOI: 10.1103/PhysRevLett.122.180501. URL: https://link.aps.org/doi/10.1103/PhysRevLett.122.180501 (cit. on p. 76).

[329] Jarrod R. McClean, Mollie E. Kimchi-Schwartz, Jonathan Carter, and Wibe A. de Jong. "Hybrid quantum-classical hierarchy for mitigation of decoherence and determination of excited states". In: *Phys. Rev. A* 95 (4 Apr. 2017), p. 042308. DOI: 10.1103/PhysRevA.95.042308. URL: https://link.aps.org/doi/10.1103/PhysRevA.95.042308 (cit. on pp. 76, 104).

[330] William J. Huggins, Jarrod R. McClean, Nicholas C. Rubin, Zhang Jiang, Nathan Wiebe, K. Birgitta Whaley, and Ryan Babbush. "Efficient and noise resilient measurements for quantum chemistry on near-term quantum computers". In: *npj Quantum Information* 7.1 (Feb. 2021), p. 23. ISSN: 2056-6387. DOI: 10.1038/s41534-020-00341-7. URL: https://doi.org/10.1038/s41534-020-00341-7 (cit. on pp. 76, 114).

[331] Jarrod R. McClean, Zhang Jiang, Nicholas C. Rubin, Ryan Babbush, and Hartmut Neven. "Decoding quantum errors with subspace expansions". In: *Nature Communications* 11.1 (Jan. 2020), p. 636. ISSN: 2041-1723. DOI: 10.1038/s41467-020-14341-w. URL: https://doi.org/10.1038/s41467-020-14341-w (cit. on pp. 76, 104, 114).

[332] Zhenyu Cai. "Quantum Error Mitigation using Symmetry Expansion". In: *Quantum* 5 (Sept. 2021), p. 548. ISSN: 2521-327X. DOI: 10.22331/q-2021-09-21-548. URL: https://doi.org/10.22331/q-2021-09-21-548 (cit. on pp. 76, 104, 114).

[333] Suguru Endo, Zhenyu Cai, Simon C. Benjamin, and Xiao Yuan. "Hybrid Quantum-Classical Algorithms and Quantum Error Mitigation". In: *Journal of the Physical Society of Japan* 90.3 (2021), p. 032001. DOI: 10.7566/JPSJ.90.032001. URL: https://doi.org/10.7566/JPSJ.90.032001 (cit. on p. 76).

[334] Tobias Schmale and Hendrik Weimer. "Stabilizing quantum simulations of lattice gauge theories by dissipation". In: *Phys. Rev. Res.* 6 (3 Sept. 2024), p. 033306. DOI: 10.1103/PhysRevResearch.6.033306. URL: https://link.aps.org/doi/10.1103/PhysRevResearch.6.033306 (cit. on p. 76).

[335] ERICH POPPITZ and YANWEN SHANG. ""LIGHT FROM CHAOS" IN TWO DIMENSIONS". In: *International Journal of Modern Physics A* 23.27n28 (2008), pp. 4545–4556. DOI: 10.1142/S0217751X08041281. eprint: https://doi.org/10.1142/S0217751X08041281. URL: https://doi.org/10.1142/S0217751X08041281 (cit. on p. 78).

[336] J.R. Johansson, P.D. Nation, and F. Nori. "QuTiP: An open-source Python framework for the dynamics of open quantum systems". In: *Computer Physics Communications* 183.8 (Aug. 2012), pp. 1760–1772. DOI: 10.1016/j.cpc.2012.02.021. URL: https://doi.org/10.1016/j.cpc.2012.02.021 (cit. on p. 78).

[337] J.R. Johansson, P.D. Nation, and F. Nori. "QuTiP 2: A Python framework for the dynamics of open quantum systems". In: *Computer Physics Communications* 184.4 (Apr. 2013), pp. 1234–1240. DOI: 10.1016/j.cpc.2012.11.019. URL: https://doi.org/10.1016/j.cpc.2012.11.019 (cit. on p. 78).

[338] Fabrizio Minganti, Alberto Biella, Nicola Bartolo, and Cristiano Ciuti. "Spectral theory of Liouvillians for dissipative phase transitions". In: *Phys. Rev. A* 98 (4 Oct. 2018), p. 042118. DOI: 10.1103/PhysRevA.98.042118. URL: https://link.aps.org/doi/10.1103/PhysRevA.98.042118 (cit. on p. 81).

[339] Zoltán Zimborás et al. *Myths around quantum computation before full fault tolerance: What no-go theorems rule out and what they don't*. 2025. arXiv: 2501.05694 [quant-ph]. URL: https://arxiv.org/abs/2501.05694 (cit. on pp. 87, 113).

[340] Joseph Kerckhoff, Hendra I. Nurdin, Dmitri S. Pavlichin, and Hideo Mabuchi. "Designing Quantum Memories with Embedded Control: Photonic Circuits for Autonomous Quantum Error Correction". In: *Phys. Rev. Lett.* 105 (4 July 2010), p. 040502. DOI: 10.1103/PhysRevLett.105.040502. URL: https://link.aps.org/doi/10.1103/PhysRevLett.105.040502 (cit. on p. 93).

[341] J. Cramer, N. Kalb, M. A. Rol, B. Hensen, M. S. Blok, M. Markham, D. J. Twitchen, R. Hanson, and T. H. Taminiau. "Repeated quantum error correction on a continuously encoded qubit by real-time feedback". In: *Nature Communications* 7.1 (May 2016), p. 11526. ISSN: 2041-1723. DOI: 10.1038/ncomms11526. URL: https://doi.org/10.1038/ncomms11526 (cit. on p. 93).

[342] F Battistel, C Chamberland, K Johar, R W J Overwater, F Sebastiano, L Skoric, Y Ueno, and M Usman. "Real-time decoding for fault-tolerant quantum computing: progress, challenges and outlook". In: *Nano Futures* 7.3 (Aug. 2023), p. 032003. DOI: 10.1088/2399-1984/aceba6. URL: https://dx.doi.org/10.1088/2399-1984/aceba6 (cit. on p. 93).

[343] Howard M. Wiseman and Gerard J. Milburn. *Quantum Measurement and Control*. Cambridge University Press, 2009. DOI: 10.1017/CBO9780511813948 (cit. on p. 97).

[344] Piotr Sierant, Marco Schirò, Maciej Lewenstein, and Xhek Turkeshi. "Measurement-induced phase transitions in $(d+1)$-dimensional stabilizer circuits". In: *Phys. Rev. B* 106 (21 Dec. 2022), p. 214316. DOI: 10.1103/PhysRevB.106.214316. URL: https://link.aps.org/doi/10.1103/PhysRevB.106.214316 (cit. on p. 97).

[345] Yulin Chi et al. "A programmable qudit-based quantum processor". In: *Nature Communications* 13.1 (Mar. 2022), p. 1166. ISSN: 2041-1723. DOI: 10.1038/s41467-022-28767-x. URL: https://doi.org/10.1038/s41467-022-28767-x (cit. on p. 99).

[346] Roger A. Horn and Charles R. Johnson. *Matrix Analysis*. 2nd ed. Cambridge: Cambridge University Press, 2012. DOI: 10.1017/CBO9780511810817 (cit. on p. 103).

[347] Edoardo Ballini. *Data for "Symmetry verification for noisy quantum simulations of non-Abelian lattice gauge theories"*. May 2025. DOI: 10.5281/zenodo.15464248 (cit. on p. 108).

[348] Elisa Bäumer, Vinay Tripathi, Derek S. Wang, Patrick Rall, Edward H. Chen, Swarnadeep Majumder, Alireza Seif, and Zlatko K. Minev. "Efficient Long-Range Entanglement Using Dynamic Circuits". In: *PRX Quantum* 5 (3 Aug. 2024), p. 030339. DOI: 10.1103/PRXQuantum.5.030339. URL: https://link.aps.org/doi/10.1103/PRXQuantum.5.030339 (cit. on pp. 112, 114).

[349] Akel Hashim, Arnaud Carignan-Dugas, Larry Chen, Christian Jünger, Neelay Fruitwala, Yilun Xu, Gang Huang, Joel J. Wallman, and Irfan Siddiqi. "Quasiprobabilistic Readout Correction of Midcircuit Measurements for Adaptive Feedback via Measurement Randomized Compiling". In: *PRX Quantum* 6.1 (Jan. 2025). ISSN: 2691-3399. DOI: 10.1103/prxquantum.6.010307 (cit. on p. 112).

[350] Petr Ivashkov, Gideon Uchehara, Liang Jiang, Derek S. Wang, and Alireza Seif. "High-Fidelity, Multiqubit Generalized Measurements with Dynamic Circuits". In: *PRX Quantum* 5 (3 July 2024), p. 030315. DOI: 10.1103/PRXQuantum.5.030315. URL: https://link.aps.org/doi/10.1103/PRXQuantum.5.030315 (cit. on p. 112).

[351] C. J. Turner, A. A. Michailidis, D. A. Abanin, M. Serbyn, and Z. Papić. "Weak ergodicity breaking from quantum many-body scars". en. In: *Nature Physics* 14.7 (July 2018), pp. 745–749. ISSN: 1745-2481. DOI: 10.1038/s41567-018-0137-5. URL: https://www.nature.com/articles/s41567-018-0137-5 (visited on 04/22/2026) (cit. on p. 121).

[352] Sanjay Moudgalya, B Andrei Bernevig, and Nicolas Regnault. "Quantum many-body scars and Hilbert space fragmentation: a review of exact results". In: *Reports on Progress in Physics* 85.8 (Aug. 2022), p. 086501. ISSN: 0034-4885, 1361-6633. DOI: 10.1088/1361-6633/ac73a0. URL: https://iopscience.iop.org/article/10.1088/1361-6633/ac73a0 (visited on 04/22/2026) (cit. on p. 121).

[353] Maksym Serbyn, Dmitry A. Abanin, and Zlatko Papić. "Quantum many-body scars and weak breaking of ergodicity". en. In: *Nature Physics* 17.6 (June 2021), pp. 675–685. ISSN: 1745-2481. DOI: 10.1038/s41567-021-01230-2. URL: https://www.nature.com/articles/s41567-021-01230-2 (visited on 04/22/2026) (cit. on p. 121).

[354] Anushya Chandran, Thomas Iadecola, Vedika Khemani, and Roderich Moessner. "Quantum Many-Body Scars: A Quasiparticle Perspective". en. In: *Annual Review of Condensed Matter Physics* 14.1 (Mar. 2023), pp. 443–469. ISSN: 1947-5454, 1947-5462. DOI: 10.1146/annurev-conmatphys-031620-101617. URL: https://www.annualreviews.org/doi/10.1146/annurev-conmatphys-031620-101617 (visited on 04/22/2026) (cit. on p. 121).

[355] Debasish Banerjee and Arnab Sen. "Quantum Scars from Zero Modes in an Abelian Lattice Gauge Theory on Ladders". en. In: *Physical Review Letters* 126.22 (June 2021), p. 220601. ISSN: 0031-9007, 1079-7114. DOI: 10.1103/PhysRevLett.126.220601. URL: https://link.aps.org/doi/10.1103/PhysRevLett.126.220601 (visited on 04/22/2026) (cit. on p. 121).

[356] Jad C. Halimeh, Luca Barbiero, Philipp Hauke, Fabian Grusdt, and Annabelle Bohrdt. "Robust quantum many-body scars in lattice gauge theories". In: *Quantum* 7 (May 2023), p. 1004. ISSN: 2521-327X. DOI: 10.22331/q-2023-

05-15-1004. URL: https://doi.org/10.22331/q-2023-05-15-1004 (cit. on p. 121).

[357] Jean-Yves Desaules, Ana Hudomal, Debasish Banerjee, Arnab Sen, Zlatko Papi ć, and Jad C. Halimeh. "Prominent quantum many-body scars in a truncated Schwinger model". In: *Phys. Rev. B* 107 (20 May 2023), p. 205112. DOI: 10.1103/PhysRevB.107.205112. URL: https://link.aps.org/doi/10.1103/PhysRevB.107.205112 (cit. on p. 121).

[358] Jean-Yves Desaules, Debasish Banerjee, Ana Hudomal, Zlatko Papi ć, Arnab Sen, and Jad C. Halimeh. "Weak ergodicity breaking in the Schwinger model". In: *Phys. Rev. B* 107 (20 May 2023), p. L201105. DOI: 10.1103/PhysRevB.107.L201105. URL: https://link.aps.org/doi/10.1103/PhysRevB.107.L201105 (cit. on p. 121).

[359] Giuseppe Calajó, Giovanni Cataldi, Marco Rigobello, Darvin Wanisch, Giuseppe Magnifico, Pietro Silvi, Simone Montangero, and Jad C. Halimeh. "Quantum many-body scarring in a non-Abelian lattice gauge theory". In: *Phys. Rev. Res.* 7 (1 Mar. 2025), p. 013322. DOI: 10.1103/PhysRevResearch.7.013322. URL: https://link.aps.org/doi/10.1103/PhysRevResearch.7.013322 (cit. on p. 121).

[360] D. Bluvstein et al. "Controlling quantum many-body dynamics in driven Rydberg atom arrays". en. In: *Science* 371.6536 (Mar. 2021), pp. 1355–1359. ISSN: 0036-8075, 1095-9203. DOI: 10.1126/science.abg2530. URL: https://www.science.org/doi/10.1126/science.abg2530 (visited on 04/22/2026) (cit. on p. 121).

[361] Guo-Xian Su, Hui Sun, Ana Hudomal, Jean-Yves Desaules, Zhao-Yu Zhou, Bing Yang, Jad C. Halimeh, Zhen-Sheng Yuan, Zlatko Papić, and Jian-Wei Pan. "Observation of many-body scarring in a Bose-Hubbard quantum simulator". en. In: *Physical Review Research* 5.2 (Apr. 2023), p. 023010. ISSN: 2643-1564. DOI: 10.1103/PhysRevResearch.5.023010. URL: https://link.aps.org/doi/10.1103/PhysRevResearch.5.023010 (visited on 04/22/2026) (cit. on p. 121).

[362] Pengfei Zhang et al. "Many-body Hilbert space scarring on a superconducting processor". en. In: *Nature Physics* 19.1 (Jan. 2023), pp. 120–125. ISSN: 1745-2481. DOI: 10.1038/s41567-022-01784-9. URL: https://www.nature.com/articles/s41567-022-01784-9 (visited on 04/22/2026) (cit. on p. 121).

[363] Aron Kerschbaumer, Marko Ljubotina, Maksym Serbyn, and Jean-Yves Desaules. "Quantum Many-Body Scars beyond the PXP Model in Rydberg Simulators". In: *Phys. Rev. Lett.* 134.16 (Apr. 2025), p. 160401. DOI: 10.1103/PhysRevLett.134.160401. URL: https://link.aps.org/doi/10.1103/PhysRevLett.134.160401 (cit. on p. 121).

[364] J. O. Austin-Harris, I. Rana, S. E. Begg, C. Binegar, T. Bilitewski, and Y. Liu. "Observation of Ergodicity Breaking and Quantum Many-Body Scars in Spinor Gases". en. In: *Physical Review Letters* 134.11 (Mar. 2025), p. 113401. ISSN: 0031-9007, 1079-7114. DOI: 10.1103/PhysRevLett.134.113401. URL: https://link.aps.org/doi/10.1103/PhysRevLett.134.113401 (visited on 04/22/2026) (cit. on p. 121).

[365] Peter Græns Larsen, Anne E. B. Nielsen, André Eckardt, and Francesco Petiziol. "Experimental protocol for observing single quantum many-body scars with transmon qubits". en. In: *SciPost Physics* 20.2 (Feb. 2026), p. 036. ISSN: 2542-4653. DOI: 10.21468/SciPostPhys.20.2.036. URL: https://www.scipost.org/SciPostPhys.20.2.036 (visited on 04/22/2026) (cit. on p. 121).

[366] Erik J. Gustafson, Andy C. Y. Li, Abid Khan, Joonho Kim, Doga Murat Kurkcuoglu, M. Sohaib Alam, Peter P. Orth, Armin Rahmani, and Thomas Iadecola. "Preparing quantum many-body scar states on quantum computers". In: *Quantum* 7 (Nov. 2023), p. 1171. ISSN: 2521-327X. DOI: 10.22331/q-2023-11-07-1171. URL: https://doi.org/10.22331/q-2023-11-07-1171 (cit. on p. 121).

[367] Jean-Yves Desaules, Erik J. Gustafson, Andy C. Y. Li, Zlatko Papić, and Jad C. Halimeh. "Robust finite-temperature many-body scarring on a quantum computer". en. In: *Physical Review A* 110.4 (Oct. 2024), p. 042606. ISSN: 2469-9926, 2469-9934. DOI: 10.1103/PhysRevA.110.042606. URL: https://link.aps.org/doi/10.1103/PhysRevA.110.042606 (visited on 04/22/2026) (cit. on p. 121).

[368] Leonard Logarić, John Goold, and Shane Dooley. *Dynamical signatures of conventional and asymptotic quantum many-body scars on a trapped ion simulator*. 2026. arXiv: 2604.12296 [quant-ph]. URL: https://arxiv.org/abs/2604.12296 (cit. on p. 121).

[369] Jutho Haegeman, J. Ignacio Cirac, Tobias J. Osborne, Iztok Pi žorn, Henri Verschelde, and Frank Verstraete. "Time-Dependent Variational Principle for Quantum Lattices". In: *Phys. Rev. Lett.* 107 (7 Aug. 2011), p. 070601. DOI: 10.1103/PhysRevLett.107.070601. URL: https://link.aps.org/doi/10.1103/PhysRevLett.107.070601 (cit. on p. 121).

[370] Jutho Haegeman, Christian Lubich, Ivan Oseledets, Bart Vandereycken, and Frank Verstraete. "Unifying time evolution and optimization with matrix product states". In: *Phys. Rev. B* 94 (16 Oct. 2016), p. 165116. DOI: 10.1103/PhysRevB.94.165116. URL: https://link.aps.org/doi/10.1103/PhysRevB.94.165116 (cit. on p. 121).

[371] Boye Buyens, Jutho Haegeman, Karel Van Acoleyen, Henri Verschelde, and Frank Verstraete. "Matrix Product States for Gauge Field Theories". In: *Phys. Rev. Lett.* 113 (9 Aug. 2014), p. 091601. DOI: 10.1103/PhysRevLett.

113.091601. URL: https://link.aps.org/doi/10.1103/PhysRevLett.113.091601 (cit. on p. 121).

[372] Stefan Kühn, Erez Zohar, J Ignacio Cirac, and Mari Carmen Bañuls. "Non-Abelian string breaking phenomena with matrix product states". In: *Journal of High Energy Physics* 2015.7 (2015), pp. 1–26. DOI: https://doi.org/10.1007/JHEP07(2015)130. URL: https://link.springer.com/article/10.1007/JHEP07(2015)130 (cit. on pp. 121, 122).

[373] Boye Buyens, Jutho Haegeman, Henri Verschelde, Frank Verstraete, and Karel Van Acoleyen. "Confinement and String Breaking for QED_2 in the Hamiltonian Picture". In: *Phys. Rev. X* 6 (4 Nov. 2016), p. 041040. DOI: 10.1103/PhysRevX.6.041040. URL: https://link.aps.org/doi/10.1103/PhysRevX.6.041040 (cit. on p. 121).

[374] T. Pichler, M. Dalmonte, E. Rico, P. Zoller, and S. Montangero. "Real-Time Dynamics in U(1) Lattice Gauge Theories with Tensor Networks". In: *Phys. Rev. X* 6 (1 Mar. 2016), p. 011023. DOI: 10.1103/PhysRevX.6.011023. URL: https://link.aps.org/doi/10.1103/PhysRevX.6.011023 (cit. on p. 121).

[375] Marco Rigobello, Simone Notarnicola, Giuseppe Magnifico, and Simone Montangero. "Entanglement generation in (1+1)D QED scattering processes". In: *Phys. Rev. D* 104 (11 Dec. 2021), p. 114501. DOI: 10.1103/PhysRevD.104.114501. URL: https://link.aps.org/doi/10.1103/PhysRevD.104.114501 (cit. on p. 121).

[376] Ron Belyansky, Seth Whitsitt, Niklas Mueller, Ali Fahimniya, Elizabeth R. Bennewitz, Zohreh Davoudi, and Alexey V. Gorshkov. "High-Energy Collision of Quarks and Mesons in the Schwinger Model: From Tensor Networks to Circuit QED". In: *Phys. Rev. Lett.* 132 (9 Feb. 2024), p. 091903. DOI: 10.1103/PhysRevLett.132.091903. URL: https://link.aps.org/doi/10.1103/PhysRevLett.132.091903 (cit. on p. 121).

[377] Irene Papaefstathiou, Johannes Knolle, and Mari Carmen Bañuls. "Real-time scattering in the lattice Schwinger model". In: *Phys. Rev. D* 111 (1 Jan. 2025), p. 014504. DOI: 10.1103/PhysRevD.111.014504. URL: https://link.aps.org/doi/10.1103/PhysRevD.111.014504 (cit. on p. 121).

[378] Mattia Morgavi, Peter Majcen, Marco Rigobello, Simone Montangero, and Pietro Silvi. *Preparation and detection of quasiparticles for quantum simulations of scattering*. 2026. arXiv: 2604.16210 [quant-ph]. URL: https://arxiv.org/abs/2604.16210 (cit. on p. 121).

[379] Giovanni Cataldi, Simone Orlando, and Jad C. Halimeh. *Real-Time String Dynamics in a $2+1D$ Non-Abelian Lattice Gauge Theory: String Breaking, Glueball Formation, Baryon Blockade, and Tension Reduction*. 2025. arXiv: 2509.08868 [hep-lat]. URL: https://arxiv.org/abs/2509.08868 (cit. on p. 122).

[380] D. M. Brink and G. R. Satchler. *Angular momentum*. Oxford University Press, 1993 (cit. on p. 126).

List of Figures

List of Tables